Enhancement of the BRICK constitutive model to incorporate viscous soil behaviour

Samuel David Clarke
MENG

Thesis submitted to

The University of Sheffield
Department of Civil and Structural Engineering

for the degree of Doctor of Philosophy

August 2009

For Elaine

Declaration

I, Samuel David Clarke, confirm that the work presented in this thesis is my own. Where information has been derived from other sources, I confirm that this has been indicated in the thesis.

August 2009

Abstract

Enhancement of the BRICK constitutive model to incorporate viscous soil behaviour

The Brick model is an advanced elasto-plastic constitutive model for soils and has become a recognised tool for modelling ground behaviour, following its implementation into the finite element program Safe. The model can reproduce many essential elements of soil behaviour, which is viewed from a strain-based perspective. An analogue for the model is that of a man walking around a room, pulling a number of bricks with strings of different lengths behind him. The room represents strain space, the man's movement is the applied strain and each brick movement is the response of a proportion of the soil.

The present Brick model, although advanced, does not account for viscous behaviour, including creep and strain rate dependent stiffness, which can be very significant for clay soils. The principal aim of the work was to incorporate such behaviour into the Brick model. Two main approaches were identified manipulating either the velocity of the bricks or the string lengths. Both approaches were implemented into the Brick model allowing a series of tests to be conducted into their predictive capabilities. Isotach strain rate behaviour was investigated with both models by simulating both constant and step rate of strain tests.

Simulations of past experimental work into the combined effects of creep and recent stress history on clay soil stiffness were also conducted. It was demonstrated, in accordance with the experiments, that creep can erase the effects on the initial stiffness of recent stress history involving relatively short stress paths approaching the current state, though this was not true for longer approach paths. The experimental results were more correctly simulated using the model with manipulated, strain rate dependent string lengths, the SRD Brick model.

The SRD Brick model was then implemented into Safe to allow the analysis of two case histories, thereby quantifying the influence that viscous effects can have. The first involved the analysis of surface displacements above the westbound tunnel forming part of the Jubilee Line extension beneath St James's Park, London. The second analysis was concerned with the prediction of heave displacements of a deep basement in Horseferry Road, London. The SRD Brick model was able to significantly improve on the predictions given by the original Brick model in both cases.

Acknowledgements

Firstly, I would like to thank my supervisor Dr Charles Hird for being a source of constant guidance and advice throughout the period of this research. The quality of the work owes much to his dedication and attention to detail. My thanks also go to Dr Brian Simpson of Arup Geotechnics for his support in the understanding of the Brick model and its implementation into the finite element program Safe.

The research project was made possible through an Engineering and Physical Sciences Research Council (EPSRC) DTA award from the Civil and Structural engineering department at the University of Sheffield.

I would also like to thank all those in the numerical skills team at Arup, especially Anton and Hoe, for supporting me through my placements with the team during my PhD. Working in industry helped broaden my perspectives, which has been very valuable.

Many thanks are due to the academic staff in the Geotechnical Engineering Group, who have supported me in my work. Special thanks go to Prof. Adrian Hyde and Dr Colin Smith for the useful soil mechanics discussions and helping guide my academic goals.

Being part of the geotechnics research group has been a great experience and I owe a great deal to the productive environment that was created by having such supportive colleagues. Thanks are especially due to Sam and Lu for helping me stay motivated when things did not go exactly as expected.

Finally, I am very grateful to my family for their ever-present support which has kept me going throughout the research. I am also indebted to my wonderful wife Elaine, who has stood by my side and provided love, support and encouragement when I needed it most.

Contents

Contents v

List of Tables x

List of Figures xi

List of Symbols xviii

List of Abbreviations xxii

List of Brick Terms xxiii

1 Introduction 1

1.1 Background . . . 1
1.2 Aims of Research . . . 2
1.3 Outline of Thesis . . . 2

2 Literature Review 4

2.1 Introduction . . . 4
2.2 Soil Behaviour . . . 4
2.2.1 Small strain stiffness . . . 4
2.2.2 Stress history . . . 9
2.2.3 Time dependent behaviour . . . 15
2.2.4 Strain rate dependent behaviour . . . 21
2.2.5 Other influencing factors . . . 28
2.3 Constitutive Models for Soil . . . 29
2.3.1 Elasto-plastic models . . . 29
2.3.2 Critical state soil mechanics . . . 31
2.3.3 Some kinematic hardening models . . . 34
2.4 The BRICK Model . . . 39
2.4.1 Variations of BRICK . . . 40
2.5 Discussion . . . 43

3 The BRICK Model 45

3.1 Introduction . . . 45

3.2 Parameters used in the BRICK Model 46
3.2.1 Two-dimensional BRICK 46
3.2.2 Three-dimensional BRICK 47
3.2.3 Derivation of geotechnical parameters 49
3.2.4 Strain paths to simulate common geotechnical scenarios 50
3.3 BRICK Computations 51
3.3.1 The beta effect 54
3.3.2 Plastic strain reduction 55
3.4 BRICK Behaviour 56
3.4.1 String lengths 56
3.4.2 Modelling stress history 58
3.4.3 Predicting failure in BRICK 61
3.4.4 Prediction of the critical state line 63
3.4.5 Initial brick positions 66
3.5 The BRICK Program 70

4 Bricks on Ice 72

4.1 Introduction 72
4.2 Brick-led Viscous Motion 72
4.2.1 Introducing time 73
4.2.2 Generating brick velocities 73
4.2.3 Including viscous brick strains 74
4.3 Recreating results of Den Haan (2001) 76
4.3.1 Stress relaxation 77
4.3.2 Strain fixation 79
4.3.3 Biaxial testing 79
4.4 Comparing Coaxial Deceleration Models 83
4.5 Testing the Capabilities of the Bricks on Ice Model 84
4.5.1 Test sequence 84
4.5.2 Swelling and recompression tests 85
4.5.3 Undrained shearing 87
4.5.4 Undrained shearing with varying overconsolidation ratios 91
4.5.5 Undrained shearing with holding period prior to shearing 97
4.5.6 Constant stress (virgin creep) 99

4.6 Manipulating the Bricks on Ice Model . . . 101
4.6.1 Failure angle increase due to Bricks on Ice . . . 101
4.6.2 Modifications to the initial brick positions . . . 103
4.7 Benchmarking Bricks on Ice with Experimental Data . . . 104
4.7.1 Calibration of the Bricks on Ice model. . . . 107
4.7.2 Short approach path with creep (17SH). . . . 107
4.7.3 Short approach path, no creep allowed (17.3SH) . . . 110
4.7.4 Repeat simulation of the 17.3SH tests (17.3SH-B) . . . 113
4.7.5 Long approach path, creep allowed (17.3SH-L). . . . 113
4.7.6 Overview . . . 115

5 Strain Rate Dependent String Lengths 116

5.1 Introduction . . . 116
5.1.1 Model components . . . 117
5.2 Man-led Strain Rate Dependency . . . 121
5.2.1 Implementing the SRD approach into BRICK . . . 123
5.2.2 Initial tests . . . 123
5.2.3 Constant rate of strain (CRS) tests . . . 124
5.2.4 Step rate of strain (SRS) tests . . . 126
5.2.5 Stress relaxation tests . . . 128
5.2.6 Gradual change in strain rate (GCS) tests . . . 130
5.2.7 Discussion . . . 132
5.3 Brick-led Strain Rate Dependency . . . 133
5.3.1 Iterative approach. . . . 133
5.3.2 Accounting for time . . . 134
5.3.3 Initial tests . . . 137
5.3.4 Step change of strain rate (SRS) tests . . . 138
5.3.5 Stress relaxation tests . . . 139
5.3.6 Swelling and recompression tests . . . 141
5.4 Benchmarking the SRD Model . . . 142
5.4.1 Graham et al. (1983) . . . 143
5.4.2 Gasparre (2005) . . . 146
5.4.3 Comparing the SRD model with Bricks on Ice . . . 155
5.5 Discussion . . . 159

6 Finite Element Modelling 161

6.1 Introduction . . . 161

6.2 Implementation into SAFE . . . 161
6.3 Model Validation . . . 163
6.4 Case History 1: Jubilee Line Extension . . . 166
6.4.1 Previous work . . . 169
6.4.2 Assumptions and mesh. . . . 174
6.4.3 Mohr-Coulomb analysis . . . 177
6.4.4 BRICK analysis . . . 181
6.4.5 SRD BRICK analysis . . . 185
6.4.6 Discussion . . . 188
6.5 Case History 2: Horseferry Road . . . 193
6.5.1 Background . . . 193
6.5.2 Assumptions and mesh. . . . 193
6.5.3 BRICK & SRD BRICK analyses . . . 200
6.5.4 Discussion . . . 204

7 Summary and Conclusions 206
7.1 Introduction . . . 206
7.2 The BRICK Model . . . 206
7.3 Bricks on Ice . . . 207
7.4 Strain Rate Dependent String Lengths . . . 208
7.5 Finite Element Modelling . . . 210
7.6 Future Research . . . 212

References 214

A BRICK Parameter Proofs 221
A.1 Stress-strain relationships . . . 221
A.2 Octahedral shear strain . . . 222

B MATLAB code 223
B.1 The BRICK model . . . 223
B.2 Theory code comparison . . . 227
B.3 The Bricks on Ice model . . . 228
B.4 The strain rate dependency model . . . 231
B.4.1 Man-led strain rate code . . . 231
B.4.2 Brick-led strain rate code. . . . 234

C BRICK Program Modifications 239
C.1 Introduction . . . 239
C.2 The Language Barrier . . . 239
C.3 Testing . . . 240

D SAFE Modifications 242
D.1 Implementation into SAFE . . . 242
D.2 Finite Element Models and Runs . . . 243
D.2.1 St James's Park . . . 244
D.2.2 Horseferry Road . . . 244

E Computing Requirements 245
E.1 Hardware . . . 245
E.2 Software . . . 246

List of Tables

2.1 Classification of common time effects, Sorensen (2006) 29

3.1 Rankine BRICK string parameters, Simpson (1992b) 56
3.2 Modified BRICK string parameters, Kanapathipillai (1996) 57

4.1 BRICK parameters used with Bricks on Ice 87
4.2 Test stage analysis 105
4.3 Specific stages for the 17SH tests 108
4.4 Specific stages for the 17.3SH tests 111
4.5 Specific stages for the 17.3SH-L tests 115

5.1 BRICK parameters for man-led SRD model testing 124
5.2 BRICK parameters for the brick-led SRD model testing 137
5.3 SRS data from Graham et al. (1983) 143
5.4 BRICK parameters for Graham, Crooks & Bell (1983) simulation 144
5.5 SRD BRICK parameters for modelling Gasparre (2005) 150

6.1 Soil parameters for London Clay - single element analysis 163
6.2 Verification of single element test 165
6.3 Volume loss achieved, Addenbrooke, Potts & Puzrin (1997) 170
6.4 Constant model parameters - St James's Park, Addenbrooke et al. (1997) 177
6.5 Mohr-Coulomb parameters for London Clay - St James's Park 178
6.6 BRICK soil parameters for London Clay - St James's Park analysis . . . 181
6.7 BRICK string parameters for St James's Park 182
6.8 SRD BRICK string parameters for St James's Park 185
6.9 SRD BRICK rate parameters for St James's Park 185
6.10 Maximum vertical displacements for St James's Park 188
6.11 Mohr-Coulomb parameters for the Horseferry Road analysis 197
6.12 Horseferry Road finite element model stage analysis 199
6.13 Comparison of predicted heave displacements 205

List of Figures

2.1 Comparison between laboratory and in-situ stiffnesses, St. John (1975) . 5
2.2 Approximate strain limits for reliable measurement of soil stiffness, after Atkinson (2000), Atkinson & Sallfors (1991) and Mair (1993) 6
2.3 Definition of p' and p'_p on a plot of specific volume versus mean stress . 7
2.4 Variation of G_{max} (or G_0) for London Clay 8
2.5 Schematic diagram of kinematic sub-yield surfaces, after Jardine (1992) 9
2.6 Comparison of the stiffness of Chalk, London Clay and Bothkennar Clay, showing linear elastic very small strain region, Clayton & Heymann (2001) 10
2.7 Stress paths followed in constant p' tests, after Atkinson, Richardson & Stallebrass (1990) 11
2.8 Stiffness of reconstituted London Clay versus strain measured in constant p' tests, after Atkinson et al. (1990) 11
2.9 Stress paths applied to London Clay, after Clayton & Heymann (2001) . 12
2.10 Strain-dependent stiffness of a single London Clay specimen under two different loading paths, Clayton & Heymann (2001) 13
2.11 Tangent stiffness degradation curves, Gasparre, Nishimura, Minh, Coop & Jardine (2007) 14
2.12 Drained creep tests on undisturbed London Clay, Bishop (1966) 16
2.13 Strain rate versus time relationships during drained creep of London Clay, Singh & Mitchell (1968) 17
2.14 Definition of instant and delayed compression, after Bjerrum (1967) . . 18
2.15 Comparison between theories A and B for secondary compression, after Hight, Jardine & Gens (1987) 19
2.16 Concept of isochrones, Bjerrum (1967) 20
2.17 Gain in undrained strength due to creep, Vaid & Campanella (1977) . . 20
2.18 Constant rate of strain (CRS) testing, after Sorensen (2006) 21
2.19 Step-changed rate of strain (SRS) testing, after Sorensen (2006) 22
2.20 Stress-strain behaviour of Saint-Jean-Vianney clay in CRS triaxial compression, after Vaid, Robertson & Campanella (1979) 22
2.21 Stress-strain curves for triaxial compression tests, Graham et al. (1983) 23
2.22 Stress-strain curves for one-dimensional compression tests, after Leroueil, Kabbaj, Tavernas & Bouchard (1985) 24

2.23 SRS oedometer tests on Batiscan Clay, Leroueil et al. (1985) 25
2.24 Different viscosity types for geomaterials, after Tatsuoka (2007) 25
2.25 Consolidated undrained triaxial tests on Hostun sand, Tatsuoka, Ishihara, Di Benedetto & Kuwano (2002) 26
2.26 Undrained triaxial compression tests on normally consolidated clay, Oka, Kodaka, Kimoto, Ishigaki & Tsuji (2003) 27
2.27 Behaviour of Toyoura and Hostun sands at the residual state, after Duttine, Tatsuoka, Lee & Kongkitkul (2009) 28
2.28 Elastic perfectly plastic response of a soil leading to failure 29
2.29 Total stress yield surfaces 30
2.30 Effective stress yield surfaces 31
2.31 Critical state framework 32
2.32 Normalised state boundary surface in stress space 33
2.33 State boundary surface of the critical state framework in $e-p'-q$ space, Burland (1989) 33
2.34 The kinematic yield surface effect, after Simpson, O'Riordan & Croft (1979) 35
2.35 Yield locus. Cam clay locus; stable (S) and unstable (U) regions, Al-Tabbaa & Wood (1989) 36
2.36 Sketch of the 3-SKH model in triaxial stress space, after Stallebrass & Taylor (1997) 36
2.37 Constant p' loading after four stress path rotations: G against q, predictions of the 3-SKH model as implemented into ICFEP, Grammatikopoulou (2004) 37
2.38 Constant p' loading after four stress path rotations: G against q, predictions of the M3-SKH model as implemented into ICFEP, Grammatikopoulou (2004) 38
2.39 Predictions of the 3-SKH and M3-SKH models for undrained triaxial compression test: normalised stiffness vs. strain curve, Grammatikopoulou, Zdravkovic & Potts (2008) 38
2.40 The S-shaped curve represented in stepwise fashion, after Simpson (1992b) 39
2.41 Surface settlements above the Heathrow trial tunnel, after Kanapathipillai (1996) 41
2.42 Stress relaxation with Bricks on Ice, Den Haan (2001) 42
2.43 Strain fixation with Bricks on Ice, Den Haan (2001) 42

3.1 Mohr's circle of strain 46

3.2 Flow chart showing internal workings of the BRICK model 52
3.3 Comparison between models for the effect of overconsolidation on stiffness 55
3.4 Reduction in string lengths 58
3.5 How BRICK models stress history 59
3.6 Stress path plots for differing overconsolidation ratios 60
3.7 Brick paths for differing overconsolidation ratios 62
3.8 Wet and dry states defined by the critical state framework 64
3.9 Critical state lines predicted by BRICK for normally consolidated and overconsolidated soils 65
3.10 Critical state lines predicted by BRICK for normally consolidated and heavily overconsolidated soils 65
3.11 Stress paths from plane strain undrained shearing, Sketchley & Bransby (1973) 66
3.12 Diagram of plausible initial brick positions 66
3.13 Effect of initial brick positions - v versus s 67
3.14 Effect of initial brick positions - stress path plot 68
3.15 Effect of initial brick positions - normalised stiffness 69
3.16 Routines within BRICK and SAFE 70

4.1 Calculation of brick velocities 75
4.2 Stress relaxation during 1D compression, Den Haan (2001) 78
4.3 Stress relaxation during 1D compression, MATLAB recreation 78
4.4 Strain fixation with Bricks on Ice, Den Haan (2001) 80
4.5 Strain fixation with Bricks on Ice, MATLAB recreation using CoAD v1 . 80
4.6 Strain fixation with Bricks on Ice, MATLAB recreation using CoAD v2 . 81
4.7 CIU tests with variation of creep parameter, Den Haan (2001) 82
4.8 Plane strain biaxial testing with variation of creep parameter 82
4.9 Stress path plots for swelling and recompression tests showing the comparison between the two CoAD models 83
4.10 Volumetric strain versus mean stress plot for swelling and recompression tests, for both CoAD models 84
4.11 Stress path plot for 1D swelling and recompression 86
4.12 Volumetric strain versus mean stress for 1D swelling and recompression 86
4.13 Stress path plot for undrained isotropic shearing 88
4.14 Schematic diagram for undrained shearing in strain space 88
4.15 Stress path plot for undrained shearing following 1D compression 89

4.16 Comparison between the angle of failure in both extension and compression after isotropic or 1D compression 90
4.17 Comparison between the angle of failure in both extension and compression after isotropic or 1D compression with the effect of creep 90
4.18 Stress-strain plot for shearing following isotropic compression 91
4.19 Stress-strain plot for shearing following 1D compression 92
4.20 Stress-small strain plot for compressive shearing following 1D compression 92
4.21 1D stress path plots showing the effects of overconsolidation and creep . 94
4.22 1D stress-strain plots showing the effects of overconsolidation and creep 95
4.23 Stress strain plots for varying OCRs following 1D compression 96
4.24 Extension stress-strain plots for varying OCRs following 1D compression 96
4.25 Stress path plot for undrained shearing following 1D compression with a holding period 98
4.26 Stress path plots for undrained shearing following 1D compression comparing the effects of the duration of the holding period 98
4.27 Volumetric strain versus mean stress for virgin creep showing the effects of the modified approach 100
4.28 Shear stiffness during virgin creep tests 100
4.29 Parametric study into the effects of creep and overconsolidation on the rise in theta 102
4.30 Parametric study of theta versus creep rate for varying Brick theories . 102
4.31 Modifications to the initial brick positions 103
4.32 Creep strains before undrained shear tests- 17SH, Gasparre (2005) . . . 106
4.33 Dissipation of creep strains before undrained shear tests 106
4.34 Stiffness degradation curves for 17SH, Gasparre (2005) 109
4.35 Stiffness degradation curves for 17SH, Bricks on Ice model 109
4.36 Stiffness degradation curves for 17.3SH, Gasparre (2005) 112
4.37 Stiffness degradation curves for 17.3SH, Bricks on Ice model 112
4.38 Stiffness degradation curves for 17.3SH-B, Bricks on Ice model 113
4.39 Stiffness degradation curves for 17.3SH-L, Gasparre (2005) 114
4.40 Stiffness degradation curves for 17.3SH-L, Bricks on Ice model 114

5.1 Framework for the strain rate dependent approach 116
5.2 Comparison between strain rate dependency laws 119
5.3 Time dependent behaviour within the SRD framework 120
5.4 Man-led SRD model CRS tests, $v - \log p'$ plot 125

5.5 Schematic diagram of isotach isotropic compression curves with lower limit of initial volumetric strain, Sorensen (2006) 125
5.6 Man-led SRD model CRS tests, stress path plot 126
5.7 Man-led SRD model SRS tests, $v - \log p'$ plot 127
5.8 Man-led SRD model SRS tests, stress path plot 128
5.9 Man-led SRD model stress relaxation tests, $v - \log p'$ plot 129
5.10 Man-led SRD model stress relaxation tests, stress path plot 129
5.11 Man-led SRD model gradual change in strain rate tests, $v - \log p'$ plot . 130
5.12 Changes in string length modification factor during the gradual change in strain rate tests 131
5.13 Man-led SRD model gradual change in strain rate tests, stress path plot 132
5.14 Visualisation of Equation 5.8 135
5.15 Framework for the calculation of the current strain rate 136
5.16 Brick-led SRD model SRS test results, $v - \log p'$ plot 138
5.17 Brick-led SRD model SRS test results, stress path plot 139
5.18 Brick-led SRD model stress relaxation tests, $v - \log p'$ plot 140
5.19 Brick-led SRD model stress relaxation tests, stress path plot 140
5.20 Brick-led SRD model swelling and recompression tests, $v - \log p'$ plot . 141
5.21 Brick-led SRD model swelling and recompression tests, stress path plot 142
5.22 Graham et al. (1983) comparison 145
5.23 Stiffness developed during SRS tests 145
5.24 Viscosity index from tests on London Clay, Sorensen, Baudet & Simpson (2007a) 147
5.25 Sorensen (2006) test comparison 147
5.26 Fitting the Brick parameters to Gasparre (2005) 148
5.27 Stiffness degradation for samples from sub-unit B2(c) sheared from their in situ stress state, Gasparre (2005) 148
5.28 Strain rates for Sample 17SH during approach paths, Gasparre (2005) . 149
5.29 Shear stiffness during the undrained shear tests on sample 17SH, Gasparre (2005) 152
5.30 Stiffness degradation following 10kPa approach paths with creep allowed 152
5.31 Shear stiffness for the undrained shear test on sample 17.3SH, Gasparre (2005) 154
5.32 Stiffness degradation following 10kPa approach paths with no creep allowed 154
5.33 Shear stiffness during the undrained shear tests on sample 17.3SH-L, Gasparre (2005) 156

5.34 Stiffness degradation following 100kPa approach paths with creep allowed 156
5.35 Comparison of SRD and BOI models for short approach path tests with creep . . . 157
5.36 Comparison of SRD and BOI models for short approach path tests without creep . . . 158
5.37 Comparison of SRD and BOI models for long approach path tests with creep . . . 159

6.1 Implementation of the SRD model into SAFE . . . 162
6.2 Single finite element . . . 163
6.3 Single element test result comparison . . . 164
6.4 Soil profile and tunnel geometry at St James's Park, after Addenbrooke et al. (1997) . . . 167
6.5 Progression of volume loss at St James's Park, Dimmock & Mair (2007) 167
6.6 Monitoring data from the St James's Park twin tunnels, Nyren, Standing & Burland (2001) . . . 168
6.7 Surface settlement profiles for the westbound tunnel after Addenbrooke et al. (1997) . . . 170
6.8 Finite element mesh for St James's Park, Addenbrooke (1996) . . . 171
6.9 Configuration of the kinematic surfaces in the M3-SKH model, Grammatikopoulou (2004) . . . 172
6.10 Comparison of predictions of modified three-surface model (M3-SKH) for analyses sh-c and sh, after Grammatikopoulou et al. (2008) . . . 173
6.11 Comparison of ground surface settlement profiles predicted by M3-SKH model, adapted from Grammatikopoulou et al. (2008) . . . 173
6.12 Regions for SAFE mesh generation, St James's Park twin tunnels . . . 174
6.13 Finite element mesh, St James's Park twin tunnels . . . 175
6.14 Parametric study on the effect of number of nodes used to approximate the tunnel lining . . . 176
6.15 Calculation of g for St James's Park . . . 178
6.16 Tunnel geometry comparison . . . 179
6.17 Displacement contours for the Mohr-Coulomb analysis of St James's Park 180
6.18 Surface displacement plot for the Mohr-Coulomb analysis . . . 180
6.19 BRICK predicted K_0 profile . . . 182
6.20 Mohr-Coulomb and BRICK tunnel geometry comparison . . . 183
6.21 Displacement contours for the BRICK analysis of St James's Park . . . 184
6.22 Surface displacement plot for the BRICK analysis . . . 184

6.23 SRD BRICK and BRICK tunnel geometry comparison 186
6.24 Displacement contours for the SRD BRICK analysis of St James's Park . 187
6.25 Surface displacement plot for the SRD BRICK analysis 187
6.26 Surface comparison plots for St James's Park 189
6.27 Propagation of displacements analysis of St James's Park 190
6.28 Parametric study into the effect of the string length on the predicted surface displacements for St James's Park 192
6.29 Horseferry Road site plan, after Chapman (1999) 194
6.30 Site section showing relevant borehole information, Chapman (1999) . . 195
6.31 Original heave data with initial predictions, May (1975) 196
6.32 Diagrammatic section of the basement, May (1975) 196
6.33 Finite element mesh for Horseferry Road 197
6.34 Calculation of g for Horseferry Road 199
6.35 Contours of pore water pressure immediately after the basement slab construction 201
6.36 Change in pore pressure with time at Point A 201
6.37 Contours of resultant displacement for March 1990 202
6.38 Heave predictions starting from September 1967 203
6.39 Comparison of heave predictions with field measurements 204

B.1 Volumetric strain versus mean stress for swelling and recompression code comparison test 226
B.2 Mean stress versus shear stress for swelling and recompression code comparison test 226

C.1 Validation of the BRICK program - SRS and stress relaxation test . . . 241
C.2 Validation of the BRICK program - creep test 241

List of Symbols

α	Exponential decay factor used in the man-led SRD model.
α	Viscous constant relating the log change in axial strain to the log change in deviator stress.
β	Viscous constant.
β_G	The effect that overconsolidation has on the increase in stiffness.
β_{mod}	Beta modification factor.
β_ϕ	The effect that overconsolidation has on the increase in failure angle.
β^*	Rate parameter from Biscontin & Pestana (2001).
δ	Small change.
ε	Current strain (position of the man).
ε_a	Axial strain.
$\dot{\varepsilon}_a$	Axial strain rate.
ε_b	Position of the Brick.
ε_e	Plastic strain reduction.
ε_{ir}	Irrecoverable strain.
$\dot{\varepsilon}_{\text{prev}}$	Strain rate during the previous increment.
$\dot{\varepsilon}$	Applied strain rate.
$\dot{\varepsilon}_{\text{ref}}$	Reference strain rate.
ε_s	Shear strain.
$\dot{\gamma}$	Vectorial shear strain rate.
$\dot{\varepsilon}_{\text{test}}$	Testing strain rate.
ε_v	Volumetric Strain.
ε_{vec}	Vectorial strain (separation of man and brick).
ε_x	Horizontal strain.
ε_y	Vertical strain.
Γ	Specific volume on CSL at a mean normal stress of 1kPa.
$\dot{\gamma}$	Applied strain rate.
γ	Vectorial sum of the shear strain components.
${\gamma_{oct}}^2$	Octahedral Shear Strain.
γ_{dry}	Dry bulk unit weight.
γ_e	Elastic shear strain.
$\dot{\gamma}_{\text{ref}}$	Reference strain rate.

$\dot{\gamma}_0$	Rate of vectorial shear strain in the previous increment (2D).
γ_{sat}	Saturated bulk unit weight.
γ_{w}	Bulk unit weight of water.
γ_{xy}	Shear strain in 2 component BRICK model.
ι	Gradient of the pure elastic behaviour line in log-log space.
κ	Gradient of the swelling and recompression line.
κ^*	Gradient of the swelling and recompression line in log-log space.
λ	Gradient of the normal consolidation line.
λ	Rate of increase per log cycle.
λ^*	Gradient of the normal consolidation line in log-log space.
ν	Poisson's Ratio.
ϕ'	Angle of shearing resistance.
ϕ'_{mob}	Mobilised angle of shearing resistance.
σ_1	Major principal stress.
σ_3	Minor principal stress.
σ_a	Axial stress.
σ'_h	Horizontal effective stress.
σ_r	Radial stress.
σ'_v	Vertical effective stress.
σ_x	Horizontal stress 1.
σ_y	Vertical stress.
σ_z	Horizontal stress 2.
θ	Failure angle.
c	Creep constant Den Haan (2001).
c'	Cohesive strength.
C_α	Secondary compression index.
E'	Drained Young's modulus.
${E_h}'$	Horizontal Young's modulus.
E_{max}	Elastic Young's modulus.
E_u	Undrained Young's modulus.
${E_v}'$	Vertical Young's modulus.
G	Tangential shear modulus.
G_{hh}	Shear modulus in horizontal plane.

G_{max}	Maximum shear stiffness.
G_{vh}	Shear modulus in the vertical planes (Independent shear modulus).
G_{vh}	Shear modulus in vertical plane.
k	Permeability of the soil.
K_0	In situ earth pressure coefficient in undisturbed soil.
m	Gradient of the line relating the logarithm of strain rate with the logarithm of time.
m'	Ratio of the independent shear modulus to vertical Young's modulus.
M	Gradient of the stress path in critical state soil mechanics.
n'	Ratio of horizontal to vertical Young's modulus.
N	Specific volume on NCL at a mean normal stress of 1kPa.
p'	Effective mean normal stress in triaxial testing.
p'_0	Initial mean effective stress (1kPa).
p_a	Atmospheric pressure.
p'_e	Equivalent pressure on the isotropic compression line at the current specific volume.
q	Deviator stress in triaxial testing.
R_0	Overconsolidation ratio defined using p'.
s	Mean normal stress in two-dimensions.
s_0	Initial mean normal stress.
s_u	Undrained shear strength.
$s_{u,\mathrm{ref}}$	Undrained shear strength measured at the reference strain rate $\dot{\gamma}_{\mathrm{ref}}$.
$\mathrm{SL}_{\mathrm{prev}}$	String lengths during the previous increment.
$\mathrm{SL}_{\mathrm{ref}}$	References string lengths.
$\mathrm{SL}_{\mathrm{test}}$	String lengths measured during testing.
t	Current time in seconds.
$\mathrm{t}_{\mathrm{prev}}$	Time in seconds at the end of the previous BRICK increment.

v	Specific volume (Chapter 2 only).
v	Volumetric strain.
v_0	Initial volumetric strain.
v'	Angle of dilation.
v_e	Elastic volumetric strain.
v_k	Specific volume on the swelling line at a mean normal stress of 1kPa.
v_p	Plastic volumetric strain.
$\dot{v}$	Volumetric strain rate.
$\dot{v}_0$	Rate of volumetric strain in the previous increment.
V_l	Volume loss for defining tunnelling efficiency.
V_s	Volume of transverse settlement trough per metre length of tunnel (m^3/m).
Y_1	Yield surface characterising a change from linear elastic to non-linear elastic Jardine (1992) behaviour.
Y_2	Yield surface characterising a change from elastic to elasto-plastic behaviour Jardine (1992).
Y_3	Local boundary surface Jardine (1992).

List of Abbreviations

3-SKH	Three-surface kinematic hardening model (Stallebrass & Taylor 1997).
BOI	Bricks on Ice.
CoAD v1	Coaxial deceleration model version 1 (Den Haan 2001).
CoAD v2	Coaxial deceleration model version 2.
CRS	Constant rate of strain.
CSL	Critical state line.
EOP	End of primary consolidation.
GCS	Gradual change in strain rate.
ICFEP	Imperial College finite element program.
KYS	Kinematic yield surface.
M3-SKH	Modified 3-SKH model (Grammatikopoulou 2004).
NCL	Normal compression line.
OCR	Overconsolidation ratio.
SRD	Strain rate dependent.
SRS	Step change of strain rate.
TBM	Tunnel boring machine.
TESRA	Temporary effect of strain rate and strain acceleration.
TXC	Undrained triaxial compression test.
TXE	Undrained triaxial extension test.

List of Brick Terms

BETA(1)	Beta-G.
BETA(2)	Beta-ϕ.
BRICKA	Control routine for the BRICK program.
BRICKB	Routine containing the main BRICK model code.
BRICK	The program into which the BRICK model was implemented.
BRICK	ARUP Geotechnics constitutive model for soils used within the SAFE finite element program and the BRICK program, (Simpson 1992).
GGMAX	Stiffness Reduction Array.
NB	Number of Bricks used for BRICK calculations.
NC	Number of Components used for BRICK calculations.
SL	String Length.
SAFE	ARUP Geotechnics finite element program.
SN(1)	Strain component 1- Volumetric Strain.
SN(2)	Strain component 2- Shear Strain.
SS(1)	Stress component 1- Mean Stress.
SS(2)	Stress component 2- Shear Stress.
ZERO(2)	Initial conditions array (1)- Volumetric Strain (2)- Mean Stress.

1 Introduction

1.1 Background

The accurate prediction of displacements is key to the successful completion of complex problems in our increasingly crowded urban environment, where much time and effort needs to be spent to safeguard existing structures from the impact of new construction projects. Sophisticated finite element analyses can be used to predict deformations, but the accuracy of these predictions is dependent upon the ability of the underlying constitutive model to represent the true behaviour of the soil.

The pre-failure deformation of overconsolidated clays is known to be governed by the highly non-linear, inelastic behaviour of the soil. In recent years a number of constitutive models have been developed to attempt to model the small strain behaviour more accurately (Stallebrass & Taylor (1997), Simpson (1992b) & Jardine (1992)) with the results being a large improvement over the predictions of simple linear elastic / perfectly plastic models.

These advanced models can be split into three main categories: non-linear elastic, kinematic yield surface or 'bubble' models and strain-based models such as Brick. Recent testing conducted on London Clay has shown that not only is the small strain behaviour inelastic and non-linear but it is also susceptible to the effects of creep and other viscous phenomena (Gasparre (2005) & Sorensen (2006)). Thus a constitutive model that encompassed small-strain and time-related effects could help improve the predictions made by numerical modelling. Previous research conducted by Kanapathipillai (1996) has already shown that the modelling of time related effects can improve the predictions of currently problematic areas such as surface displacements above tunnels.

1.2 Aims of Research

The main aim of the research described in this thesis has been to develop the current Brick model to be able to deal with viscous effects such as creep, stress relaxation and strain rate dependency. A review of literature has been carried out to classify those facets of soil behaviour that were already encompassed by the Brick model and those that were to be introduced into the model. The detailed workings of the Brick model and other recent variations have been fully explored to identify areas of behaviour that were modelled well and those where modelling could have been improved. The enhanced Brick model has been benchmarked against previous physical tests that combined the effects of stress history, strain rate and creep (Gasparre 2005) to see if the enhanced model is able to deal with these features. Finally, the enhanced model has been implemented into the Arup finite element program Safe, and a set of case histories has been modelled to see the impact of the enhancements in realistic scenarios.

1.3 Outline of Thesis

The thesis contains seven chapters in total. This chapter (Chapter 1) gives the introduction as well as an overview of the contents of the subsequent chapters.

Chapter 2 presents a detailed review of the published literature. The areas of interest are those of soil behaviour, including stress history, time and strain rate dependent effects, and constitutive models for soils. Simple linear elastic / perfectly plastic models are initially reviewed, before an overview of the critical state framework and some advanced kinematic hardening models is given. The aim of the literature review is to assess which factors are likely to govern the behaviour of overconsolidated clays and to see if and how they have been previously modelled.

Chapter 3 details the internal workings of the Brick model, from the formulation of the stress and strain components to examples of the predicted behaviour. This chapter is designed to give the reader the necessary background of the Brick model to allow an easier understanding of the more complex behaviour modelled in subsequent chapters.

Chapter 4 demonstrates the capabilities of a variation of the Brick model called 'Bricks on Ice' developed by Den Haan (2001). This includes recreating the published test results and then modifying the code to try to improve the predicted behaviour. A series of tests was conducted on the modified Bricks on Ice model to assess its capabilities

when modelling the effects of creep and stress relaxation. The Bricks on Ice model was also used to simulate the testing conducted by Gasparre (2005). The Bricks on Ice model has no way of accounting for the effects of strain rate but this was the main focus of Chapter 5.

Chapter 5 deals with modelling strain rate and time dependent effects simultaneously. A overview of the relevant strain rate models is presented along with a framework to allow these effects to be modelled within BRICK. Two sets of logic are presented for the implementation of the strain rate dependency effects into BRICK, both being used to simulate simple tests. The one seen to simulate the tests with most accuracy is then used to model physical tests from the literature review (Graham et al. (1983) & Gasparre (2005)).

Chapter 6 presents the finite element implementation of the strain rate dependent BRICK model, along with single element tests to ensure that the code is functioning correctly in the ARUP finite element program, SAFE. Two case histories from London are then described, along with any previous modelling work. The first case history is that of the construction of the westbound Jubilee Line Extension running tunnel beneath St James's Park. The second is a back-analysis of the long term heave experienced due to the construction of the a deep basement in Horseferry Road.

Chapter 7 summarises the findings of the research, highlighting the capabilities of the enhanced BRICK model. Areas for possible future research that have become apparent during the current work are also identified.

2

Literature Review

2.1 Introduction

This chapter presents a review of the published literature in relation to the understanding and modelling of the deformation behaviour of saturated clays, with particular attention given to viscous effects. This includes the background to the development of the Brick model including the key effects that the model incorporated, along with the equivalent approaches adopted by conventional stress based models and their development. A description of viscous effects seen in clays has also been included. For the purposes of this thesis viscous effects are taken to include both time and strain-rate dependent behaviour. The literature review has been split into two main sections, those of soil behaviour and constitutive models for soils.

2.2 Soil Behaviour

2.2.1 Small strain stiffness

In the case of many construction projects fine control over the generated deformations is required to minimise disturbance to the surrounding area. This is especially true for deep excavations in heavily overconsolidated soils such as London Clay. It was found that in this type of project the shear strains governing the movements lie between the small strain region, $< 0.01\%$, and the large strain region, $> 1\%$, (Simpson et al. 1979). St. John (1975) compared the stiffness measured in laboratory tests with those back-calculated from field data and found a considerable variation, seen in Figure 2.1. The higher stiffnesses observed in the field were attributed to 'threshold effects' in the clay, whereby if the soil is subjected to a small stress probe the stiffness recorded is higher than that recorded when using a large probe. A comparison of the strains used to generate the data shown (Figure 2.1) was given in Simpson et al. (1979) who showed the strains in the field were in the 0.01-0.1% region while conventional laboratory

testing was done using strains greater than 0.2%. This identified the need to measure the stiffness in the small strain region.

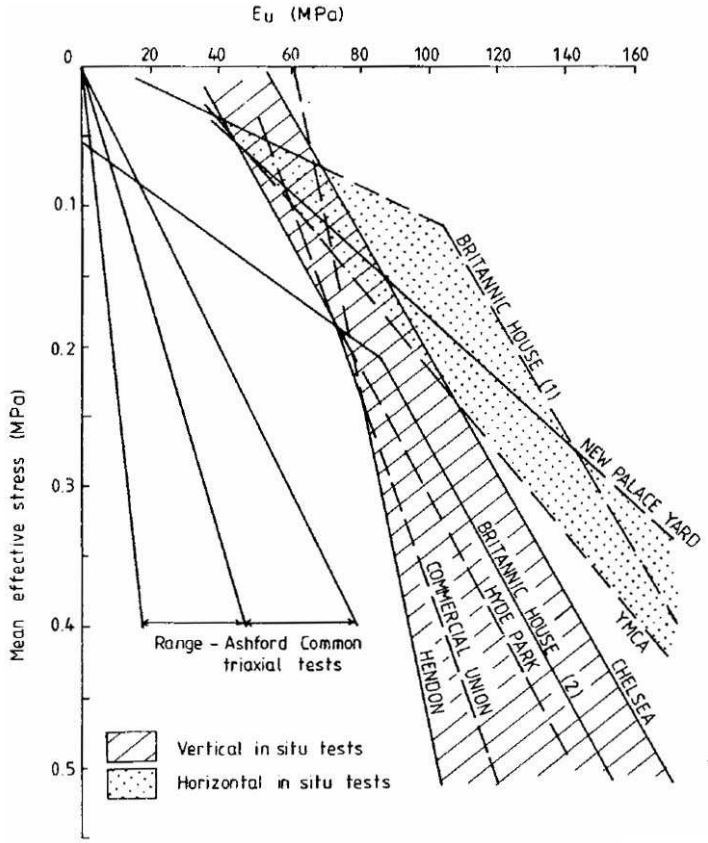

Figure 2.1: Comparison between laboratory and in-situ stiffnesses, St. John (1975)

Jardine, Symes & Burland (1984) set about measuring the small strain stiffness of North Sea clay using a electrolytic level device that allowed the strains to be resolved down to 0.01%. The stiffness at small strains was found to be highly non-linear and could be modelled by the use of an S-Shaped curve as seen in Figure 2.2. In the very small strain region (<0.001%) the behaviour of the soil is assumed to be perfectly elastic with the strains being fully recoverable. As further straining occurs the shear modulus degrades smoothly with increasing strain (Burland 1989). The linear elastic region was identified accurately by Clayton & Heymann (2001) as being below 0.002-0.003% axial strain in triaxial tests. It was also noted that a sample should be allowed a period of rest before shearing to allow the creep strains to decline so as not to affect the measured initial stiffness. This period ranges from 1-3 days for clay from the Scottish soft clay test site at Bothkennar to 6-12 days for stiff overconsolidated deposits such as London Clay. As the stiffness of a soil is dependent on the strain rate, in Figure 2.2 the soil is assumed

to have been sheared at a constant strain rate to eliminate any associated effects.

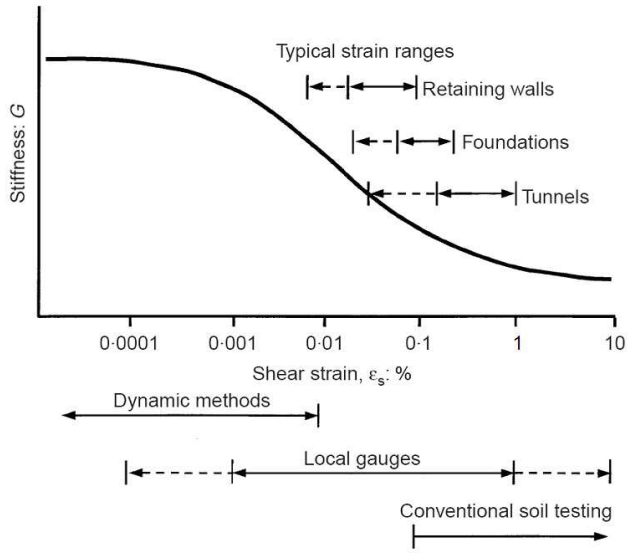

Figure 2.2: Approximate strain limits for reliable measurement of soil stiffness, after Atkinson (2000), Atkinson & Sallfors (1991) and Mair (1993)

The initial shear stiffness shown in Figure 2.2 is normally termed G_{max} or G_0 and represents the elastic shear stiffness of the soil. G_{max} can be determined in the laboratory using dynamic testing methods such as bender element or resonant column testing, or from static triaxial tests conducted at very small strains using very high resolution local measurement systems. Although G_{max} relates to the shear stiffness at very small strains, it can in fact be determined at any strain level by using a stress path reversal to develop the elastic shear stiffness, as will be shown in Section 2.2.2.

It was noted by Jardine (1992) that the linear elastic region in stress space can grow in size as a result of overconsolidation or ageing effects, which has direct implications for the formulation of the BRICK model as explained in detail in Section 3.3.1. The implications of non-linear soil behaviour for practical design were discussed by Atkinson (2000).

A formulation for the increase in elastic shear stiffness with overconsolidation for clays was proposed by Hardin (1978):

$$G_{max} = S\mathrm{f}(v)\mathrm{OCR}^k {p_a}^{1-n} {p'}^n \tag{2.1}$$

where:

S = dimensionless coefficient which depends on the nature of the soil,

f(v) = function of the specific volume,
p' = mean effective stress,
p_a = atmospheric pressure,
OCR = overconsolidation ratio and
k & n are material constants.

Equation 2.1 can be simplified by redefining the overconsolidation ratio in terms of the stress at the intersection of a swelling line with the normal consolidation line, seen in Figure 2.3.

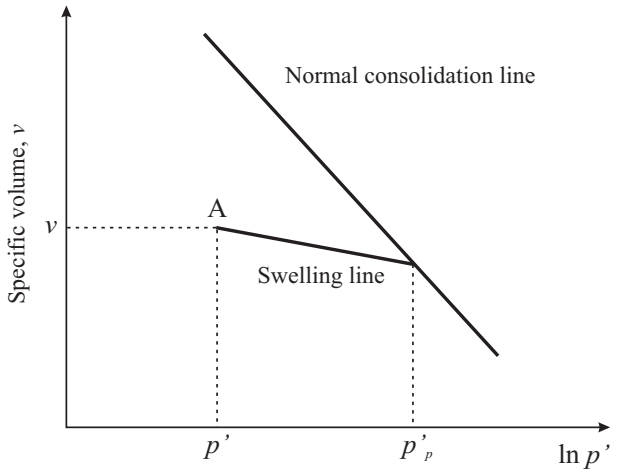

Figure 2.3: Definition of p' and p'_p on a plot of specific volume versus mean stress

Viggiani & Atkinson (1995) proposed the following equation based on laboratory triaxial compression and extension tests conducted on reconstituted clay samples with bender elements used to determine G_{max}:

$$\frac{G_{max}}{p_a} = A \left(\frac{p'}{p_a} \right)^n {R_0}^m \tag{2.2}$$

where:

p_a = reference pressure (1kPa),
R_0 = overconsolidation ratio p'_p/p' from Figure 2.3 and
A, n and m are material constants.

This form of equation was shown to be applicable to the behaviour of London Clay by the tests done by Viggiani & Atkinson (1995) and Jovičić & Coop (1998) as seen in Figure 2.4. The testing conducted by Viggiani & Atkinson (1995) concentrated on the measurement of the vertical elastic shear stiffness, whereas Jovičić & Coop (1998) investigated both horizontal and vertical elastic shear stiffnesses. Figure 2.4(b) shows the

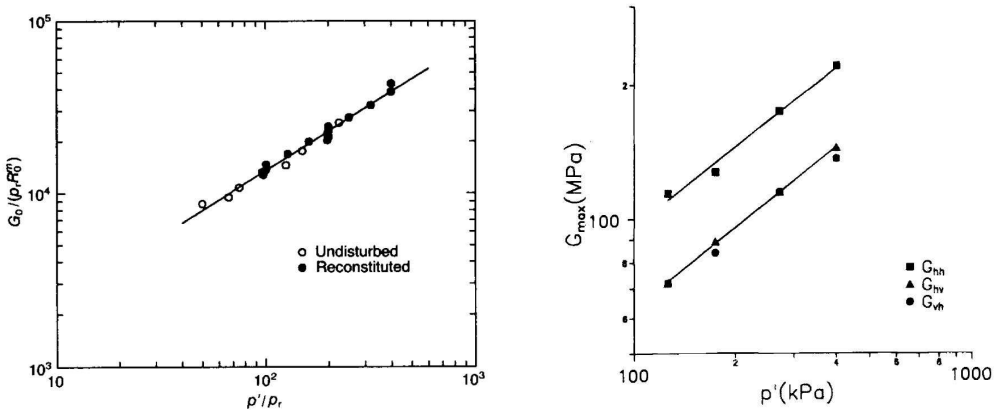

(a) Normalised results, Viggiani & Atkinson (1995)

(b) Directional results, Jovičić & Coop (1998)

Figure 2.4: Variation of G_{max} (or G_0) for London Clay

cross-anisotropy present in natural samples of London Clay with the horizontal shear stiffness being greater than the vertical shear stiffnesses, which was also seen in the Young's modulus plots in Figure 2.1. This anisotropy is a result of the predominantly one-dimensional stress history, as would be expected for London Clay.

A framework for the characterisation of the small strain behaviour of soils was introduced by Jardine, Potts, St John & Hight (1991) who proposed an empirical framework based on triaxial tests done using locally-measured strains. In the Jardine framework, three sub-surfaces are defined within a bounding surface, each defined by progressively larger stresses, as seen in Figure 2.5, where p'_e is the equivalent pressure on the isotropic compression line at the current specific volume. The framework uses the three sub-surfaces to define the behaviour pre-yield, effectively creating three kinematic zones and a yield surface, which will be discussed later in Section 2.3.3.

a) Y_1 Surface

The area inside the Y_1 surface defines the zone of linear elastic response. Within this zone the strains are directly proportional to the stresses applied, and hence the load-unload paths are expected to coincide giving fully recoverable strains. The real limits of this zone have only recently been measured and correspond to very small strains, typically less than 0.002%. This can be seen in Figure 2.6. The position of the Y_1 surface can be affected by the influence of creep as the soil strains without any change in stress giving rise to a stiffer response than expected when straining recommences. Currently there are no models which dynamically move the position of the Y_1 surface

to account for the rise in stiffness caused by creep or other time related effects.

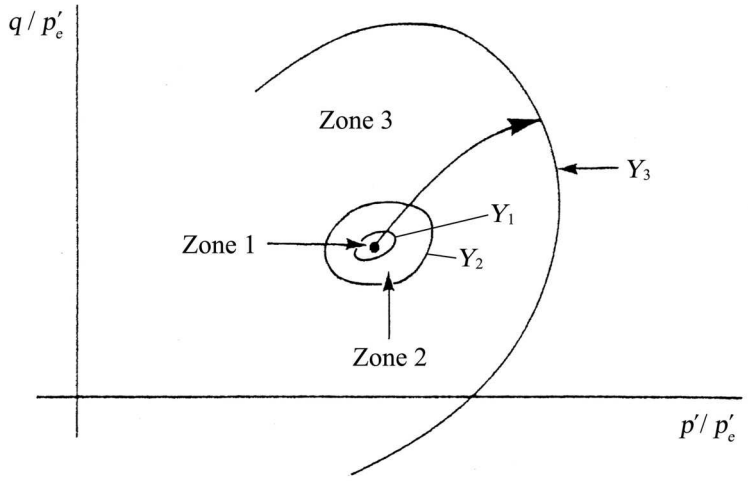

Figure 2.5: Schematic diagram of kinematic sub-yield surfaces, after Jardine (1992)

b) Y_2 Surface

In zone two (between the Y_1 and Y_2 surfaces) the behaviour changes from linear elastic to a non-linear but hysteretic behaviour, so that complete load-unload cycles show fully recoverable behaviour. Jardine (1992) also suggests that, as clays with non-linear hysteretic loops can return to their original state after unloading, this may be evidence to support the idea that viscous effects contribute to the non-linear behaviour observed.

c) Y_3 Surface

Zone three (between the Y_2 and Y_3 surfaces) is defined as the area of irrecoverable plastic strains, which become increasingly important as the stress path approaches the Y_3 (local boundary) surface.

The definition of the yield surfaces used by Jardine (1992) has widely been adopted when describing stiffness degradation, especially in regard to the features of kinematic yield surface models.

2.2.2 Stress history

It was shown in Section 2.2.1 that the shear stiffness of an overconsolidated soil depends heavily upon its previous stress history. From a general point of view this is covered by the use of the overconsolidation ratio which can be used to calculate the elastic shear stiffness of an overconsolidated soil based upon the pre-consolidation pressure and the

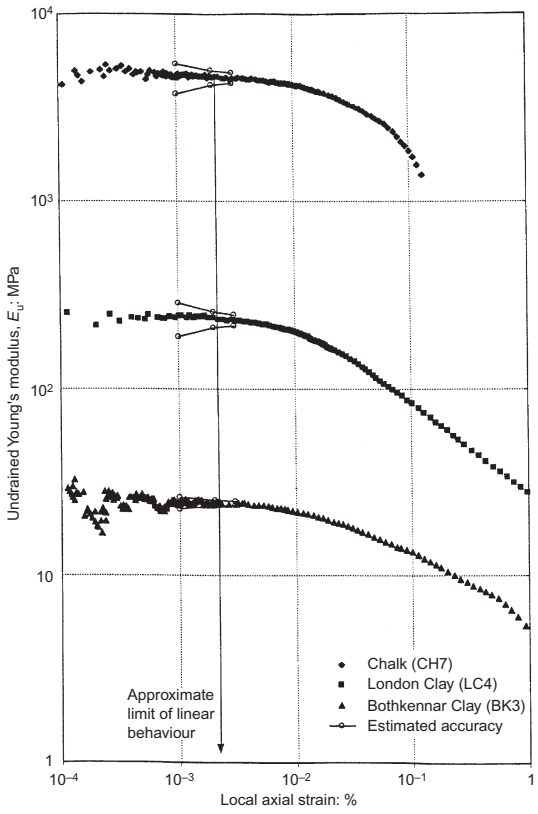

Figure 2.6: Comparison of the stiffness of Chalk, London Clay and Bothkennar Clay, showing linear elastic very small strain region, Clayton & Heymann (2001)

current stresses in the soil. The effects of non-geological or 'recent' stress history have been found to also have a large effect of the stiffness response of a sample under testing, especially in the small strain region. Atkinson et al. (1990) defined the term 'recent stress history' as the current path undertaken by the soil in relation to the previous stress path, which might take the form of a change of direction in the stress path or an extended period of rest.

Atkinson et al. (1990) conducted drained constant effective mean stress, p', and deviator stress, q, tests on reconstituted overconsolidated London Clay, where the samples were brought to the same stress state (O in Figure 2.7) by different approach paths before being sheared along a common load path, OA in the constant p' tests shown in Figure 2.7. The approach paths were 90kPa in length and a period of 3 hours was allowed before loading along path OA. At the end of the holding period it was noted that the rates of volumetric creep were too small to be measured by the volume gauge.

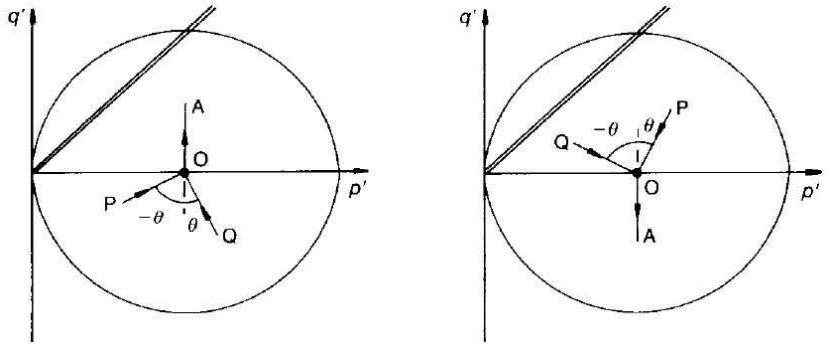

Figure 2.7: Stress paths followed in constant p' tests, after Atkinson et al. (1990)

Atkinson et al. (1990) found that the direction of the stress path immediately before the shearing phase (OA) of a test dramatically affected the measured stiffness within the soil during the shearing phase. The degree of rotation in the path was linked to an increase in shear stiffness, i.e. the greater the rotation of the path, the higher the measured stiffness would be during the shearing phase, which is demonstrated in Figure 2.8. It was noted that at small strains of the order of 0.01% the stiffness for the $\theta = 180°$ test was approximately an order of magnitude larger than the corresponding stiffness for the

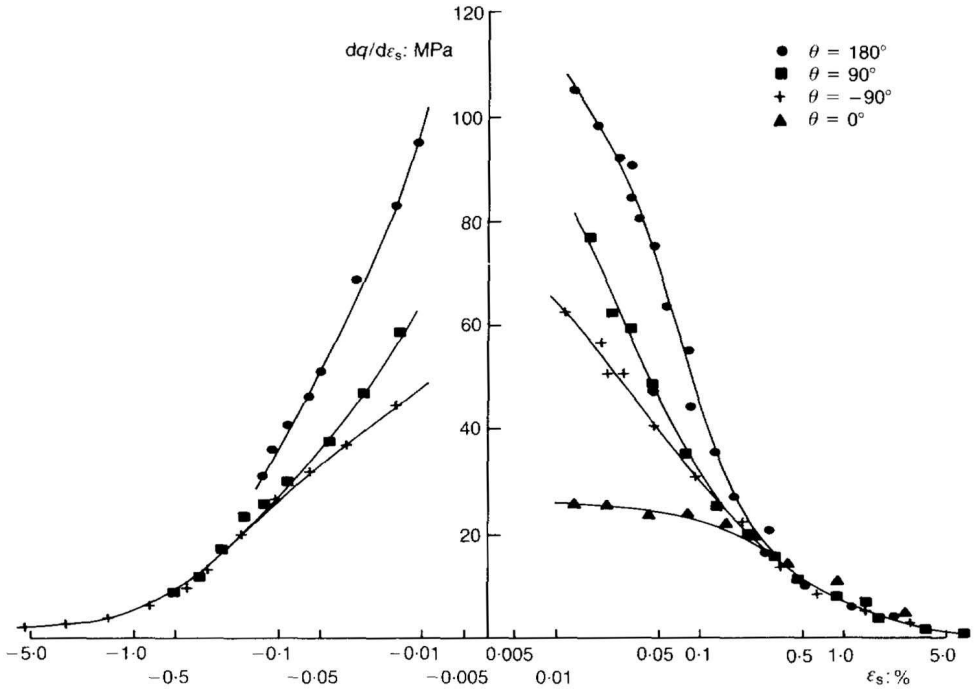

Figure 2.8: Stiffness of reconstituted London Clay versus strain measured in constant p' tests, after Atkinson et al. (1990)

$\theta = 0°$ test, but at strains of the order of 0.5% the differences had been largely removed.

Tests were also conducted holding q constant, which gave a similar pattern of results as seen in Figure 2.8, indicating that the variation in bulk modulus was just as dependent upon the angle of rotation in the approach stress path as the shear modulus.

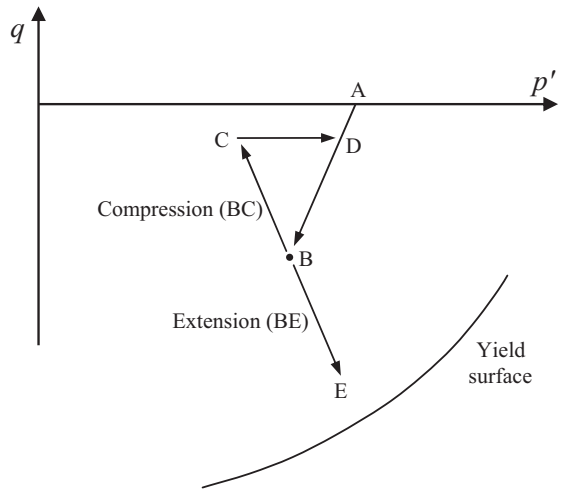

Figure 2.9: Stress paths applied to London Clay, after Clayton & Heymann (2001)

One criticism of the Atkinson et al. (1990) tests was that the samples were not allowed to rest sufficiently to completely rule out the possibility of creep strains affecting the generated stiffness (Clayton & Heymann 2001). The testing completed by Heymann (1998) was conducted on natural samples of London Clay and included a much longer holding period, prior to the loading stage, of approximately 6-12 days. The sample was consolidated to its in-situ effective mean stress, p', of 383kPa (A in Figure 2.9) and then brought to a deviator stress, q, of -200kPa (B), at which point the the sample was sheared in either compression (BC) or extension (BE). The testing was multi-stage meaning that both the extension and compression tests were conducted on the same sample. Hence the length of the compression path BC is of critical importance to the observed stiffness during the extension test.

Clayton & Heymann (2001) found that allowing the dissipation of creep strains meant that the measured initial stiffness was independent of the rotation in the stress path. This dramatically reduced the effects of recent stress history, to the point that it is no longer necessary to model the change in stress path. This leads to the initial stiffness of the soil being very close to the elastic Young's modulus, E_{max}, independent of the path taken, which can be seen for tests on London Clay in Figure 2.10. Although the

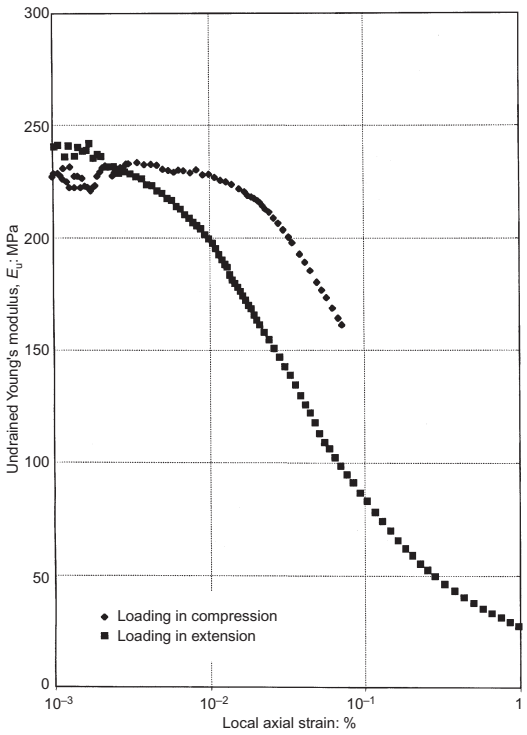

Figure 2.10: Strain-dependent stiffness of a single London Clay specimen under two different loading paths, Clayton & Heymann (2001)

initial stiffness is the same for both tests the reduction in stiffness occurs at different strain levels for the different rotations, which could be a sign of the persistent effects of the recent stress history. It can be inferred from the results that the compression path BC must have been short enough for the effects to be erased by the period of creep. For tests on Bothkennar Clay also completed by Clayton & Heymann (2001) a probe length of 10kPa was used which resulted in the same pattern of results as seen in Figure 2.10. The measured stiffnesses depend upon the magnitude of the creep that occurs in the soil prior to testing. If this is of sufficient magnitude it may be able to obscure and even erase the trends observed in creep free testing and thus erase the variation in the initial stiffness.

The effects of creep and the length of the stress probe were investigated by Gasparre (2005) to better understand the relationship between creep and the effects of recent stress history, and to clarify the cause of the contrasting results in Atkinson et al. (1990) and Clayton & Heymann (2001). Gasparre et al. (2007) found in tests on natural London Clay samples that a period of creep can eliminate the effects of the recent stress history (as found by Clayton & Heymann (2001)), if the approach path is less

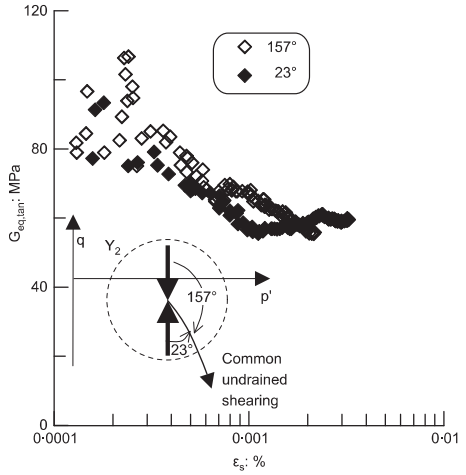

(a) Tangential stiffness degradation within the Y_2 surface with creep allowed

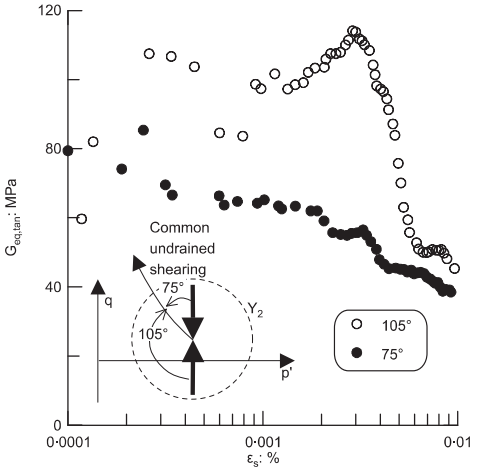

(b) Within Y_2 surface and creep not allowed

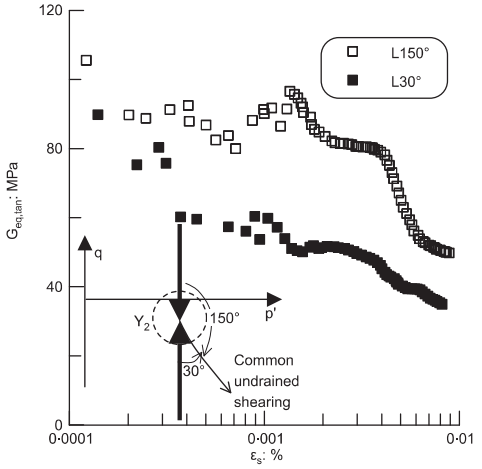

(c) Approach path engaging Y_2 surface and creep allowed

Figure 2.11: Tangent stiffness degradation curves, Gasparre et al. (2007)

than 10kPa, Figure 2.11(a). If creep is not allowed during the same short approach path test then the results show the same reduction in stiffness seen in Atkinson et al. (1990), Figure 2.11(b). Gasparre et al. (2007) also showed that for a longer (100kPa) approach stress path the results showed the influence of the recent stress history even with allowances for creep, Figure 2.11(c). Although both previous authors were correct, Gasparre et al. (2007) concluded that differences in the measured stiffnesses were due to the length of the approach path used in the testing. For tests where the Y_2 surface was engaged and moved, subsequent creep was not of a great enough magnitude to reduce the effects of the approach path and the usual reduction of stiffness due to a rotation in the stress path was observed.

2.2.3 Time dependent behaviour

Creep and stress relaxation are taken to be those effects that are directly related to the influence of time, and specifically not the effect of the rate of strain rate, which is to be discussed in Section 2.2.4. Creep refers to the time dependent shear and/or volumetric strains that develop at a rate controlled by the 'viscous resistance' of the soil (Mitchell 1993). The magnitude of the creep rate appears to be positively correlated with an increase in plasticity, water content and stress level.

Primary consolidation is normally attributed solely to the dissipation of excess pore water pressures within the soil giving rise to changes in effective stress. At the end of primary consolidation (EOP) the soil continues to strain at a reducing rate under constant stress. This stage is known as secondary compression and is normally attributed to creep alone as all the excess pore water pressures have dissipated. Hence the soil is under constant effective stress. Tertiary creep or creep rupture is a phenomenon observed when the soil creeps close to failure with a sufficiently large deviator stress. This leads to an acceleration of the creep strains towards failure of the soil.

Among the first studies to look in depth at the creep movements generated within clays was that of Bishop (1966) who undertook long term constant stress triaxial tests to develop an understanding of how creep behaviour changes over time. London Clay samples were loaded up to a specified percentage of their drained shear strength, determined from previous triaxial tests. This initial loading took place over a period of one week to allow the primary consolidation to complete.

It can be seen from the results shown in Figure 2.12 that there is a linear relationship

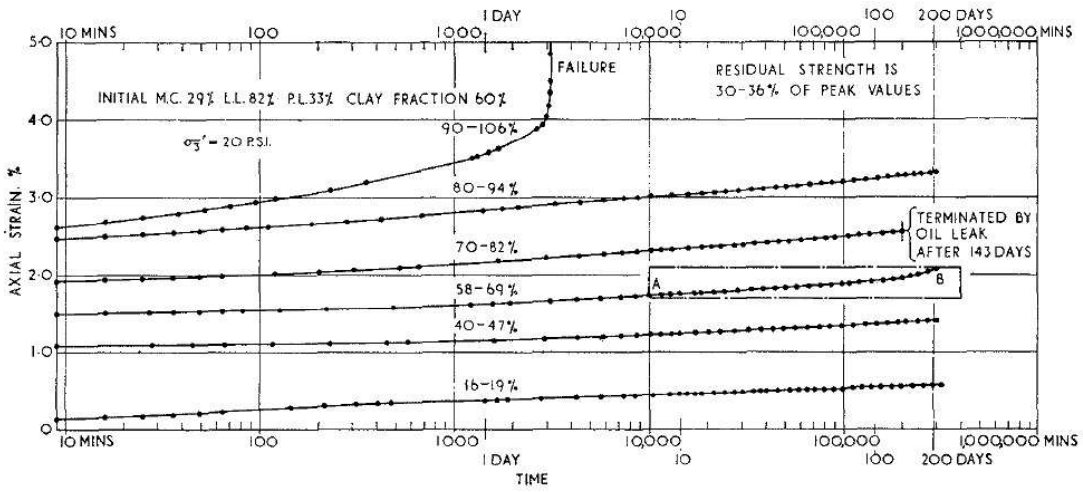

Figure 2.12: Drained creep tests on undisturbed London Clay, Bishop (1966)

between the axial strain and logarithm of time during the secondary stage of consolidation. The sample loaded to 90% of the drained strength can be seen to enter the tertiary stage of creep, leading to creep rupture and the failure of the clay after only 2 days and 4 hours. Singh & Mitchell (1968) replotted the results shown in Figure 2.12 to demonstrate the linear relationship between the logarithm of strain rate and the logarithm of time, Figure 2.13. As the initial loading of the samples took place over a week independent of the load applied, this led to different starting strain rates. The decay in strain rate is independent of the stress level applied to the sample, leading the authors to suggest an equation relating strain rate to time, Equation 2.3.

$$\dot{\varepsilon} = Ae^{\alpha q}\left(\frac{t_1}{t}\right)^m \tag{2.3}$$

where:

$\dot{\varepsilon}$ = strain rate,
A = strain rate at some arbitrarily chosen time, t_1,
α = constant of integration in the creep function,
q = deviator stress (σ_1-σ_3),
m = negative of the slope of the relationship between the logarithm of strain rate and the logarithm of time,
t = increase in time.

It is generally accepted that creep is the cause of secondary compression. It is however harder to be sure if creep affects the consolidation during the primary stage before all pore water pressures have been dissipated, as a result of the interdependence between

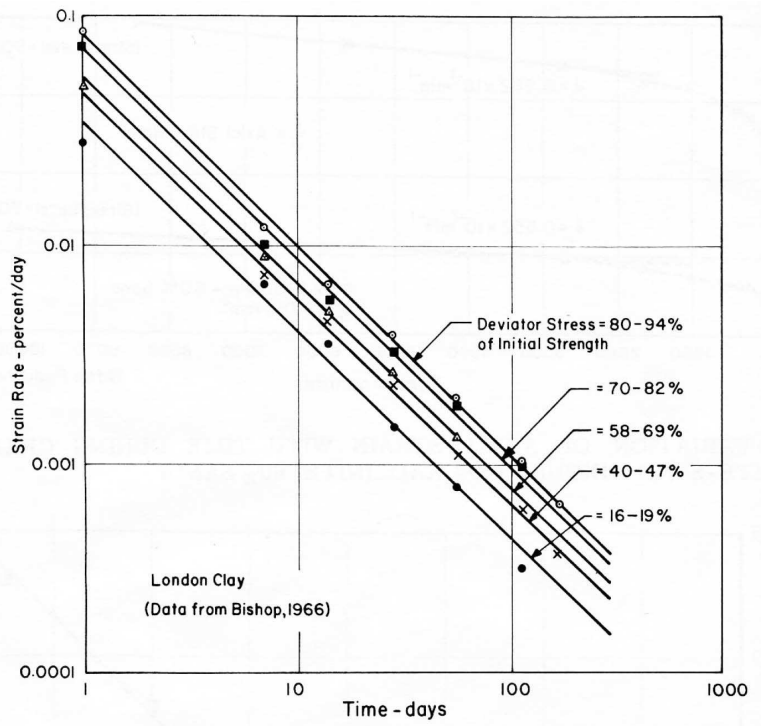

Figure 2.13: Strain rate versus time relationships during drained creep of London Clay, Singh & Mitchell (1968)

the void ratio and both the effective stress and time. Bjerrum (1967) presented tests conducted on a very sensitive normally consolidated marine clay. In the analysis of the findings Bjerrum suggested that there may also be another method for describing the consolidation stages of soft clays, that of 'instant' and 'delayed' compression. Instant compression is taken to occur simultaneously with an increase in effective stress and causes a reduction in void ratio until an equilibrium point is reached. Delayed compression represents a reduction in volume at unchanged effective stress.

The terms 'instant' and 'delayed' refer to the effective stresses, as opposed to the classical terms of primary and secondary which refer to the dissipation of pore water pressures. It can be noted that the definition of delayed compression is identical to that of secondary compression, the difference being in the starting point. It is inferred from Bjerrum (1967) that creep occurs during the primary consolidation phase as otherwise the instant and primary consolidations would be the same. This can be seen in Figure 2.14.

If creep settlements do occur during primary consolidation then there are two theories

pertaining to how the creep rate affects it (Ladd 1977).

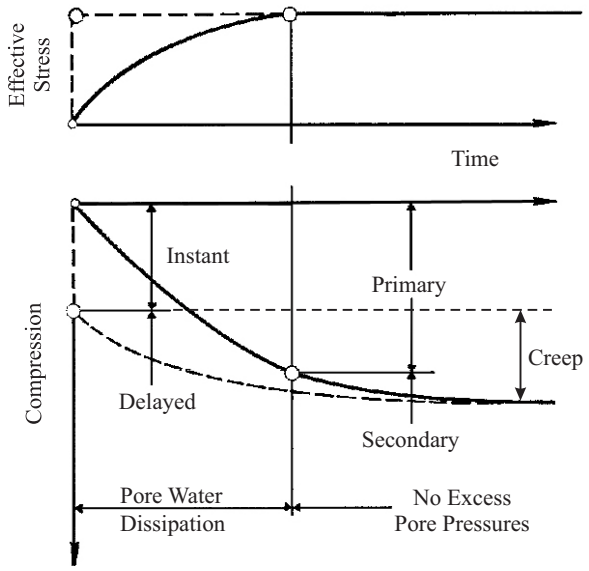

Figure 2.14: Definition of instant and delayed compression, after Bjerrum (1967)

Theory A, assumes that the creep component is independent of the time taken to reach EOP and therefore that the void ratio to vertical stress relationship is unique. Thus, the compression curve in the laboratory can be used directly for settlement analysis in the field, as supported by Mesri & Choi (1985).

Theory B, assumes the creep component is dependent upon the time taken to reach EOP and therefore that the void ratio to vertical stress relationship is not unique. This is based on the principle that clays are viscous and therefore influenced by the effects of strain rate during primary consolidation. The differing approaches are illustrated in Figure 2.15.

Leroueil (1995) examined both theories concluding that, for strain rates encountered in the laboratory, clays exhibit viscous behaviour during primary consolidation.

Although it is normally assumed that there are no excess water pressures during secondary compression this cannot be true. As the soil further consolidates any water contained within the structure will be forced out setting up pore water pressures within the soil. These pore water pressures are normally assumed to be negligible due to the

extensive period in which the secondary compression takes place. The rate of secondary compression can be modelled by the secondary compression index, C_α.

$$C_\alpha = \Delta e / \Delta log\, t \tag{2.4}$$

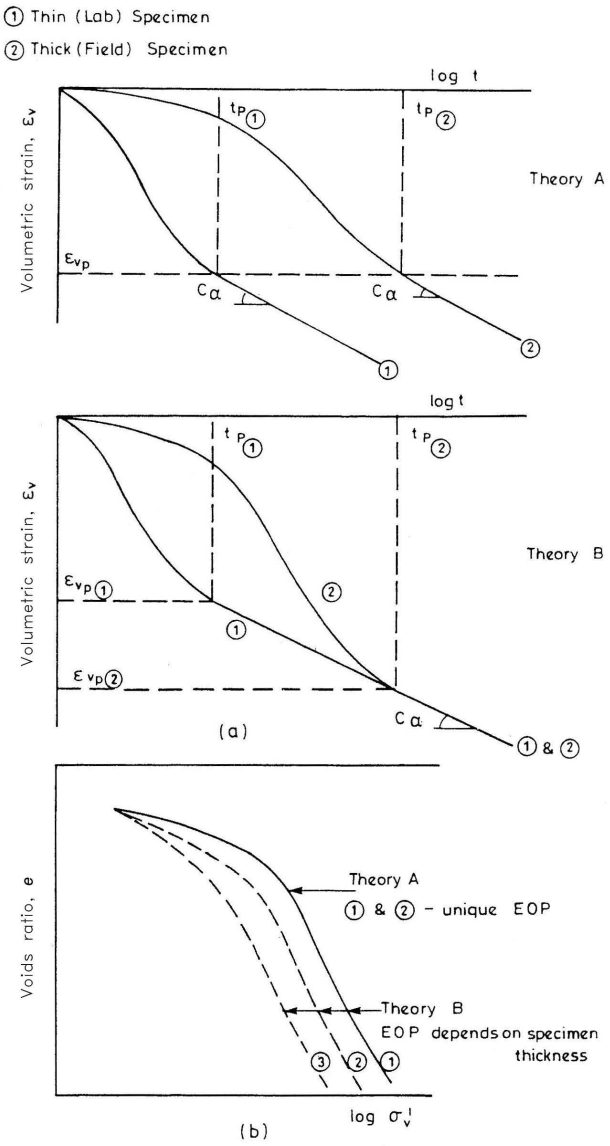

Figure 2.15: Comparison between theories A and B for secondary compression, after Hight et al. (1987)

Bjerrum (1967) introduced the idea of 'isochrones' which show the predicted amount of creep based upon a given increase in time, Figure 2.16. The reduction in void ratio was governed by a logarithmic decay law similar to that in Equation 2.3.

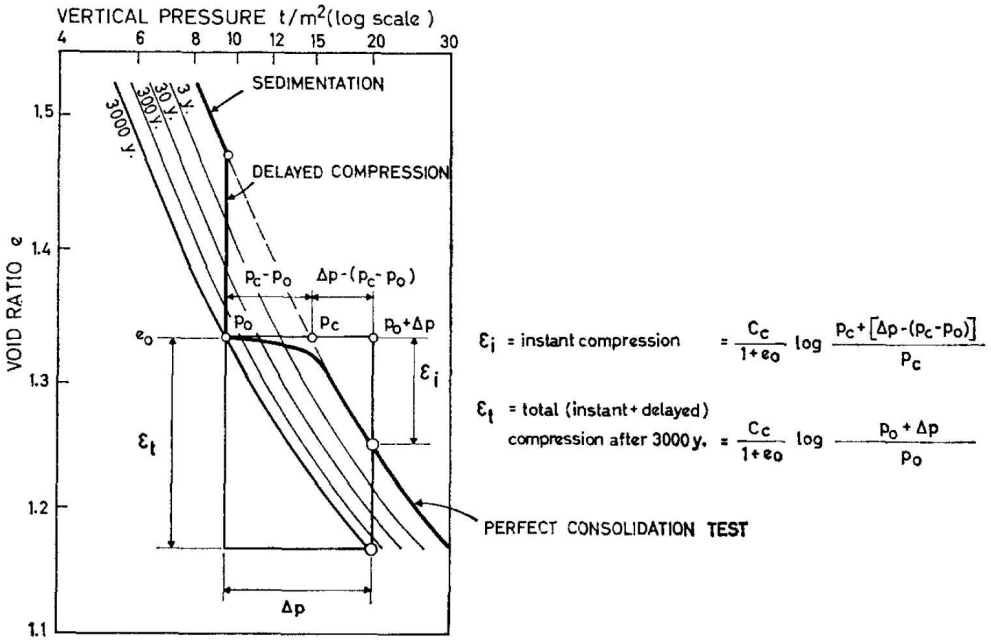

Figure 2.16: Concept of isochrones, Bjerrum (1967)

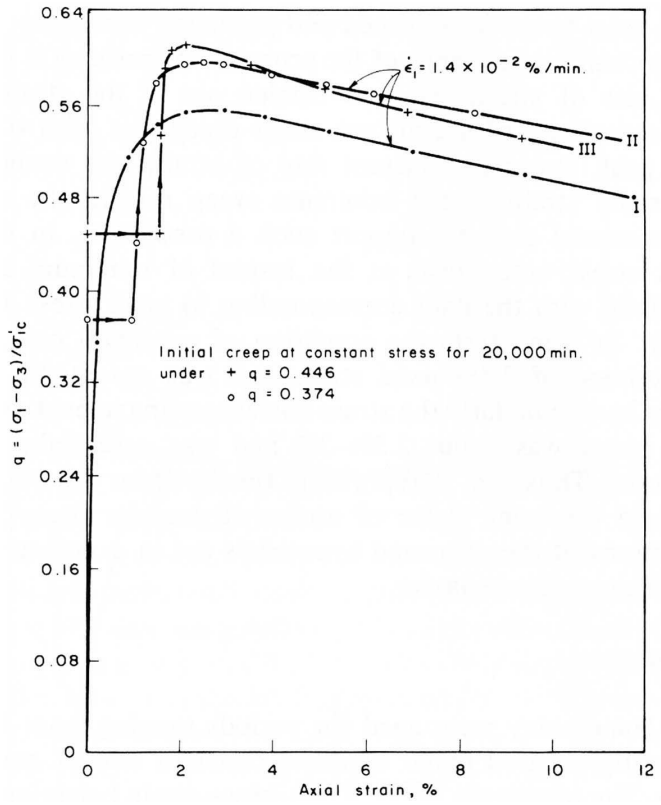

Figure 2.17: Gain in undrained strength due to creep, Vaid & Campanella (1977)

After a period of creep, the stiffness of a soil will be higher than that of an equivalent soil that has not been allowed to creep. This is implied by Figure 2.16 by the rejoining of the normal consolidation line after a period of creep. The increase in stiffness and also undrained strength post creep was investigated by Vaid & Campanella (1977), where samples of Haney Clay were allowed to creep for periods ranging from 2-48 days. They were subsequently sheared under identical CRS conditions, giving rise to the stress-strain plots seen in Figure 2.17. The tests with the creep period can be seen to exhibit a higher strength and also higher stiffness (steeper gradient at the same stress) when compared with the test conducted without creep.

The behaviour in this section has focused on the classification and influence of time dependent soil behaviour and the decay of creep with time. None of the results presented have focused directly on the effect of strain rate on the behaviour of a soil, which is the focus of Section 2.2.4.

2.2.4 Strain rate dependent behaviour

It was noted by Jardine et al. (1984) that the undrained stiffness depends not only upon the strain level, stress history and method of formation, but also possibly on strain rate.

Two main types of testing are used to determine the strain rate behaviour of soils. The first is constant strain rate (CRS) testing, which involves conducting a test with a fine control over the strain rate to keep it constant as the soil deforms. CRS tests are able to establish the rate dependent stiffness of the soil, but nothing about the transition between differing rates of strain can be learned. The soil response during CRS tests has been idealised in Figure 2.18.

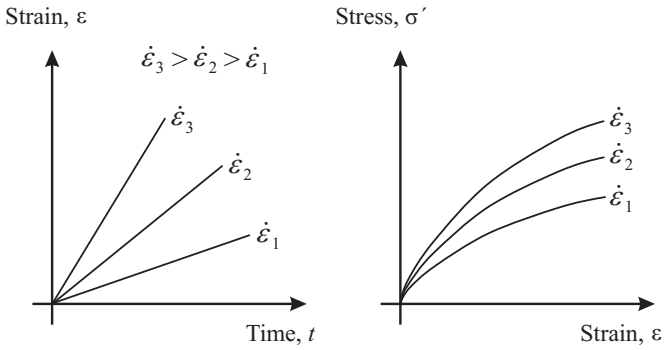

Figure 2.18: Constant rate of strain (CRS) testing, after Sorensen (2006)

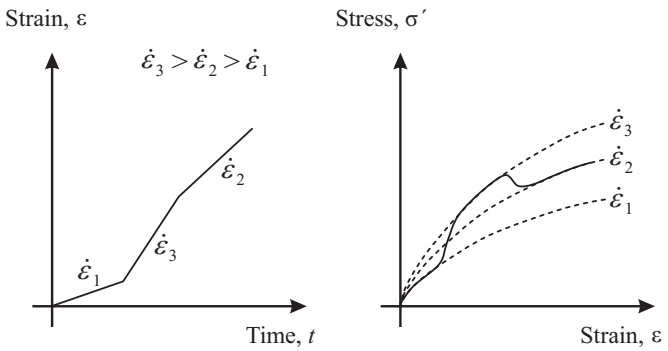

Figure 2.19: Step-changed rate of strain (SRS) testing, after Sorensen (2006)

The second form of testing is step-changed rate of strain (SRS) testing, where the rate of strain applied to the soil is varied during a single test. This form of testing is able to identify the behaviour investigated by CRS testing as well as establishing how the transition between different rates of strain occurs. This can play an important role in categorising the strain rate behaviour of a soil (Tatsuoka et al. 2002). SRS testing has the advantage of being able to identify the strain rate behaviour in a single test, thus minimising problems with sample variability and the time requirements associated with low strain rates (Richardson & Whitman 1963). The expected pattern of results for SRS tests can be seen in Figure 2.19.

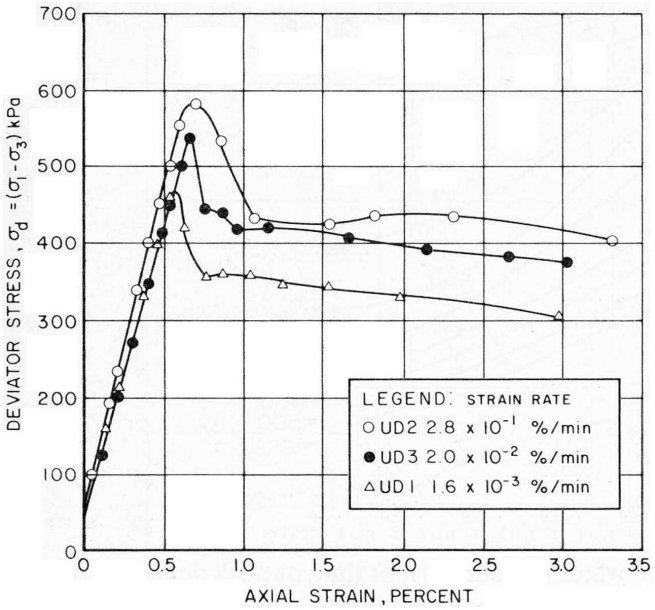

Figure 2.20: Stress-strain behaviour of Saint-Jean-Vianney clay in CRS triaxial compression, after Vaid et al. (1979)

Early work done by Vaid et al. (1979) using a CRS testing system showed that, the higher the rate at which a soil is strained, the higher the undrained strength of the soil. Figure 2.20 shows the results of tests done on Saint-Jean-Vianney clay, where a factor of 175 change in axial strain rate gave an increase in peak strength of 28%.

Graham et al. (1983) conducted a series of triaxial compression tests on lightly over-consolidated clays, advancing the work done by Vaid et al. (1979) by introducing both SRS and stress relaxation periods into the test procedure. Figure 2.21(a) shows the results of the SRS tests with the stepping of the curve between the different strain rates, each rate associated with a unique parallel path. When compared with CRS test results shown in Figure 2.21(b) the improvement afforded by SRS testing over CRS testing is apparent, with the CRS tests showing non parallel paths, probably as a result of sample variation or disturbance. The relaxation periods in Figure 2.21(a) show the reduction in stress at constant axial strain, mimicking a considerable reduction in the strain rate. Upon a recommencement of the applied strain rate the path rapidly returns to the previously predicted path, demonstrating a unique stress-strain-strain rate relationship.

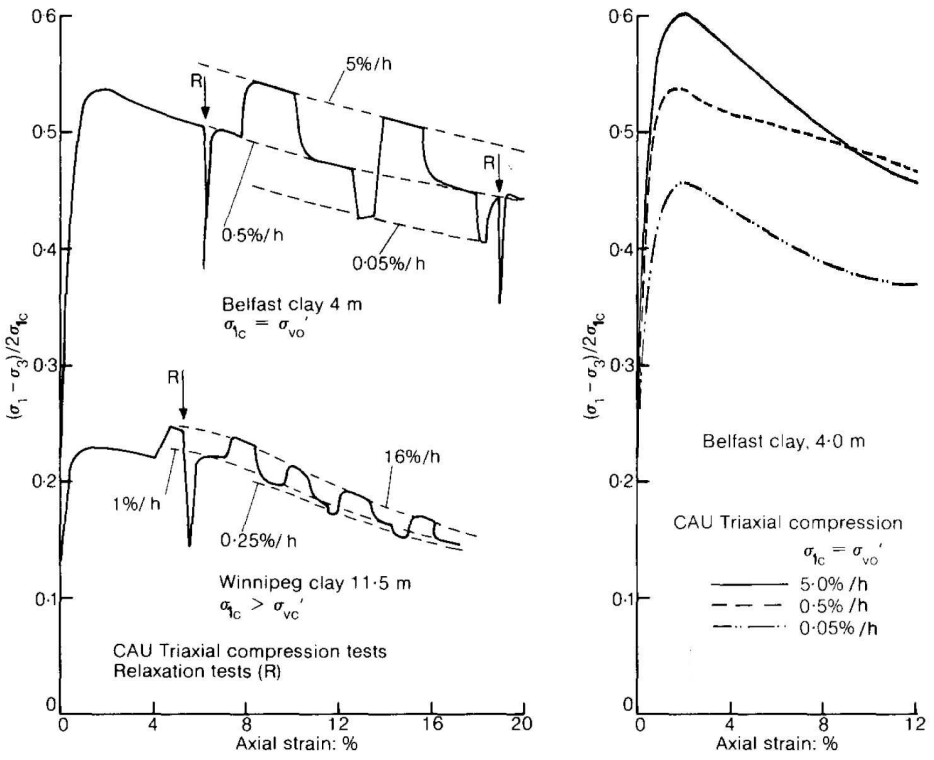

(a) SRS with relaxation periods

(b) CRS

Figure 2.21: Stress-strain curves for triaxial compression tests, Graham et al. (1983)

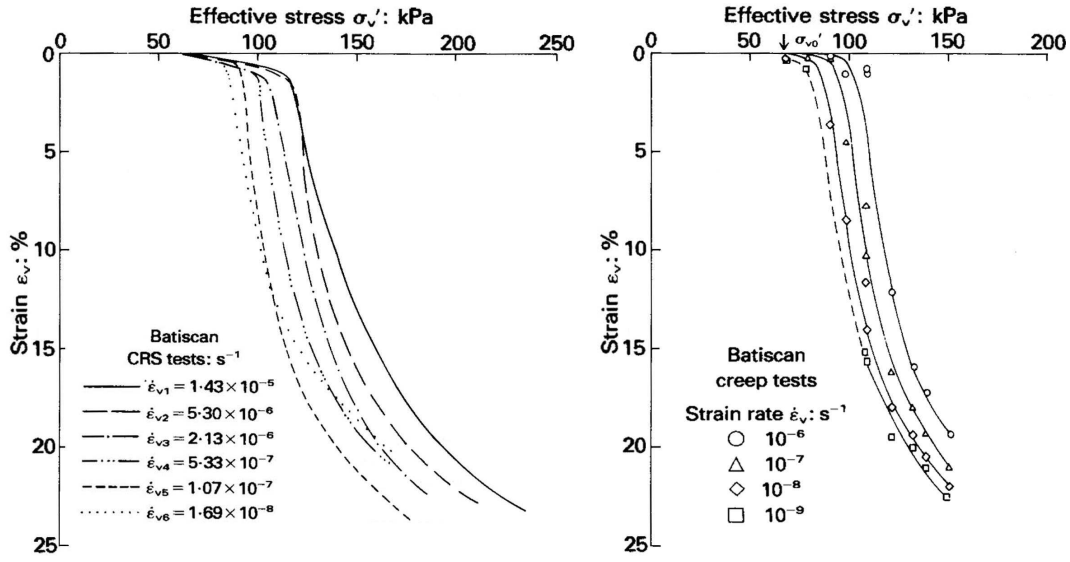

(a) CRS Oedometer tests (b) Creep test deduced curves

Figure 2.22: Stress-strain curves for one-dimensional compression tests, after Leroueil et al. (1985)

Leroueil et al. (1985) compared the effect of a directly applied volumetric strain rate with results derived from drained creep tests. The testing was conducted on samples of Batiscan clay under one-dimensional conditions using an oedometer. The results in Figure 2.22 show the same stress-strain-strain rate response during CRS testing (Figure 2.22(a)) as derived from creep tests (Figure 2.22(b)). The 1.07x10^{-7} (CRS) and 10^{-7} (creep) tests show a near identical response, establishing that strain rate and creep rate induced effects are comparable. This demonstrates the fact that it is only the rate at which the soil is strained which governs the behaviour and not the method of applying the strain rate. In Figure 2.22 an increase in strain rate leads to a shift to the right of the normal consolidation line, allowing the soil to sustain a higher effective stress.

Leroueil et al. (1985) also conducted SRS tests under one-dimensional conditions, allowing the type of relationship seen in Figure 2.21 to be observed under different conditions, Figure 2.23. All the testing described up to this point has been concerned with the identification of unique stress-strain-strain rate relationships, also known as isotach behaviour. During SRS tests, elastic strains are mobilised upon a change in strain rate, leading to a jump between isotache lines. Di Benedetto & Tatsuoka (1997) reasoned it is more accurate to state that the current stress is a function of irrecoverable strain, ε_{ir}, and its rate, as seen in Figure 2.24.

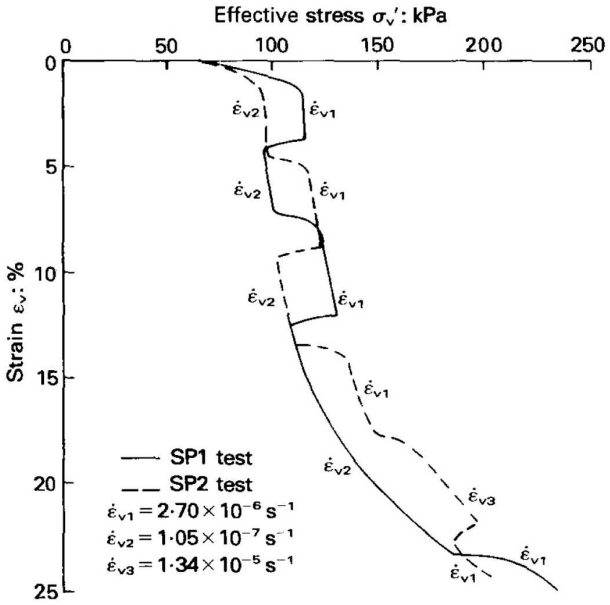

Figure 2.23: SRS oedometer tests on Batiscan Clay, Leroueil et al. (1985)

One of the main distinguishing features of isotach behaviour is the persistent effect of the changes in strain rate. Advanced testing from the late 1990s onwards on soils other than clay has identified forms of behaviour in soils that cannot be classified as isotach (Tatsuoka et al. 2002). Currently, four differing sets of characteristics have been identified in soils during SRS testing. These are known as isotach, intermediate, temporary effect of strain rate and strain acceleration (TESRA) and positive and negative (P & N) viscous behaviour (Tatsuoka 2007). Figure 2.24 illustrates the four types of viscosity.

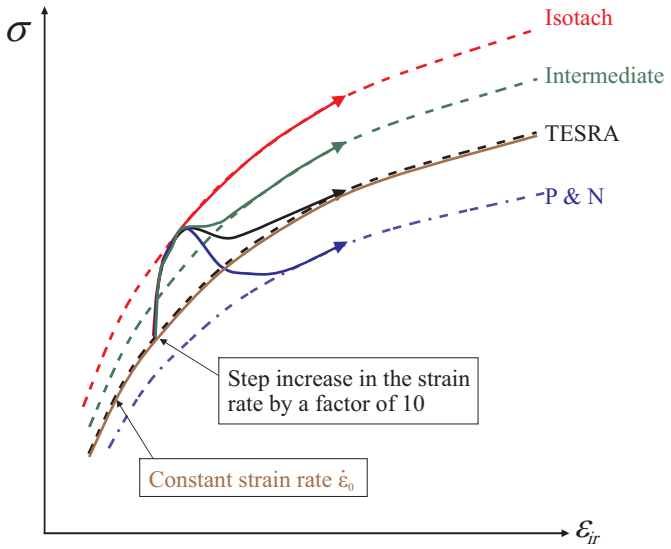

Figure 2.24: Different viscosity types for geomaterials, after Tatsuoka (2007)

Temporary Effect of Strain Rate and strain Acceleration (TESRA)

In undrained triaxial compression SRS tests on Metramo silty sand, Santucci de Magistris & Tatsuoka (1999) observed that at small strains the behaviour followed that of the Isotach model, but changed at larger strains close to and post peak strength. At small strains, an increase in strain rate caused a persistent change to the stress-strain curve, as would be predicted by the Isotach model. At larger strains, the change in deviator stress experienced after a change in strain rate became temporary and the stress-strain curve was found to decay to a curve independent of strain rate. This behaviour was termed TESRA by Tatsuoka, Ishihara & Maruyama (2000).

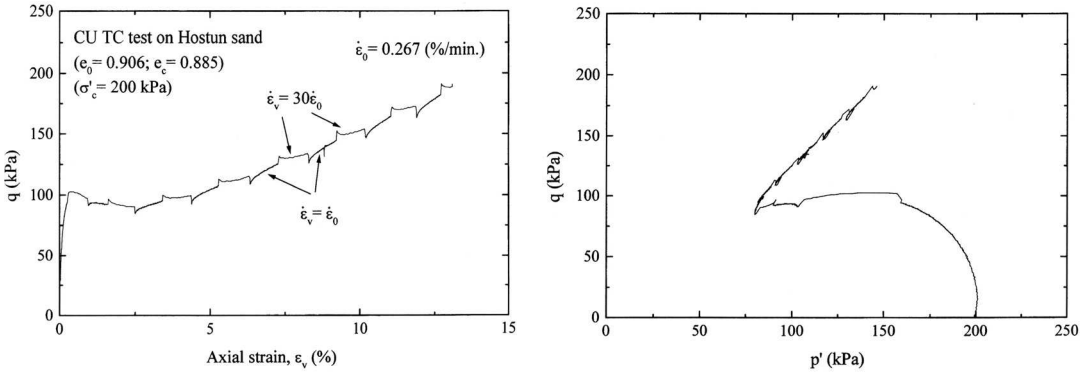

(a) $q - \varepsilon_v$ relationship (b) Effective stress path

Figure 2.25: Consolidated undrained triaxial tests on Hostun sand, Tatsuoka et al. (2002)

Tatsuoka et al. (2002) demonstrated TESRA behaviour in clean sand over the full shearing range, until failure. Figure 2.25 shows the behaviour of Hostun sand in undrained triaxial compression SRS tests. Figure 2.25(a) shows that the stress-strain relationship is independent of the applied strain rate. Following a change in strain rate an overshoot or undershoot of the persistent stress-strain curve is experienced before the path rejoins a unique CRS curve. As the behaviour of Hostun sand is totally independent of the applied strain rate, being only affected by strain acceleration and deceleration the behaviour can be more accurately described as Pure TESRA. Materials that demonstrate Pure TESRA behaviour can misleadingly be thought to be time and rate independent, because CRS tests performed at different strain rates yield the same stress-strain relationship (Bodas 2008). Despite the apparent lack of strain rate effects on the CRS curves, significant creep and stress relaxation have been observed in other materials that exhibit TESRA behaviour, such as in plane strain compression tests on Toyoura Sand (Di Benedetto, Tatsuoka & Ishihara 2002).

Intermediate or General TESRA

Oka et al. (2003) conducted SRS tests on both normally and overconsolidated reconstituted samples of Fukakusa clay. Figure 2.26(a) shows that at small strains, the behaviour can be seen to be isotach but as the straining continues the stress-strain curve starts to overshoot the persistent CRS curve, before decaying to a strain rate dependent CRS curve. In Pure TESRA behaviour the paths would decay to a unique curve not one dependent upon strain rate. Thus the tests showed traits of both isotach and TESRA behaviour, a combination which has since been termed Intermediate or General TESRA viscous behaviour (Tatsuoka 2007). In the stress paths shown in Figure 2.26(b) upon reaching the critical state line, if the strain rate is changed, then the stress path temporarily either overshoots or undershoots the critical state line. Similar behaviour has been identified by Sorensen, Baudet & Simpson (2007b) in tests on reconstituted London Clay. Generally, in soils that show a combination of isotach and TESRA behaviour, the magnitude of the TESRA effects are found to increase with strain level (Tatsuoka 2007).

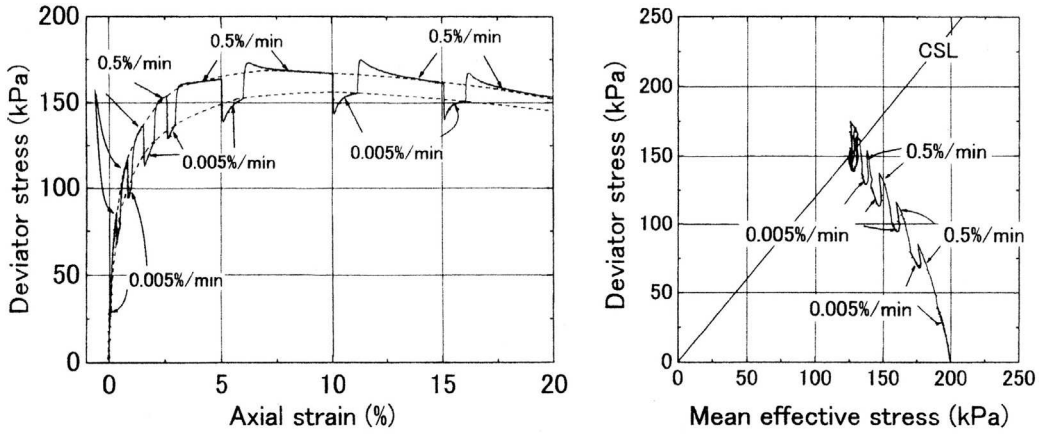

(a) $q - \varepsilon_a$ relationship (b) Effective stress path

Figure 2.26: Undrained triaxial compression tests on normally consolidated clay, Oka et al. (2003)

Positive and Negative (P & N)

Positive and negative (P & N) viscosity is a very new concept, described in detail by Tatsuoka (2007). The concept differs from the other types of viscosity in that an increase in strain rate can lead to a decrease in strength, exactly the opposite behaviour to that predicted by the isotach concept. Through the development of a new direct shear apparatus, Duttine et al. (2009) were able to identify P & N viscosity during testing

of Toyoura and Hostun sands. The testing showed a TESRA stress-strain response at pre-peak strength, with a gradual transition post-peak from TESRA to P & N. The most obvious P & N behaviour was observed at the residual state, Figure 2.27, where an increase of two orders of magnitude in the applied strain rate leads to an initial peak, followed by a persistent reduction in the stress ratio.

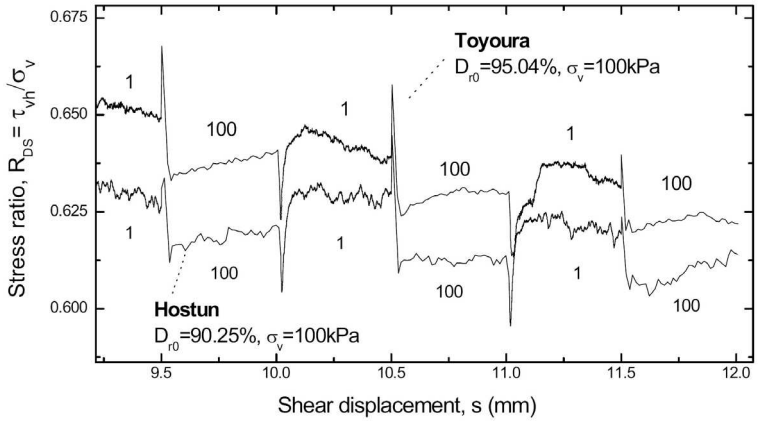

Figure 2.27: Behaviour of Toyoura and Hostun sands at the residual state, after Duttine et al. (2009)

Sorensen (2006), in a summary of previously published work, established that isotach behaviour is predominantly exhibited by natural clays, whereas the other forms of behaviour are demonstrated by reconstituted stiff clays, cemented soils and sands. As the aim of the current work is to modify a model primarily for predictions of ground movements in natural clays, it was decided the research should focus on the modelling of isotach behaviour.

2.2.5 Other influencing factors

There are many other factors that are known to have an influence on the observed behaviour of soil. The effects that have been described in this chapter thus far relate either to behaviour currently included in the Brick model or to behaviour that it is within the scope of this thesis to attempt to include in the Brick model, with the exception of non-isotach viscous behaviour. In Table 2.1 a brief overview of the mechanisms that can give rise to time effects is given. In this thesis only the viscous effects will be considered for implementation into the Brick model.

Phenomenon		Micro-mechanism
Viscous effects		Creep, stress relaxation, strain rate effects, apparent structuration from creep.
Ageing Effects	Inherent (no external influence)	Thixotropy, bonding, cementation etc.
	Environmental (external influence)	Weathering, chemical changes to pore water (e.g. leaching), heat and pressure induced changes to the soil structure etc.

Table 2.1: Classification of common time effects, Sorensen (2006), modified after Kongsukprasert & Tatsuoka (2003)

2.3 Constitutive Models for Soil

2.3.1 Elasto-plastic models

The simplest form of elasto-plastic constitutive model is one that assumes the soil body is perfectly elastic until the point of yielding at which the soil behaves in a plastic manner until failure. In the elastic portion of the behaviour the soil deforms in accordance with Hooke's law, where the deformation is directly proportional to the stress applied. This behaviour is limited by either the Tresca or Von Mises failure criterion, where the plastic phase is modelled as being perfectly plastic, as seen in Figure 2.28.

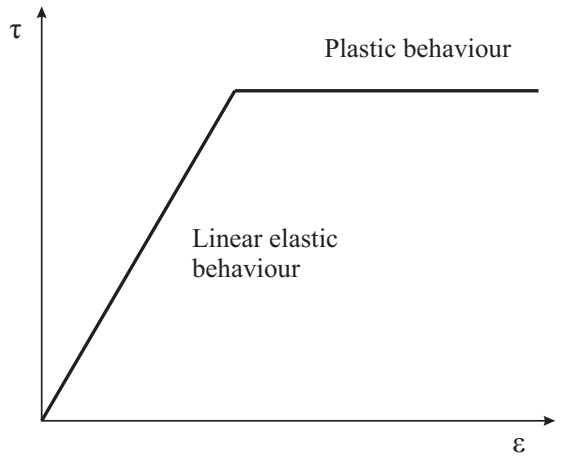

Figure 2.28: Elastic perfectly plastic response of a soil leading to failure

The Tresca failure surface takes the shape of a hexagon when plotted in the deviatoric stress plane, which is perpendicular to the space diagonal where all principal stresses

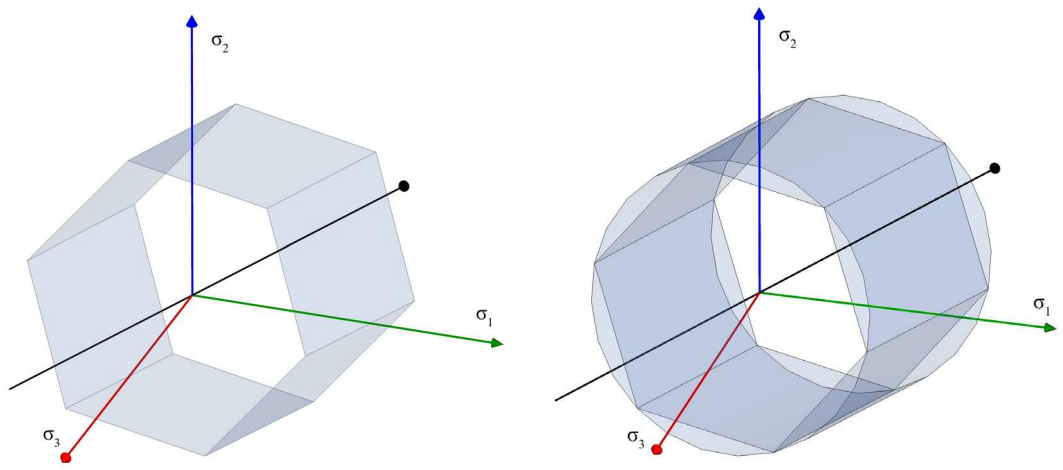

(a) Tresca yield surface plotted in 3D space of principal stresses

(b) Comparison between Tresca and Von Mises yield surfaces

Figure 2.29: Total stress yield surfaces

are equal. In comparison the Von Mises model plots as a perfect circle when plotted in the same plane. Both the Tresca and Von Mises models are suitable for expressing the undrained shear strength of clay when plotted in terms of total stresses. They can be visualised as a hexagonal prism or cylinder respectively, Figure 2.29.

The Mohr-Coulomb and Drucker-Prager yield surfaces are variations on the above models, allowing yield to be dependent on the stress level and thus applicable to effective stress analysis. The visualised yield surfaces can be seen in Figure 2.30. The models revert back to the Tresca and Von Mises surfaces respectively for undrained analyses. The yield surface generated by the Drucker-Prager model is used in variations of the BRICK program (Section 3.5). Currently, the most commonly used model in soil mechanics, especially for finite element analyses, is the Mohr-Coulomb model as the parameters are comparatively easy to determine and the generated results are easier to interpret due to the lack of complexity in the soil model. The problems with using the Mohr-Coulomb model are numerous, as the model does not account for many facets of soil behaviour. It is known that soil does not behave purely elastically before failure and that any overconsolidation of the soil will have a large effect on the pre-failure deformations. The Mohr-Coulomb model may be acceptable for use in situations where failure is reached (such as stability analyses) but the predicted deformations are likely to be inaccurate compared with more advanced models.

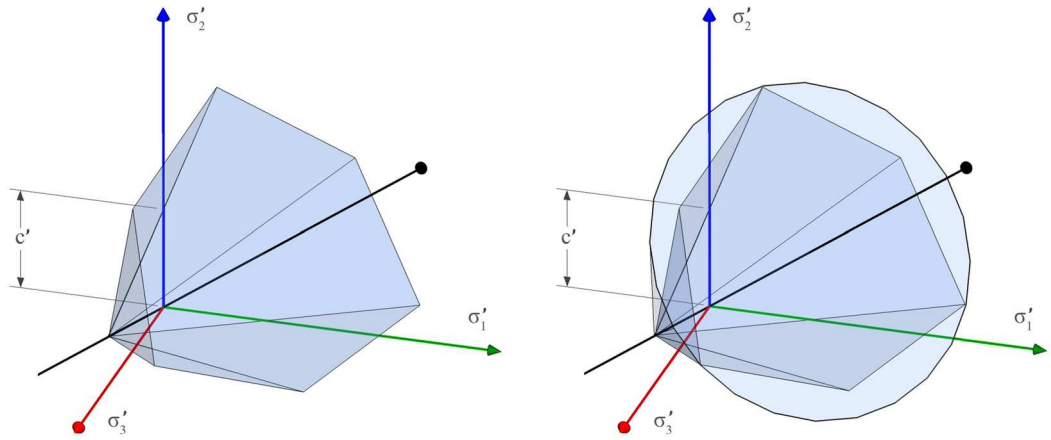

(a) Mohr-Coulomb yield surface plotted in 3D space of principal stresses

(b) Comparison between Mohr-Coulomb and Drucker-Prager yield surfaces

Figure 2.30: Effective stress yield surfaces

2.3.2 Critical state soil mechanics

The critical state framework proposed by Schofield & Wroth (1968) was developed from triaxial tests done on reconstituted soils at the University of Cambridge in the 1960s. The isotropic normal consolidation line (NCL) is assumed to be a straight line in $v - \ln p'$ space (see Figure 2.31) and can be expressed as:

$$v = N - \lambda \, ln \, \frac{p'}{p'_0} \tag{2.5}$$

where:

v = specific volume,
N = specific volume on NCL at a mean normal stress of 1kPa,
λ = gradient of the NCL,
p' = mean normal effective stress,
p'_0 = initial mean effective stress (1kPa).

It is assumed that the strains generated on the isotropic NCL are largely plastic and irrecoverable. Any swelling that occurs does so on a line of gradient κ given by the equation:

$$v = v_k - \kappa \, ln \frac{p'}{p'_0} \tag{2.6}$$

where:

v_k = specific volume on the swelling line at a mean normal stress of 1kPa.

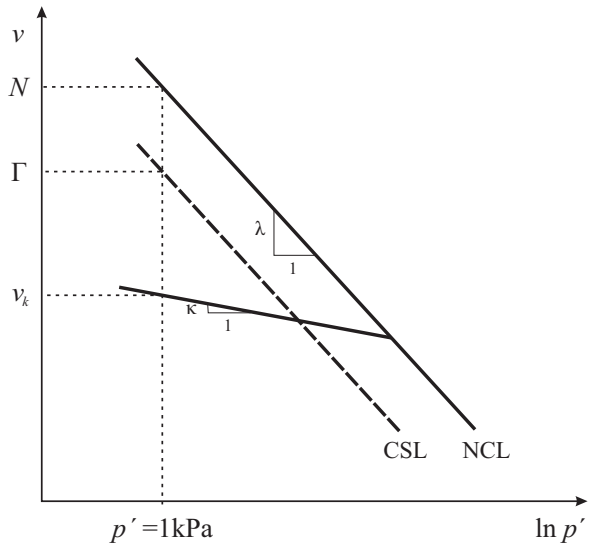

Figure 2.31: Critical state framework

As the strains induced during a period of swelling are occurring in an overconsolidated state, they are deemed to be elastic and recoverable. Projected above the swelling line in $q-p'-v$ space is the aptly named 'elastic wall' which allows purely elastic behaviour to lead to a boundary surface. For normally consolidated soils this boundary surface is the Rendulic surface and for overconsolidated soils the Hvorslev surface, shown in Figure 2.32. The behaviour of the soil inside the boundary surface is effectively elastic and turns elasto-plastic only as the boundary surface in engaged. The soil becomes perfectly plastic upon reaching the apex of the boundary surfaces, the critical state line (CSL). The location of the CSL is given by the equations:

$$v = \Gamma - \lambda \, ln \, p' \tag{2.7}$$

$$q = Mp' \tag{2.8}$$

where:

Γ = specific volume on CSL at a mean normal stress of 1kPa.

M, Γ and N are material constants that can be determined from triaxial testing.

The components that make up the critical state framework are illustrated in Figure 2.33. The critical state framework makes the assumption that all sheared soils ultimately reach a critical state. This is a good assumption for normally consolidated and lightly overconsolidated clays but lacks the ability to model heavily overconsolidated clays, especially those with high plasticity. In reality, localisation of the strains will occur bringing the soil to critical state within shear bands. However the stresses in these bands cannot be easily measured externally.

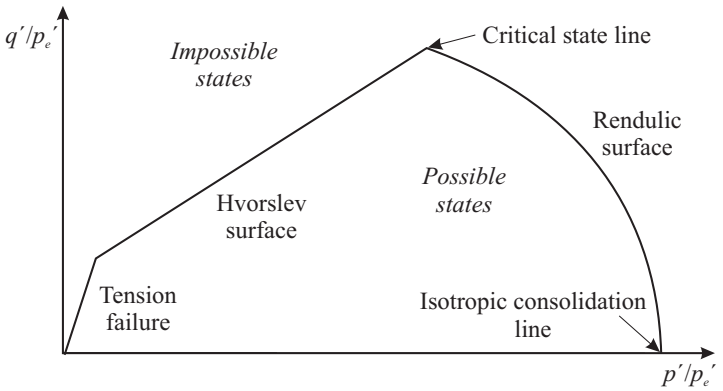

Figure 2.32: Normalised state boundary surface in stress space

Two well known models that utilise the critical state framework are the Cam-Clay (Schofield & Wroth 1968) and Modified Cam-Clay models (Roscoe & Burland 1968). The models use mathematical approximations for the shape of the yield locus, which in the case of the Cam-Clay model is a logarithmic curve and in the case of the Modified Cam-Clay model is an ellipse. The most widely used implementation of the critical state framework is the Modified Cam-Clay model of Roscoe & Burland (1968). The main drawback with both models is the fact that the shape of the boundary surface bears little resemblance to experimental results from natural soils (Muir-Wood 1990).

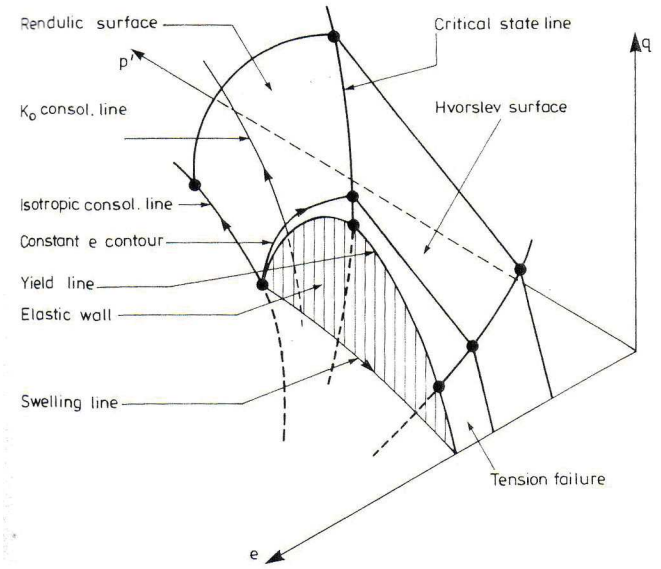

Figure 2.33: State boundary surface of the critical state framework in $e - p' - q$ space, Burland (1989)

For soils that remain within the boundary surfaces, the Cam-Clay and Modified Cam-Clay models assume elastic behaviour until a boundary surface is engaged. In the case of heavily overconsolidated soils, elasticity is a poor approximation to the highly non-linear elasto-plastic behaviour that such soils exhibit. Many models have been generated that attempt to overcome this drawback in the modelling of overconsolidated soils, examples being described in the next section. It should also be noted that the critical state framework was based on tests done on reconstituted soils and does not encompass effects such as structure which are part of natural clay behaviour.

2.3.3 Some kinematic hardening models

The concept of kinematic hardening modelling was originally introduced for the work hardening of metals (Mroz 1967). This was then applied to soils by, among others, Mroz, Norris & Zienkiewicz (1979) and Mroz & Norris (1982). An overview of the history of kinematic hardening models is given by Grammatikopoulou (2004). In this section selective attention is given to those models developed for analysis of heavily overconsolidated deposits such as London Clay.

Model LC was developed by Simpson et al. (1979) specifically to model the behaviour of London Clay. Three ranges of strains were considered in Model LC:

a) Very small strains (within the elastic strain threshold): elastic behaviour, equivalent to the Y_1 yield surface of the Jardine et al. (1991) framework.

b) Moderate strains (the linear range measured in the laboratory): intermediate behaviour giving a reduction in stiffness but still purely elastic behaviour.

c) Large strains, approaching the limiting shear strength of the material: plastic behaviour accompanying further intermediate behaviour.

Figure 2.34 demonstrates the concept of a kinematic yield surface (KYS) in strain space that defines the stiffness at very small strains. In Model LC the stiffness within the KYS was taken to be ten times that taken from laboratory results at intermediate strains. Straining within the KYS is purely elastic, though non-linear (2.34a). As the soil is strained further the yield surface moves and the effective stiffness is reduced (2.34b). If the direction of straining is reversed the higher stiffness again applies (2.34c) until the KYS starts to move again (2.34d). Simpson et al. (1979) assumed a spherical yield surface defined within strain space with axes, $(\varepsilon_x + \varepsilon_y, \varepsilon_x - \varepsilon_y, \gamma_{xy})$. They noted that the model is initialised with the KYS centralised around the in-situ stress, but

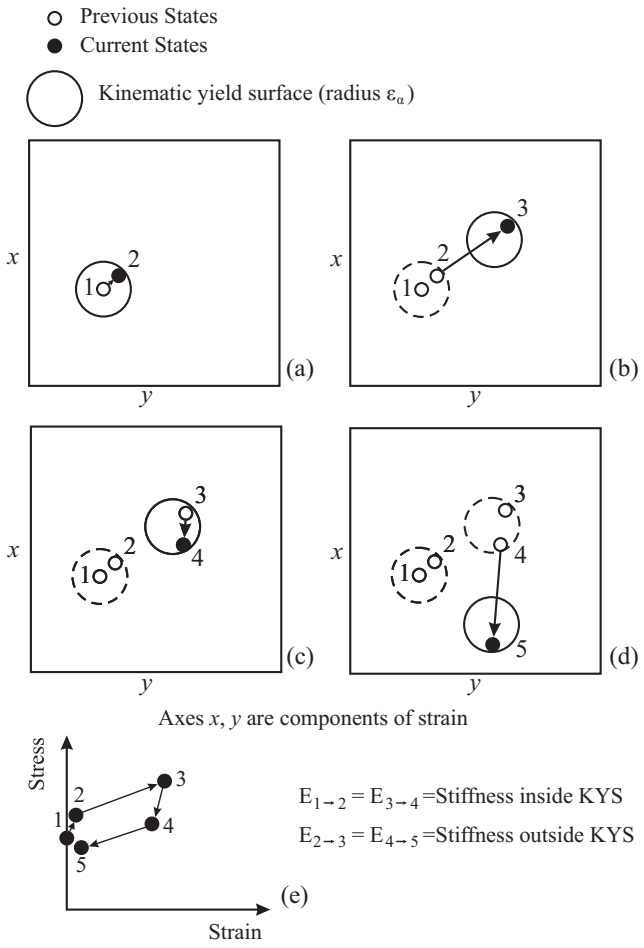

Figure 2.34: The kinematic yield surface effect, after Simpson et al. (1979)

that the location of the KYS could be affected by factors such as creep. Model LC was able to improve the predicted surface settlement troughs behind diaphragm walls, as compared to those predicted by analyses assuming linear elastic behaviour.

The Cam-Clay models provide typically accurate results for tests on normally consolidated and lightly overconsolidated clays. However the results generated for heavily overconsolidated clays do not match those seen in practice (Section 2.3.2). Implementations originally tried adding a kinematic yield surface within the Cam-Clay framework to try to model the areas of stiffer response generated by overconsolidated clays. This was first attempted by Al-Tabbaa & Wood (1989), where the non-linearity is modelled by an area of higher stiffness, bounded by a kinematic zone lying within the Modified Cam-Clay boundary surface, as seen in Figure 2.35. As the soil strains so the inner kinematic yield zone moves so that upon a change in direction of shearing, the soil shows

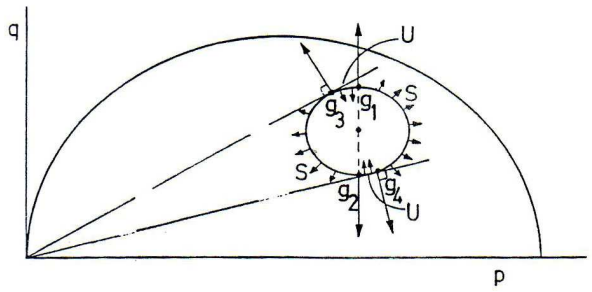

Figure 2.35: Yield locus. Cam clay locus; stable (S) and unstable (U) regions, Al-Tabbaa & Wood (1989)

an initially stiff response as its path moves through the area of higher stiffness, denoted by this inner zone. This stiffness reduces to Cam-Clay levels as the soil approaches the outer Cam-Clay boundary surface. In this way the model takes into account the stiffness increase caused by overconsolidation but fails to account for the more persistent effects of the stress history (Grammatikopoulou 2004).

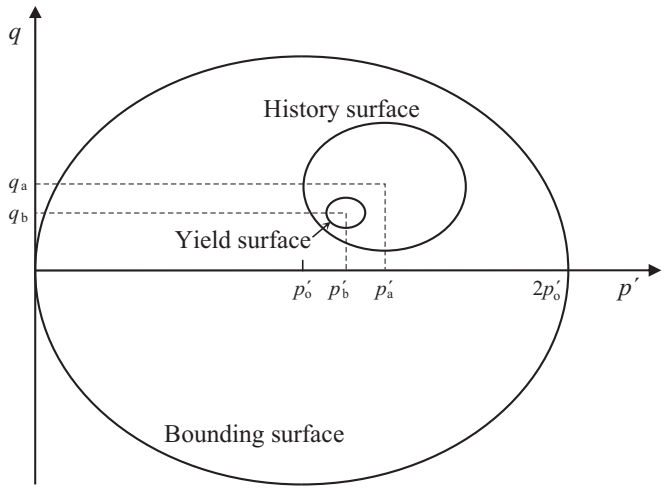

Figure 2.36: Sketch of the 3-SKH model in triaxial stress space, after Stallebrass & Taylor (1997)

At the same time as the development of the Jardine three surface framework (Section 2.2.1) came the development of the Stallebrass three-surface kinematic hardening model (3-SKH). In this model there are two kinematic surfaces within the conventional Modified Cam-Clay boundary surface. The three surfaces in the 3-SKH model are named the yield surface (equivalent to the Y_1 surface of Jardine et al. (1991)), history surface and bounding surface, as seen in Figure 2.36. The 3-SKH model is capable of

modelling the effects of recent stress history on the small strain stiffness of overconsolidated soils as seen by Richardson (1988) and Stallebrass (1990). However it was found that the stiffness predicted by the 3-SKH model reduced dramatically upon the engaging of the Y_1 yield surface after a 180° rotation in the stress path, leading to a step in the normally smooth S-shaped stiffness curve (Grammatikopoulou 2004). This can be seen in Figure 2.37 which shows the predicted stiffness of the 3-SKH model having been implemented into the Imperial College finite element program, ICFEP.

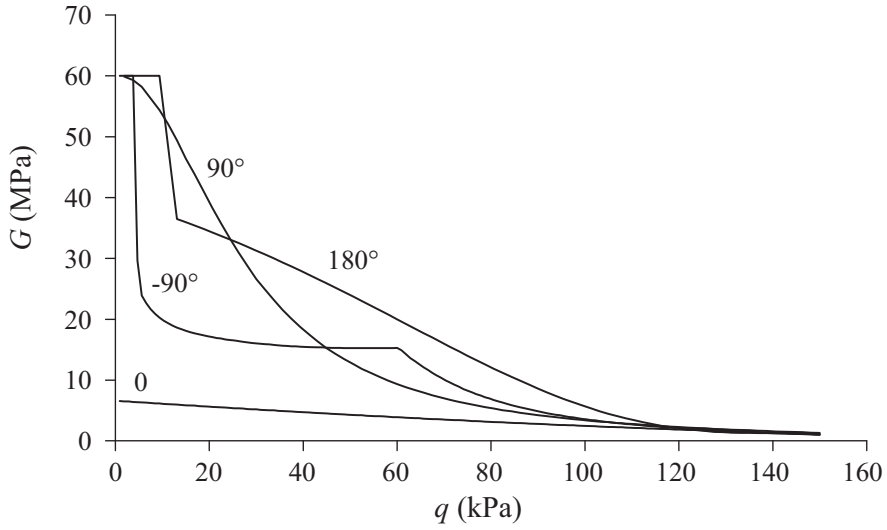

Figure 2.37: Constant p' loading after four stress path rotations: G against q, predictions of the 3-SKH model as implemented into ICFEP, Grammatikopoulou (2004)

The modified 3-SKH model known as M3-SKH was developed by Grammatikopoulou (2004) to smooth the drop in stiffness predicted by the original 3-SKH model, Figure 2.38. A direct comparison of the stiffness versus strain plots can be seen in Figure 2.39 (p'_i is mean effective stress at the start of shearing) where the step in stiffness can clearly be seen in the plot for the 3-SKH model. Grammatikopoulou et al. (2008) showed that the M3-SKH model was capable of enhancing predictions for surface displacements above tunnels. Attempts were made to introduce an allowance for creep by centralising the two kinematic surfaces around the current point of stress, but this led to worse predictions of the surface displacements.

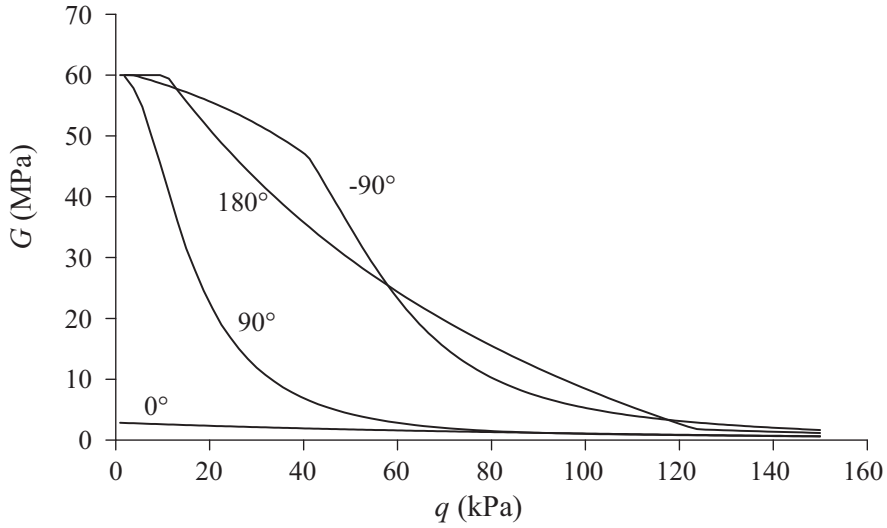

Figure 2.38: Constant p' loading after four stress path rotations: G against q, predictions of the M3-SKH model as implemented into ICFEP, Grammatikopoulou (2004)

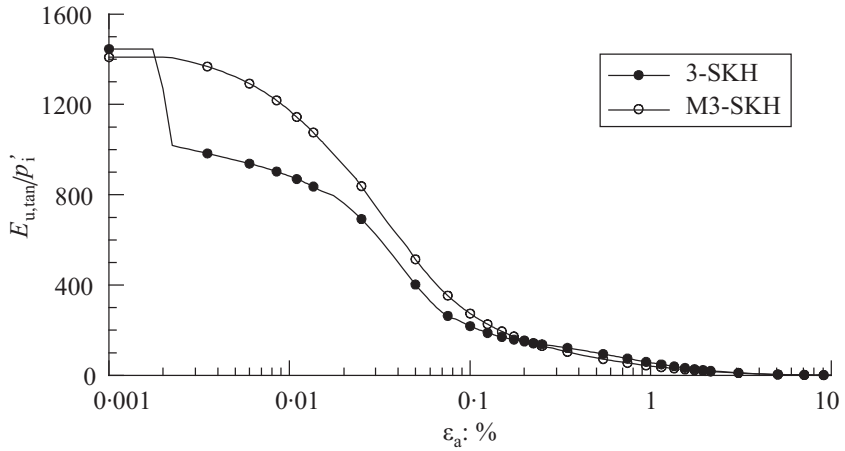

Figure 2.39: Predictions of the 3-SKH and M3-SKH models for undrained triaxial compression test: normalised stiffness vs. strain curve, Grammatikopoulou et al. (2008)

2.4 The BRICK Model

The Brick model can be regarded as a kinematic yield surface model developed within strain space. The model itself has an analogue, which is that of a man walking around a room with a series of bricks tied to him on separate strings. Each brick represents a proportion of the soil, and each string length represents the amount of strain required to create plastic deformations in the soil. The walls of the room can be thought of as axes in strain space. As the man moves through strain space, initially the strings are slack so the soil strains elastically, but as the man moves further so the bricks start to move too in the same direction. The more bricks that move the higher the proportion of soil undergoing plastic deformation and the lower the stiffness of the soil. This relationship between the soil proportions and strain gives rise to the s-shaped curved used in the Brick model to recreate small strain stiffness. This can be seen in Figure 2.40.

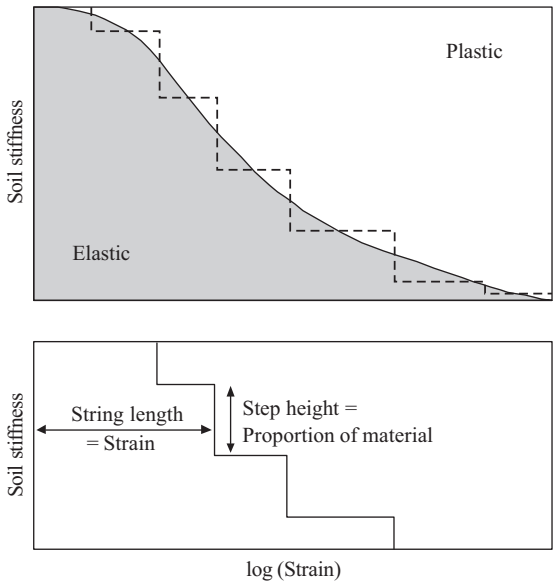

Figure 2.40: The S-shaped curve represented in stepwise fashion, after Simpson (1992b)

Defining kinematic zones within the Brick model is done by defining the relative lengths of the strings. In stress space the Y_1 surface of Jardine et al. (1991) is defined as the zone of fully elastic behaviour. This equates to all the strings being slack in the Brick model and hence the extent of the Y_1 zone is dictated by the shortest string length in strain space. The Brick model accounts for recent stress history through the current position of the bricks relative to the man. To allow an accurate representation of this, the geological history of the soil is modelled back to when the clay was first

deposited as a slurry, through the deposition and erosion of the various overlying strata to the present day. The positions of the bricks give a unique stiffness response dependent upon the strain path followed when straining recommences. The failure surface in the BRICK model is loosely defined by the longest string length and the positions of the bricks relative to the current position of the man, as will be explored in Section 3.4.3.

One of the concepts within the BRICK model is that of plastic strain reduction, a process by which pure plastic strains generated by taut strings can be partially transformed into elastic strains, which give rise to changes in stress, giving the correct gradient to the normal consolidation line. This bears a striking resemblance to the work by Collins (2005) on the concept of stored plastic work or frozen elastic energy. Collins (2005) argues the case that, due to inter-particle movements, elastic strains can become trapped within the fabric of the soil, only being released upon further plastic straining.

2.4.1 Variations of BRICK

There have been a number of attempts to manipulate the BRICK model to incorporate viscous effects. Kanapathipillai (1996) modelled the construction of the Heathrow Express trial tunnel and obtained an under-prediction of the surface settlements when compared with the field data. He then attempted to simulate the rise in stiffness seen after periods of rest by halving the string lengths before the start of construction. The tunnel construction was then modelled with the original string lengths, which has the effect of causing an elastic response in the soil and hence a higher stiffness than would be predicted otherwise. Figure 2.41 shows the three runs conducted by Kanapathipillai (1996) compared with the field data. The 'Rankine' prediction used the BRICK parameters as presented in Simpson (1992b), with the 'New' results showing the predictions made by modified BRICK parameters as proposed by Kanapathipillai (1996) (see Section 3.4.1). It can be seen that both these models still under-predict the measured settlements. The third 'Ageing' test shows the effects of halving the string lengths prior to the construction of the tunnel, with the predictions showing a dramatic improvement over the initial tests.

Den Haan (2001) introduced the 'Bricks on Ice' idea, by which the bricks continue to move at an ever decreasing rate after the motion of the man has ceased. This in turn means that upon recommencing the motion of the man, rather than the strings being all taut and the behaviour plastic, the strings have become slack and therefore the response is elastic. The continued viscous motion leads to a reduction in stresses at

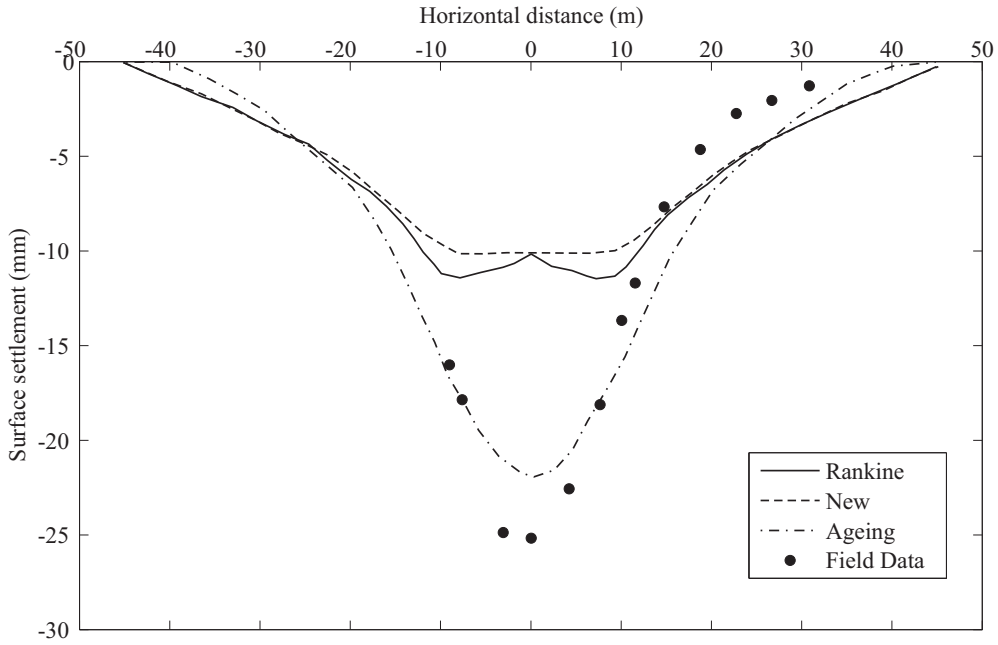

Figure 2.41: Surface settlements above the Heathrow trial tunnel, after Kanapathipillai (1996)

constant volume during a period of rest. It also leads to a higher stiffness after the period of rest which is the expected trend after a stress relaxation, as can be seen in Figure 2.42. The deceleration of the bricks is calculated using a simple logarithmic decay equation and hence only needs a single additional parameter for calculating the expected continued motion, that being the creep constant, c.

$$\delta\varepsilon = c\, ln\left(1 + \frac{\Delta t\, |\dot{\varepsilon}|}{c}\right) \tag{2.9}$$

where:

$\delta\varepsilon$ = continued motion (strain) in the next increment,

Δt = time increase between BRICK increments,

$\dot{\varepsilon}$ = strain rate in the previous increment.

After a period of swelling, the direction of brick movement reverses so that during a rest period the bricks now carry on moving in the opposite direction to that seen in a stress relaxation. This leads to a rise in stresses at constant volume and has been termed 'strain fixation' by Den Haan (2001), shown in Figure 2.43. The ideas proposed in Den Haan (2001) give rise to the expected pattern of stress changes seen during stress relaxation and strain fixation. This cannot however be said about the patterns shown in the stress-strain plots. The creep movements of the bricks during normal

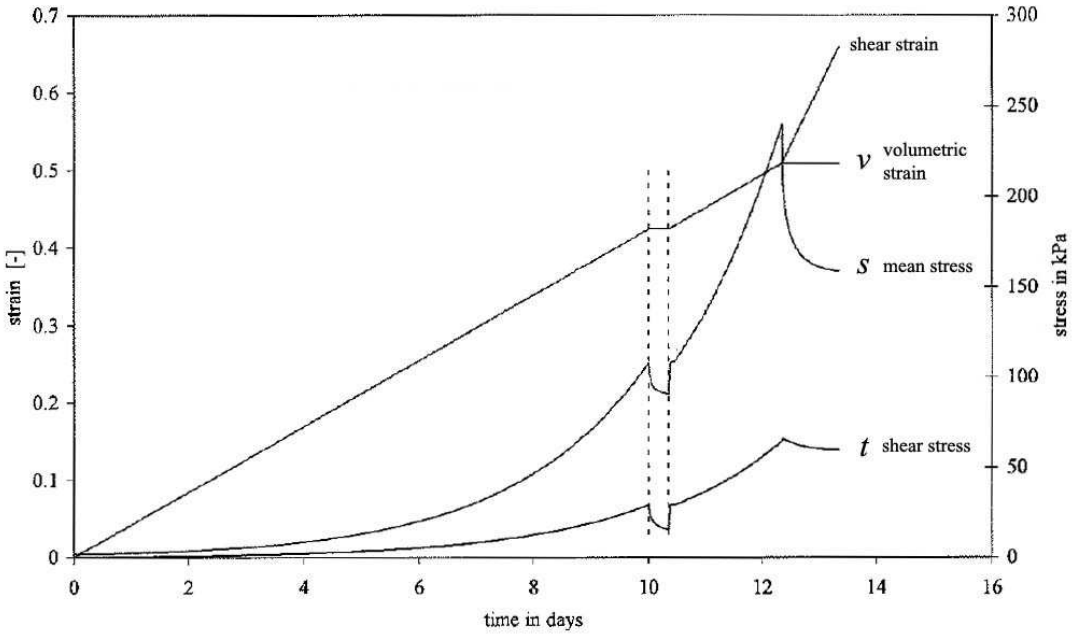

Figure 2.42: Stress relaxation with Bricks on Ice, Den Haan (2001)

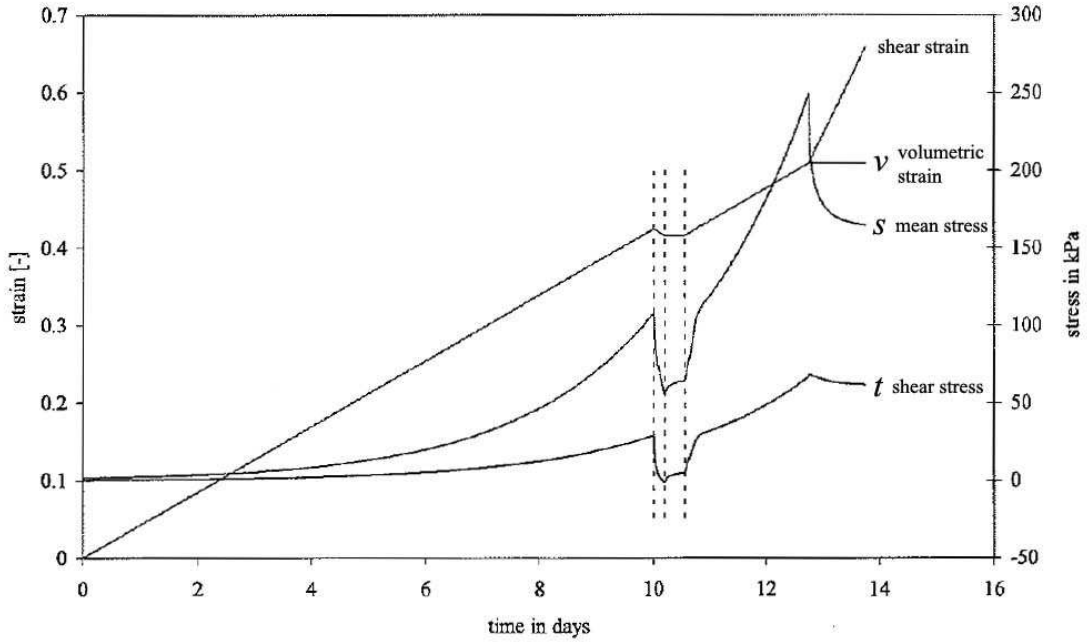

Figure 2.43: Strain fixation with Bricks on Ice, Den Haan (2001)

consolidation lead to non-parallel isotache lines.

Sorensen (2006) introduced the idea of strain rate dependent string lengths, where the effects of step changes in strain rate (Section 2.2.4) can be modelled in the Brick model by varying the string lengths as a function of the strain rate. The work done by Sorensen (2006) concentrated on the theoretical implementation of isotach and TESRA behaviour into the Brick model and not specifically the modelling of the effects of creep.

2.5 Discussion

In this chapter, it has been shown that viscous effects have an observable impact on soil behaviour. These viscous effects were divided into two main categories to help define the framework that will be developed later in Chapter 5. These categories were:

(a) time dependent behaviour, such as creep and stress relaxation,

(b) strain rate dependent behaviour, as characterised by Tatsuoka (2007).

The time dependent behaviour was seen to govern the stiffness of the soil after a holding period, in which the strains could increase at constant stress (creep) or the stress can decrease at constant strain (stress relaxation). In both cases the the time dependent behaviour causes a movement away from the normal consolidation line with an increase in time. The viscous strains developed are seen to decay linearly with the logarithm of time.

The strain rate dependent behaviour can be subdivided into four categories: isotach, TESRA, intermediate or general TESRA and positive and negative viscosity. Isotach behaviour, where a unique stress-strain-strain rate response is predicted, was established as being able to encompass the behaviour seen in natural clay deposits. The strain rate for use in the Isotach model can either be a directly applied strain rate or one deduced from creep testing, as seen in the work done by Leroueil et al. (1985).

The constitutive models reviewed in Section 2.3.3, although advanced, are unable to account for viscous effects. There are many models for both time and rate dependency (Bodas 2008) which have not been included in this literature review due to their inability to model the fundamental aspects of soil behaviour that the Brick model can model. These models are almost always formulated within stress space making their

interpretation for use with BRICK difficult.

The aim of the current work will be to introduce the ability to model time dependent effects and isotach strain rate effects into the existing BRICK model. To enable the reader to distinguish between native 'BRICK' effects and those introduced by the new implementations into the BRICK model, the behaviour shown by the unmodified BRICK model will be explored in detail in Chapter 3.

3

The BRICK Model

3.1 Introduction

The BRICK model, as stated in Section 2.4, can be regarded as a kinematic yield surface model developed within strain space. The model has an analogue, which is that of a man walking around a room with a series of bricks tied to him on separate strings. Each brick represents a proportion of the soil and each string length represents the amount of strain required to generate plasticity in that proportion of soil. The walls of the room can be thought of as axes in strain space. As the man moves through strain space, initially the strings are slack so the soil strains elastically; as the man moves further the bricks start to move too, in the same direction. The more bricks that move the higher the proportion of soil undergoing plastic deformation and the lower the stiffness of the soil. This relationship between the soil proportions and strain gives rise to the s-shaped curved used in BRICK to model the progressive reduction in stiffness with strain, which can be seen in Figure 2.40 on page 39.

Defining kinematic zones within the BRICK model is done by defining the lengths of the strings. The Y_1 surface (Section 2.3.3) is defined as the zone of fully elastic behaviour and corresponds to all the strings being slack in the BRICK model. Hence, the extent of the Y_1 zone is defined by the shortest string length. The Y_2 surface cannot be defined directly in the BRICK model. Recent stress history is accounted for by the current positions of the bricks relative to the man. To allow an accurate representation of stress history, the geological history of the soil is modelled back to when the clay was first deposited as a slurry, through the deposition and erosion of the various overlying strata to the present day. The positions of the bricks give a unique stiffness response which is dependent upon the path followed when straining recommences. This approach is able to simulate the results seen by Atkinson et al. (1990). The failure surface in the BRICK model is loosely defined by the longest string length and the positions of

the bricks relative to the current position of the man. All the strings must be taut in shearing (i.e. representing plastic shear strain) for the model to predict 'failure'. This will be discussed further in Section 3.4.3.

3.2 Parameters used in the BRICK Model

3.2.1 Two-dimensional BRICK

To simplify the explanation of the BRICK model, the two-dimensional (plane strain) version will be initially explored. This version lacks the extra three components of shear strain and three of shear stress that give BRICK its full three-dimensional functionality. This model was described in the 1992 Rankine Lecture, Simpson (1992b).

The three component, two-dimensional BRICK model was developed within a framework of volumetric and shear strains rather than principal strains for ease of application to geotechnical problems. With reference to the analogue described in Section 3.1, the axes of the room in the plane strain model are volumetric strain, v, and shear strain, γ. The shear strain is taken to be the diameter of the Mohr's circle of strain as seen in Figure 3.1.

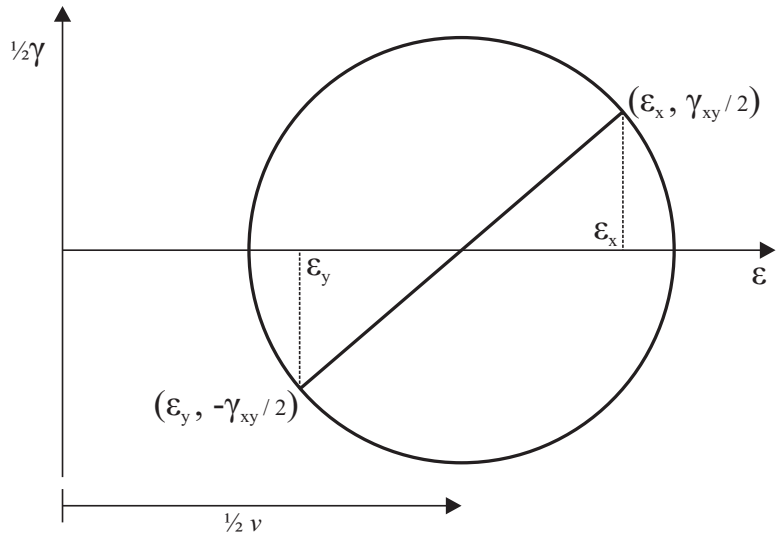

Figure 3.1: Mohr's circle of strain

Therefore:

$$\gamma = \sqrt{(\varepsilon_x - \varepsilon_y)^2 + {\gamma_{xy}}^2} \tag{3.1}$$

Since γ is the vector sum of two components, along with v these form the three strain components (v, $\varepsilon_x - \varepsilon_y$, γ_{xy}) used in the plane strain BRICK model, (Simpson 1992b), where ε_x and ε_y are the horizontal and vertical strain respectively. Thus the three strain components used in the BRICK model can be defined as:

$$\begin{aligned} \text{Volumetric strain} &= v &&= \varepsilon_y + \varepsilon_x \\ \text{Shear strain component 1} &= \varepsilon_y - \varepsilon_x \\ \text{component 2} &= \gamma_{xy} \end{aligned} \tag{3.2}$$

The three stress components are:

$$\begin{aligned} \text{Mean stress} &= s &&= \frac{(\sigma_x + \sigma_y)}{2} \\ \text{Shear stress component 1} &= t &&= \frac{(\sigma_y - \sigma_x)}{2} \\ \text{component 2} &= \tau_{xy} \end{aligned} \tag{3.3}$$

In elastic materials the strain components can be related to the corresponding stress components through the shear modulus, G, and the Poisson's ratio, ν.

3.2.2 Three-dimensional BRICK

In a continuous elastic material the stresses are related to the strains through the thirty-six elastic constants, grouped in the 'compliance matrix', which can be written in general terms as:

$$\begin{bmatrix} \varepsilon_x \\ \varepsilon_y \\ \varepsilon_z \\ \gamma_{xy} \\ \gamma_{yz} \\ \gamma_{zx} \end{bmatrix} = \begin{bmatrix} C_{11} & C_{12} & C_{13} & C_{14} & C_{15} & C_{16} \\ C_{21} & C_{22} & C_{23} & C_{24} & C_{25} & C_{26} \\ C_{31} & C_{32} & C_{33} & C_{34} & C_{35} & C_{36} \\ C_{41} & C_{42} & C_{43} & C_{44} & C_{45} & C_{46} \\ C_{51} & C_{52} & C_{53} & C_{54} & C_{55} & C_{56} \\ C_{61} & C_{62} & C_{63} & C_{64} & C_{65} & C_{66} \end{bmatrix} \bullet \begin{bmatrix} \sigma_x \\ \sigma_y \\ \sigma_z \\ \tau_{xy} \\ \tau_{yz} \\ \tau_{zx} \end{bmatrix} \tag{3.4}$$

It should be noted that only twenty-one of the elastic constants need to be defined for any isotropic soil as the compliance matrix is symmetric. The values contained within the compliance matrix can be found by substituting in the generalised form of

the equations that form Hooke's Law:

$$\begin{aligned}
\varepsilon_x &= \sigma_x/E - \nu\sigma_y/E - \nu\sigma_z/E, \\
\varepsilon_y &= -\nu\sigma_x/E + \sigma_y/E - \nu\sigma_z/E, \\
\varepsilon_z &= -\nu\sigma_x/E - \nu\sigma_y/E + \sigma_z/E, \\
\gamma_{xy} &= \tau_{xy}\ 2(1+\nu)/E, \\
\gamma_{yz} &= \tau_{yz}\ 2(1+\nu)/E, \\
\gamma_{zx} &= \tau_{zx}\ 2(1+\nu)/E
\end{aligned} \tag{3.5}$$

These equations can be written in matrix form as:

$$\begin{bmatrix} \varepsilon_x \\ \varepsilon_y \\ \varepsilon_z \\ \gamma_{xy} \\ \gamma_{yz} \\ \gamma_{zx} \end{bmatrix} = \begin{bmatrix} 1/E & -\nu/E & -\nu/E & 0 & 0 & 0 \\ -\nu/E & 1/E & -\nu/E & 0 & 0 & 0 \\ -\nu/E & -\nu/E & 1/E & 0 & 0 & 0 \\ 0 & 0 & 0 & 1/G & 0 & 0 \\ 0 & 0 & 0 & 0 & 1/G & 0 \\ 0 & 0 & 0 & 0 & 0 & 1/G \end{bmatrix} \bullet \begin{bmatrix} \sigma_x \\ \sigma_y \\ \sigma_z \\ \tau_{xy} \\ \tau_{yz} \\ \tau_{zx} \end{bmatrix} \tag{3.6}$$

where the elastic shear modulus:

$$G = E/2(1+\nu) \tag{3.7}$$

As the Brick model operates within strain space it is more useful for these relationships to be manipulated to give stresses from strains:

$$\begin{bmatrix} \sigma_x \\ \sigma_y \\ \sigma_z \\ \tau_{xy} \\ \tau_{yz} \\ \tau_{zx} \end{bmatrix} = A \begin{bmatrix} (1-\nu) & \nu & \nu & 0 & 0 & 0 \\ \nu & (1-\nu) & \nu & 0 & 0 & 0 \\ \nu & \nu & (1-\nu) & 0 & 0 & 0 \\ 0 & 0 & 0 & (\frac{1-2\nu}{2}) & 0 & 0 \\ 0 & 0 & 0 & 0 & (\frac{1-2\nu}{2}) & 0 \\ 0 & 0 & 0 & 0 & 0 & (\frac{1-2\nu}{2}) \end{bmatrix} \bullet \begin{bmatrix} \varepsilon_x \\ \varepsilon_y \\ \varepsilon_z \\ \gamma_{xy} \\ \gamma_{yz} \\ \gamma_{zx} \end{bmatrix} \tag{3.8}$$

where:

$$A = \frac{E}{(1-2\nu)(1+\nu)} \tag{3.9}$$

The Brick model does not use the six components of stress and strain shown in Equation 3.8. Instead Brick uses six components, relating to mean and shear stresses or volumetric and shear strains. The subscript y is used to denote the vertical direction,

with the z direction being the second horizontal component. The six components of strain are:

$$\text{Volumetric strain} = v = \varepsilon_x + \varepsilon_y + \varepsilon_z \tag{3.10}$$

$$\text{Shear strain component 1} = g_{zx} = \varepsilon_z - \varepsilon_x \tag{3.11}$$

$$\text{component 2} = g_y = \frac{(2\,\varepsilon_y - \varepsilon_x - \varepsilon_z)}{\sqrt{3}} \tag{3.12}$$

$$\text{component 3} = \gamma_{xy} \tag{3.13}$$

$$\text{component 4} = \gamma_{yz} \tag{3.14}$$

$$\text{component 5} = \gamma_{zx} \tag{3.15}$$

The six components of stress are:

$$\text{Mean stress} = p = \frac{(\sigma_x + \sigma_y + \sigma_z)}{3} \tag{3.16}$$

$$\text{Shear stress component 1} = t_{zx} = \frac{(\sigma_z - \sigma_x)}{2} \tag{3.17}$$

$$\text{component 2} = t_y = \frac{(2\,\sigma_y - \sigma_x - \sigma_z)}{2\sqrt{3}} \tag{3.18}$$

$$\text{component 3} = \tau_{xy} \tag{3.19}$$

$$\text{component 4} = \tau_{yz} \tag{3.20}$$

$$\text{component 5} = \tau_{zx} \tag{3.21}$$

In elastic materials the shear stress components are again related to the corresponding shear strain components through the shear modulus G (see Section A.1).

3.2.3 Derivation of geotechnical parameters

In common geotechnical scenarios, such as the triaxial test, parameters such as deviator and mean stress can be derived from the BRICK parameters.

Calculation of triaxial stresses

In the three-dimensional model, the mean normal stress, p, is part of the BRICK formulation but the value of the deviator stress, q, needs to be calculated. In terms of the triaxial stresses:

$$q = \sigma_a - \sigma_r \tag{3.22}$$

where, σ_a is the axial stress and σ_r is the radial stress.

As both σ_x and σ_z are in the horizontal direction, $\sigma_r = \sigma_x = \sigma_z$, leaving $\sigma_a = \sigma_y$. These stresses can expressed as follows:

$$\sigma_y = p + \frac{2t_y}{\sqrt{3}} \tag{3.23}$$

$$\sigma_x = \sigma_y - \sqrt{3}t_y - t_{zx} \tag{3.24}$$

Therefore:

$$q = \sqrt{3}t_y + t_{zx} \tag{3.25}$$

Octahedral shear strain

The BRICK model uses the root sum of the squares of its shear and volumetric components to calculate the changes in stress. The formulation of the BRICK vectorial strain (Section 3.3) resembles the formulation of the octahedral shear strain as given in Atkinson & Bransby (1978):

$${\gamma_{oct}}^2 = \frac{4}{9}\left[(\varepsilon_x - \varepsilon_y)^2 + (\varepsilon_y - \varepsilon_z)^2 + (\varepsilon_z - \varepsilon_x)^2 + \frac{3}{2}({\varepsilon_{xy}}^2 + {\varepsilon_{yz}}^2 + {\varepsilon_{zx}}^2)\right] \tag{3.26}$$

It can be shown that the Octahedral shear strain can be written in terms of the BRICK components of shear strain, Equation 3.27, the proof of which can be found in Appendix A.2.

$${\gamma_{oct}}^2 = \frac{2}{3}\left({g_y}^2 + {g_{zx}}^2 + \frac{{\gamma_{xy}}^2}{4} + \frac{{\gamma_{yz}}^2}{4} + \frac{{\gamma_{zx}}^2}{4}\right) \tag{3.27}$$

3.2.4 Strain paths to simulate common geotechnical scenarios

To allow the BRICK model to simulate specific scenarios, a strain path vector can be used to specify the required behaviour. The vector consists of three or six values depending on whether the two or three-dimensional model is being used, with the values being a ratio of applied strains rather than absolute values.

Isotropic compression

The simulation of isotropic conditions is very simple in BRICK. The strains in all directions are equal and therefore the only non-zero variable is the volumetric strain, v. In the case of the two-dimensional BRICK model the strain path vector, $[v,\ \varepsilon_x - \varepsilon_y,\ \gamma_{xy}]$, becomes [1, 0, 0], while in the three-dimensional BRICK model the strain tensor becomes [1, 0, 0, 0, 0, 0].

One-dimensional compression

To simulate one-dimensional conditions the vertical strains are allowed to increase while the horizontal strains are kept at zero. The volumetric strain now equals the vertical strain. Therefore for the two-dimensional model, $[v,\ \varepsilon_x - \varepsilon_y,\ \gamma_{xy}]$ needs to be specified as [1, 1, 0] to maintain one-dimensional conditions. With the three-dimensional BRICK model the strain tensor, $[v,\ g_{zx},\ g_y,\ \gamma_{xy},\ \gamma_{yz},\ \gamma_{zx}]$, must be specified in the ratio [1, 0, 1.1547, 0, 0, 0].

Undrained triaxial compression and extension

In an undrained triaxial test on saturated soil, the volumetric strain $v = 0$. The vertical strain, ε_y, and horizontal strain, ε_x, also sum to zero. Therefore, ε_y = -2ε_x and the shear strain component $g_{xy} = 2\varepsilon_y$. In this case γ_{xy} is also equal to zero so in the two-dimensional (plane strain biaxial test) formulation the three components of strain, [ε_v, $\varepsilon_x - \varepsilon_y$, γ_{xy}], need to be specified as [0, 1, 0] for compression or [0, -1, 0] for extension.

In the three-dimensional BRICK model the same conditions apply but the six component strain path vector is now defined as [0, 0, 1, 0, 0, 0]. Under these conditions the applied axial strain, ε_a or ε_y can be simplified to $g_y/\sqrt{3}$ and the shear strain $\varepsilon_s = 2g_y/\sqrt{3}$.

3.3 BRICK Computations

The basic concept of BRICK has been introduced at the beginning of this chapter. This section shows how calculations are implemented in the BRICK model, to enable a discussion of more complex predicted behaviour in subsequent sections. The code is easiest to understand when visualised in a flow diagram, as in Figure 3.2. The BRICK model was originally programmed in FORTRAN, but to allow a more sequential implementation, the BRICK code was first translated into the scientific programming code, MATLAB. The full MATLAB code for the BRICK model is given in Appendix B.1 along with a comparison of the results generated by the original FORTRAN code and the MATLAB translation.

Figure 3.2 shows the linear flow of the program, with a progression in each increment from the top to the bottom of the diagram, looping where required. The FORTRAN version of the BRICK model uses 'goto' loops to dictate the program flow. Although these fulfil the same purpose as 'for' and 'while' loops, it is more difficult to visualise the flow of the program. For the purposes of this section, the three component BRICK model will be discussed, thus mean stress and shear stress are represented by s and t respectively.

The first stage in the BRICK model is to initialise the variables and supply a strain increment. These parameters are passed from a control routine which can take the form of another MATLAB script. The gradient of the swelling line (in $\ln v - \ln p'$ space), κ^*, and elastic constant, ι, are then modified to account for the effects of overconsolidation, referred to in BRICK as the 'beta effect'. (The formulation of this is explained

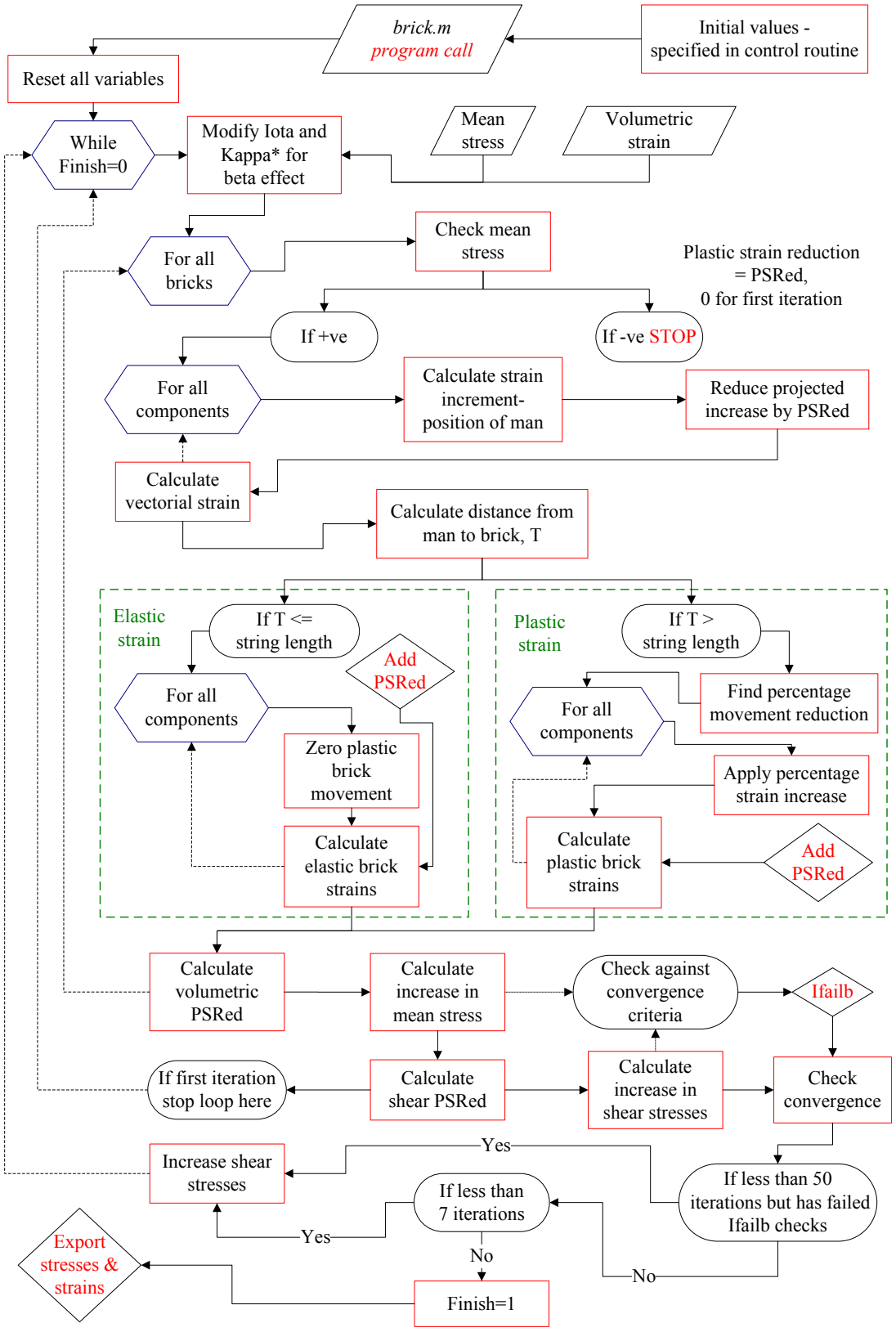

Figure 3.2: Flow chart showing internal workings of the BRICK model

in Section 3.3.1). The program then performs a check on the mean stress to ensure the stresses are still positive, before applying a reduced strain increment (applied strain minus the plastic strain reduction, explained in Section 3.3.2) to the position of the man, shown in Equation 3.28.

$$\varepsilon_{vec} = \sqrt{\sum \left(\varepsilon_i + \delta\varepsilon_i - \varepsilon_{bi} - \varepsilon_{ei}\right)^2} \tag{3.28}$$

for $i = 1$: the number of components in the model, where:

ε_{vec} = vectorial strain (separation of man and brick),

ε = current strain (position of the man),

$\delta\varepsilon$ = strain increment,

ε_b = position of the brick,

ε_e = plastic strain reduction.

The vectorial distance from each brick to the man is calculated and for each brick compared to the relevant string length. If the vectorial distance from the man to the brick is greater than the string length then the brick must be moved and therefore must be behaving plastically. If the vectorial distance between the man and the brick is less than the string length, the string has not yet become taut and the behaviour of that brick is elastic and thus the brick remains stationary.

From the individual changes in plastic strain the volumetric plastic strain reduction can be calculated, which is fed back into the calculations during the next iteration. This leads to the calculation of the change in mean stress in the soil, based on the change in elastic strain, as seen in Equation 3.29.

$$\delta s = s\delta v_e/\iota \tag{3.29}$$

where:

s = mean normal stress,

ι = elastic constant,

v_e = elastic volumetric strain (v − plastic volumetric strain, v_p).

The plastic shear strain reduction can then be calculated based on the increment of mean stress using Equation 3.36, which is explained in Section 3.3.2. The change in shear stress can be computed based on the new increased capacity for elastic shear strain, γ_e, generated by the plastic shear strain reduction.

$$\delta t = s\ \delta\gamma_e(1 - 2\nu)/\iota \tag{3.30}$$

3.3.1 The beta effect

As a soil becomes overconsolidated it demonstrates stiffer behaviour at a given normal stress level. In the BRICK model the beta effect is used to define the increase in stiffness for a given change in overconsolidation ratio:

$$\beta_{mod} = 1 + \beta \left(v - v_0 - \lambda^* \ln \left(\frac{s}{s_0} \right) \right) \tag{3.31}$$

where:

β_{mod} = beta modification factor,
β = beta constant,
v_0 = initial volumetric strain,
λ^* = gradient of the NCL plotted as ln v versus ln s,
s_0 = initial mean normal stress.

This formulation gives similar results to the equation proposed by Viggiani (1992), who conducted a series of small strain triaxial tests using Hall effect transducers and bender elements for the measurement of G_{max}. Viggiani (1992) suggested a relationship between stiffness and overconsolidation ratio in the very small strain region (<0.001%) of:

$$G_{max\ oc} = G_{max\ nc}\ {R_0}^m \tag{3.32}$$

where:

R_0 = overconsolidation ratio as defined from Figure 2.3 on page 7,
m = 0.25 for London Clay.

Figure 3.3 shows a comparison between equations 3.31 and 3.32, where the predicted overconsolidated stiffness, $G_{max\ oc}$, is compared to the normally consolidated stiffness at the same stress level $G_{max\ nc}$. For this purpose Equation 3.31 has been modified to directly compare the effect of the overconsolidation ratio by neglecting the small strain effects as unloading starts:

$$\beta_{mod} = 1 + \beta \left(\lambda^* - \kappa^* \right) \ln \left(\mathrm{OCR} \right) \tag{3.33}$$

where:

$\beta_{mod} = G_{max\ oc}/G_{max\ nc}$,
$\beta = 4$, $\lambda^* = 0.1$ and $\kappa^* = 0.02$.

A comparison of the plots in Figure 3.3 shows that both the beta effect and the Viggiani (1992) equations give similar results for overconsolidation ratios up to around ten, with

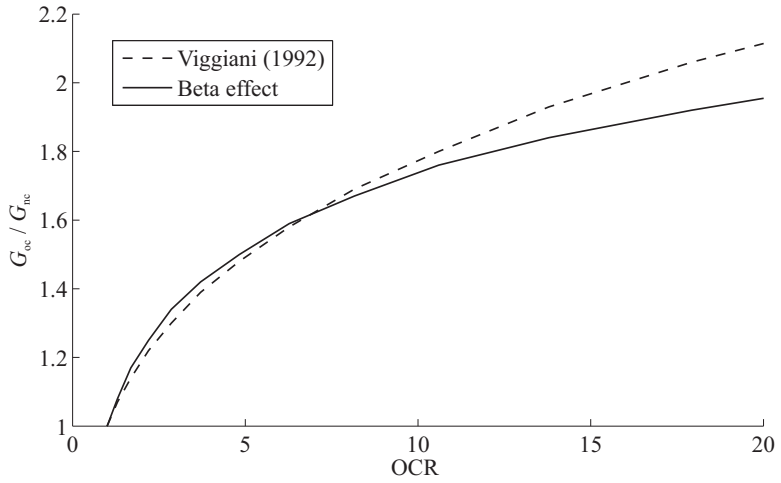

Figure 3.3: Comparison between models for the effect of overconsolidation on stiffness

the plots diverging for higher overconsolidation ratios. It should be noted that the values used in the beta effect equation have not been fitted to the Viggiani (1992) equation, the values used being typical for London Clay. Although the trends are similar there is no mathematical equivalence between the two equations (Simpson 2006).

3.3.2 Plastic strain reduction

In the BRICK model elastic movements lead to changes in stress, whereas plastic movements do not. When all the bricks are moving, the soil behaves perfectly plastically and without modification the stress increment would be zero. The plastic strain reduction acts to increase the elastic capacity for strain in an increment, thus allowing stress changes to be generated even when all the bricks are moving. The amount of plastic strain reduction is dependent upon the direction of the applied strain. The volumetric plastic strain reduction generates the compression and swelling lines by reducing the plastic strain by an amount depending upon the position of the man relative to the normal consolidation line. When the soil is normally consolidated:

$$\delta v_e = \left(\frac{\iota}{\lambda^*}\right) \delta v \tag{3.34}$$

When the soil is overconsolidated:

$$\delta v_e = \left(\frac{\iota}{\kappa^*}\right) \delta v \tag{3.35}$$

The formulation of the shear plastic strain reduction is computed differently to the volumetric plastic strain reduction, Equation 3.36. This enables BRICK to predict a unique point of failure depending upon the stress history of the soil, which is explained in more detail in Section 3.4.3.

$$\delta\gamma_e = \left(\frac{t}{s}\right)\delta v_e(1-2\nu) \tag{3.36}$$

3.4 BRICK Behaviour

In this section the concepts behind the model are explored with illustrated examples where applicable to show how BRICK models soil behaviour. This will include how the bricks aid the modelling of stress history and how the BRICK model predicts failure.

3.4.1 String lengths

The relationship between string lengths and the stiffness degradation curve has been briefly explained in Section 2.4. The original parameters for the BRICK model (Table 3.1) were given in Simpson (1992a), (1992b).

London Clay			Singapore Clay		
String	String length	G/G_{max}	String	String length	G/G_{max}
1	$8.3e^{-5}$	0.92	1	$8.0e^{-5}$	0.92
2	$2.1e^{-4}$	0.75	2	$2.0e^{-4}$	0.75
3	$4.1e^{-4}$	0.53	3	$4.0e^{-4}$	0.53
4	$8.3e^{-4}$	0.29	4	$8.0e^{-4}$	0.29
5	0.0022	0.13	5	0.002	0.13
6	0.0041	0.075	6	0.004	0.075
7	0.0082	0.044	7	0.008	0.044
8	0.021	0.017	8	0.018	0.017
9	0.041	0.0035	9	0.036	0.0035
10	0.08	0	10	0.075	0

Table 3.1: Rankine BRICK string parameters, Simpson (1992b)

The parameters contained within Table 3.1 were derived from a combination of the triaxial testing conducted by Richardson (1988) and back analysis of case histories at ARUP Geotechnics. This allowed a relatively high degree of confidence to be placed in the string lengths, as was shown for example in the modelling of the British Library deep basement in Simpson (1992b).

Kanapathipillai (1996) modified the string lengths for London Clay to reflect the back

analysis of the Heathrow Trial tunnel monitoring data and advanced laboratory testing. This led to a reduction in the original string lengths to those seen in Table 3.2.

London Clay		
String	String length	G/G_{max}
1	$3.040e^{-5}$	0.92
2	$6.0863e^{-5}$	0.75
3	$1.0143e^{-4}$	0.53
4	$1.2106e^{-4}$	0.29
5	$8.200e^{-4}$	0.13
6	0.00171	0.075
7	0.00352	0.044
8	0.00969	0.017
9	0.02223	0.0035
10	0.0646	0

Table 3.2: Modified BRICK string parameters, Kanapathipillai (1996)

It was previously discussed in Section 2.4 that each string length relates a proportion of the soil to the amount of strain required to develop plasticity in that specific proportion. What is not initially apparent, is that the string lengths also determine the angle of shearing resistance in the soil. If the S-shaped curve (Figure 2.40) is plotted using shear modulus, G, assuming the stiffness is proportional to mean stress, s, then the area under the curve, A, is equal to $\sin\phi'$ for normally consolidated soils. This is shown in Equation 3.37 for the case s = constant.

$$\begin{aligned} A &= \int \left(\frac{G}{s}\right) \mathrm{d}\gamma \\ &= \left(\frac{1}{s}\right) \int \left(\frac{\mathrm{d}t}{\mathrm{d}\gamma}\right) \mathrm{d}\gamma \\ &= \frac{t}{s} \\ &= \sin\phi' \text{at failure} \end{aligned} \tag{3.37}$$

For overconsolidated soils, the beta effect acts to increase the area under the S-shaped curve which also causes an increase in $\sin\phi'$. Hence the BRICK model automatically accounts for the increase in strength seen in overconsolidated soils. In the original version of the BRICK model (Simpson 1992b) the same β value used to calculate the increase of stiffness was used to calculate the increase in $\sin\phi'$. In later revisions, which

will be discussed in Section 3.5, the calculations for G and $\sin\phi'$ were split, giving rise to two independent β parameters known as β_G and β_ϕ respectively. Setting $\beta_G = \beta_\phi$ allows the program to use the original theory. In general $\beta_\phi < \beta_G$, (Oasys 2001). Typical values for London Clay are $\beta_G = 4$ and $\beta_\phi = 3$.

Strength and string length

The link between strength and the beta effect has been established. This principle can be extended to relate the strength to changes in the string lengths directly. If the string lengths are reduced, in accordance with Equation 3.37 the angle of shearing resistance also decreases, as shown in Figure 3.4.

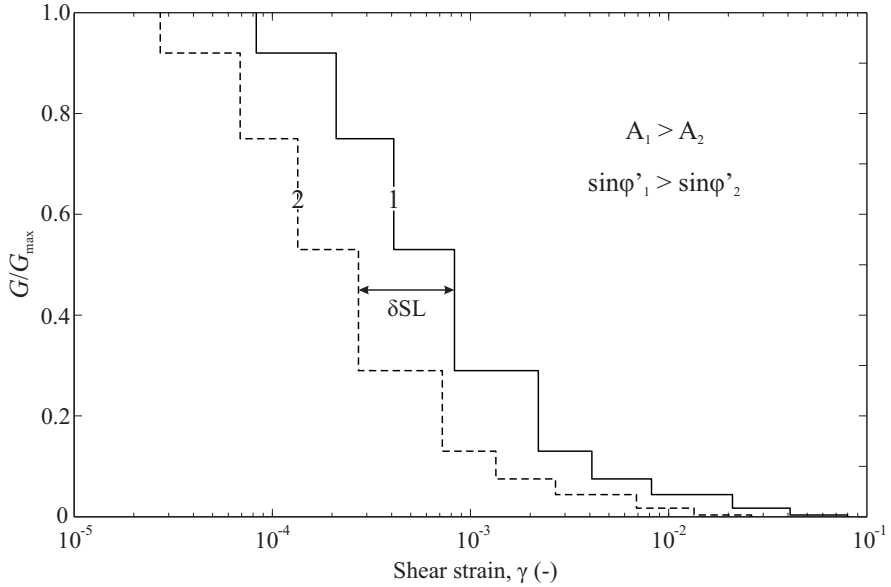

Figure 3.4: Reduction in string lengths

As the strings shorten not only does the angle of shearing resistance reduce, but so does the undrained strength of the soil. Conversely, if the string lengths increase so does the capacity for elastic straining, and hence the stiffness and ultimate strength are higher than for a soil with shorter string lengths. This principle is utilised in Chapter 5 where equations for undrained strength are used to govern the increase in string lengths.

3.4.2 Modelling stress history

The use of bricks and string lengths in the Brick model has another predictive ability other than the degradation of stiffness. As the predicted stiffness of the soil is dependent upon which bricks are moving, if the direction of the straining changes so a unique

stiffness response will be generated in the soil by the relative positions of all the bricks. This is a key factor in the modelling of stress history, especially in the case of heavily overconsolidated soils such as London Clay with a complex geological history of sedimentation, loading and unloading. BRICK models the soil from the original deposition through to the current day, allowing the stiffness of the soil to be a product of its complex stress history.

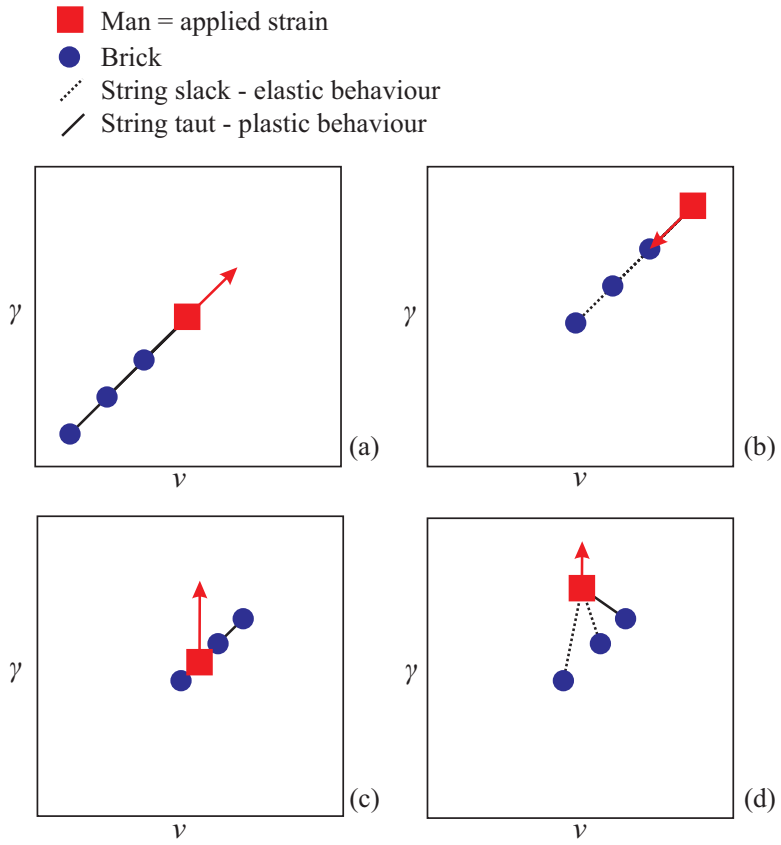

Figure 3.5: How BRICK models stress history

The initial one-dimensional consolidation stress ratio, K_0, is also derived from the S-shaped curve, as the BRICK model does not take K_0 as an input parameter (K_0 = horizontal effective stress, σ'_h / vertical effective stress, σ'_v). Figure 3.5a shows the gradient of the one-dimensional normal consolidation line in strain space, with the man and the bricks aligned at a 45° angle. The elastic shear strain, which governs the increase in shear stress, will be cos(45°) times that developed in a pure shear failure. Hence in one-dimensional consolidation the angle of shearing resistance mobilised, $\sin\phi'_{mob} = \sin\phi'/\sqrt{2}$ leading to Equation 3.38, (Simpson 1992b).

$$K_0 = \frac{1-\sin\phi'/\sqrt{2}}{1+\sin\phi'/\sqrt{2}} = \frac{\sqrt{2}-\sin\phi'}{\sqrt{2}+\sin\phi'} \tag{3.38}$$

Using the analogue Figure 3.5 demonstrates how BRICK models stress history. As the soil swells, the direction of the man's movement in strain space is reversed, as seen in Figure 3.5b, and initially all the strings are slack, giving rise to a purely elastic response controlled by ι. As the strings become taut, so the bricks start to move in the new direction and the stiffness of the soil is reduced. The more the soil swells, the more bricks lie to the right of the man in the figure. In Figure 3.5c the undrained shearing in compression phase commences. Again, due to the rotation in the strain path, the initial stiffness will be purely elastic, with the bricks starting to move as straining continues, as seen in Figure 3.5d. The stiffness response and the stress path followed during the undrained shearing are a product of the positions of the bricks relative to the man.

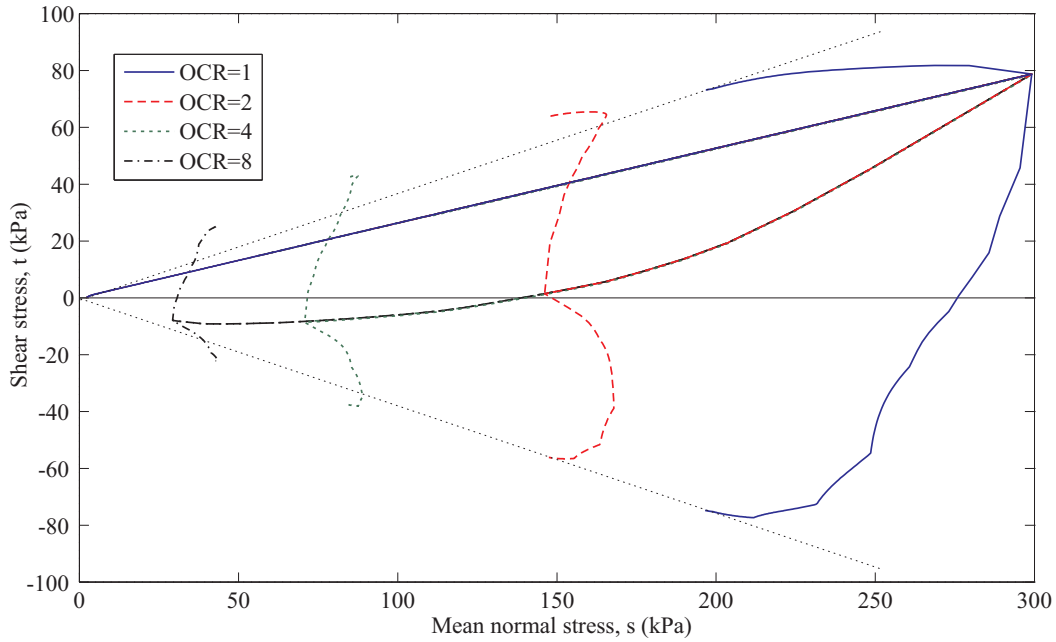

Figure 3.6: Stress path plots for differing overconsolidation ratios

When the bricks lie to the right of the man in strain space, as shearing occurs, they move with increasing shear strain but decreasing volumetric strain. Following Equation 3.29, a decrease in brick volumetric strain leads to an increase in mean stress, as

$\delta v_e = \delta v - \delta v_p$, and δv is determined by the volumetric movement of the man. Therefore $\delta v = 0$. As the bricks are experiencing a decrease in plastic volumetric strain, δv_p is negative and δv_e is positive leading to an increase in mean stress. This can be seen in Figure 3.6, where the the plots for overconsolidation ratios greater than one show an increase in mean stress during the initial undrained shearing. In the normally consolidated case the bricks lie at a 45° angle in strain space (Figure 3.5a), with all the strings taut (if the amount of vectorial strain is greater than the longest string length). In this case when the soil undergoes undrained straining all the bricks lie to the left of the man in strain space, leading to a positive plastic volumetric strain and hence, by the previous reasoning, a decrease in mean stress.

The complete stress path followed for each overconsolidation ratio can be made up of any combination of these two behaviours, depending on whether the bricks lie at a higher or lower volumetric strain than the man in strain space. In Figure 3.6 it can be seen that for the test with an overconsolidation ratio of two, the path initially displays an increase in mean stress (brick volumetric strain decreasing) but as straining continues, bricks that have longer string lengths and are lying at a lower volumetric strain are engaged, leading to the stress path curving to the left, the mean stress decreasing as the brick volumetric strain increases.

Computed examples of the paths of the bricks in strain space are given in Figure 3.7 where the OCR is changed for the different tests. The figure shows the bricks being engaged from both the left and the right side of the path of the man. For the generation of the plots shown in Figure 3.7 the original string parameters were used as stated in Table 3.1. The man's one-dimensional compression path is at a lower angle than the 45° that it represents due to the use of unequal scales on the axes required to display the full range of motion of the bricks. The longest string length used was 8% or 0.08, which gives the brick path that takes the largest shear strain to converge on the path of the man.

3.4.3 Predicting failure in BRICK

In the Brick model failure of the soil is defined as the point in stress space which the model converges upon under large scale shear strains, that is, the point at which, no matter now much further shear strain occurs, the soil will act perfectly plastically and effectively has a stiffness of zero.

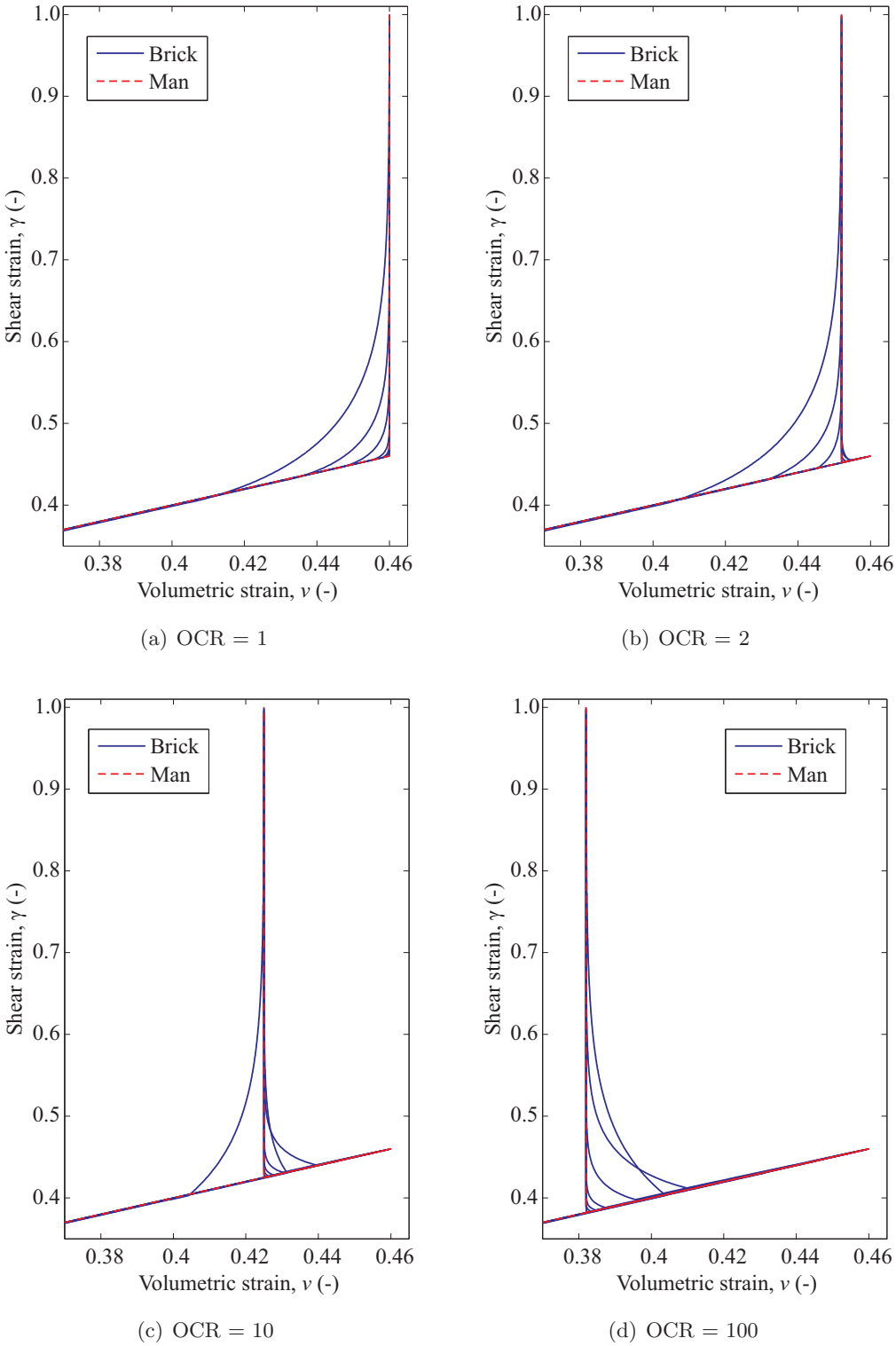

(a) OCR = 1

(b) OCR = 2

(c) OCR = 10

(d) OCR = 100

Figure 3.7: Brick paths for differing overconsolidation ratios

In Brick, if there is any element of volumetric strain, then there will be either an elastic stress change or a plastic strain reduction in the volumetric direction, leading to a change in mean stress, as seen in Equation 3.29. The two methods by which volumetric strains can be generated are:

1. Direct changes in applied volumetric strain (movement of the man).
2. Indirect changes in volumetric strain caused by taut strings moving the bricks.

The first method will obviously not apply to undrained shearing of saturated soils. The second method involves movements of the bricks as discussed in Section 3.4.2. These movements affect the change in mean stress, but as the bricks approach the path of the man in strain space, as seen in Figure 3.6, the amount of volumetric strain movement is reduced.

The changes in mean stress are directly linked to changes in volumetric strain, as are the changes in shear stress. No change in mean stress implies no elastic volumetric strains. If there is no change in elastic volumetric strain, there is no change in elastic shear strain, (Equation 3.36) and hence no change in shear stress. In the Brick model this occurs in undrained shearing when all the bricks are in line behind the man in strain space. Hence the Brick model can predict a unique point of undrained failure for any soil based upon the previous positions of the bricks and the amount of strain required to bring them into line behind the path of the man in strain space.

3.4.4 Prediction of the critical state line

In critical state models for any given initial stress state and stress path there will be a unique critical state predicted for the soil, and this will be met independent of the current soil state. Normally consolidated soils on the 'wet' side of the critical state line (CSL) are relatively loose and have to compress under shearing to reach the critical state. Overconsolidated soils, being dense, sit on the 'dry' side of the CSL, having to dilate to reach the CSL under shearing. The principle of wet and dry soils is shown in Figure 3.8

Brick does not predict a unique CSL for each soil, but the model does predict a unique CSL for each overconsolidation ratio (OCR). Figure 3.9 shows a study of the CSLs predicted by Brick in undrained test simulations. For both the normally consolidated soil (NC) and the overconsolidated soil, the soil is taken to the same volumetric strain on the normal compression line (NCL) and then sheared under undrained conditions in the

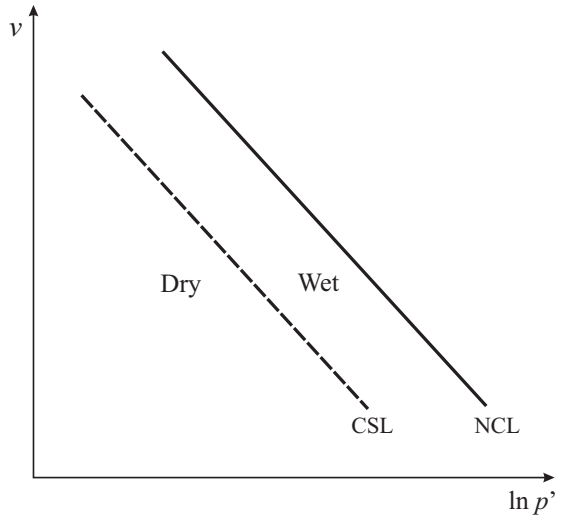

Figure 3.8: Wet and dry states defined by the critical state framework

case of a normally consolidated test and swelled back to the required stress and then sheared in the case of an overconsolidated test. This was repeated for five volumetric strains ranging from 10% to 50% with 10% increments. Joining the predicted failure points shows the predicted CSL for each test set. In Figure 3.9 the predicted CSLs are relatively close to each other, showing that, although there is not a unique CSL, for lightly overconsolidated soil the difference is relatively small. Figure 3.10 shows corresponding results with a higher OCR, leading to a much greater degree of swelling before the undrained shearing commences. The dilative tendency in the OCR=10 case is greater than in the OCR=2 case in Figure 3.9. However, this is still not enough to bring the soil back to the same CSL as predicted by the normally consolidated tests.

In practice failure of overconsolidated soils often occurs on the dry side of the CSL, which leads to failure on the Hvorslev surface before the CSL is reached, as seen in the Brick predictions in Figure 3.6. This behaviour can also be seen in the biaxial testing done by Sketchley & Bransby (1973) on Spestone Kaolin, shown in Figure 3.11. The normally consolidated and lightly overconsolidated tests (40 & 34) show a similar point of failure, but the overconsolidated test (37) fails well before reaching a similar point. This can usually be attributed to rupture in the sample with localised drainage and non-uniform deformations occuring.

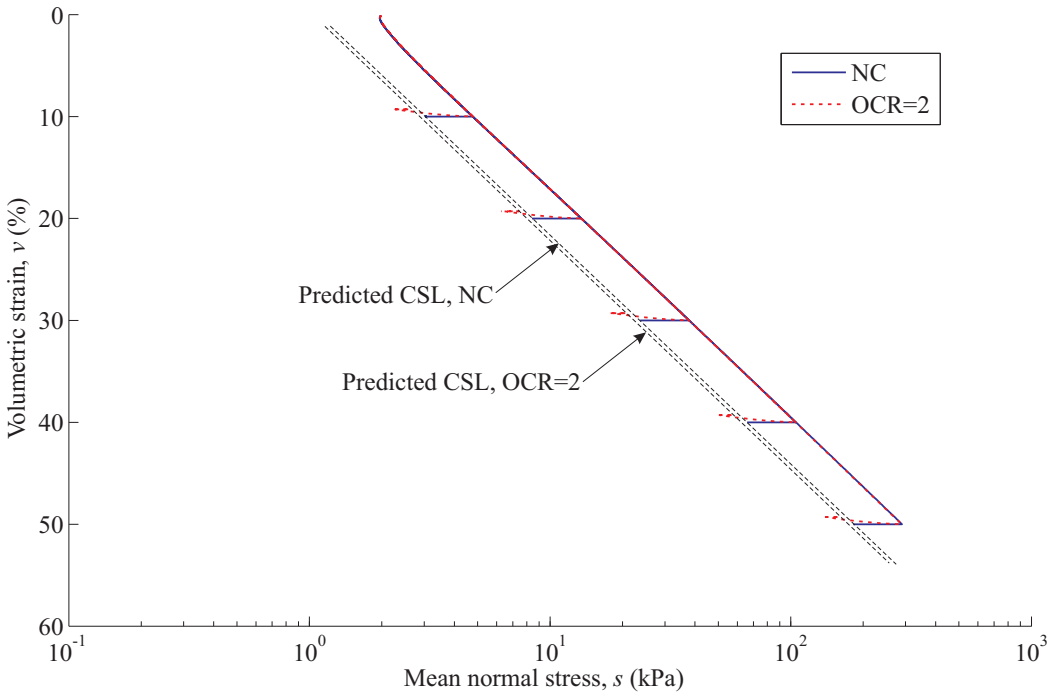

Figure 3.9: Critical state lines predicted by BRICK for normally consolidated and overconsolidated soils

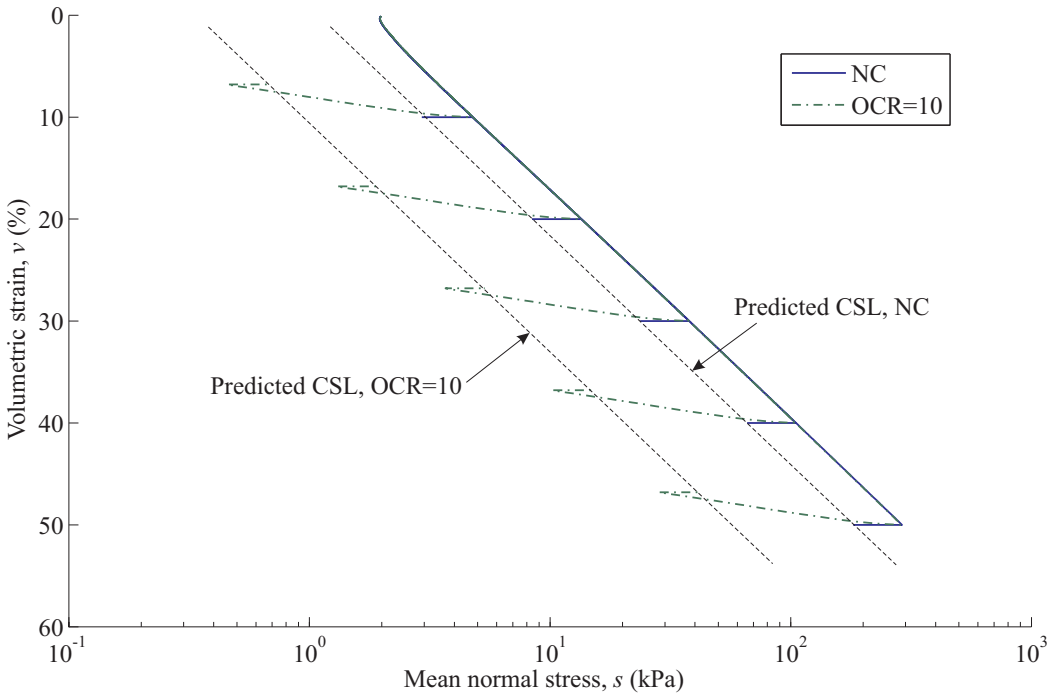

Figure 3.10: Critical state lines predicted by BRICK for normally consolidated and heavily overconsolidated soils

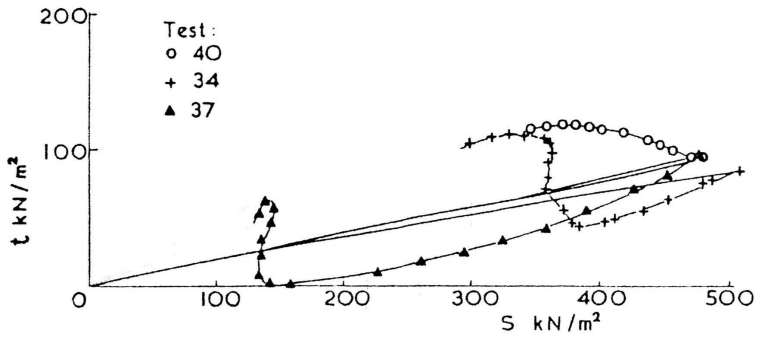

Figure 3.11: Stress paths from plane strain undrained shearing, Sketchley & Bransby (1973)

3.4.5 Initial brick positions

The magnitude of the stresses generated by the BRICK model are dependent upon whether the bricks are moving or not. One thing that must be considered is the initial position of the bricks in strain space, for which there are two main possibilities:

1. The bricks are all placed on the origin in strain space at the start of the modelling.
2. The bricks are placed along the volumetric strain axis at a distance from the origin equal to the string length for that brick.

The two scenarios are illustrated in Figure 3.12, where the symbols are the same as used in Figure 3.5. In Figure 3.12a all the bricks have an initial purely elastic stage before the strings become taut. Conversely in Figure 3.12b there is no purely elastic phase as the string lengths are initially taut along the volumetric strain axis. In the figure the man would start at the origin also but has been moved an arbitrary distance for illustrative purposes.

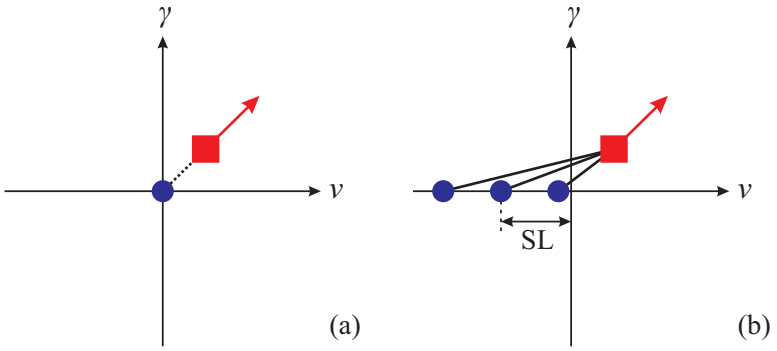

Figure 3.12: Diagram of plausible initial brick positions

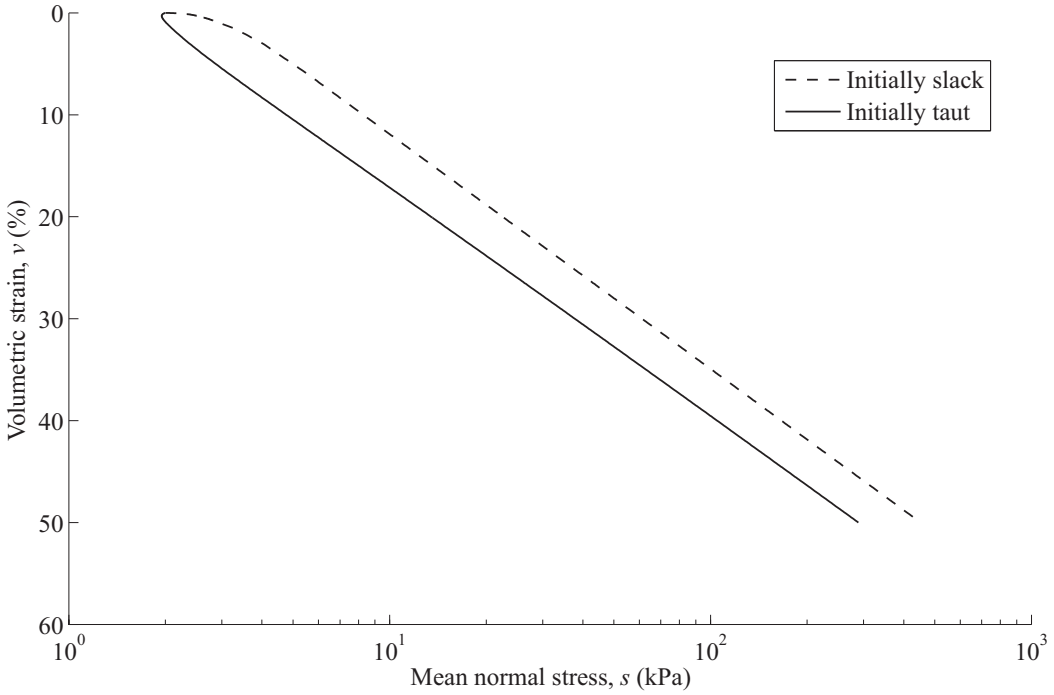

Figure 3.13: Effect of initial brick positions - v versus s

To demonstrate the effects that the initial brick positions have on the BRICK model predictions a simple one-dimensional consolidation test has been simulated. The soil was one-dimensionally compressed to 50% volumetric strain in both cases. The plot of volumetric strain, v, versus mean normal stress, s, shown in Figure 3.13 clearly shows the effects of the initial brick positions. The 'Initially taut' test shows nearly linear behaviour, whereas in the 'Initially slack' test the generated stresses are much higher with an initial stiffer period as the bricks are engaged.

The two extremes are presented in Figure 3.13 with the strings either initially completely slack or taut. Parallel stress paths that lie between those plotted can be generated by moving the bricks along the volumetric strain axis by a proportion of their string length. For example to generate a path that lies in the middle of those plotted in Figure 3.13, initial brick positions equal to half the string length along the volumetric axis could be specified.

The magnitudes of the stresses generated can be seen clearly in Figure 3.14 where the ratio of s/t is very similar for both tests. However, whereas the 'Initially slack' plot reaches a mean normal stress of 450kPa, the 'Initially taut' one only reaches 290kPa, a 35% reduction for the same increase in volumetric strain.

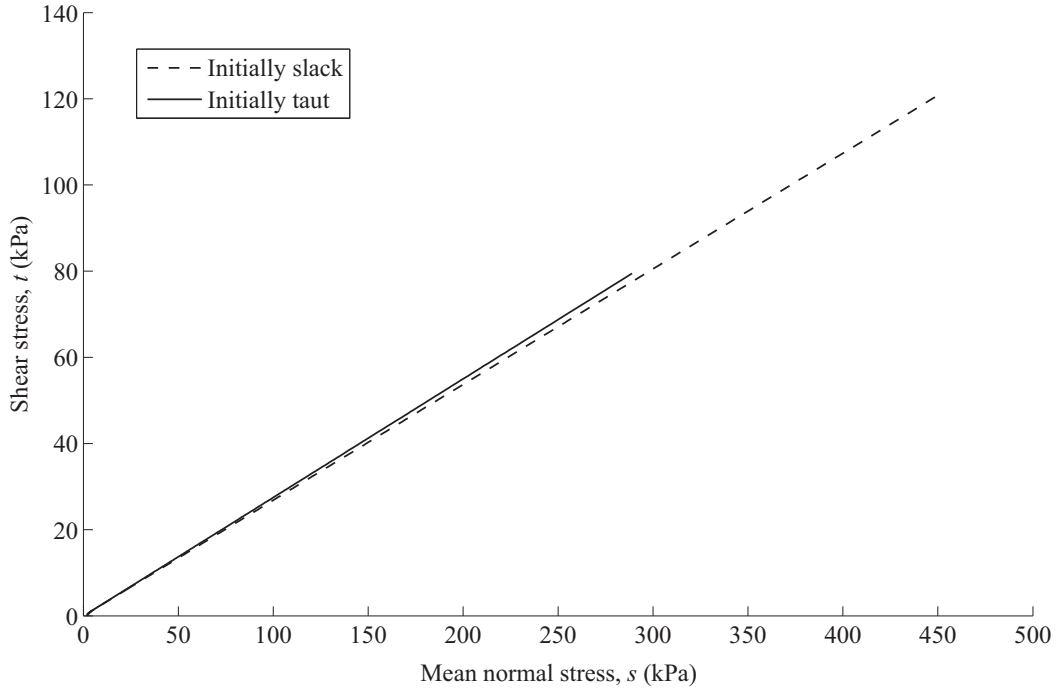

Figure 3.14: Effect of initial brick positions - stress path plot

The stiffness degradation curve for the current tests is shown in Figure 3.15, where the main differences between the curves are the smoothness of the curves and the initial predicted stiffness. The plot shows the normalised tangential stiffness, G_t/s, versus shear strain during the one-dimensional compression. The 'Initially slack' curve shows the stepwise nature of the approximated stiffness degradation curve. The steps relate to points at which another brick is engaged and the stiffness drops accordingly. The 'Initially taut' curve is much smoother due to the fact that all the bricks move as soon as compression starts, thus the drops in stiffness associated with the engagement of the stationary bricks never occur. There is no point at which a new string becomes taut and the stiffness drops stepwise. The smoothness of the 'Initially taut' curve is only demonstrated in the initial phases of compression, due to the initial brick positions. If the soil were allowed to swell after a period of one-dimensional compression, the predicted stiffness degradation curve in the new direction would be stepwise rather than smooth due to the reversal in strain direction. This means that, although the initial brick positions look to have a relatively large effect on the initial behaviour, the residual effect in the modelling of stress history and large degrees of overconsolidation is relatively small. The initial stiffness in the 'Initially taut' test is slightly less than that predicted in the 'Initially slack' test. The correct initial stiffness can be derived from the input parameters (Simpson 1992b), shown in (Table 3.1). For an ι value equal

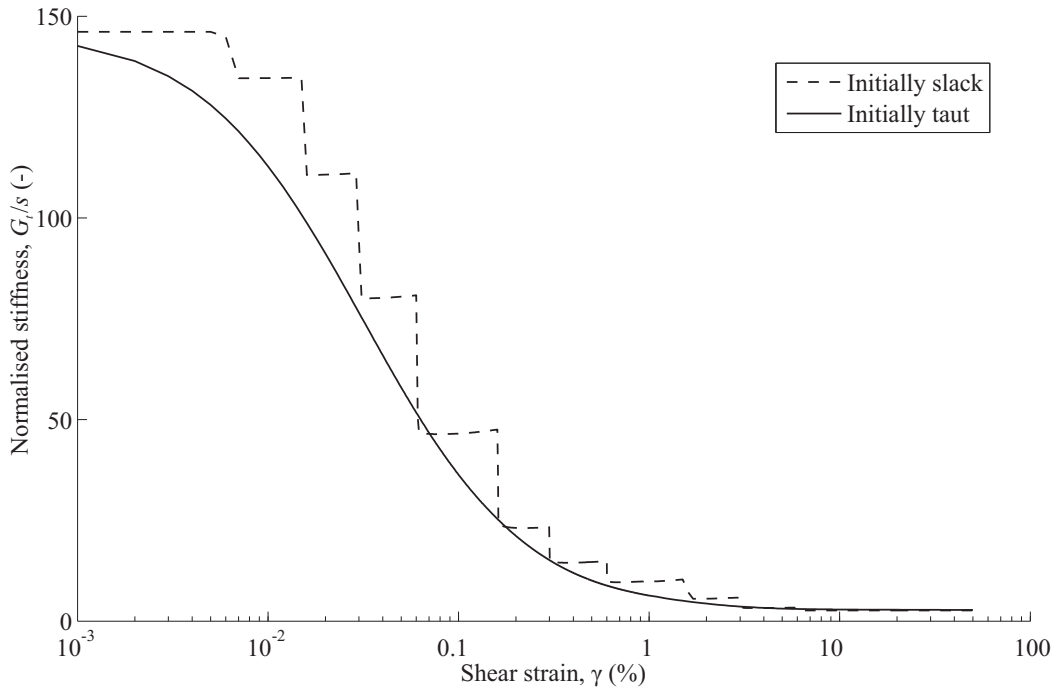

Figure 3.15: Effect of initial brick positions - normalised stiffness

to 0.0041 and a Poisson's ratio $\nu = 0.2$, the theoretical value of $G_t/s = 146$ which is the same as predicted in the 'Initially slack' test.

In the BRICK program (see next section) and SAFE, the brick positions have been initialised with the string lengths taut in volumetric strain (approach(2)), as this gives a smoother stiffness degradation for the applications to work with. For the purposes of this thesis, in the MATLAB implementation of the BRICK model, where many of the demonstrations of BRICK behaviour are purely conceptual, the initial brick positions have mostly been taken to lie at the origin in strain space (approach(1)). This allows the stepwise nature of the stiffness degradation curve to be observed, allowing visual checks on the predicted behaviour to be completed more easily during the initial stages of compression.

It should be noted that aligning the bricks at a 45° angle in negative strain space (so that the string lengths are initially taut in both shear and volumetric strain) causes the model to predict no increase in shear stresses during one-dimensional consolidation as there is no initially generated shear stress. Obviously this behaviour is nonsensical and the approach has not been considered further.

3.5 The BRICK Program

The BRICK model has been implemented into both the ARUP finite element program SAFE and another program, BRICK. The BRICK program allows the BRICK model to run without being incorporated in a finite element program and is capable of running laboratory test simulations, allowing the model to be calibrated. Inside the BRICK program are three main routines, of which two control the behaviour of the BRICK model. The third, BRICKC, contains constitutive models other than BRICK. BRICKA is the control routine for the BRICK program that passes the parameters to the BRICK model for calculation. BRICKA also has a stress path hunting routine built into it allowing the strain formulated BRICK model contained within BRICKB to follow a specific stress path. The BRICK program is capable of simulating any combination of stresses and strains.

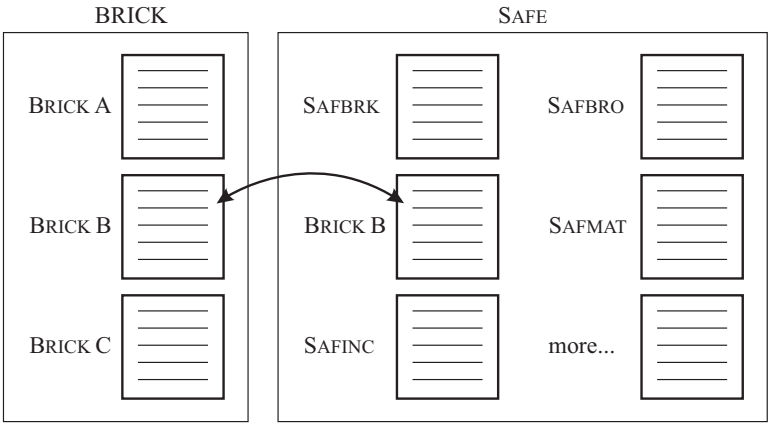

Figure 3.16: Routines within BRICK and SAFE

Figure 3.16 illustrates the main routines contained within the SAFE and BRICK programs. The BRICK program allows the BRICK model parameters to be fully tested before implementation into finite element analysis. The implementation process has been massively simplified by ARUP with the same BRICKB routine being employed in both SAFE and BRICK allowing the routine to simply be copied across. The implementation into SAFE will be further discussed in Section 6.2.

Currently, within the BRICK program there are 4 complete versions of BRICK theory that are available for use:

1. Original plane strain theory, Simpson (1992b).

2. As Theory 1 but with enhancements to remove iterative anomalies. Also contains a different formulation for κ^* creating a linear $v - \ln(s)$ line for swelling. The differences in the code between Theories 1 and 2 are listed in Appendix B.2.

3. 3D theory, with linear $v - \ln(s)$ line for swelling and modified Drucker-Prager shape for the failure surface, determined by current stresses. *Working model not intended for external release.*

4. As Theory 3 but with the failure surface determined by the ratios of brick positions and the predicted stress change relative to the Drucker-Prager yield surface.

The main work in this thesis has used Theories 1 and 2, but with modifications to the code to allow for full 3D analysis. This allows the native behaviour of BRICK to be observed rather than having to determine what part of the predicted behaviour is dependent on changes to the workings of BRICK and what is a product of external forcing functions such as the Drucker-Prager failure surface.

The BRICK program keeps no direct record of time, unlike SAFE, but specifying different size strain increments using an arbitrary time step of 1 allows the BRICK program to demonstrate time effects.

A check was conducted to test the correct translation and implementation of the MATLAB code (Appendix B.1). This was done by comparing the MATLAB results directly with those generated by the BRICK program.

The implementation of the models developed in later chapters into the BRICK program is given in Appendix C. More details on the workings of the BRICK program are given in Oasys (2001).

4

Bricks on Ice

4.1 Introduction

The Bricks on Ice idea was originally put forward by Den Haan (2001) whose paper, although only ever internally published, demonstrated a possible implementation of time dependent viscous effects into the BRICK model. In the BRICK model analogue the current strain is represented by the position of the man and the bricks are attached to the man by a series of strings of different lengths. In the Bricks on Ice (BOI) approach, the velocity of each brick is individually calculated and allowed to continue into the next BRICK increment. If, for example, the man were to stop moving the bricks would keep moving at a logarithmically decreasing rate which would lead to the distance from the man to the bricks reducing. This movement would generate negative elastic strains which decrease the stresses. Such behaviour is known as stress relaxation and is one amongst a number of effects that can be simulated by the BOI approach. In this chapter the theory behind the BOI approach will be explained before being implemented into the MATLAB recreation of the BRICK model. The BOI model will then be benchmarked against the results given in Den Haan (2001), before being tested under a wider range of conditions to assess its capabilities.

4.2 Brick-led Viscous Motion

In the BOI approach, as described in Den Haan (2001), time dependent viscous effects were accounted for by allowing the motion of the bricks to continue from one BRICK increment to the next, generating viscous strains. These viscous strains acted to reduce the stresses at any given point as less of the applied strain was treated as being elastic, effectively turning what would be elastic strains into viscous strains. In the original BRICK model the strain applied in any one increment, $\delta\varepsilon$, could be split into its corresponding elastic, $\delta\varepsilon_e$, and plastic, $\delta\varepsilon_p$, components:

$$\delta\varepsilon = \delta\varepsilon_e + \delta\varepsilon_p \tag{4.1}$$

In the BOI approach viscous strains, $\delta\varepsilon_{visc}$, were developed by reducing the amount of previously available elastic strain while keeping the generated plastic strain the same, therefore Equation 4.1 becomes:

$$\delta\varepsilon = \delta\varepsilon_e + \delta\varepsilon_p + \delta\varepsilon_{visc} \tag{4.2}$$

Viscous strains were treated by the BRICK model in the same way as the plastic strains, the difference being the cause of the strain.

4.2.1 Introducing time

In the original BRICK model there was no ability to account for the passage of time in any given increment, as predicting time dependent behaviour was not part of the model's capabilities. The model operated solely upon the increment of strain, either predefined or generated by the stress-path hunting routine BRICKA (Section 3.5).

The introduction of time into the BRICK model meant that the strain increment became dependent on both time and a new variable, strain rate. For any given BRICK increment the strain increment was given by the strain rate, $\dot{\varepsilon}$, multiplied by the time increment between steps, δt.

$$\delta\varepsilon = \dot{\varepsilon}\ \delta t \tag{4.3}$$

4.2.2 Generating brick velocities

The introduction of individual brick velocities was key to generating the movement of the bricks in the next increment. In any BRICK increment the current velocity of a brick can be calculated from the velocity of the brick in the previous increment, multiplied by the time increase between increments and a logarithmic decay function. In the original BOI model, the logarithmic decay was applied separately to the volumetric and vectorial shear components of strain (Section 3.2.1), referred to by Den Haan (2001) as a coaxial deceleration model:

$$\delta\dot{\varepsilon}_i = \dot{\varepsilon}_{i,0}\ \delta t \left(\frac{Llog}{Llin}\right) \tag{4.4}$$

where:

i = 1 - NC, relating to the individual brick components (Section 3.2.1) and:

$$Llog = \sqrt{\left[c \ln\left(1 + \frac{\dot{v}_0 \delta t}{c}\right)\right]^2 + \left[c \ln\left(1 + \frac{\dot{\gamma}_0 \delta t}{c}\right)\right]^2} \tag{4.5}$$

$$Llin = \sqrt{\dot{v}_0 \delta t^2 + \dot{\gamma}_0 \delta t^2} \tag{4.6}$$

$\dot{\varepsilon}_{i,0}$ = strain rate at the end of the previous increment,
c = creep constant,
$\dot{v}_0$ = rate of volumetric strain in the previous increment,
$\dot{\gamma}_0$ = rate of shear strain in the previous increment.

The formulation of the deceleration of the bricks shown in Equation 4.4, termed CoAD v1, calculated accurate results for most cases. The main exception was the case where the continued motion of the bricks and the motion of the man were in opposite directions. In this case there were multiple solutions leading to the motion of the bricks being underestimated. This issue was resolved by using the resultant velocity from the end of the previous increment instead of the separate components of strain. Thus, the formulation of the coaxial deceleration model was modified to use resultant, rather than component brick velocities. This model is referred to as CoAD v2. Equation 4.6 remained the same while the calculation of *Llog* was modified to reflect the new coaxial relationship:

$$Llog = c \ln\left(1 + \frac{Llin}{c}\right) \tag{4.7}$$

In both versions of the coaxial deceleration model the c parameter is a creep constant. The calculation of the deceleration of the bricks along with the method of implementation into the BRICK model is shown in Figure 4.1. It should be noted that the creep constant must be different in the two coaxial deceleration models for the generated stresses to be the same. By comparison it can be found that the ratio of c values between CoAD v1 and CoAD v2 is $1{:}\sqrt{2}$ for one-dimensional compression.

4.2.3 Including viscous brick strains

The calculation of the viscous brick strains was discussed in Section 4.2.2. In this section a detailed description of how these viscous strains are included in the calculations of the BRICK model is presented.

For each brick the viscous movements are calculated, using one of the coaxial deceleration models, and added to the current position of the bricks. This has the effect of

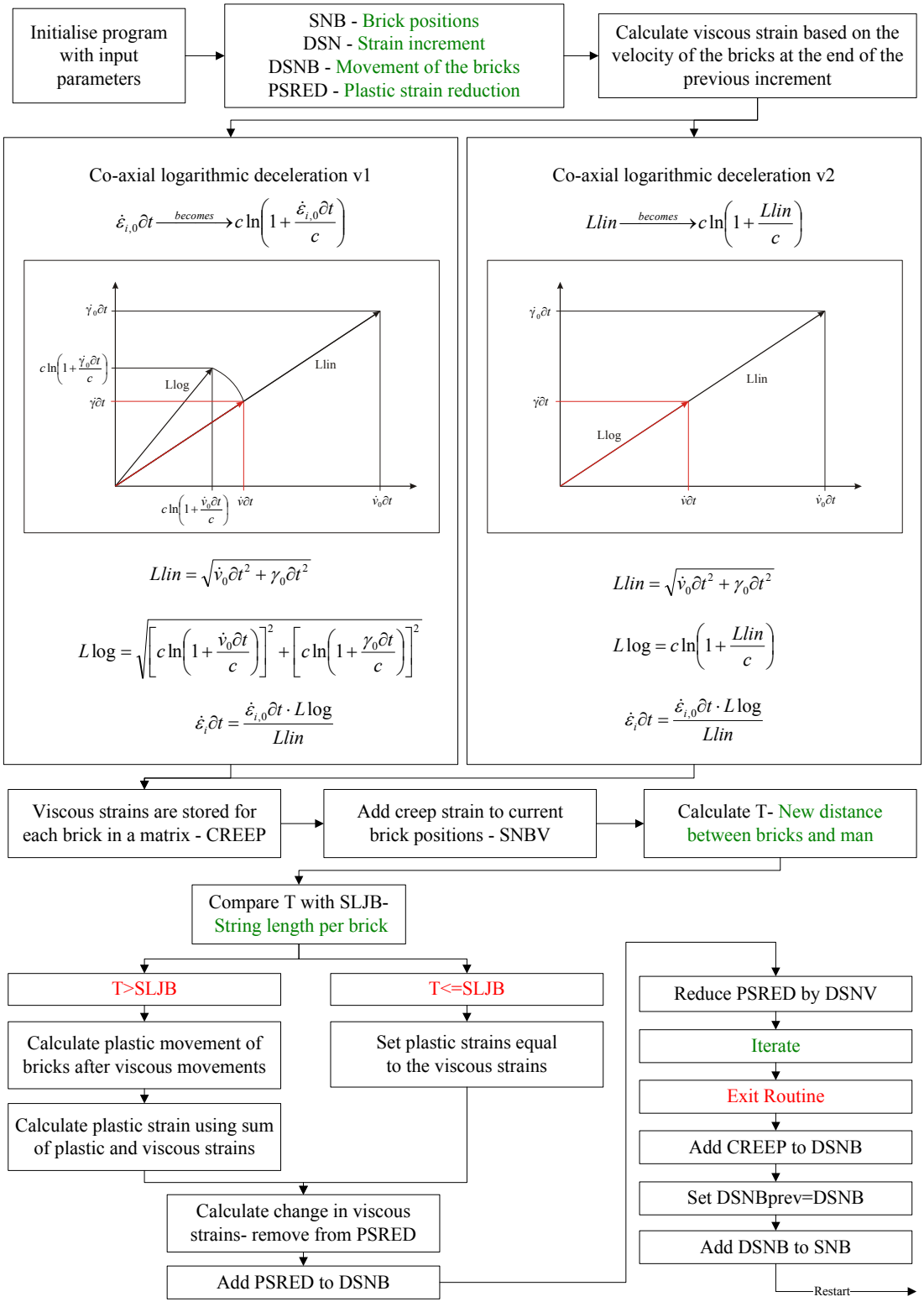

Figure 4.1: Calculation of brick velocities

reducing the distance between the man and the bricks, thus giving a reduced capacity for elastic strains. The effects of this movement are dependent upon whether the soil is predicted to behave elastically (slack strings) or plastically (taut strings).

Visco-elastic strains

When the strings are slack, no plastic strains are generated. The calculated viscous strains are treated as plastic strains by the BRICK model except that the plastic strain reduction does not apply. This can be termed a *visco-elastic* response. In this scenario the reduction in the distance between the man and the bricks caused by the viscous strains causes a reduction in the predicted change in stresses for a given strain level.

Visco-elasto-plastic strains

When the strings are taut, the viscous strains act to reduce the amount of plastic strain generated. This leads to a reduction in the elastic strains generated by the plastic strain reduction and hence, reduced stress changes. This form of deformation can be termed *visco-elasto-plastic* behaviour as the plastic strains induce a reduced element of elastic strain via the plastic strain reduction.

The velocity of the bricks is governed by the movement of the man (applied strain, $\delta\varepsilon$) and is automatically updated every increment. In some scenarios updating the velocity of the bricks would be necessary even if there were no strain increment. One such circumstance would be when the velocity of the man reduces to zero and the soil enters a stress relaxation stage. The man is then stationary but the bricks continue to move, which will be discussed further in Section 4.3.1.

4.3 Recreating results of Den Haan (2001)

To test the implementation of the BOI approach into the BRICK model, a set of results was produced for comparison with Den Haan (2001). Simulations of stress relaxation and strain fixation behaviour seen in CRS oedometer tests were presented by Den Haan, as well as biaxial shearing simulations done with different creep constants. From a digital analysis of the original figures in Den Haan's paper, the strain rate was calculated as 0.175% per hour, except during the biaxial test where the rate went up to 0.641% per hour. The digital analysis involved a program called Plot Digitiser (see Appendix E.2) which allows an image of a plot to be opened and the scale of the x and y axes to be measured and specified. Once the scales have been calibrated, the plot is selected using the mouse and the coordinates of the points selected are generated. It has been

assumed that the BRICK parameters used by Den Haan (2001) were the same as those given in Simpson (1992b).

4.3.1 Stress relaxation

Stress relaxation was demonstrated in Den Haan (2001), Figure 4.2, using the BOI model. In the simulation the soil was one-dimensionally compressed to 42% volumetric strain and then held at constant strain for a period of twelve hours. The one-dimensional compression was then continued to 51% volumetric strain, at which point an undrained shear compression stage was initiated.

During the constant strain period the position of the man stays constant and the motion of the bricks continues in the previous direction towards the man. This means that the strings are slack and that plastic strains are being generated by the movement of the bricks. As the applied strain is zero, a positive plastic strain requires a negative elastic strain, leading to a reduction in stresses at constant strain.

Upon the recommencement of straining the soil exhibits stiffer behaviour due to the slack strings. This allows the soil to return to the stress path generated before the relaxation commenced. Figure 4.3 shows a plot generated by the MATLAB recreation of Den Haan's work. The plot shows the stresses and strains generated versus the time taken in days. It can be seen that up to the ten day point the volumetric (SN(1)) and shear (SN(2)) strains increase at the same rate, as expected for one-dimensional compression. After ten days the sample is held at constant strain, while the continued motion of the bricks means that the stresses decrease, seen in the sudden drops in the mean stress (SS(1)) and shear stress (SS(2)). Upon the recommencement of straining the stresses jump back to magnitude that was reached before the relaxation occurred. This 'jump' results from a much higher stiffness generated by the relaxation period. After twelve and a half days, the soil is sheared in undrained conditions. This is shown by the volumetric strain remaining constant while the shear strain increases at a higher rate. This period of shearing leads to a drop in both mean and shear stresses as the soil shears towards failure, as predicted in the normally consolidated test simulations shown in Figure 3.6 on page 60.

From a comparison of Figures 4.2 and 4.3 it can be seen that the current implementation of the BOI approach is giving the same magnitudes of stresses and behaviour patterns during the relaxation phase as Den Haan (2001). Thus the MATLAB recreation can be

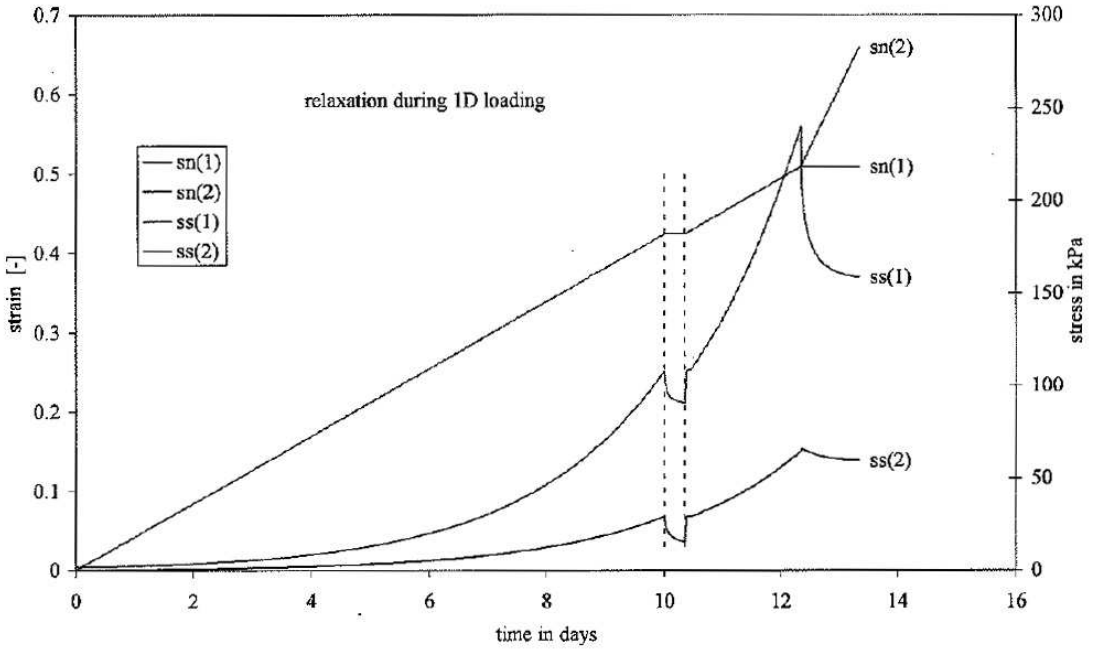

Figure 4.2: Stress relaxation during 1D compression, Den Haan (2001)

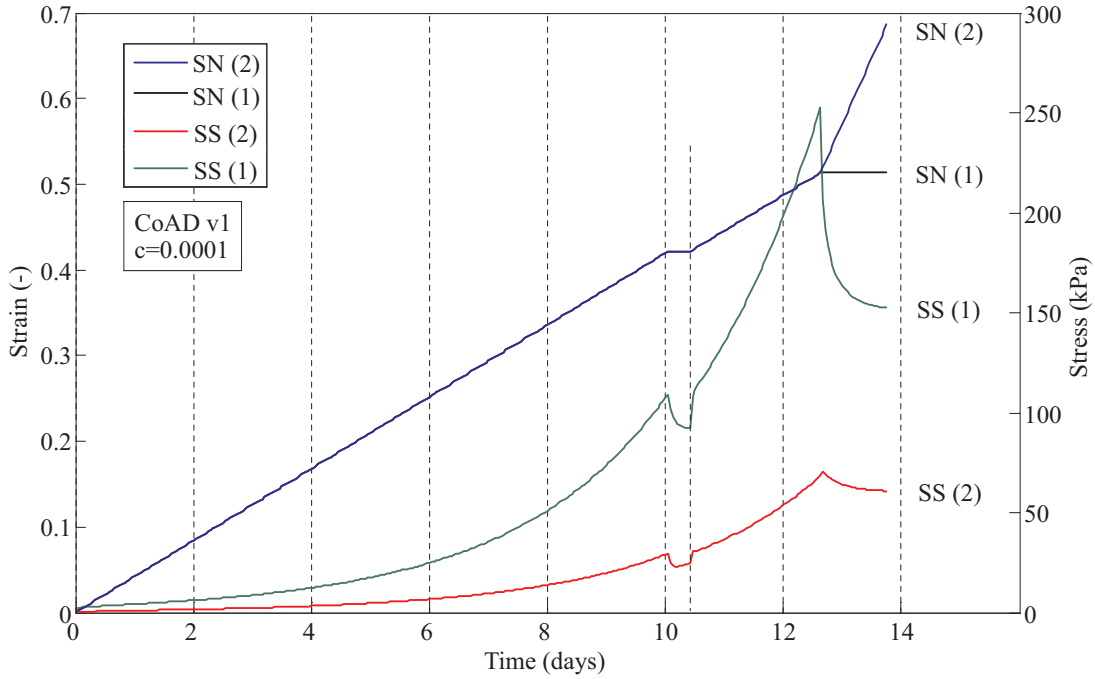

Figure 4.3: Stress relaxation during 1D compression, MATLAB recreation

said to be correctly implemented.

4.3.2 Strain fixation

Strain fixation was a term originally coined by Den Haan (2001). It refers to an increase in stresses while the strains are held constant and occurs after a period of unloading. In the BOI model this equates to the bricks moving towards the man from a higher strain level. This generates negative plastic strains, leading to positive elastic strains and an increase rather than a decrease in stresses. Upon the recommencement of straining in the positive direction, the stresses return to the pre-fixation level.

In the strain fixation simulation, Figure 4.4, the soil was one-dimensionally compressed to 42% volumetric strain and then one-dimensionally swelled to 40% volumetric strain. The strains were then held constant for twelve hours after which the one-dimensional compression recommenced taking the soil to 50% volumetric strain, at which point an undrained shear compression test was conducted.

The results of the MATLAB recreation shown in Figure 4.5 show a similar pattern to those seen in Figure 4.4 from Den Haan (2001). However, the stresses generated in the fixation period are much higher in Figure 4.5 than in Figure 4.4. Den Haan does not explicitly state which deceleration model was used to generate his plots. In Figure 4.5 it was assumed that the original coaxial logarithmic deceleration model (CoAD v1) was implemented by Den Haan (2001) with a creep value $c = 0.0001$, which was found by iteration as the value of c was not given in his paper. While this value of c led to accurate results during the stress relaxation test simulation in Figure 4.3, using CoAD v1, this was not the case for the strain fixation test simulation.

For the above reason it was decided to run an equivalent strain fixation test with the CoAD v2 model. As was noted in Section 4.2.2, the c value has to be multiplied by the square root of 2 to get the same magnitude of stresses for normal consolidation as found by using CoAD v1, so for the CoAD v2 tests $c = 0.000141$ was used. The pattern shown in Figure 4.6 during the fixation period after the swelling shows a much better fit to that shown in Figure 4.4.

4.3.3 Biaxial testing

The biaxial test simulations were conducted by isotropically compressing the soils to a mean stress of 240kPa at which point undrained shear compression tests were con-

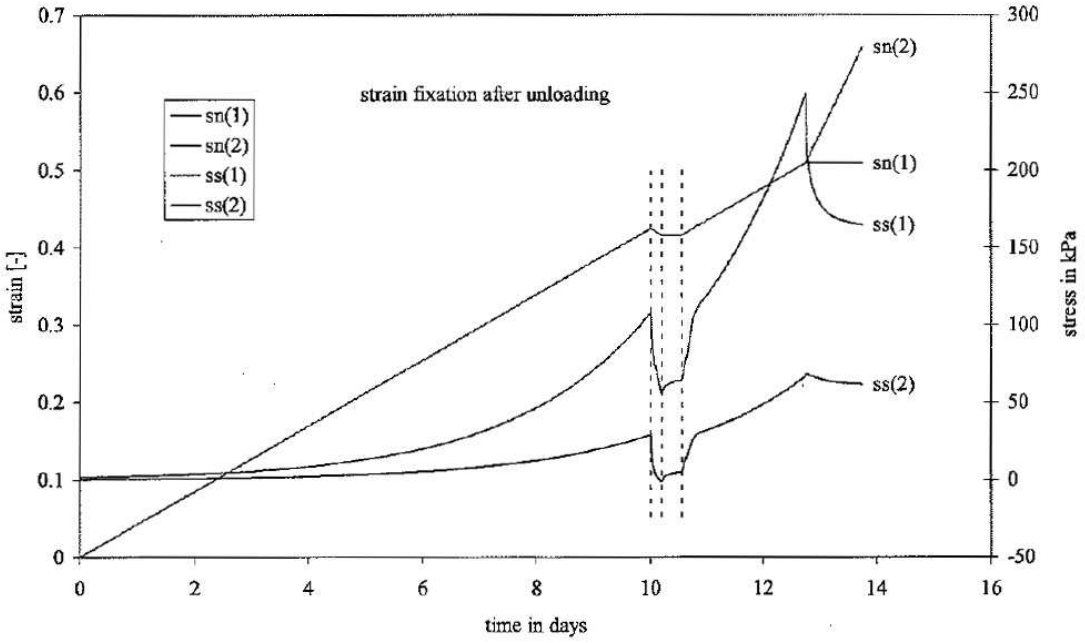

Figure 4.4: Strain fixation with BOI, Den Haan (2001)

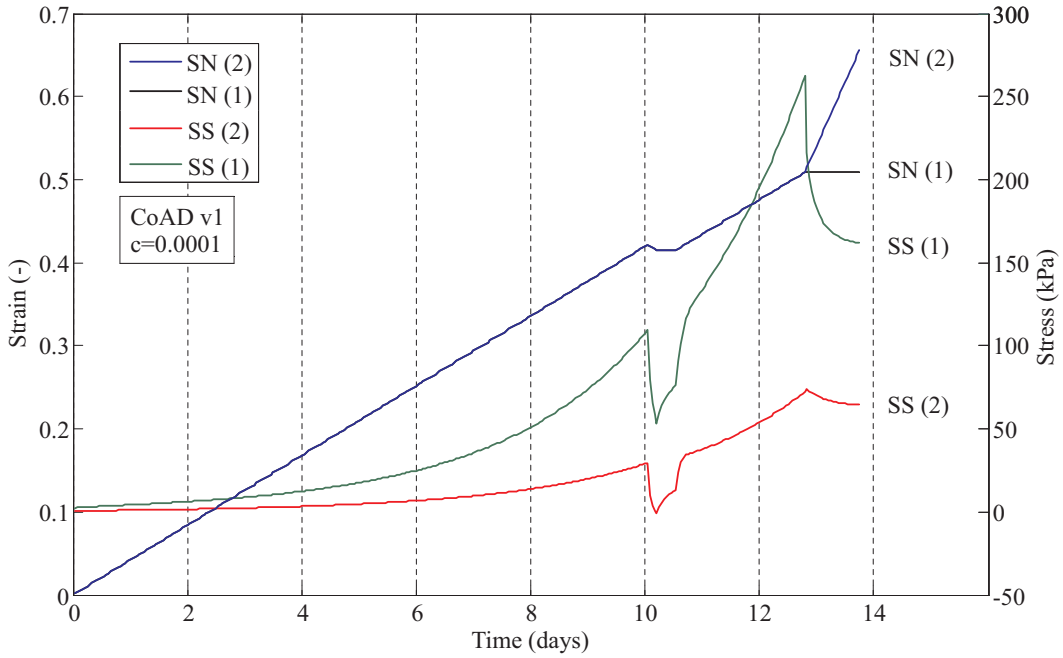

Figure 4.5: Strain fixation with BOI, MATLAB recreation using CoAD v1

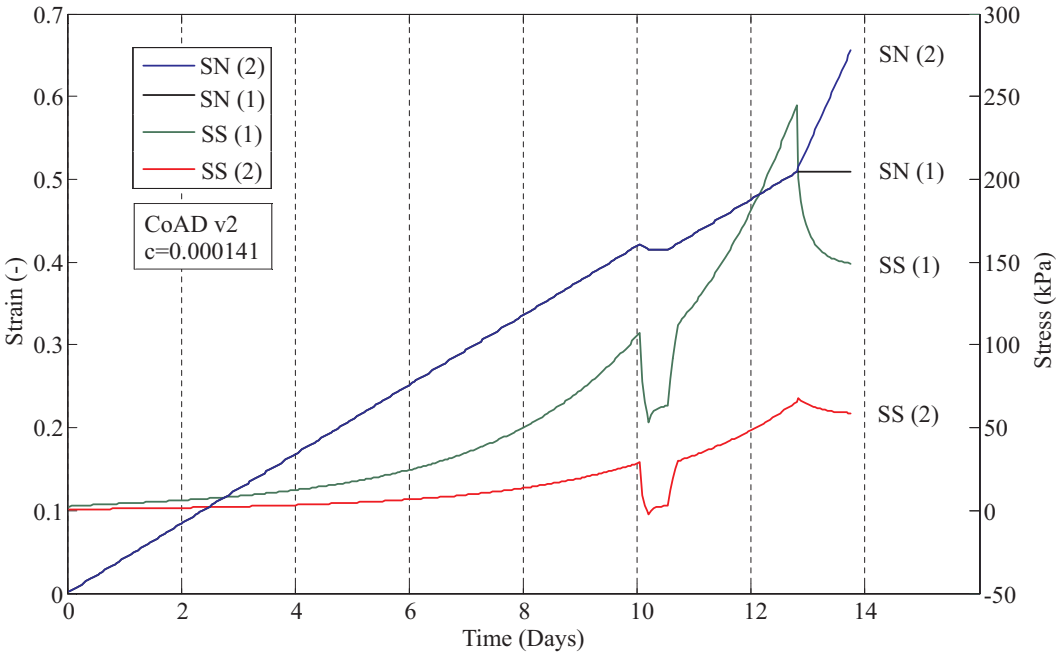

Figure 4.6: Strain fixation with BOI, MATLAB recreation using CoAD v2

ducted, each with a different creep rate, taking the soil to failure. A comparison between Figure 4.7 (Den Haan 2001) and Figure 4.8 (MATLAB recreation) shows a minimal difference between the predicted results.

One difference, however, is that the Den Haan plots for different creep rates follow the same path before diverging, whereas the plots in Figure 4.8 diverge immediately. This is assumed to be due to small undefined differences in the initial conditions assigned in Den Haan (2001) and the current work.

It can be deduced that, because all the paths start from the same isotropic stress, the effects of creep in the initial compression up to 240kPa have been ignored. This means that upon the start of the biaxial shearing the strings would be taut. This approach was was used in MATLAB recreation. If creep were allowed to occur during isotropic compression to a given volumetric strain, the starting stress for each creep rate would be different, with the higher creep rates lowering the stress at which shearing starts (Section 4.2).

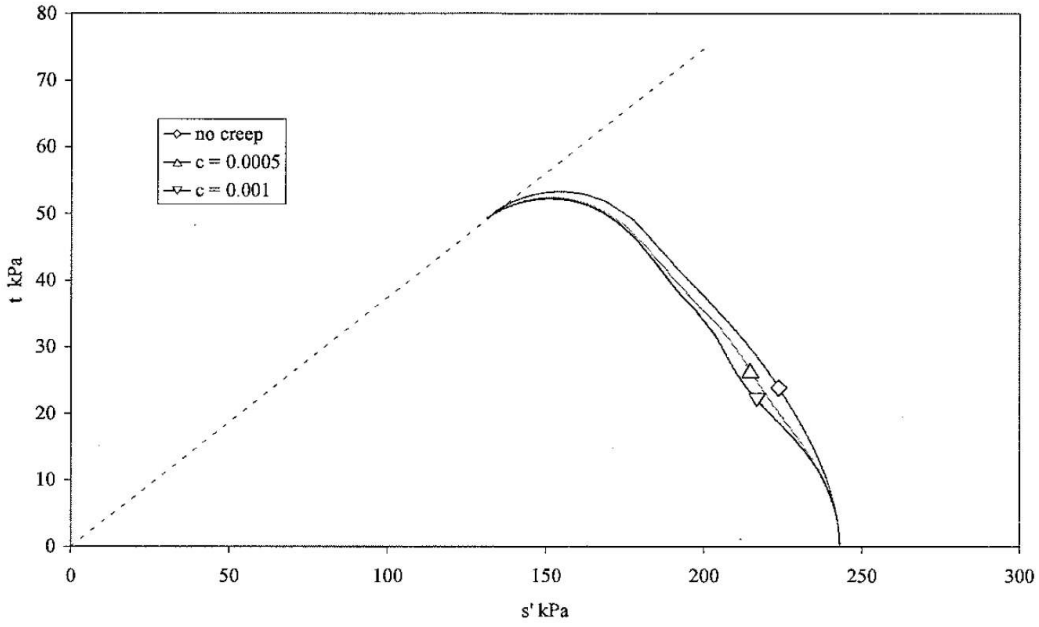

Figure 4.7: CIU tests with variation of creep parameter, Den Haan (2001)

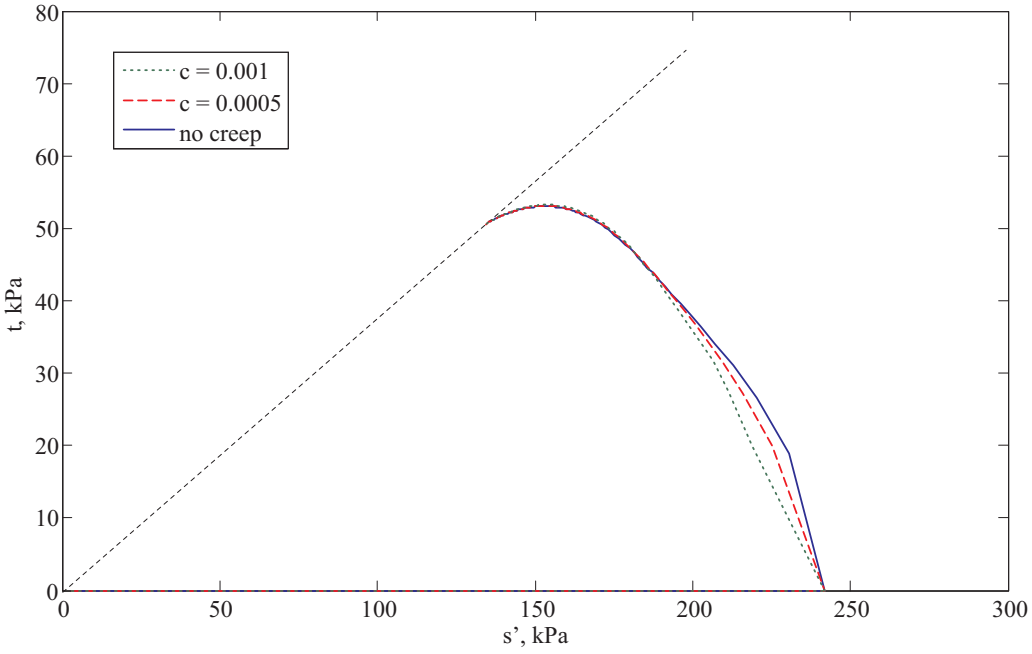

Figure 4.8: Plane strain biaxial testing with variation of creep parameter

4.4 Comparing Coaxial Deceleration Models

The comparison of the results obtained with CoAD v1 (Figure 4.5) and CoAD v2 (Figure 4.6) shown in Section 4.3.2 does not show any marked differences except in the region of strain fixation. However further comparison is required to investigate any consequences of the difference between the models.

A swelling and recompression test was performed with each CoAD model. This involved one-dimensionally compressing the soil to 42% volumetric strain then swelling the soil to 40% volumetric strain. The soil was then recompressed to 51% volumetric strain. The parameters used in the comparison were the same as those given in Simpson (1992b) with a creep constant $c = 0.0001$ used with CoAD v1 and $c = 0.000141$ with CoAD v2. The results of the tests can be seen in Figures 4.9 and 4.10. Figure 4.9 compares the stress path plots and highlights the problem with the CoAD v1 methodology. During the recompression the plot for CoAD v1 does not rejoin the original K_0 path but overshoots, predicting a higher shear stress for the same mean stress. This should not occur. The plot for CoAD v2 rejoins the original K_0 line soon after compression recommences and continues on a line of equal gradient.

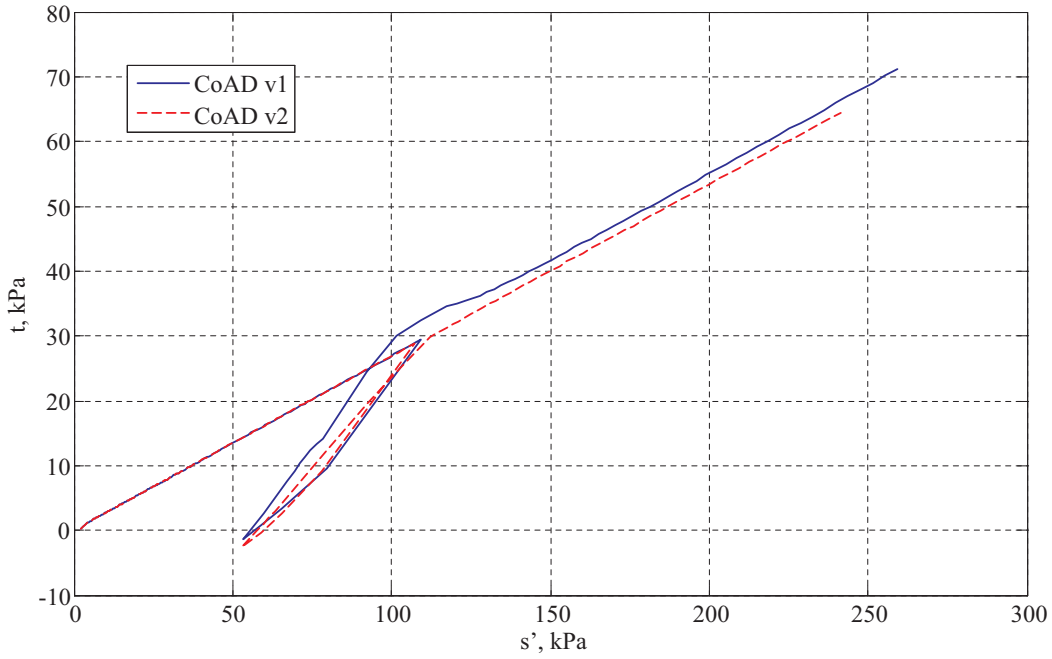

Figure 4.9: Stress path plots for swelling and recompression tests showing the comparison between the two CoAD models

Figure 4.10 shows another comparison between CoAD v1 and CoAD v2 results, this time as a plot of volumetric strain versus mean normal stress. It can be seen that after the swelling period the plot for CoAD v1 overshoots the NCL predicting a higher mean normal stress for the same volumetric strain. This again is unrealistic behaviour which is corrected by the use of CoAD v2. The lack of coaxial behaviour shown by CoAD v1 leads to higher stiffnesses generated in the tests, especially in the overconsolidated region. For these reasons CoAD v2 has been used for the current modelling with BOI.

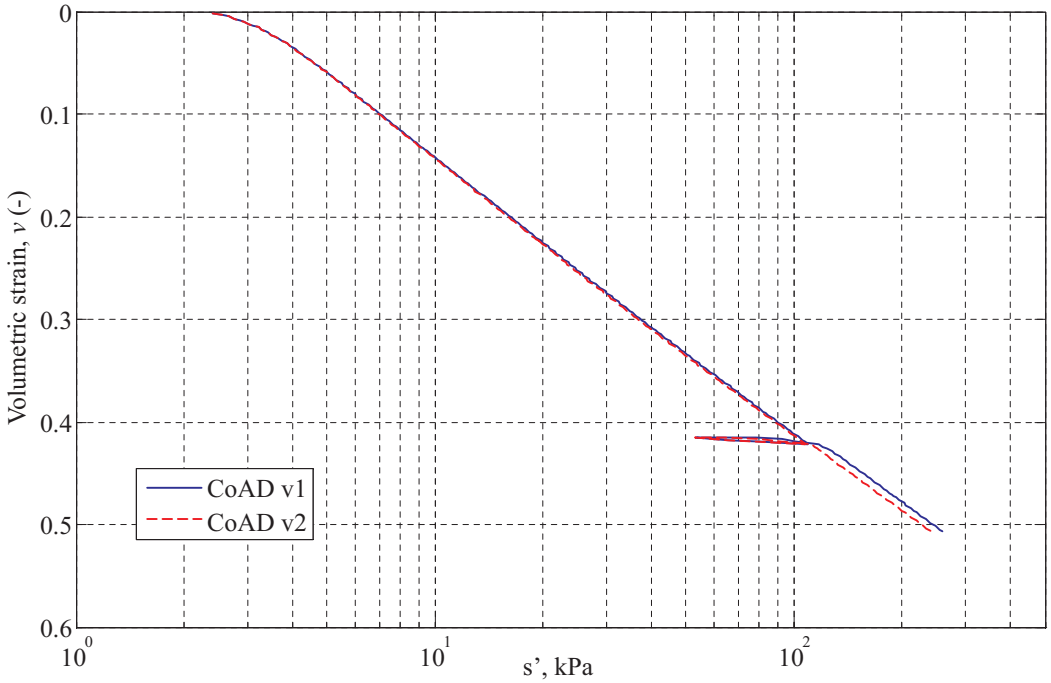

Figure 4.10: Volumetric strain versus mean stress plot for swelling and recompression tests, for both CoAD models

4.5 Testing the Capabilities of the Bricks on Ice Model

A series of tests was carried out to assess the ability of the BOI model to predict specific soil test results. These tests were intended to determine the ability of the model to cope with implementation into a finite element package such as Safe.

4.5.1 Test sequence

The following test simulations were conducted. For each test series the simulations were run with three different creep rates.

- One-dimensional swelling and recompression
- Undrained shearing (after isotropic and 1D compression)
- Undrained shearing with varying overconsolidation ratios (after 1D compression)
- Undrained shearing with holding period prior to shearing (after 1D compression)
- Constant stress* (virgin creep)

* These test simulations require a secondary component to the BRICK model to allow a designated stress path to be followed using strain increments.

In Den Haan (2001) the effect of the magnitude of creep was investigated by using two different creep rates. From a back-analysis of the plots demonstrating the effects of these two creep rates, it was found that the creep parameters required to give similar results were c=$5e^{-5}$ and c=$5e^{-6}$. The other parameters for the model used have been derived from a combination of Simpson (1992b), Den Haan (2001) and Oasys (2001) and are defined in Table 4.1.

4.5.2 Swelling and recompression tests

The swelling and recompression tests were conducted by compressing the soil to 42% volumetric strain in one-dimensional conditions and then allowing the soil to swell by 4%, to 38% volumetric strain. The soil was then recompressed to 46% volumetric strain, to show the full behaviour during a swelling and recompression loop. Each individual test is repeated three times with the creep parameter being the only variable between each test. For the purposes of these tests the soil is modelled as if it has been reconstituted from a slurry in the laboratory prior to testing.

Under one-dimensional conditions Figure 4.11 demonstrates the established effect that creep lowers the stresses, while the gradient of the K_0 line remains unchanged (Den Haan 2001). The main difficulty with the introduction of creep can be seen in Figure 4.12, being the steeper gradient of the NCL where the effects of creep are included. This is due to the fact that the viscous strains reduce the capacity for elastic strains. The expected pattern is that of a parallel NCL for the creep case, with the offset being dictated by the creep rate (Bjerrum 1967).

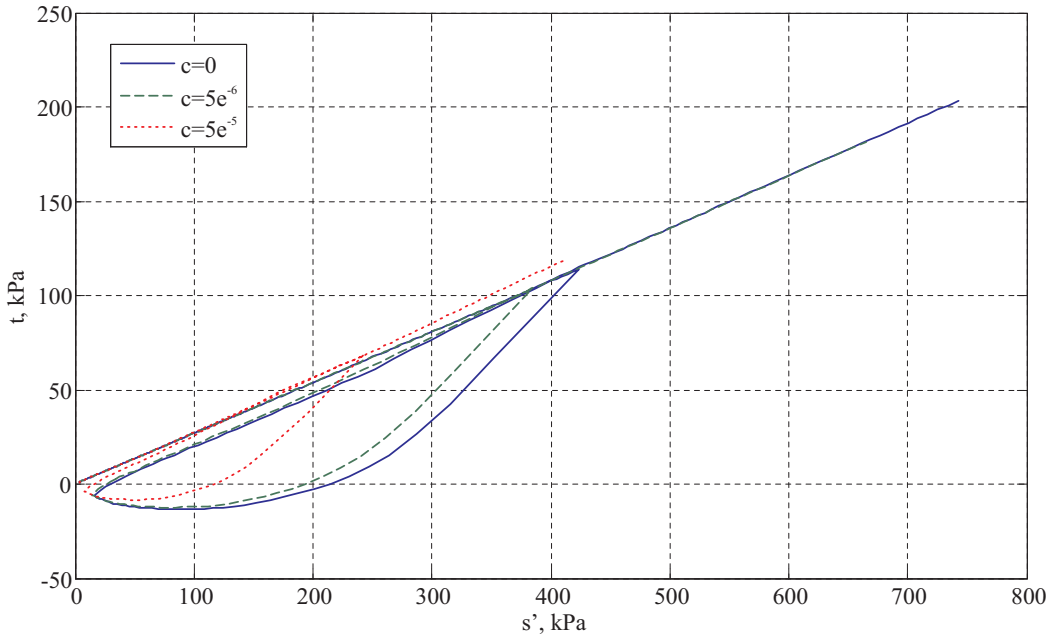

Figure 4.11: Stress path plot for 1D swelling and recompression

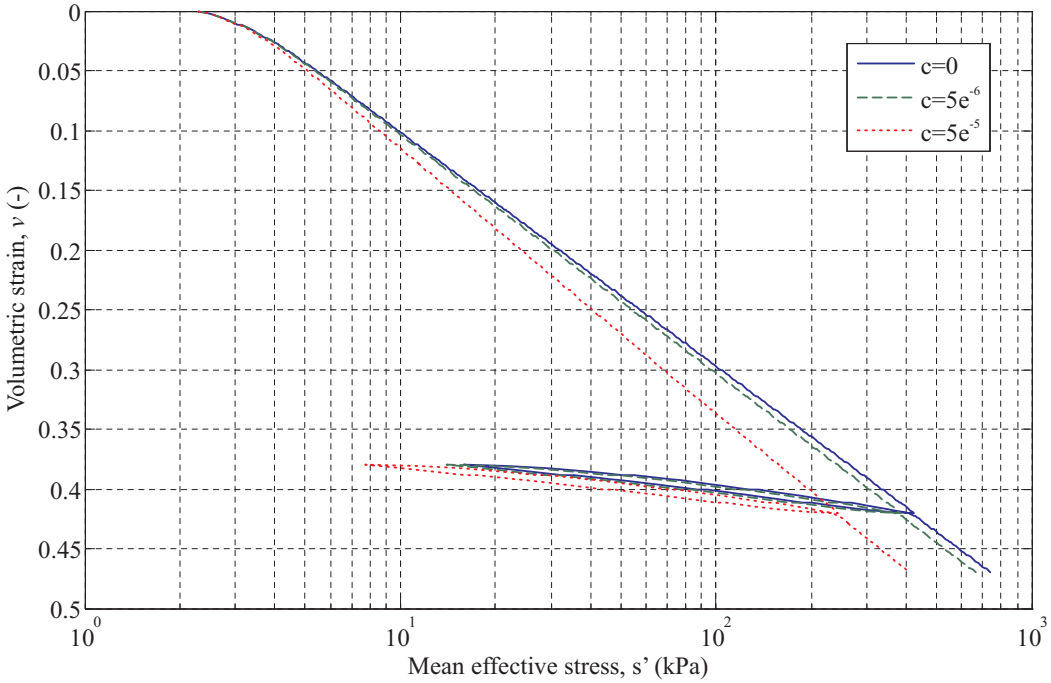

Figure 4.12: Volumetric strain versus mean stress for 1D swelling and recompression

BRICK parameters used in Chapter 4		
BRICK parameter	Code name	Value
Initial strains	SN(NC)	2D - [0, 0, 0], 3D - [0, 0, 0, 0, 0, 0]
Initial stresses	SS(NC)	2D - [2, 0, 0], 3D - [2, 0, 0, 0, 0, 0]
String lengths	SL(NB)	$[8.3e^{-5}, 2.1e^{-5}, 4.1e^{-4}, 8.3e^{-4}, 2.2e^{-3}, 4.1e^{-3}8.2e^{-3}, 0.021, 0.041, 0.08]$
Stiffness reduction	GGMAX(NB)	[0.92, 0.75, 0.53, 0.29, 0.13, 0.075, 0.044 0.017, 0.0035, 0]
Initial conditions	ZERO(2)	[0, 2]
Lambda*	λ^*	0.1
Kappa*	κ^*	0.02
Iota	ι	0.0041
Beta constant	β_G	4
Number of bricks	NB	10
Number of components	NC	3 - 2D (Plane strain, biaxial testing) 6 - 3D (Triaxial testing in Section 4.7)
Note: The string lengths are initially slack and the original position for all the bricks is the origin in strain space. The BRICK theory adopted is Theory 1, as this gives the most realistic results when combined with the BOI model.		

Table 4.1: BRICK parameters used with Bricks on Ice

4.5.3 Undrained shearing

The undrained shearing tests were completed by straining the soil along the K_0 or isotropic compression line to 42% volumetric strain. The soil was then sheared in either compression or extension until no further stress changes were induced by the shear strain increments (Section 3.4.3).

Isotropic

Figure 4.13 shows that creep lowers the stresses and that the results in both compression and extension are identical. Creep also has the effect of increasing the failure angle, θ (which is equal to $\tan^{-1}(t/s)$) due to the equivalent overconsolidation of the soil when compared with the c=0 test. The apparent OCR is 1.15 for the c=$5e^{-6}$ case and 2.13 for the c=$5e^{-5}$ case. The reason that θ is the same in both extension and compression is that, as the bricks are moving along the volumetric strain axis during compression,

the brick movements required to shear against the creep motion are the same in both directions. This principle is demonstrated in Figure 4.14a.

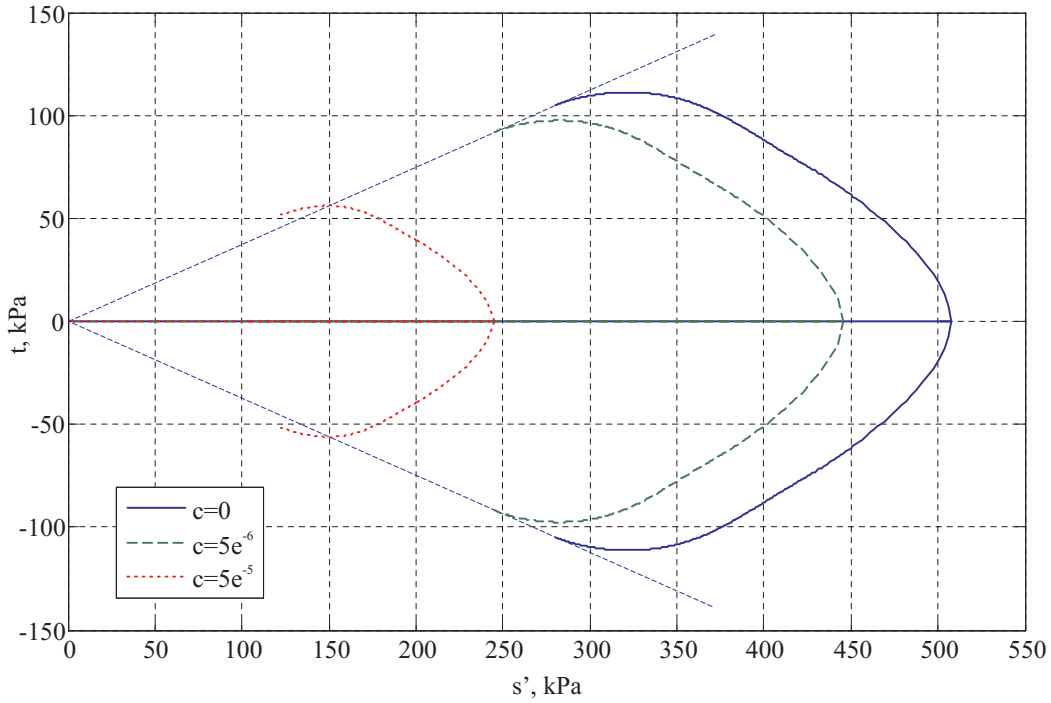

Figure 4.13: Stress path plot for undrained isotropic shearing

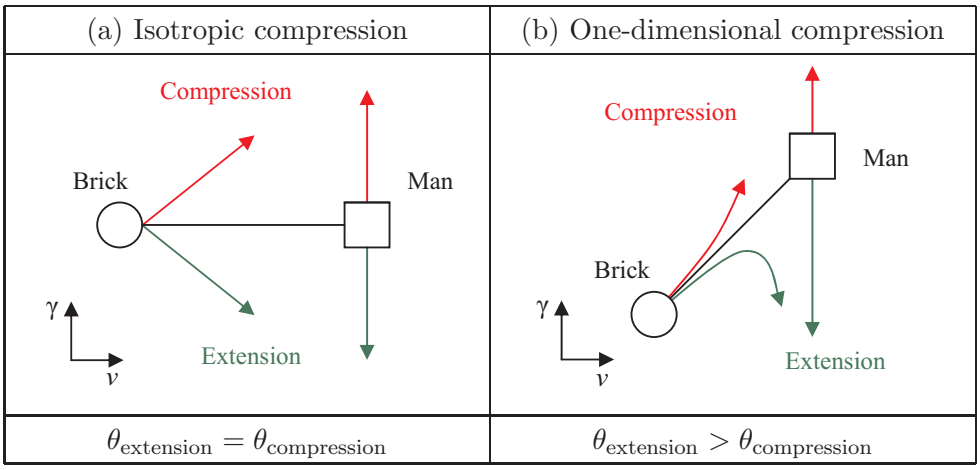

Figure 4.14: Schematic diagram for undrained shearing in strain space

One-dimensional

Figure 4.15 shows the increased lowering of the stresses due to an increase in creep rate. The patterns of results for the c=0 and c=5e^{-6} tests are similar, with both tests failing at the same θ in both extension and compression. Again the c=5e^{-5} test shows a higher θ. However, in this test the θs are no longer the same in extension and compression. Rather, the extension test demonstrates a higher θ. This is due to the amount of movement required against the creep motion of the bricks to bring the soil to failure. In the compression test the continued motion of the bricks is in the same direction as the shear strains, leading to a similar θ to that found in the c=0 test. For the extension test the creep strains are in the opposite direction, so more brick movement is needed to reverse the creep motion leading to a higher θ, Figure 4.14b.

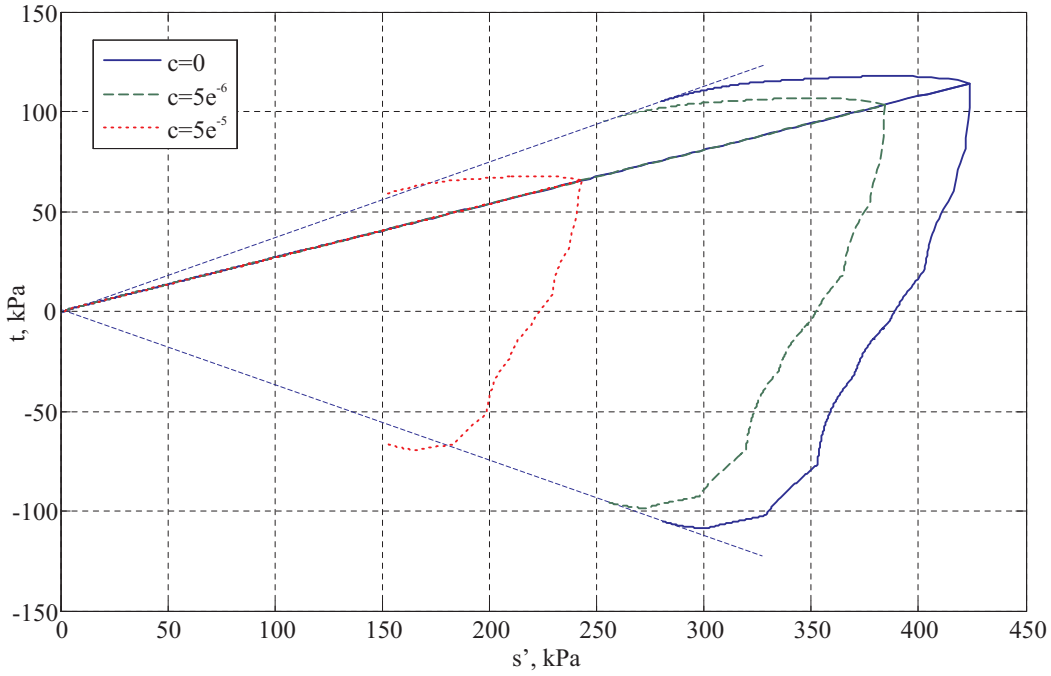

Figure 4.15: Stress path plot for undrained shearing following 1D compression

Figure 4.16 shows a comparison between normalised isotropic and one-dimensional compression tests followed by undrained shearing to failure (s_0 is the stress on the normal consolidation line before shearing commences). It can be seen that θ is the same no matter which test is used. When creep is included in the comparison (a c of 0.0002 has been used to emphasise the effects of creep), Figure 4.17, it can be seen once again that the angle is equal in 'isotropic' extension and compression, but not in the 'one-dimensional' compression tests. The increase in θ is also clear when compared with the c=0 envelope superimposed from Figure 4.16.

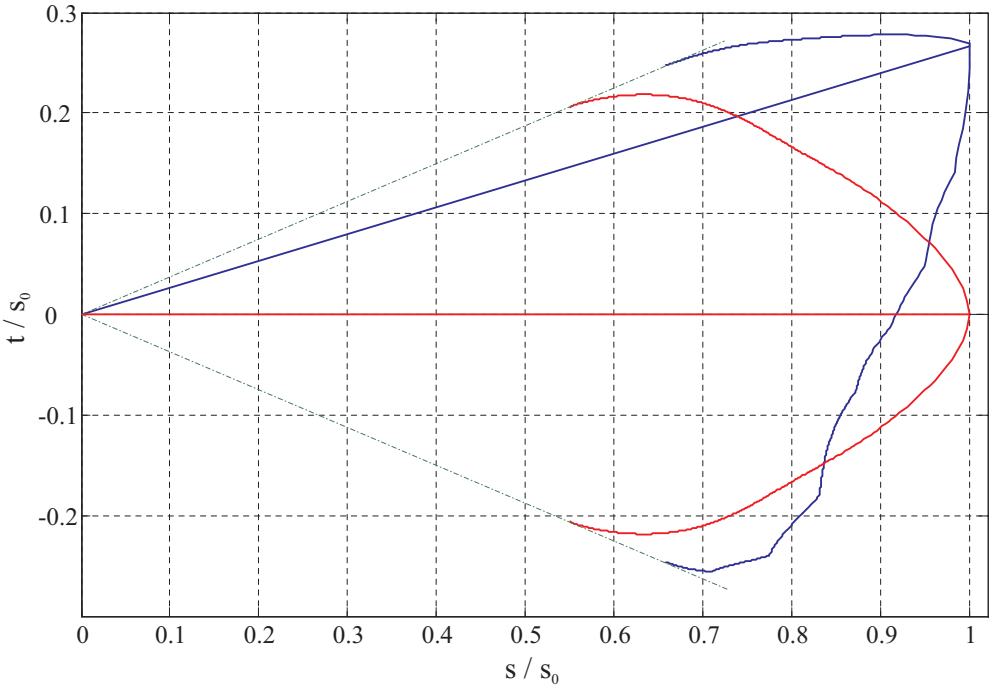

Figure 4.16: Comparison between the angle of failure in both extension and compression after isotropic or 1D compression

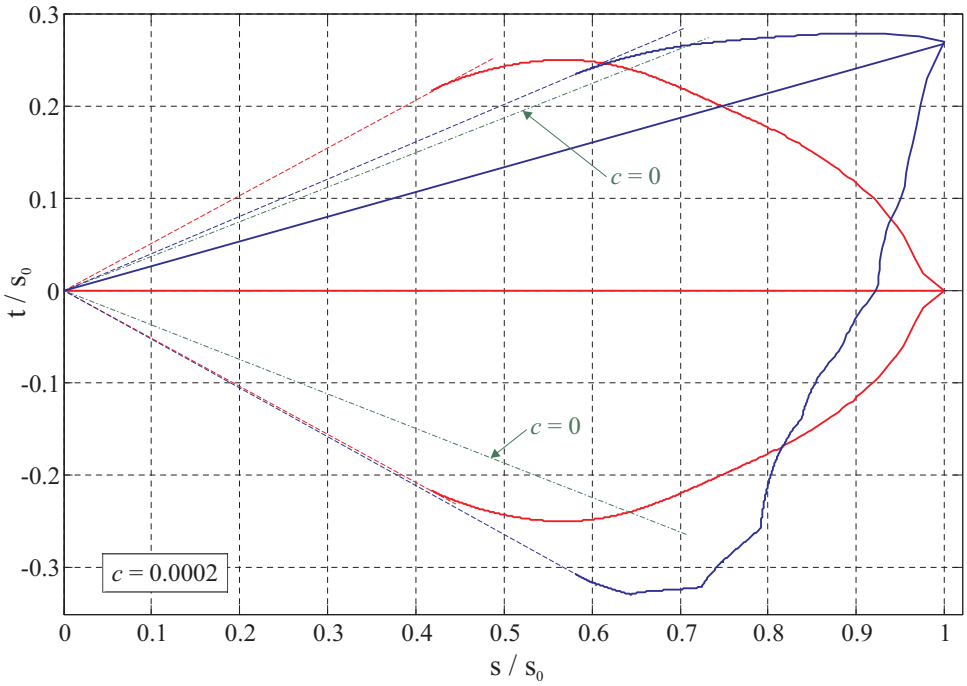

Figure 4.17: Comparison between the angle of failure in both extension and compression after isotropic or 1D compression with the effect of creep

Stress-strain plots

In this section, the shear stress developed during the undrained shearing phase has been plotted against shear strain to allow the effect of creep to be studied. Figure 4.18 shows the identical stiffnesses seen in the undrained compression and extension tests following isotropic consolidation. It can be seen that creep has the effect of increasing the pre-peak stiffness and also the undrained strength, as was found experimentally by Vaid et al. (1979). Figure 4.19 shows the 'one-dimensional' stress-strain plots. The trend shown by the extension tests shows a great similarity to that shown in the 'isotropic' extension tests in Figure 4.18. The compression tests show a completely different trend. As much shearing as already occurred during the one-dimensional compression, the general trend is for the stresses to decrease. However, there is a small rise in shear stress in the small strain region before the stress decreases, which can be seen in Figure 4.20 (t_0 is the shear stress on the one-dimensional compression line before shearing commences).

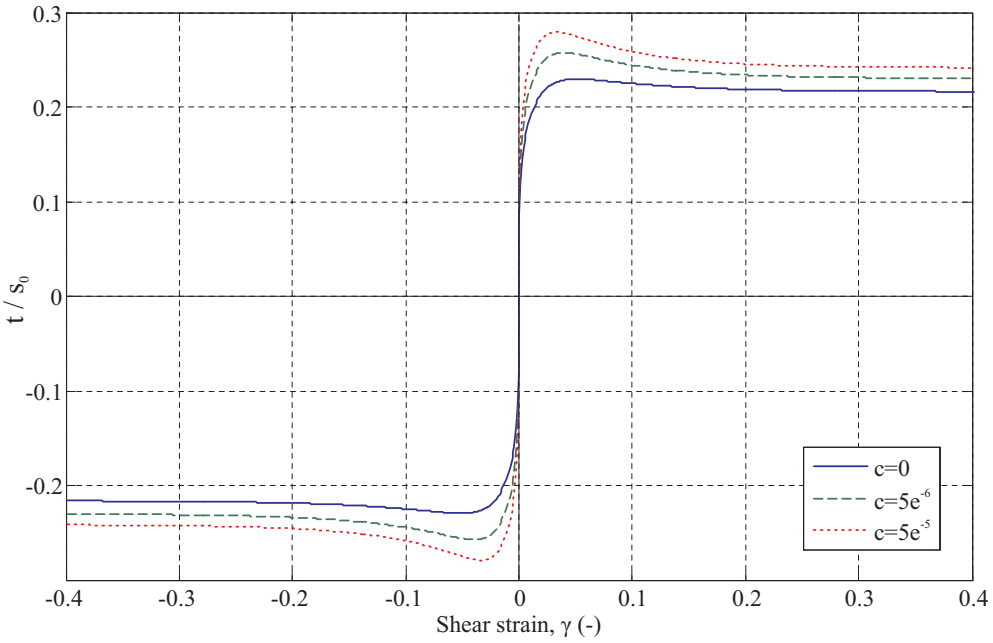

Figure 4.18: Stress-strain plot for shearing following isotropic compression

4.5.4 Undrained shearing with varying overconsolidation ratios

The effect of varying the overconsolidation ratio (OCR) was explored by conducting undrained shearing tests with four different OCRs: 1 (normally consolidated), 2, 4 and 8. Each test was initially one-dimensionally compressed to 42% volumetric strain before being swelled to the predefined OCR. Undrained shear tests were then simulated in

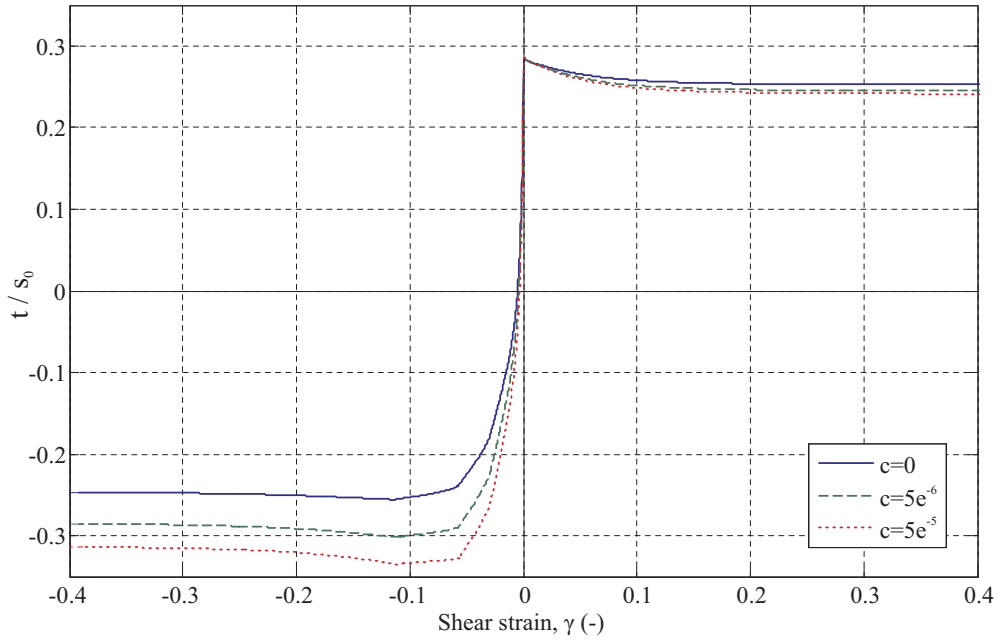

Figure 4.19: Stress-strain plot for shearing following 1D compression

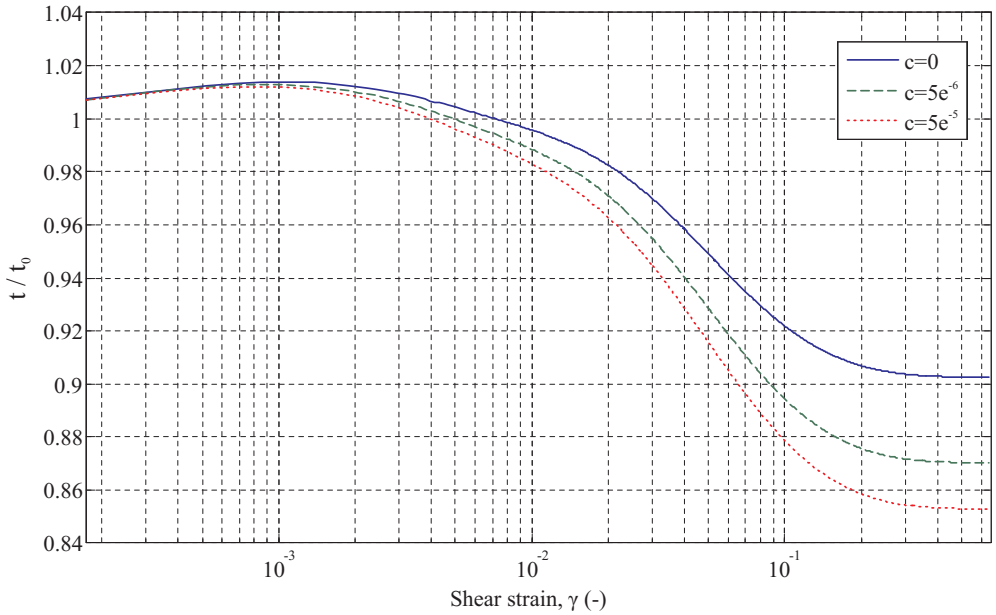

Figure 4.20: Stress-small strain plot for compressive shearing following 1D compression

both extension and compression. This test sequence was repeated for the three different creep rates to investigate the interplay between creep and OCR.

Figure 4.21 shows the results of the overconsolidation tests. It can be seen that the main effect of increasing the creep rate is the overall reduction of the stresses generated in the test, while modestly increasing θ. The paths for the low OCR tests show a striking resemblance to the results obtained in the overconsolidated plane strain tests completed by Sketchley & Bransby (1973) (Figure 3.11 on page 66). The failure angles are the same in both extension and compression, for each overconsolidation ratio, in the $c = 0$ tests. As the creep rate increases so the θ in extension becomes greater than that in compression. The failure angle also increases with OCR, as the soil demonstrates stiffer behaviour, which is explored further in Section 4.6.1. This is consistent with the characteristics of the Hvorslev surface. Figure 4.22 shows the corresponding plots of volumetric strain versus mean stress. The gradient of the normal consolidation line is different in all three tests due to the influence of creep, as seen in Figure 4.12. The prediction of a unique critical state line is not to be expected, as was discussed in Section 3.4.4, and is not in evidence.

Stress-Strain plots

Figure 4.23 shows the comparison of the normalised shear stresses versus shear strain tests. The beta effect, described in Section 3.3.1, means that the compression tests with the higher OCRs should exhibit a higher stiffness during straining. This effect is observed with the creep rate serving to increase the stiffness further. For the extension tests the pattern is a little harder to decipher. A magnified view of the extension test results is shown in Figure 4.24. If the path of the man and the bricks is taken into account the pattern can easily be rationalised. If the soil is overconsolidated, it has to go through a stage of swelling to reach the desired OCR. In the reference OCR=1 test this is not the case. This means that the bricks still lie upon a line inclined at 45 ° to the left and below the man in strain space. As the shearing then occurs in extension, the stiffness in this direction has not been fully developed and the test shows a very stiff response. In the OCR>1 tests swelling causes some bricks to lie still on a 45 ° line but above and to the right of the man. The number of bricks aligned in this way is dictated by the amount of straining required to swell the soil back to a specific OCR. Initially only the bricks with short strings will follow the man but as the straining advances so all the bricks will eventually line up again behind the man. This means that the direction of the brick movement is now in generally the same direction as the

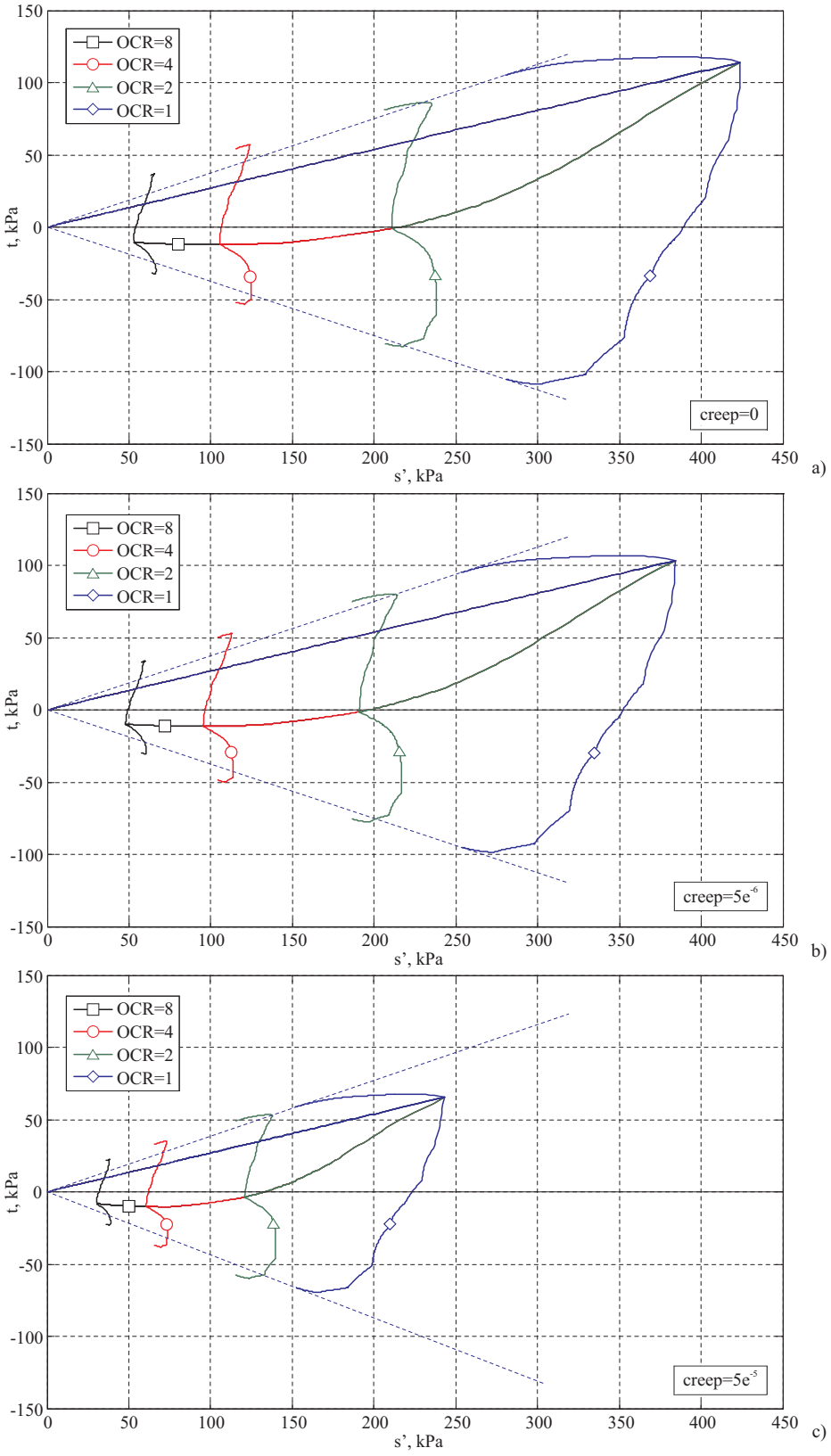

Figure 4.21: 1D stress path plots showing the effects of overconsolidation and creep

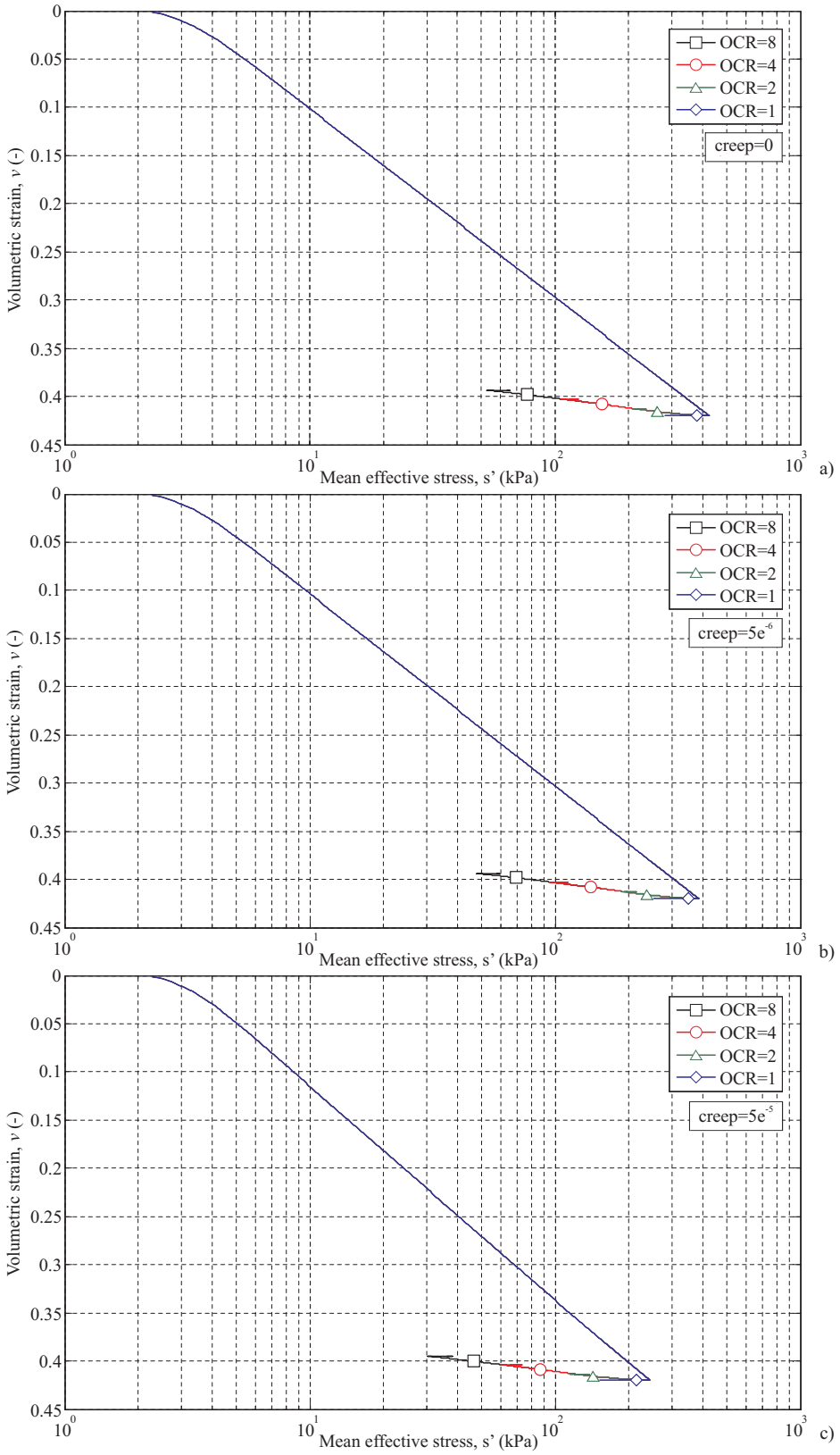

Figure 4.22: 1D stress-strain plots showing the effects of overconsolidation and creep

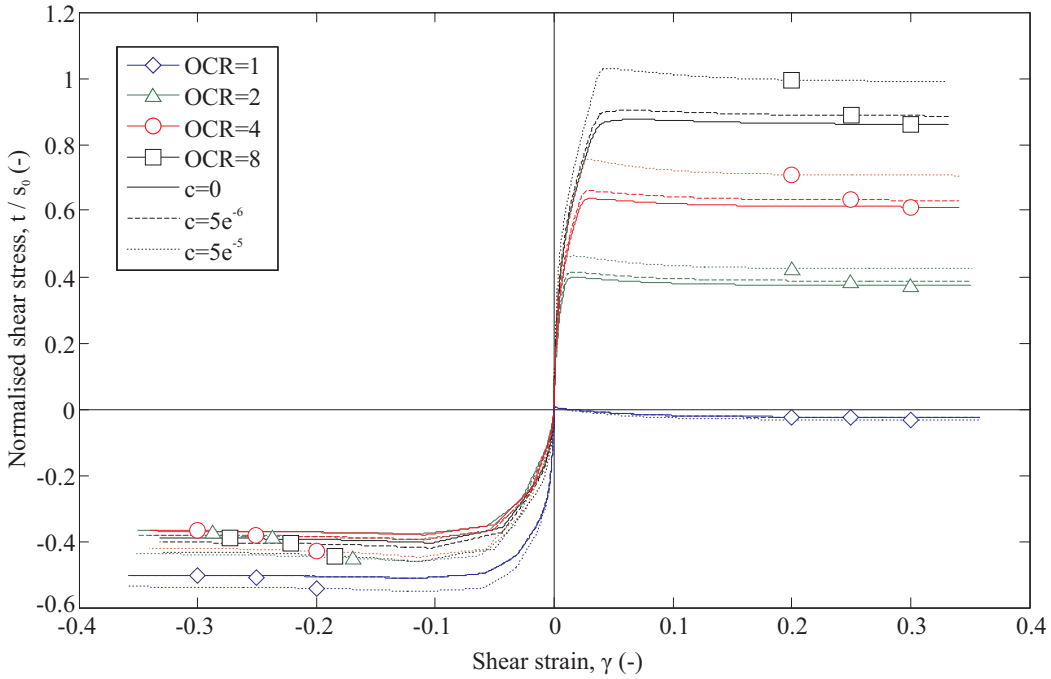

Figure 4.23: Stress strain plots for varying OCRs following 1D compression

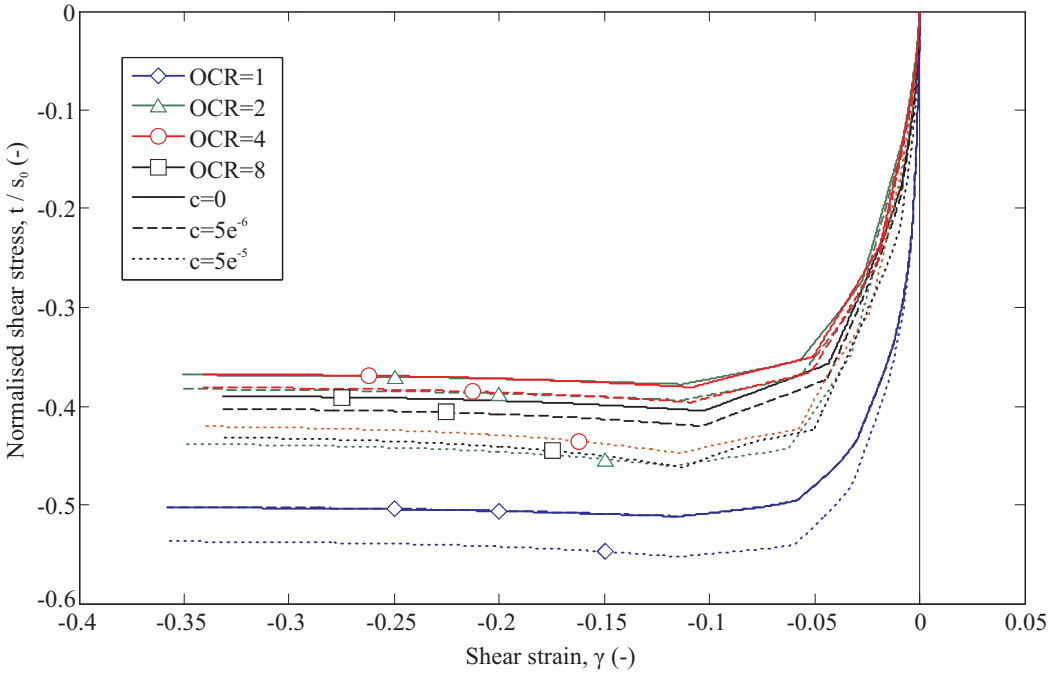

Figure 4.24: Extension stress-strain plots for varying OCRs following 1D compression

shearing that commences during the next (extension) phase. Thus some of the stiffness has already been developed in the direction of the shearing so the initial response is lower that that seen in the OCR=1 test.

The longest string length is 8%, so it can be seen from the shearing plots that all the bricks will be in motion by the end of the test; hence the entire soil has reached its failure state.

4.5.5 Undrained shearing with holding period prior to shearing

The holding period tests were conducted by straining the soil under one-dimensional conditions to 42% volumetric strain at which point the soil was held at constant strain for a holding period of five BRICK increments. As creep continues after the straining of the soil has stopped, any holding period during the test has an effect upon the stresses and the stiffness generated directly after the holding period. This is because the bricks are still moving in the previous direction of straining, causing a stress relaxation and a stiffer response in the soil upon the recommencement of straining.

The effects of the holding period on the stress path taken during shearing can be seen in Figure 4.25. The relaxation in stresses takes the form of a small loop underneath the K_0 line, which leads to a steepening of the gradient of the initial section of the shearing plot. This loop can be just seen in the c=$5e^{-6}$ test, but clearly seen in the c=$5e^{-5}$ test. The c=0 plot does not show any loop as there is no creep.

Figure 4.26 shows the effects of changing the holding period on the stress path during shearing. As the deceleration of the bricks is logarithmic, most of the movement occurs within the first few increments, which in this case was five. With a waiting period of one hundred increments, the stress path was only marginally different to that shown in the five-increment holding period test. If fewer than five increments were to be used the path would simply branch off the loop and join the shearing path earlier than currently indicated in Figure 4.26. The loop for the c=$5e^{-6}$ test can be seen more clearly in Figure 4.26 than in Figure 4.25.

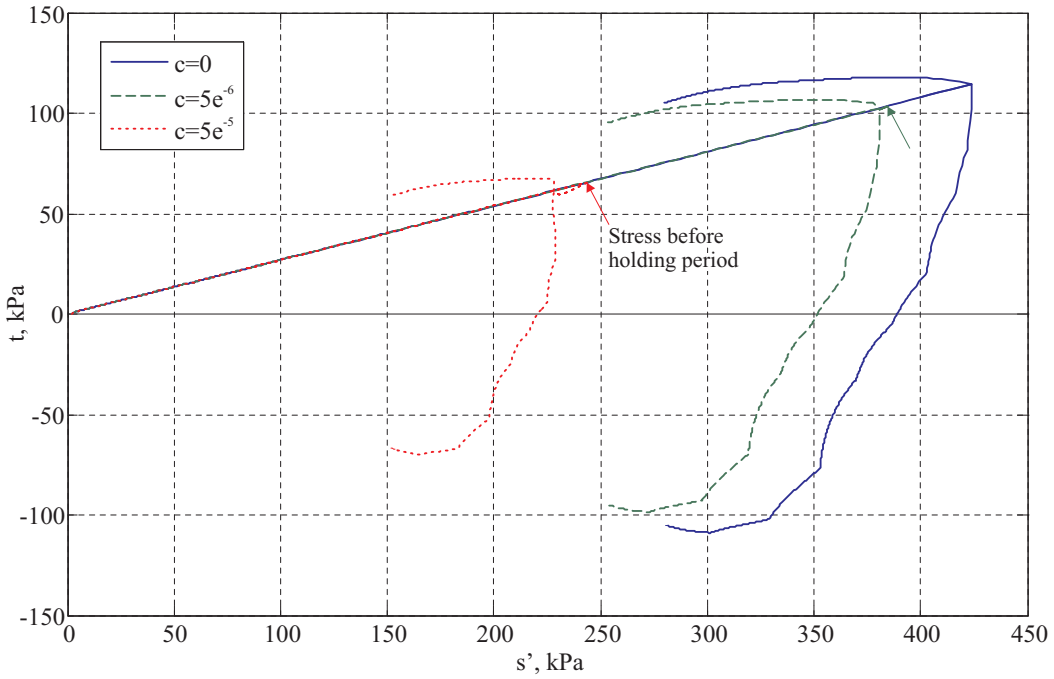

Figure 4.25: Stress path plot for undrained shearing following 1D compression with a holding period

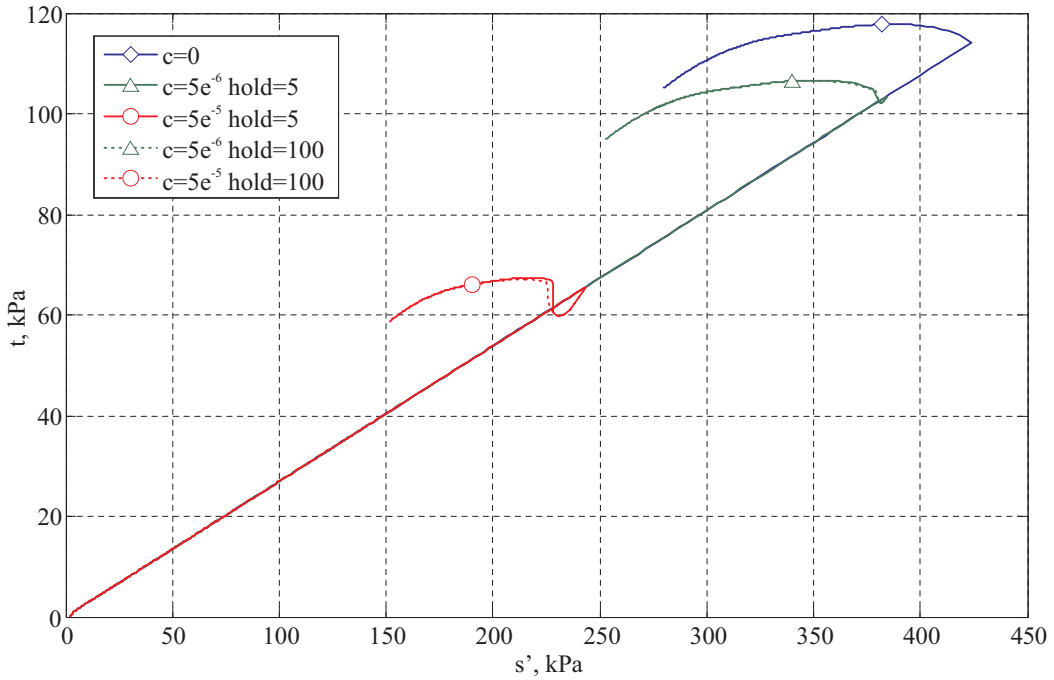

Figure 4.26: Stress path plots for undrained shearing following 1D compression comparing the effects of the duration of the holding period

4.5.6 Constant stress (virgin creep)

The constant stress tests involve one-dimensionally compressing the soil to 42% volumetric strain and then allowing creep to occur while keeping the stresses constant. The compression was then continued to see if the stress path returned to the NCL. To simulate a constant stress test the BRICK model needs to be able to follow a specific stress path. As the BRICK model is calculated within strain space, it uses strain increments and thus stress paths cannot be specified directly. This means for stress defined analyses a secondary control component is required to 'hunt' for the combinations of strains to generate the stress path required. In the BRICK program this is known as BRICKA (Section 3.5). The tests for constant stress involved using an iterative stress path routine to find a strain increment that leads to no increase in stress.

The BRICK model has no real concept of the NCL built into it. This means that the model needs to be 'told' that the soil is no longer normally consolidated. Otherwise, after virgin creep the soil state continues along a line parallel to the NCL without returning to it. This is achieved by making the BRICK model think the soil is overconsolidated to a degree equivalent to that created by the virgin creep, which is achieved by adding in a factored creep strain into the section of the BRICK model that monitors overconsolidation. Upon the continuation of normal straining the model returns to the NCL, thus correcting the path.

Figure 4.27 shows the effects of the modification and the path generated in a volumetric strain versus mean stress plot. Figure 4.28 shows how the period of virgin creep affects the stiffness of the soil. During the creep period, as the soil is straining without any change in stress, the stiffness falls to zero. Upon the recommencement of straining the soil displays a stiffer response as it returns to the NCL. This can be seen in the peak in stiffness at the 42% shear strain mark. The high stiffness to the left of the plot is the initial (small-strain) stiffness of the soil.

The tests reported in Section 4.5 form the current background into the feasibility of using the BOI model in a finite element program. It can be concluded that the model responds well to the scenarios applied here, but that there are still deficiencies, such as the modelling of normal consolidation. However, normal consolidation can be modelled adequately without the use of the BOI model, leaving the model free to be used for the modelling of creep, stress relaxation and strain fixation. These capabilities of the BOI model will be tested in Section 4.7 against experimental data.

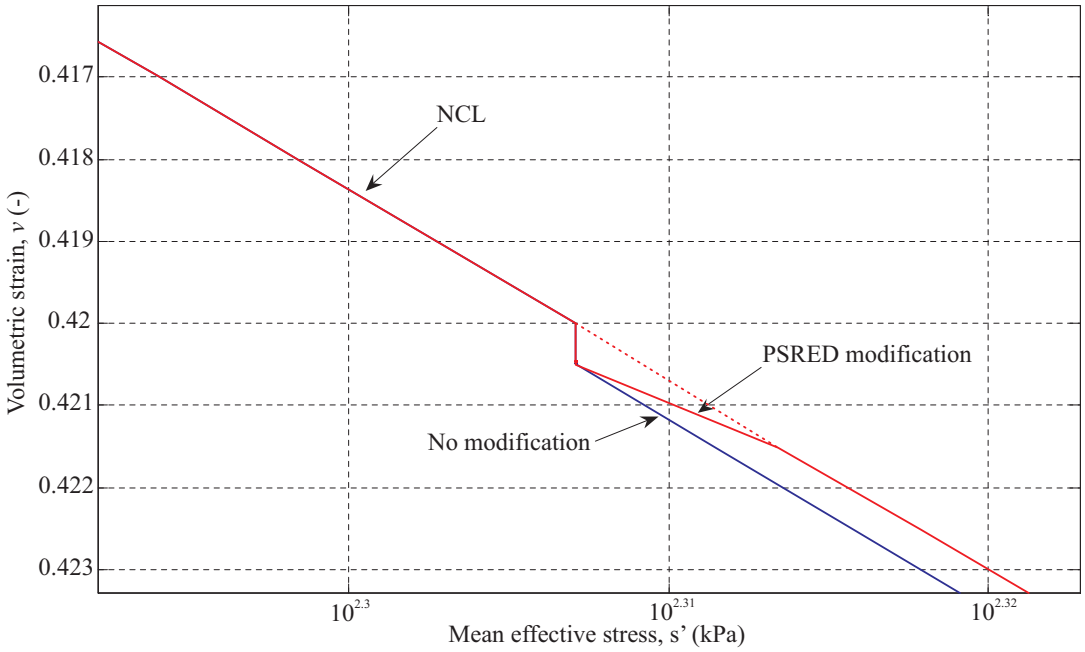

Figure 4.27: Volumetric strain versus mean stress for virgin creep showing the effects of the modified approach

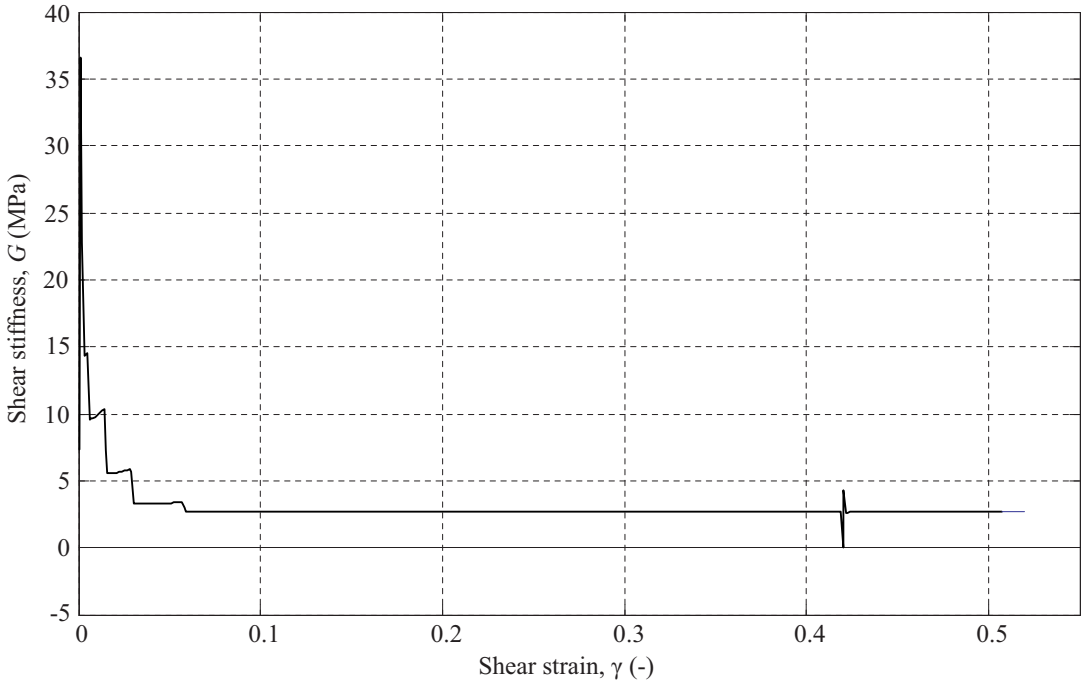

Figure 4.28: Shear stiffness during virgin creep tests

4.6 Manipulating the Bricks on Ice Model

It has been shown in Section 4.5 that the BOI model shows potential for implementation into a finite element program. The case for the model's use could be made even stronger if the BOI model were able to recreate the parallel isotache lines with different creep rates as seen by Leroueil et al. (1985) in Figure 2.22 on page 24. This section is dedicated to further manipulation of the BOI model to see if this behaviour can be generated.

4.6.1 Failure angle increase due to Bricks on Ice

To see if the apparent increase in θ caused by an increase in creep rate (Section 4.5.3) was similar to the effects caused by overconsolidation a parametric study was conducted. The creep analysis was achieved by compressing the soil isotropically to 42% volumetric strain before shearing the soil. Different creep rates were used and the apparent OCR was calculated by dividing the mean stress predicted on the isotropic compression line prior to the shearing phase, including the effects of creep, by the mean stress predicted without the effects of creep. The overconsolidation tests were compressed to 42% volumetric strain then swelled back to a specified OCR before being sheared. Figure 4.29 shows a comparison between creep and overconsolidation effects on θ. They show similar trends but the magnitude of the overconsolidation effects is much greater than that of the creep rate effects.

As β_ϕ was introduced in Theory 2 to control the increase of θ with OCR, another parametric study was conducted to assess whether β_ϕ could also control the increase caused by creep. Differences between the theories were also investigated as the BOI model was first formulated within Theory 1. It can be seen in Figure 4.30 that the Brick theory used does have a large effect on the increase in θ generated by a fixed creep rate. The results have been generated by varying the creep constant and are plotted as an increase in θ versus creep rate. This allows the direct comparison of the effects caused by changes in the Brick theory. Theory 1 produces the most satisfactory results showing a comparatively low increase in θ and the fewest anomalies.

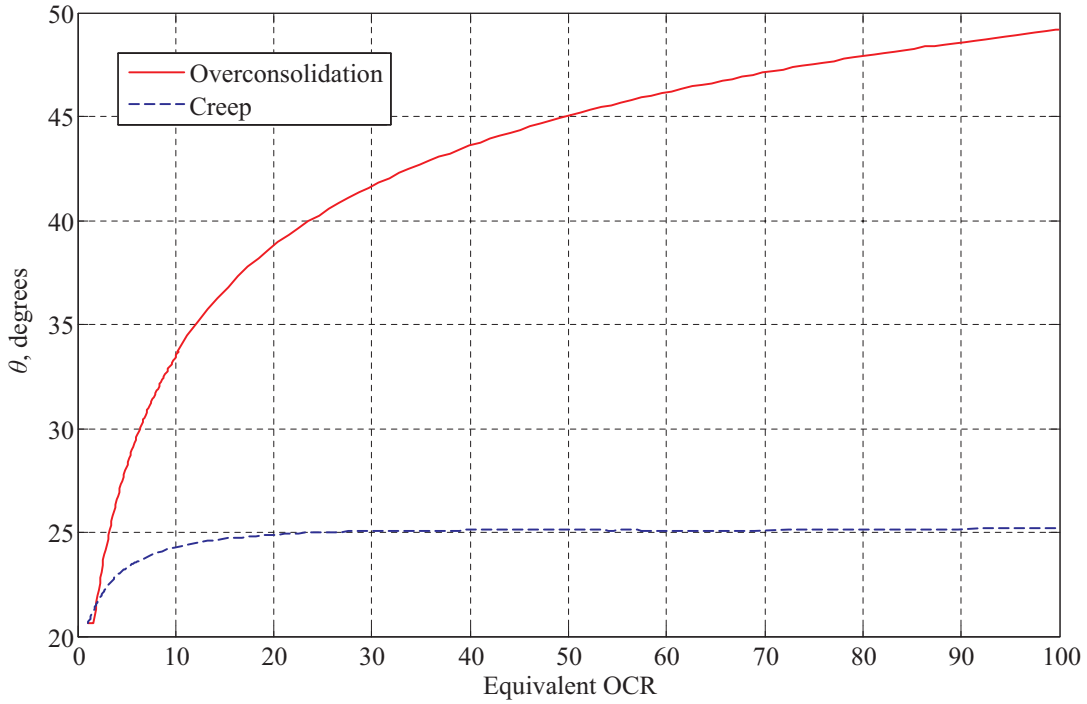

Figure 4.29: Parametric study into the effects of creep and overconsolidation on the rise in theta

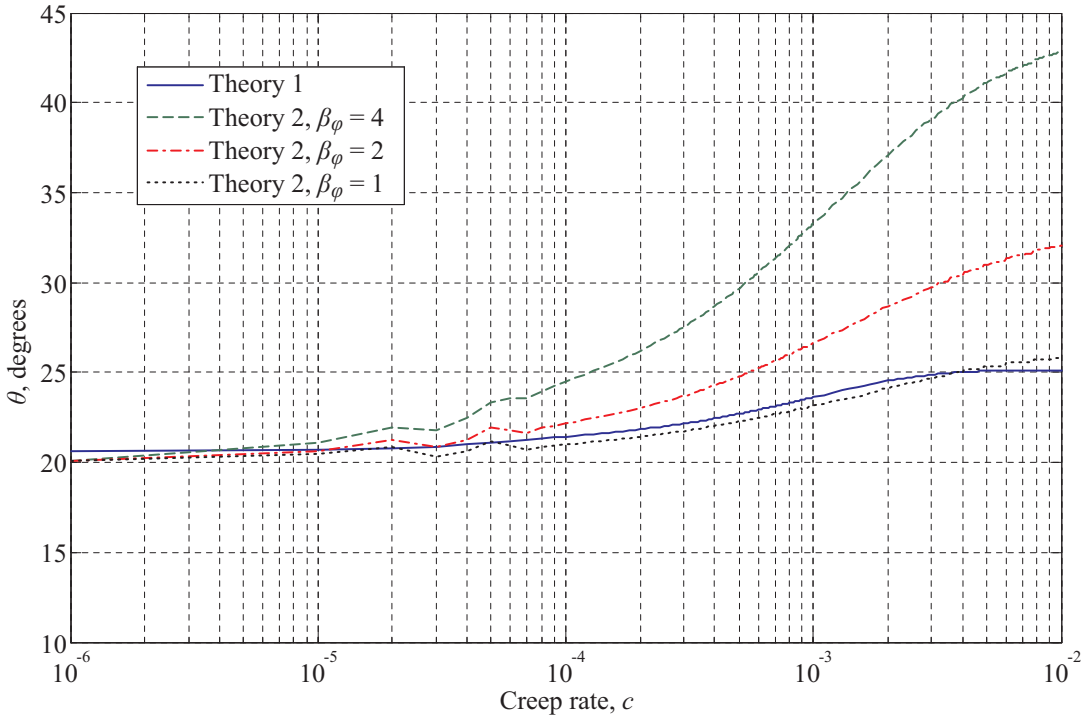

Figure 4.30: Parametric study of theta versus creep rate for varying BRICK theories

4.6.2 Modifications to the initial brick positions

The main difficulty with the results generated by the BOI model is the change in the gradient of the NCL with creep, shown in Section 4.5.2. In reality the NCL generated with creep should be parallel to the NCL without creep, with a different origin that allows the parallelism of the lines. The BOI model has no way of allowing a step change in the stresses to manipulate the origin of the NCL. However, by changing the initial brick positions the origin of the NCL can be manipulated, this has a knock on effect on the gradient of the NCL. It must be stressed that this manipulation is only possible by back analysis of the correct NCL gradient and spacing relative to the NCL generated without creep.

In a normal analysis using the BOI model the strings are all initially slack (Section 3.4.5) so that the bricks and the man start at the origin in strain space. In the current modification the bricks are moved to a location lying on the negative volumetric strain axis. This means the capacity for elastic volumetric strains is reduced. By reducing the amount of initial elastic strain, the rise in stresses can be manipulated to generate parallel isotache lines. Each of the bricks is moved a distance equal to a proportion of the string length attaching that brick to the man. For example, assume the longest

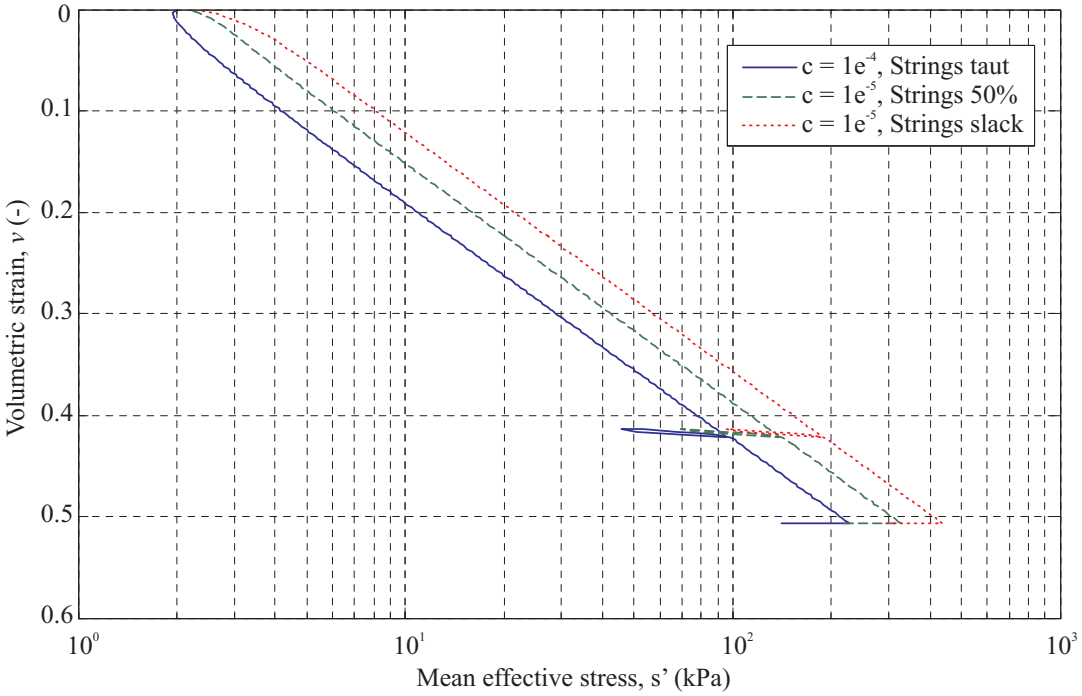

Figure 4.31: Modifications to the initial brick positions

string length is 8%, belonging to brick 10. If the initial positions of the bricks were set to 50% of the string length, brick 10 would lie at the point (-0.04, 0, 0) in the space (v, $\varepsilon_x - \varepsilon_y$, γ_{xy}).

The effects of this modification are shown in Figure 4.31, it can be seen that by matching the increase in creep rate with a more negative brick starting position, the NCLs with different creep rates can be manipulated to be parallel.

4.7 Benchmarking Bricks on Ice with Experimental Data

In Gasparre et al. (2007) it was shown that creep can have a dramatic effect on the stiffness of the soil due to the recent stress history. A set of three tests was conducted to attempt to assess the true nature of recent stress history combined with the effects of creep as previously explored by Atkinson et al. (1990) and Clayton & Heymann (2001).

To demonstrate the capability of the BOI model, a simulation of Gasparre et al. (2007)'s tests was conducted. Due to the fact that the BOI model is unable to correctly predict isotach behaviour during normal consolidation, the creep rate was set to zero during this stage. As the emphasis was on recent stress history, the lack of creep modelling during the geological history was thought not to have a significant effect upon the results. To allow the modelling of a triaxial test, the BOI model was expanded to work within the six component framework (Section 3.2.2). An element of stress path control was also required which was implemented, as mentioned in Section 4.5.6.

As Brick models the entire stress history of the soil, the simulation of laboratory tests can be rather complex. Gasparre (2005) gave the in-situ mean effective stress of the samples used as being 330kPa. This was calculated based on a K_0 value of 1.88, assuming the water table to lie at the surface of the London Clay at a depth of 6m. It is known from, among others, King (1981) that the estimated maximum thickness of the stratum in the Thames Valley is around 200m. This leads to an overconsolidation ratio of around 8.5 at the sampling depth of 17 metres in the current London Clay formation, assuming removal of around 125 metres of overburden due to weathering and erosive forces.

As well as the stress history required to generate the effect of overconsolidation on the stiffness of the clay, the effects of the sampling process must be taken into account

before the laboratory test can be considered. From Gasparre (2005) it is known that the initial mean effective stresses in the samples before the triaxial tests started were 171kPa for sample 17SH and 136kPa for 17.3SH. The effects of sampling were modelled in a simple fashion. This involved swelling the soil to the observed pre-test mean effective stress and reducing the deviator stress, q, to zero. The soil was then isotropically compressed back to the in-situ mean effective stress of 330kPa. Details of the stages in the modelling process are given in Table 4.2.

Natural	Strain control	Stage 1	1D compression up to the geological maximum mean effective stress of 2805kPa (based on an OCR of 8.5).
		Stage 2	1D swelling to the in-situ mean effective stress of 330kPa.
Sampling	Stress control	Stage 3	Stress path directly taking the soil from the in-situ mean stress (330kPa) to the pre-test mean stress of 171kPa (17SH) or 136kPa (17.3SH) with a deviator stress of zero. Creep strains are generated during this stage.
Triaxial	Stress control	Stage 4	Isotropic consolidation back to the in-situ mean stress of 330kPa with a small deviator stress being applied dependant on the test to be conducted. Creep allowed.
		Stage 5a	Outgoing approach paths conducted under constant mean stress. This affects the magnitude and direction of the approach path for the final stage stiffness. Creep allowed.
		Stage 5b	Incoming approach path. Creep allowed.
	Strain control	Stage 6a	Dissipation of creep strains generated during the approach paths, if allowed (12 hours).
		Stage 6	Undrained extension or compression test.

Table 4.2: Test stage analysis

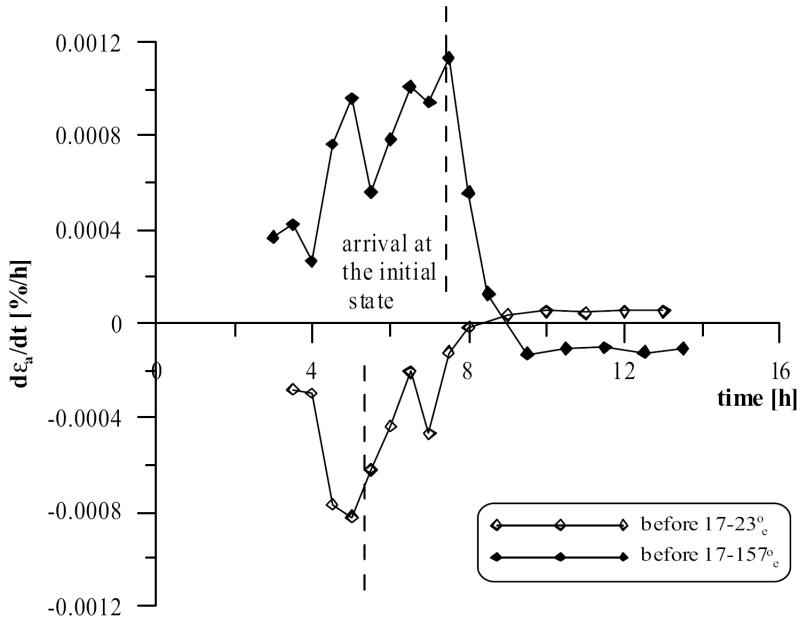

Figure 4.32: Creep strains before undrained shear tests- 17SH, Gasparre (2005)

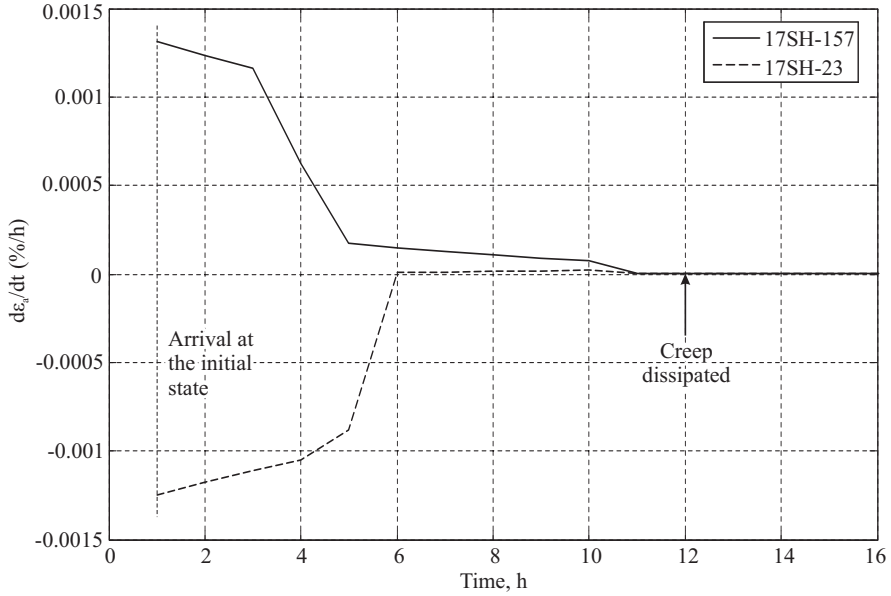

Figure 4.33: Dissipation of creep strains before undrained shear tests

4.7.1 Calibration of the Bricks on Ice model

The parameters used here for the BOI model were mainly taken directly from Oasys (2001), shown previously in Table 4.1 on page 87. These parameters were developed by ARUP Geotechnics for use in the modelling of London Clay. The one additional parameter for use in the model was the creep constant, c. This was found by comparing the creep rates (Stage 6a in Table 4.2) published in Gasparre (2005), shown in Figure 4.32 with those from the MATLAB simulation, shown Figure 4.33. It can be seen the magnitude of the creep strains is of the same order in both figures. The value of the creep constant that led to these results is $c = 1e^{-4}$. The creep dissipation period was taken to be 12 hours.

The tests conducted by Gasparre (2005) used just two soil samples for the tests. This necessitated the use of a multi-stage testing process. The first sample, 17SH, was used in 'short approach path with creep' tests, being subjected to two extension undrained shear stages. Sample 17.3SH was used for 'short approach path without creep' and 'long approach path with creep' tests, with two undrained shear stages being conducted in both sets of tests. After each undrained shear stage the sample was returned to the in-situ effective mean stress of 330kPa.

4.7.2 Short approach path with creep (17SH)

In Gasparre et al. (2007), tests on the first sample, 17SH, consisted of taking the soil from the initial mean stress point of 171kPa to the in-situ mean stress of 330kPa and a deviator stress of -10kPa. Isotropic conditions would have been ideal, but due to problems with the Imperial College load cell a deviator stress of -10kPa was necessitated. The outgoing approach path was then followed to a point just inside the Y_2 yield surface (either increasing or decreasing q) under constant mean stress, with the soil then being brought back to the previous deviator stress of -10kPa. The radius of the Y_2 surface was found to be around 10kPa from earlier tests. Here the soil was allowed to creep and was held until the creep strains had fallen to unrecordable levels. At this stage the sample was subjected to an undrained extension test which due to the differing directions of the approach paths led to a rotation in the stress path. The undrained nature of the shearing stages led to stress path rotations of 23° and 157° being created. The specific stages for the 17SH tests are given in Table 4.3, where the steps are defined in terms of strain increments for stages 1, 2 and 6, and in terms of the number of stress increments, #, in stages 3-5.

Stage	17SH-23			17SH-157		
	Target(kPa)		steps	Target(kPa)		steps
	q	p'		q	p'	
1	-	2805	0.001	-	2805	0.001
2	-	330	-.001	-	330	-.001
3	0	171	#10	0	171	#10
4	-10	330	#10	-10	330	#10
5a	0	330	#8	-20	330	#8
5b	-10	330	#8	-10	330	#8
6a	Creep		-	Creep		-
6	Extension		$-1e^{-5}$	Extension		$-1e^{-5}$

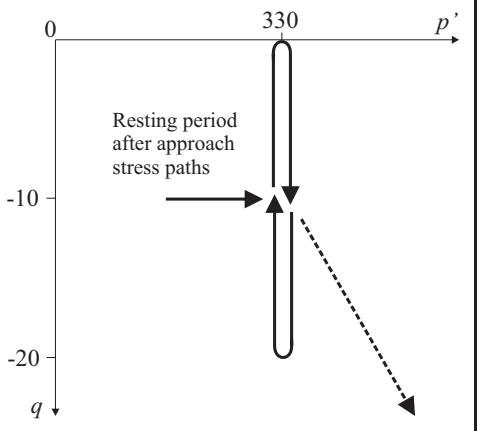

Table 4.3: Specific stages for the 17SH tests

Figure 4.34 shows the stiffness degradation curves from Gasparre (2005) measured during the undrained shearing stages. Previous literature about recent stress history suggests that the higher the rotation from the approach stress path, the stiffer the soil should be, Atkinson et al. (1990). The effects of creep in this context have never been systematically investigated, except by Gasparre (2005). The results show that creep is able to increase the stiffness seen in the low stress path rotation case, effectively erasing the effects of the recent stress history as seen previously by Clayton & Heymann (2001). It seems clear that creep can have the ability to remove the effects of the recent stress history if that history lies within the Y_2 surface. It can be seen from Figure 4.35 that the BOI model is able to recreate the lack of difference between results for the two degrees of rotation. Although the patterns are very similar, the magnitude of the strains required to cause a marked drop in stiffness is an order greater in the simulations. The initial stiffness in the low rotation test is greater that that generated during the high rotation test, and this goes against the pattern seen in the physical tests.

In the current BOI implementation, if a brick is moving in the same direction as the man, then upon the man stopping and allowing the creep strains to dissipate, its string will become slack. The soil will then develop elastic, stiffer behaviour upon the continuation of straining in that direction. The more bricks that are moving in the same direction as the man, the more strings will become slack and the more elastic and stiff the response will be upon continuation of straining in that direction. If the direction of the path of the man is reversed after a period of rest, the stiffness would be expected to be close to G_{max}, as all strings would be slack. In this case the continued motion of the bricks

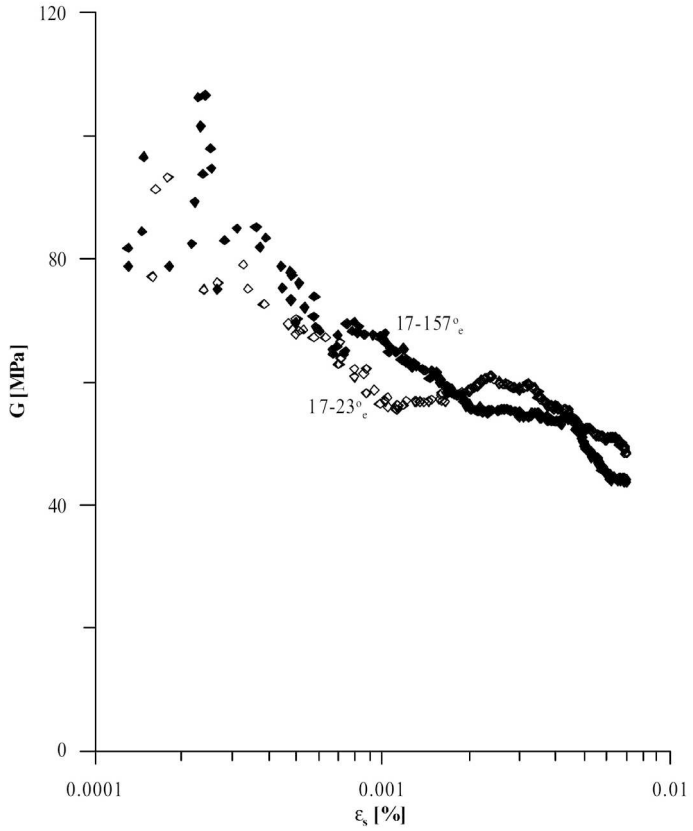

Figure 4.34: Stiffness degradation curves for 17SH, Gasparre (2005)

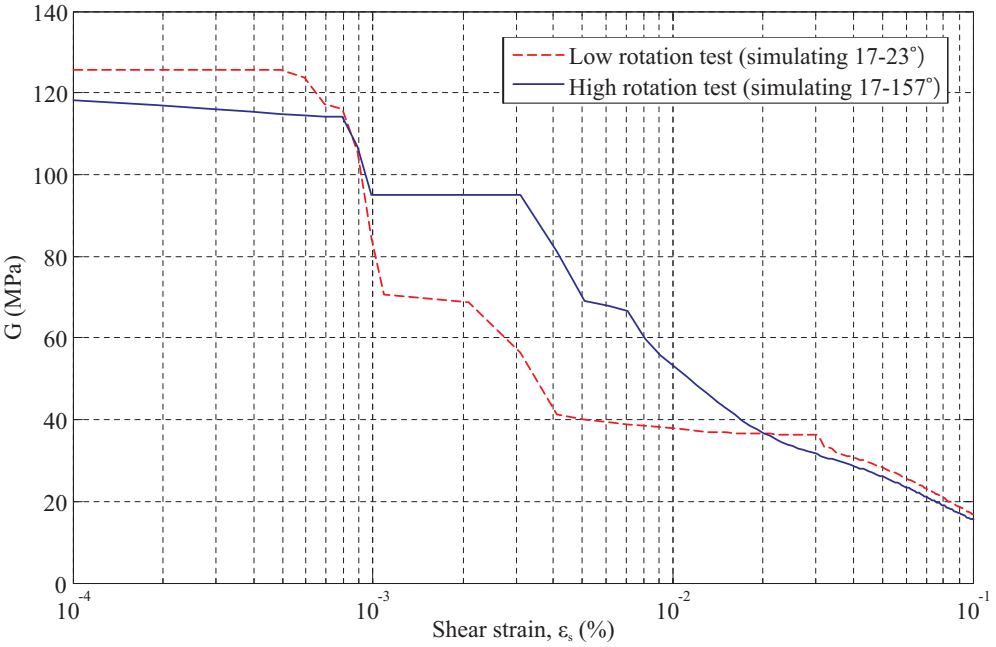

Figure 4.35: Stiffness degradation curves for 17SH, BOI model

acts to reduce the amount of elastic strain in the soil upon straining as the bricks and the man are moving towards each other. This has the effect of reducing the measured stiffness. The consequence of this is that no matter how long the stress path, if the shorter string lengths are of the same order of magnitude as the creep strains, then creep will always make the path with the least rotation to its shearing path stiffer than an equivalent path with a high rotation between the paths. This goes against the established trends seen in the modelling of the recent stress history (Clayton & Heymann 2001), leading to the conclusion that not only can creep remove the effects of the recent stress history but that in specific circumstances it can actually reverse the expected pattern.

4.7.3 Short approach path, no creep allowed (17.3SH)

The 17.3SH tests demonstrate the effect of removing the holding period after the approach paths. The exact stages in the modelling of the 17.3SH tests are given in Table 4.4. In Figure 4.36 the effects of the recent stress history can be clearly seen as a lower stiffness in the case of the low rotation stress path. Although the general trends in the plot can be accepted, the appearance of the peak in stiffness for the 105° rotation path is harder to accept. The stiffness would be expected to be greatest initially and then to reduce continuously as the sample is strained, as seen in Atkinson et al. (1990). This feature in the curve could be due to a 'flat spot' in the Imperial College load cell as mentioned in Gasparre (2005). The 'flat spot' was seen to cause a jump in stiffness in the small strain region during feasibility tests for the imposition of recent stress history (Gasparre 2005). Therefore, this could be the cause of the unrealistic stiffness response seen in Figure 4.36. The trends shown in Figure 4.37, generated by the BOI model, are more realistic and show that the lack of creep allows a longer elastic period in the 105° path rotation test. As the approach paths are within the Y_2 zone, the strains required to generate the approach paths are relatively small. Therefore, there is no reason for the stiffness of the soil in the intermediate strain region to be affected by the approach path. This can be seen by comparing Figures 4.35 and 4.37, where the paths are are very similar for shear strains greater than $> 4e^{-3}\%$.

Another anomaly in the testing procedure is to be found in the approach paths themselves. The tests were intended to investigate the effects of creep on the recent stress history. Therefore, apart from the length of the approach paths and the holding period for creep, the remainder of the test should have remained identical. In comparing the stress paths followed in the two pairs of tests (17SH & 17.3SH) it can be seen that there

Stage	17.3SH-75			17.3SH-105		
	Target(kPa)		steps	Target(kPa)		steps
	q	p'		q	p'	
1	-	2805	0.001	-	2805	0.001
2	-	330	-.001	-	330	-.001
3	0	136	#10	0	136	#10
4	0	330	#10	0	330	#10
5a	10	330	#8	20	330	#8
5b	-	-	-	10	330	#8
6a	-		-	-		-
6	Compression		$-1e^{-5}$	Compression		$-1e^{-5}$

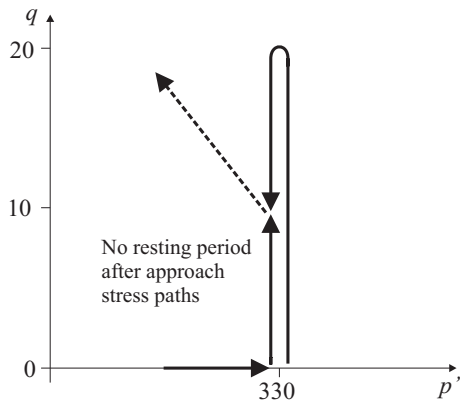

Table 4.4: Specific stages for the 17.3SH tests

were many other differences. These include:

- The position of the stress path in absolute terms. The 17SH tests were conducted in negative deviator stress space where as the 17.3SH tests were done in positive deviator stress space.
- The total length of the approach paths. Both paths were of identical length in the 17SH tests but in the 17.3SH tests, the low rotation approach path (17.3SH-75) was three times shorter than in the test with the high rotation approach path (17.3SH-105).
- The use of undrained shearing tests in different directions. In the 17SH tests the shearing was in extension, whereas in the 17.3SH tests the shearing was in compression. This would not be a problem if the soil were a reconstituted sample that had only been isotropically consolidated. The fact that the soil is a natural sample means that the 1D compression and swelling history may have a noticable impact on the relative stiffnesses in the two shearing directions.

These points have been addressed by the repeating the simulation of Test 17.3SH using the exact same methodology as in the 17SH tests.

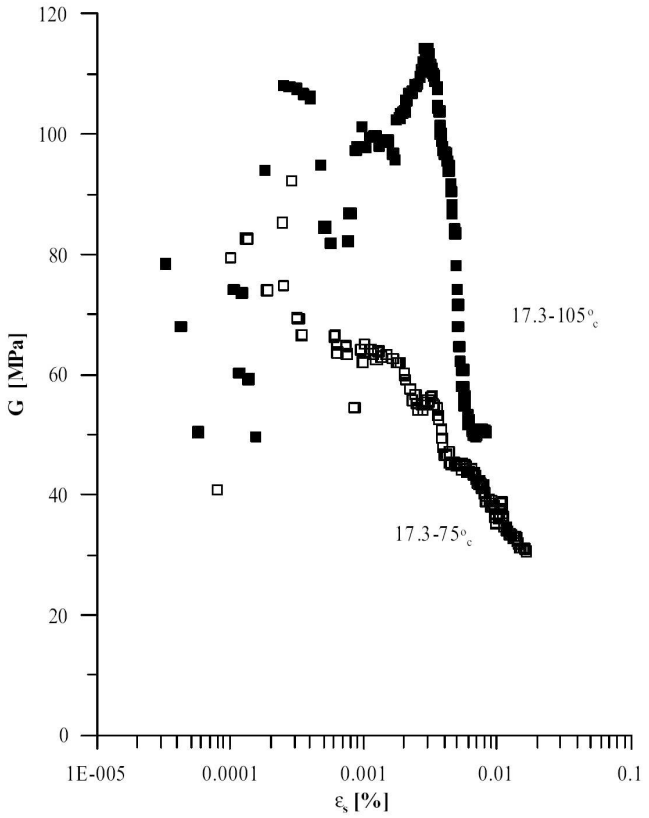

Figure 4.36: Stiffness degradation curves for 17.3SH, Gasparre (2005)

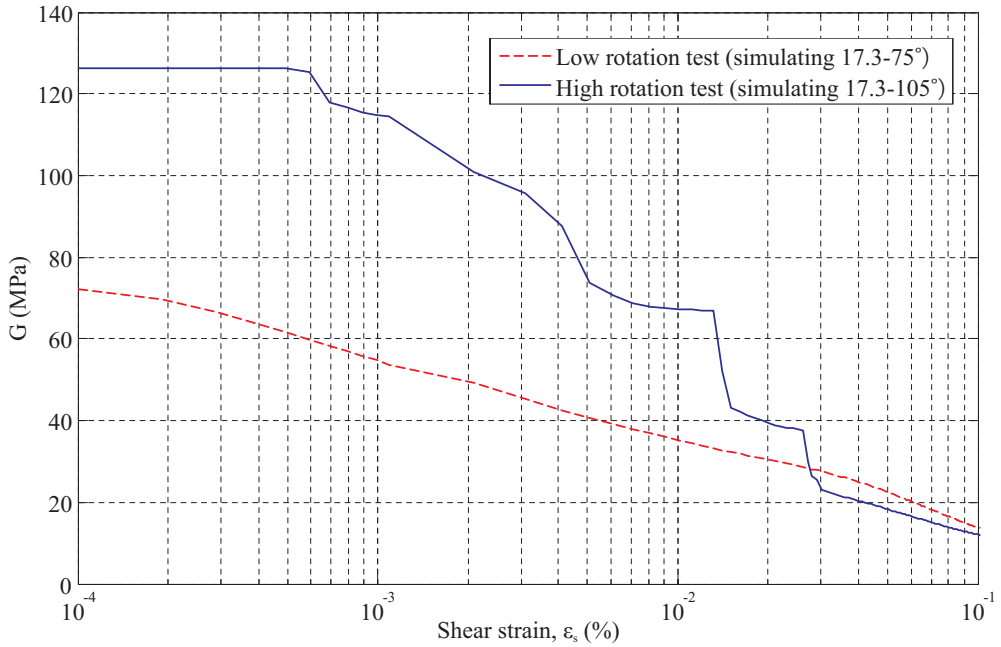

Figure 4.37: Stiffness degradation curves for 17.3SH, BOI model

4.7.4 Repeat simulation of the 17.3SH tests (17.3SH-B)

In this simulation the approach paths and initial conditions are exactly the same as in test 17SH, but without the influence of creep. The stages for this test are the same as given in Table 4.3 minus stage 6a.

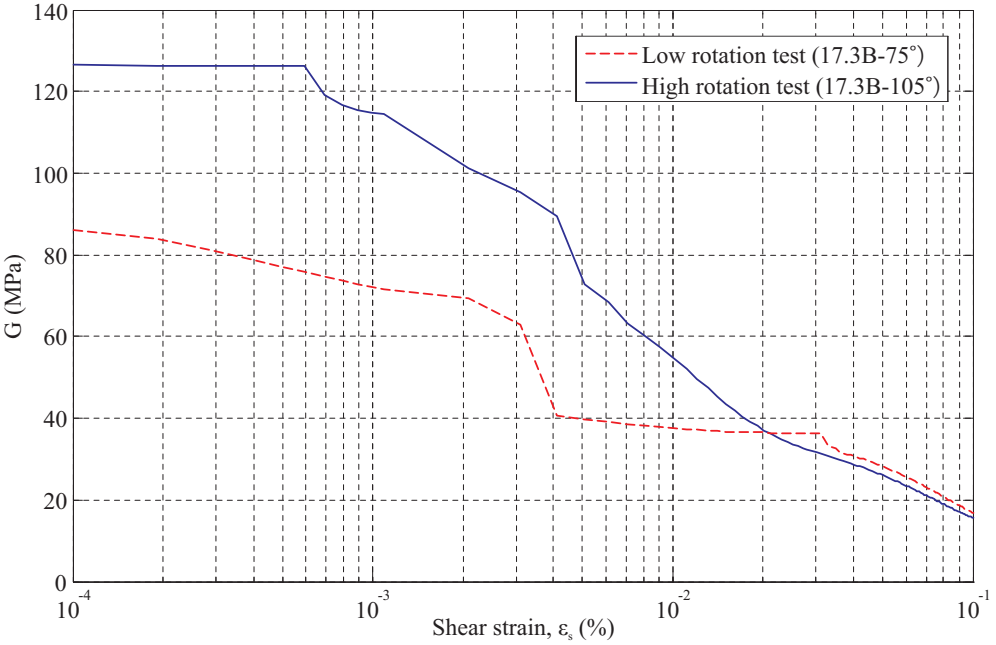

Figure 4.38: Stiffness degradation curves for 17.3SH-B, BOI model

It can be seen from Figure 4.38 that the effects of the different test sequences are relatively small; the trends are the same as those seen in Figure 4.37. The main difference is the higher initial stiffness in the low rotation approach path test. The lower initial stiffness seen in Figure 4.37 may be due the direction of the undrained shearing stage being in the same direction (compression) as the stress path required to remove the deviator stress during the sampling process. Thus in the 17.3SH-75 test the measured initial stiffness may be slightly lower than would have been measured had the methodology been the same as in the 17SH tests.

4.7.5 Long approach path, creep allowed (17.3SH-L)

In the 17.3SH-L tests, long (100kPa) approach paths were used, the results of which are shown in Figure 4.39. The details of the simulated test stages are given in Table 4.5. It can be seen that the approach stress paths, in both positive and negative directions, are of equal length and that the direction of shearing is in extension, as in the 17SH tests.

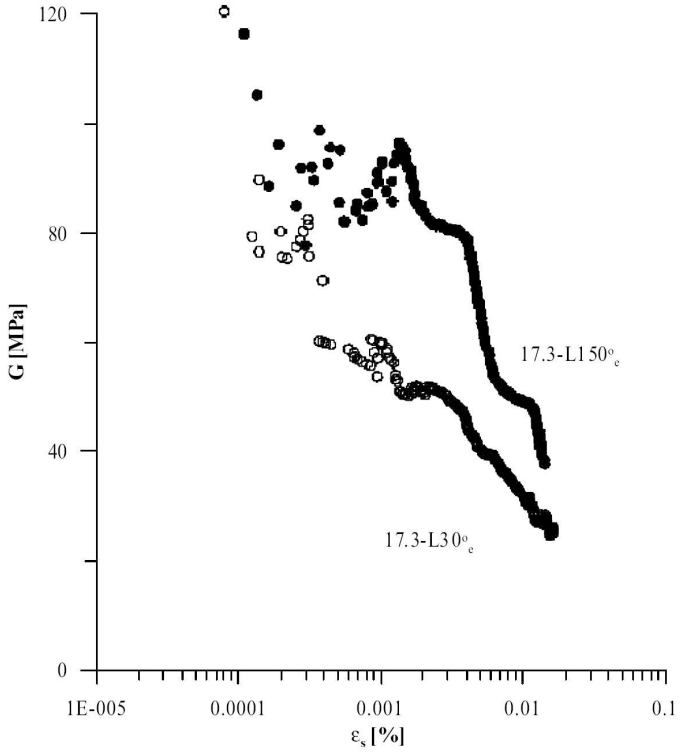

Figure 4.39: Stiffness degradation curves for 17.3SH-L, Gasparre (2005)

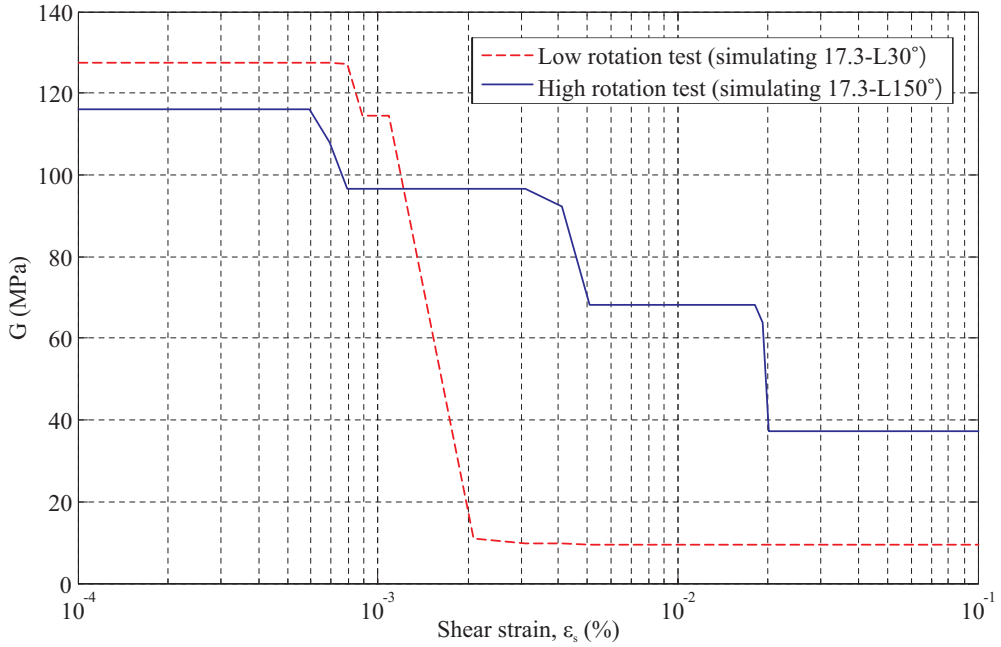

Figure 4.40: Stiffness degradation curves for 17.3SH-L, BOI model

Stage	17SH-L30			17SH-L150		
	Target(kPa)		steps	Target(kPa)		steps
	q	p'		q	p'	
1	-	2805	0.001	-	2805	0.001
2	-	330	-.001	-	330	-.001
3	0	136	#10	0	136	#10
4	0	330	#10	0	330	#10
5a	100	330	#50	-100	330	#50
5b	0	330	#50	0	330	#50
6a	Creep		-	Creep		-
6	Extension		$-1e^{-5}$	Extension		$-1e^{-5}$

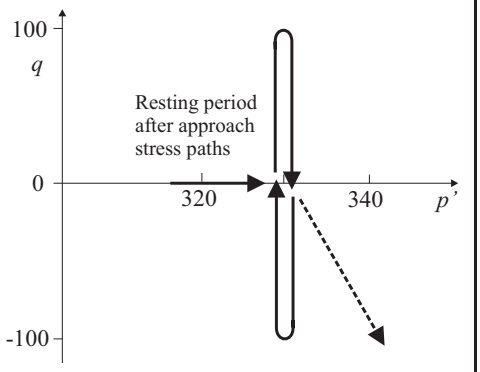

Table 4.5: Specific stages for the 17.3SH-L tests

The BOI results generated, Figure 4.40, show a overall similarity with the experimental results, Figure 4.39, with the high rotation approach stress path giving generally higher stiffness than the path with the low rotation. However in the BOI simulation, the low rotation path test has a marginally higher initial stiffness (seen and explained previously in Section 4.7.2). The stiffness in the low rotation test shows a considerable drop in stiffness after the creep strains have become relatively small. The low stiffness after the drop is attributed to the long approach path using up a large proportion of the soil stiffness.

4.7.6 Overview

It can be seen from preceding sections that, although the BOI model does have its shortcomings, in the modelling of recent stress history effects, including creep, the trends shown are very promising. The BOI model can recreate well the medium strain stiffness seen here with regard to the effects of creep. However, the model produces inaccurate predictions at very small strains when the effects of creep are included. The strain-rate dependant string lengths concept developed in the next chapter incorporates elements of the BOI model and is able to model the isotach behaviour that is difficult to simulate with the BOI model.

5

Strain Rate Dependent String Lengths

5.1 Introduction

In this chapter a new model for predicting the strain rate behaviour of soils is presented, with a demonstration of its accuracy when compared with previous research. The strain rate dependent (SRD) approach is an advance on the Bricks on Ice (BOI) approach in that it is able to model both creep and strain rate effects. The BOI approach has no way of modelling the effects of changes in strain rate. The form of the normal consolidation lines with various creep rates was also incorrect with the model predicting diverging lines with increases of stress, when plotting volumetric strain versus the logarithm of mean normal stress (Section 4.5). It is generally accepted that the normal consolidation line and isotache lines should be parallel. The SRD model simulates both creep and strain rate effects by allowing the soil state to step between these lines upon a change in strain rate or an increase in time, as seen in Figure 5.1.

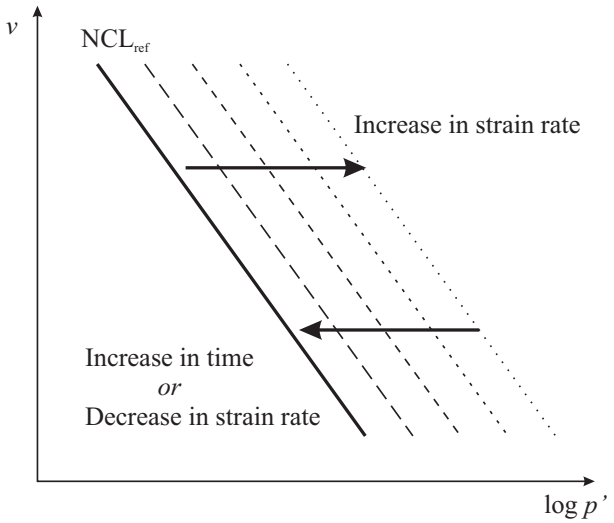

Figure 5.1: Framework for the strain rate dependent approach

5.1.1 Model components

SRD modelling laws can be split according to their two main areas of influence, strain rate behaviour and time dependent behaviour, with both sets of laws being formulated within the same framework, shown in Figure 5.1.

Strain rate behaviour

Some laws that have been proposed to govern the increase in strength of a soil with an increase in strain rate are listed below. Although this is not a definitive list, it includes those laws that would be easily applied in the SRD framework.

Biscontin & Pestana (2001):

$$s_u = s_{u,\text{ref}} \left(\frac{\dot{\gamma}}{\dot{\gamma}_{\text{ref}}} \right)^{\beta^*} \tag{5.1}$$

Graham et al. (1983):

$$s_u = s_{u,\text{ref}} \left[1 + \lambda \, log \left(\frac{\dot{\gamma}}{\dot{\gamma}_{\text{ref}}} \right) \right] \tag{5.2}$$

Einav & Randolph (2006):

$$s_u = s_{u,\text{ref}} \left[1 + \lambda' arc \, sinh \left(\frac{\dot{\gamma}}{\dot{\gamma}_{\text{ref}}} \right) \right] \tag{5.3}$$

where:

s_u = undrained shear strength,
$s_{u,\text{ref}}$ = undrained shear strength measured at the reference strain rate, $\dot{\gamma}_{\text{ref}}$,
$\dot{\gamma}_{\text{ref}}$ = reference strain rate,
$\dot{\gamma}$ = applied strain rate,
β^*, λ and λ' are soil constants.

The above equations relate strain rate to strength. It was shown previously in Section 3.4.1 that the undrained strength is directly related to the string lengths, thus the above forms of equation can also be used to govern the string lengths. The power law shown in Equation 5.1 has been shown to be most applicable to soils undergoing very high rates of shearing such as in shear vane testing (Biscontin & Pestana 2001). The semi-logarithmic relationship shown in Equation 5.2 was adopted by Graham et al. (1983), among others, who showed that the equation was valid for many soils in the range of strain rates normally experienced in the ground. This semi-logarithmic relationship has no lower limit or asymptote to the minimum value, so when the strain rate drops below the reference strain rate, the modification to $s_{u,\text{ref}}$ becomes a reduction rather than an increase. The Arcsine relationship shown in Equation 5.3 does not

generate strength reductions. No matter how low the strain rate drops, the ultimate strength will never reduce below $s_{u,\text{ref}}$ (Einav & Randolph 2006).

Equations 5.1 and 5.2 do not converge on a single solution for rates below the reference strain rate. This is a problem in terms of the BRICK model. As the laws will be used to govern the length of the strings connecting the man to the bricks, there needs to be a lower bound limit to avoid a zero stiffness being generated and to allow modelling of the geological stress history, which involves unusually low strain rates. However, the equations that have no lower bound can be modified so that each converges on a single solution for s_u as the strain rate drops below the reference strain rate.

Biscontin & Pestana (2001) modified:

$$s_u = s_{u,\text{ref}} \left(\frac{\dot{\gamma}}{\dot{\gamma}_{\text{ref}}} + 1 \right)^{\beta^*} \tag{5.4}$$

Graham et al. (1983) modified:

$$s_u = s_{u,\text{ref}} \left[1 + \lambda \, log \left(\frac{\dot{\gamma}}{\dot{\gamma}_{\text{ref}}} + 1 \right) \right] \tag{5.5}$$

Sorensen (2006) also postulated variations of the Graham et al. (1983) law by formulating it with a natural logarithm rather than base ten based on the work of Tatsuoka et al. (2002), where β replaces λ.

Sorensen (2006) A:

$$s_u = s_{u,\text{ref}} \left[1 + \beta \, ln \left(\frac{\dot{\gamma}}{\dot{\gamma}_{\text{ref}}} \right) \right] \tag{5.6}$$

Sorensen (2006) B:

$$s_u = s_{u,\text{ref}} \left[1 + \beta \, ln \left(\frac{\dot{\gamma}}{\dot{\gamma}_{\text{ref}}} + 1 \right) \right] \tag{5.7}$$

Figure 5.2 shows a comparison between the strain rate dependency laws for a reference strain rate $\dot{\gamma}_{\text{ref}} = 10^{-6}(\%/\text{hr})$. For the equations with no lower bound a reduction in strength is predicted for rates lower than the reference strain rate. It should be noted that, although in Figure 5.2 the gradients of the Einav & Randolph (2006) and Graham et al. (1983) curves are shallower than those of Sorensen (2006), due to the use of the same value for both λ and β in the calculations, λ can be changed so that the same magnitude of strain rate effects would be seen. The reference strain rate, for the equations with a lower bound, is essentially the minimum strain rate at which the

effects of changing the strain rate can be seen.

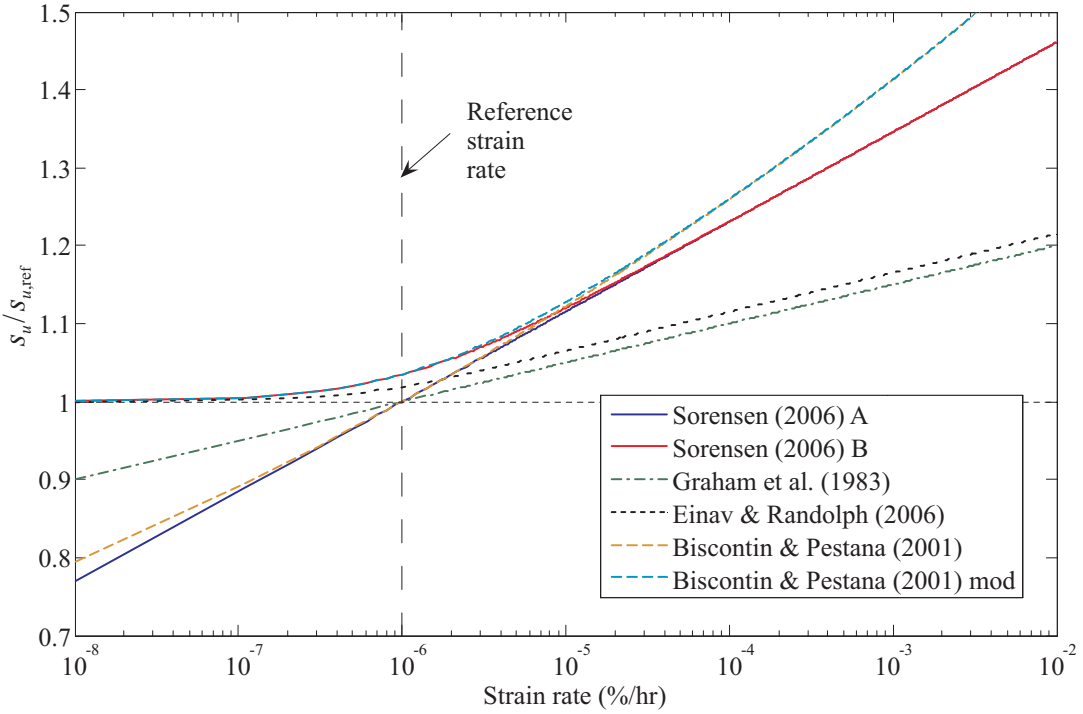

Figure 5.2: Comparison between strain rate dependency laws

The equations for strain rate behaviour do not account for time independently of the strain rate. If the NCL shown in Figure 5.1 is generated when the strain rate is equal to the reference strain rate, increases in strain rate lead to the NCL shifting to the right in a single increment. If the strain rate then decreases back to the reference strain rate, this also occurs in a single increment. The movement between isotaches is governed only by the strain rate. To model time dependent behaviour this movement between isotaches needs also to be governed by time.

Time dependent behaviour

The relationship between creep strain rate and increase in time is generally accepted to be linear when both strain rate and time are plotted on logarithmic scales, as seen in Figure 2.13 on page 17. The governing equation for this behaviour was given in Singh & Mitchell (1968), a simplification of which is shown here in Equation 5.8.

$$\dot{\varepsilon} = A \left(\frac{t_1}{t} \right)^m \tag{5.8}$$

where:

A = strain rate at some arbitrarily chosen time t_1,
m = negative of the slope of the relationship between the logarithm of strain rate and the logarithm of time (see below),
t = time.

$$\Delta log(\dot{\varepsilon}) = -m\ \Delta log(t) \tag{5.9}$$

Written in terms of logarithms, Equation 5.8 becomes Equation 5.9. Singh & Mitchell (1968) suggest a range of values for m of between 0.75 and 1. Ali (1984) expanded on this range suggesting a value of m of marginally over 1 for Kaolin.

The time dependency equation (Eq. 5.8) allows the transition between the isotache lines to be controlled. This is visualised in Figure 5.3. Stress relaxation can be predicted by holding the soil at constant volume. As the applied strain rate is zero, the strain rate equations alone would predict an immediate drop to the reference NCL. By controlling this movement with the time dependent model the reduction of stress with increasing time can be predicted. It should be noted that the equation presented here for time dependent behaviour has no lower limit on the strain rate, meaning that creep can go on indefinitely. Although this may be the case in reality, it makes the modelling of geological stress history much more complex, as the time periods involved need to be accurately known. The implications of this will be discussed further in Section 5.3.2.

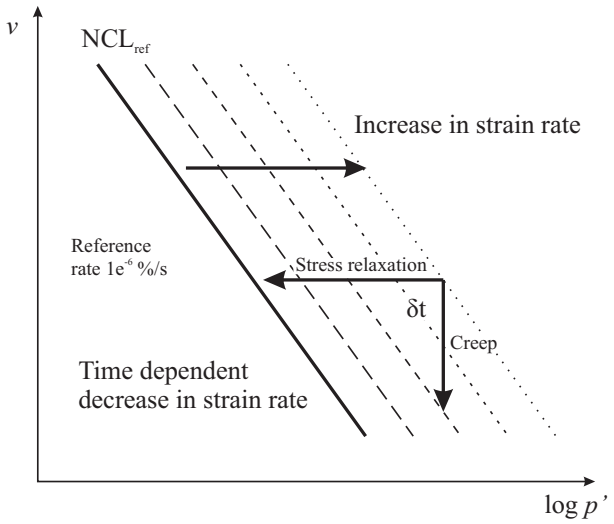

Figure 5.3: Time dependent behaviour within the SRD framework

To predict creep behaviour the soil can be held at constant stress while the straining continues at a logarithmically decreasing rate. This leads to the form of behaviour described by Bjerrum (1967) shown in Figure 2.16 on page 20. Bjerrum refers to the isotaches of time as isochrones, each separated by a constant distance relating to an order of magnitude of time. During the 'perfect consolidation test' (illustrated in Figure 2.16) the soil has to be strained at a relatively high rate so that the effects of creep can be minimised. If the applied rate of strain is stopped and the soil is maintained at constant stress, as noted above, the straining of the soil will continue at a logarithmically decreasing rate. As Singh & Mitchell (1968) showed that logarithm of strain rate is linearly related to the logarithm of time, the isotaches of strain rate shown in Figure 5.3 directly relate to the isochrones in Figure 2.16.

In this section the basic framework for the SRD approach has been presented along with the governing equations. All the effects discussed here can be classified as visco-plastic effects and do not take account of any gains in strength in the soil with time by other processes such as ageing. Before the components presented in this section are incorporated into the SRD framework, the methods of their formulation within the Brick model will be explored.

5.2 Man-led Strain Rate Dependency

It was explained in Chapter 3 that the Brick model works by taking the strain applied to the soil and letting this equate, in the analogue, to the movement of the man. As the man moves so the strings attaching the man to the bricks become taut. While the strings are slack the movement is totally elastic and as the strings become taut so plasticity is developed in the soil and the stiffness of the soil drops. When all the bricks are moving the soil can be said to be behaving plastically and the stiffness will be at the lowest possible level.

In the Brick model the string lengths are directly related to the strength of the soil, as a longer string length allows more elastic straining before the string becomes taut and the brick behaves plastically. This leads to a higher soil stiffness at any given stress level and hence a greater strength. If string length is directly proportional to the strength of the soil, then the equations given in Section 5.1.1 can be directly applied to the string lengths in the Brick model. It has been decided to use the form of the equations given in Sorensen (2006), but instead of the parameters relating to an increase in strength

they now relate to an increase in the string lengths as in Equation 5.10.

$$\mathrm{SL} = \mathrm{SL}_{\mathrm{ref}} \left[1 + \beta \; ln \left(\frac{|\dot{\varepsilon}|}{\dot{\varepsilon}_{\mathrm{ref}}} + 1 \right) \right] \tag{5.10}$$

where:

SL = predicted string length,
$\mathrm{SL}_{\mathrm{ref}}$ = reference (shortest) string lengths,
$\dot{\varepsilon}_{\mathrm{ref}}$ = reference strain rate,
$\dot{\varepsilon}$ = applied strain rate.

To allow this equation to operate, a reference set of string lengths ($\mathrm{SL}_{\mathrm{ref}}$) must be specified, along with a reference strain rate ($\dot{\varepsilon}_{\mathrm{ref}}$). Sorensen (2006) suggests a value of $1e^{-6}$%/hr as a value for the reference strain rate, a rate below which the effects of changing the rate of straining are negligible. In practice the string lengths are obtained from a stiffness degradation curve which is generated by measuring the stiffness after a 180° change in the direction of the stress path in a laboratory test. Such tests are done at a much higher strain rate than the reference strain rate to minimise the influence of time effects such as creep. So long as the strain rate ($\dot{\varepsilon}_{\mathrm{test}}$) at which the test takes place is known, the reference string lengths can be back calculated using Equation 5.11.

$$\mathrm{SL}_{\mathrm{ref}} = \frac{\mathrm{SL}_{\mathrm{test}}}{1 + \beta \; ln \left(\dot{\varepsilon}_{\mathrm{test}} / \dot{\varepsilon}_{\mathrm{ref}} + 1 \right)} \tag{5.11}$$

where:

$\mathrm{SL}_{\mathrm{test}}$ = string lengths calculated from testing.

In the man-led strain rate dependency approach the current strain rate, $\dot{\varepsilon}$, in Equation 5.10, is taken to be the vectorial movement of the man, or the root sum of the squares of the components of applied strain rate described below in Equation 5.12. This means that the movement of the man directly affects the string lengths and hence the stiffness of the soil.

$$\dot{\varepsilon} = \sqrt{(\dot{v})^2 + (\dot{\gamma})^2} \tag{5.12}$$

Thought must be also be given to the mechanism for stepping between different rates of straining. If there is no controlling function to help govern the change in string lengths in any given time increment, then the change becomes effective immediately. This can lead to oscillations within the routine as the full stiffness change is applied over a relatively small period of time. To minimise these oscillations an exponential function to help govern the rate of change of string lengths is introduced:

$$\frac{\delta \mathrm{SL}}{\delta t} = \alpha \left(\mathrm{SL}_{\mathrm{target}} - \mathrm{SL}_{\mathrm{previous}} \right) \tag{5.13}$$

where:

$\mathrm{SL}_{\mathrm{target}}$ = target string length set by the strain rate equations in that BRICK increment,
δt = time step for the current increment,
α = exponential decay factor.

The string length for the increment is given by $\mathrm{SL}_{\mathrm{previous}} + \delta \mathrm{SL}$. Equation 5.13 controls the change of the string lengths during both strain accelerations and decelerations.

5.2.1 Implementing the SRD approach into BRICK

The governing equations for man-led SRD model were implemented into the BRICK model. One of the advantages of a man-led approach is that the movement of the man is specified outside the iterative BRICK routine. This allows the change in string lengths to be easily calculated at the start of the iteration and passed on through the routine. The alternative to this approach is to allow the strain rates of the individual bricks to control the individual string lengths; this brick-led approach is discussed in Section 5.3. The code created in MATLAB to implement the man-led approach is contained within Appendix B.4.1.

5.2.2 Initial tests

To check that the current formulation of the model was working correctly a set of one-dimensional compression tests was devised. The tests were:

- Constant rate of strain tests, varying rates between tests
- Step rate of strain tests, varying rates within tests
- Stress relaxation tests
- Gradual change in strain rate (GCS) test

The parameters used in the man-led SRD model are given in Table 5.1, where the string lengths are half those given in Simpson (1992b). During some of the SRS and GCS tests the α value was changed to 1 for strain decelerations to allow an investigation into the time decay model.

BRICK parameters used in Section 5.2		
BRICK parameter	Code name	Value
Initial strains	SN(NC)	[0, 0, 0, 0, 0, 0]
Initial stresses	SS(NC)	[2, 0, 0, 0, 0, 0]
Reference string lengths	SLr(NB)	$[4.2e^{-5}, 1.1e^{-5}, 2.1e^{-4}, 4.2e^{-4}, 1.1e^{-3}, 2.1e^{-3} 4.1e^{-3}, 0.011, 0.021, 0.04]$
Stiffness reduction	GGMAX(NB)	[0.92, 0.75, 0.53, 0.29, 0.13, 0.075, 0.044 0.017, 0.0035, 0]
Initial conditions	ZERO(2)	[0, 2]
Lambda*	λ*	0.1
Kappa*	κ*	0.02
Iota	ι	0.0041
Beta constant	β_G	4
Number of bricks	NB	10
Number of components	NC	6 - Full 3D (Triaxial testing)
Exponential decay factor	α	0.5 for strain accelerations 0.05 for strain decelerations*
Reference strain rate	$\dot{\varepsilon}_{\text{ref}}$	$1e^{-6}$%/hr
Viscous constant	β	0.25
Notes: The string lengths are initially slack and the original position for all the bricks is the origin. *$\alpha = 1$ was used in some of the SRS and GCS tests.		

Table 5.1: BRICK parameters for man-led SRD model testing

5.2.3 Constant rate of strain (CRS) tests

The strain rates used for the tests were $1e^{-2}$%/hr, $1e^{-3}$%/hr and $1e^{-4}$%/hr. The CRS tests were designed to demonstrate the isotach behaviour seen in the framework illustration in Figure 5.1. The expected result would be three equally spaced parallel lines when plotted as the logarithm of mean normal stress versus volumetric strain.

Figure 5.4 shows that the current formulation of the SRD model did indeed exhibit the expected behaviour during CRS tests. It was postulated by Sorensen (2006) that the initial volumetric strain would have to be varied for the BRICK model to demonstrate isotach behaviour correctly. He formulated an equation that would govern the initial volumetric strain to allow the isotaches to be stepped apart, as given in Figure 5.5. In the current approach this modification was not used, as the initial elastic stiffness

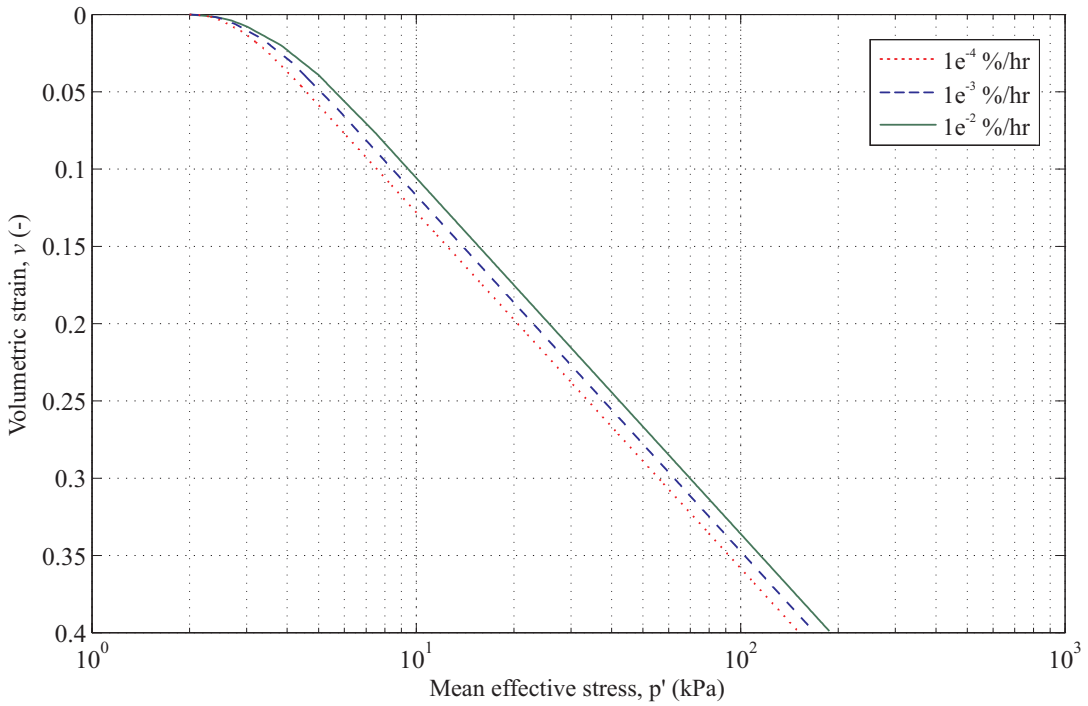

Figure 5.4: Man-led SRD model CRS tests, $v - \log p'$ plot

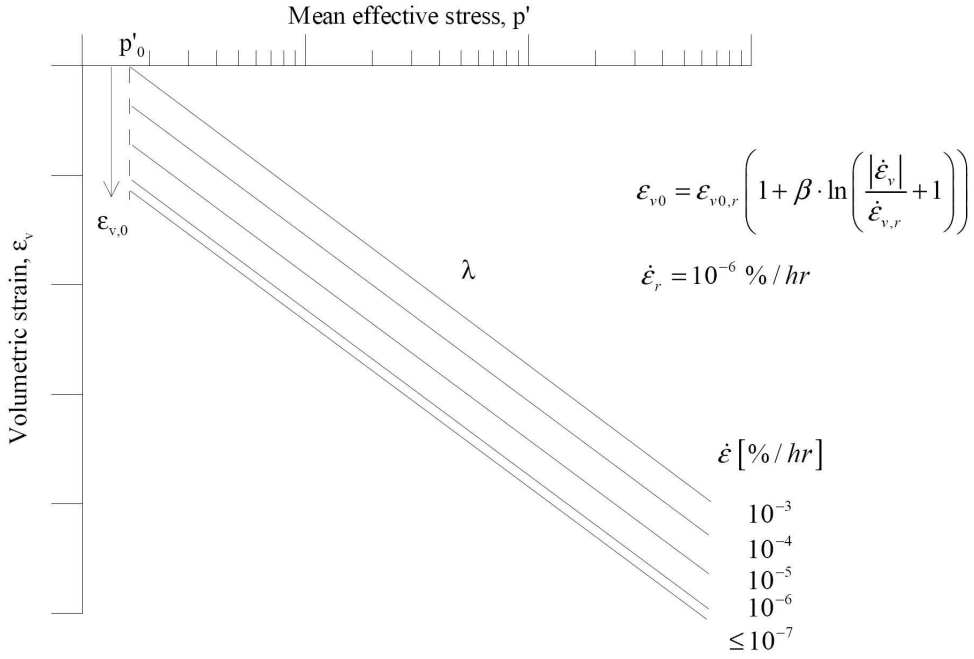

Figure 5.5: Schematic diagram of isotach isotropic compression curves with lower limit of initial volumetric strain, Sorensen (2006)

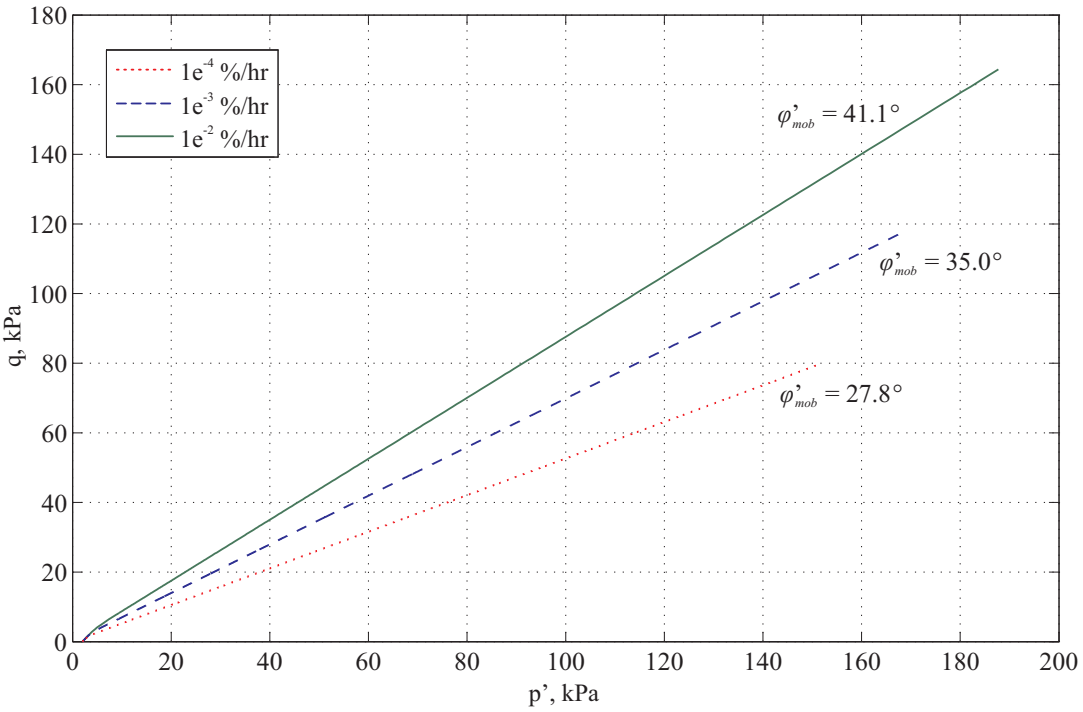

Figure 5.6: Man-led SRD model CRS tests, stress path plot

accounts for the differences in volumetric strain. The string lengths all start off equal to the reference string lengths. As the applied rate of strain causes the string lengths to lengthen, the higher the rate of straining, the larger the initial elastic region becomes. This leads to a larger region of high stiffness and higher stresses being generated at equivalent volumetric strains, enabling the model to recreate isotach behaviour without the modification seen in Figure 5.5.

The stress path plots for the constant rate of strain tests seen in Figure 5.6 show the relationship between strain rate and mobilised angle of shearing resistance, ϕ'_{mob}. The higher the rate of strain, the higher the angle in the current tests. The high ϕ'_{mob} angles are not meant to represent a real soil at this stage as the model has not been calibrated. Although the link between undrained strength and rate of shearing is well established, no data are available of both mean and shear stresses in one-dimensional compression under constant rate of strain conditions.

5.2.4 Step rate of strain (SRS) tests

The transition between the isotaches identified in the CRS tests was explored in the SRS tests. These were conducted by initially straining the soil at the lowest rate used

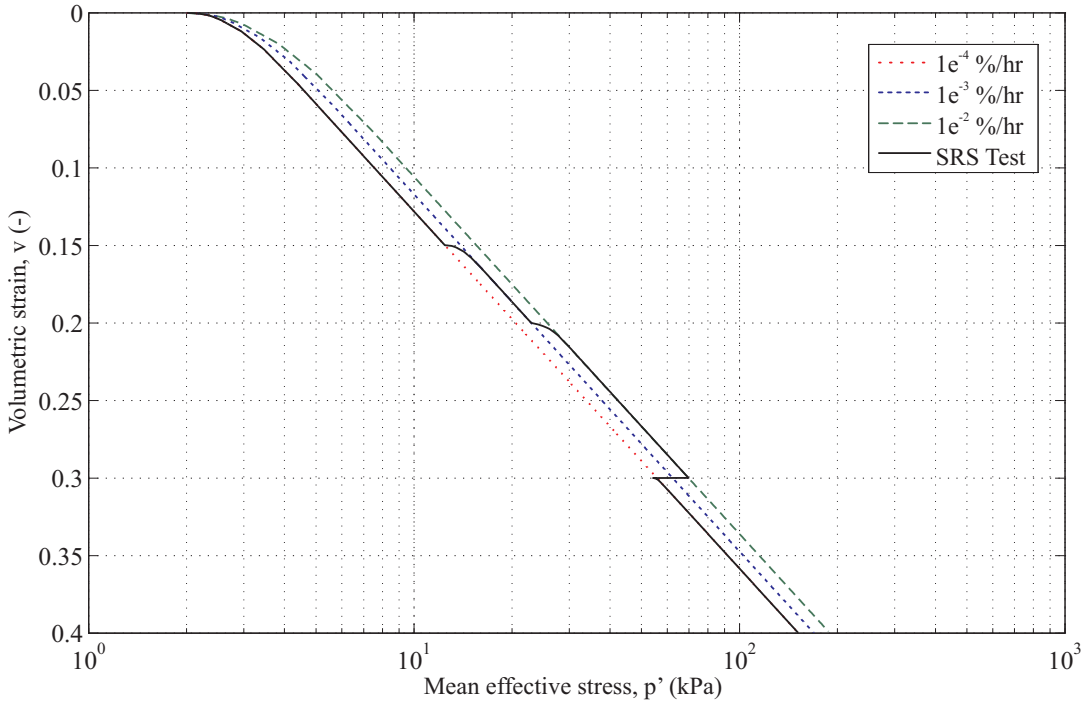

Figure 5.7: Man-led SRD model SRS tests, $v - \log p'$ plot

in the CRS tests ($1e^{-4}$%/hr) until 15% volumetric strain was reached, then increasing the applied strain rate in a single increment to $1e^{-3}$%/hr. Straining continued at this rate until a volumetric strain of 20% was reached, at which point the rate was increased again to $1e^{-2}$%/hr. Once 30% volumetric strain was reached, the rate of straining was reduced back to the lowest rate, $1e^{-4}$%/hr.

Figure 5.7 shows the isotach behaviour predicted by the man-led SRD model. The step increases in stress are caused by the lengthening of all the strings, leading to an increase in elastic straining and an increase in the stiffness of the soil. This increase in stiffness allows the soil state to step between the isotaches for the different rates of straining. Similarly, when the straining decelerates, the strings shorten leading to a decrease in stiffness and stresses. It can be seen during the strain deceleration the stresses undershoot the isotache predicted from the CRS test. This is due to the removal of the influence of the damping factor, α, by setting its value to 1 for strain decelerations. This was done to show the necessity of the exponential damping equation (Equation 5.13). The curve does rejoin the CRS predicted result but only after a small number of oscillations. The stress paths can be seen in Figure 5.8 which shows the accurate stepping between the different CRS stress paths upon a change in strain rate.

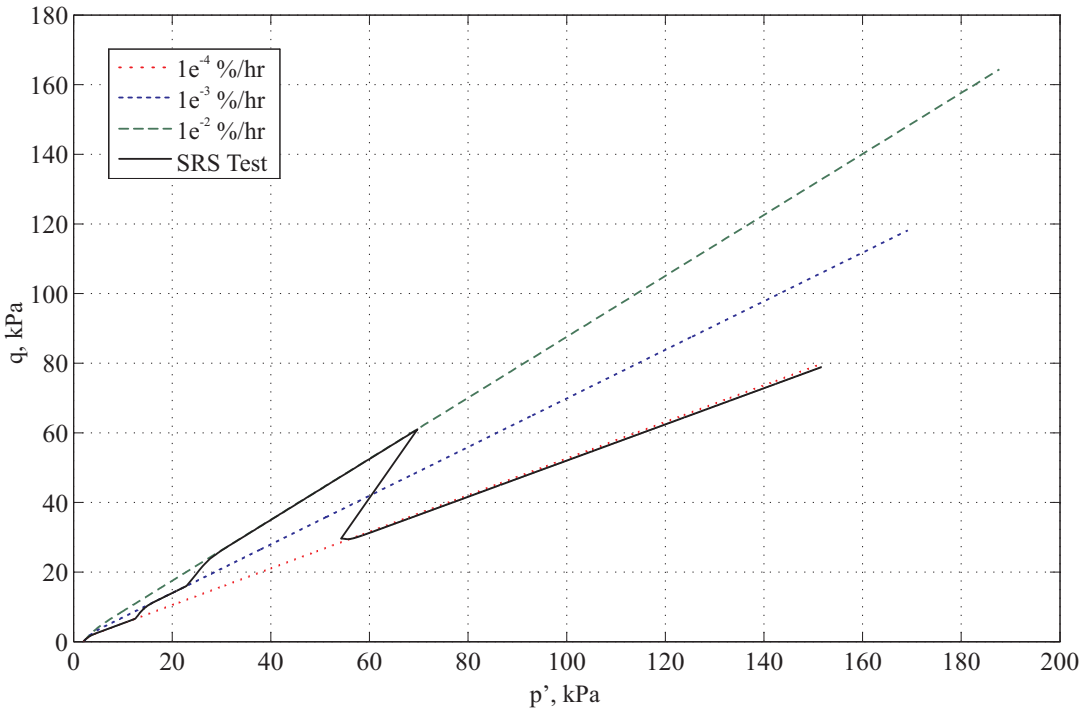

Figure 5.8: Man-led SRD model SRS tests, stress path plot

5.2.5 Stress relaxation tests

To demonstrate the ability of the model to simulate periods of stress relaxation, the strain rate applied to the soil was temporarily reduced to zero. This reduces all the string lengths to the reference values, creating a large negative stress change. Figure 5.9 shows the effect of allowing the soil to relax. It can be seen in all three tests that the stresses reduce to the same value, equivalent to that of an isotache created at a rate of $1e^{-6}$%/hr. As G_{max} is unaffected by the SRD model, the intial stiffness for all the tests after the relaxation is the same. The test at the highest strain rate takes the largest amount of strain to reach the previous stress levels; the stiffness is constantly reducing as the straining continues making it harder to reach the previous stress. This reduction in stiffness greatly affects the stress paths as seen in Figure 5.10. The shear stresses after the relaxation period do not climb back to the same magnitude as was experienced before the relaxation occured. On the other hand the mean stresses recover relatively, quickly leading to the correct trends being exhibited in Figure 5.9.

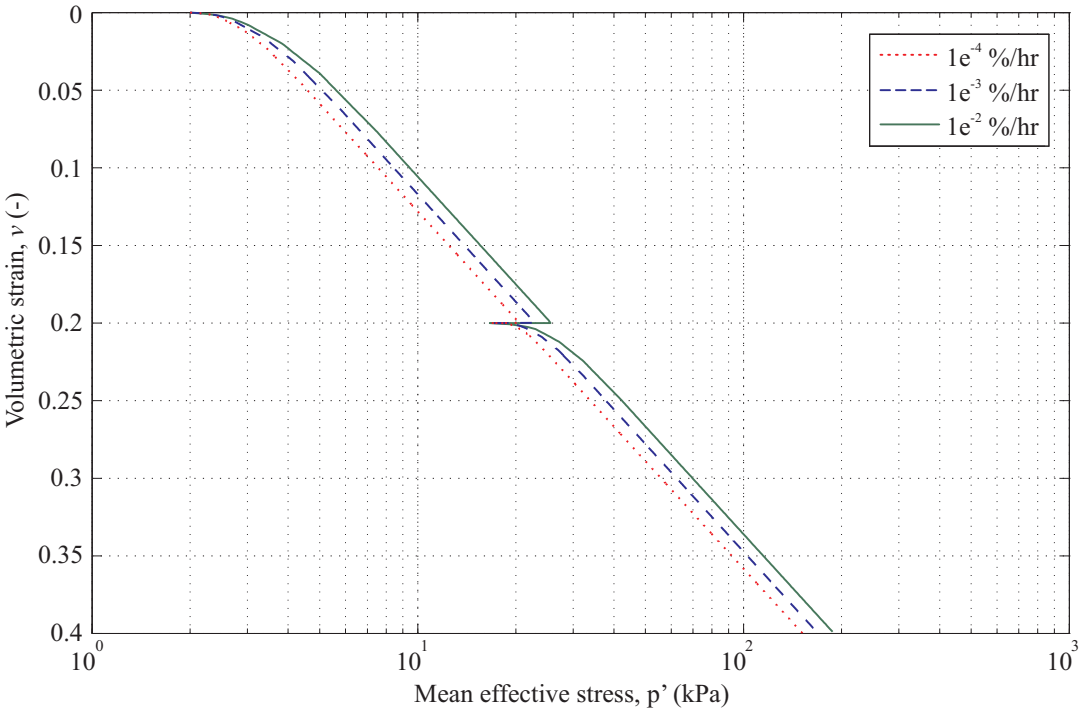

Figure 5.9: Man-led SRD model stress relaxation tests, $v - \log p'$ plot

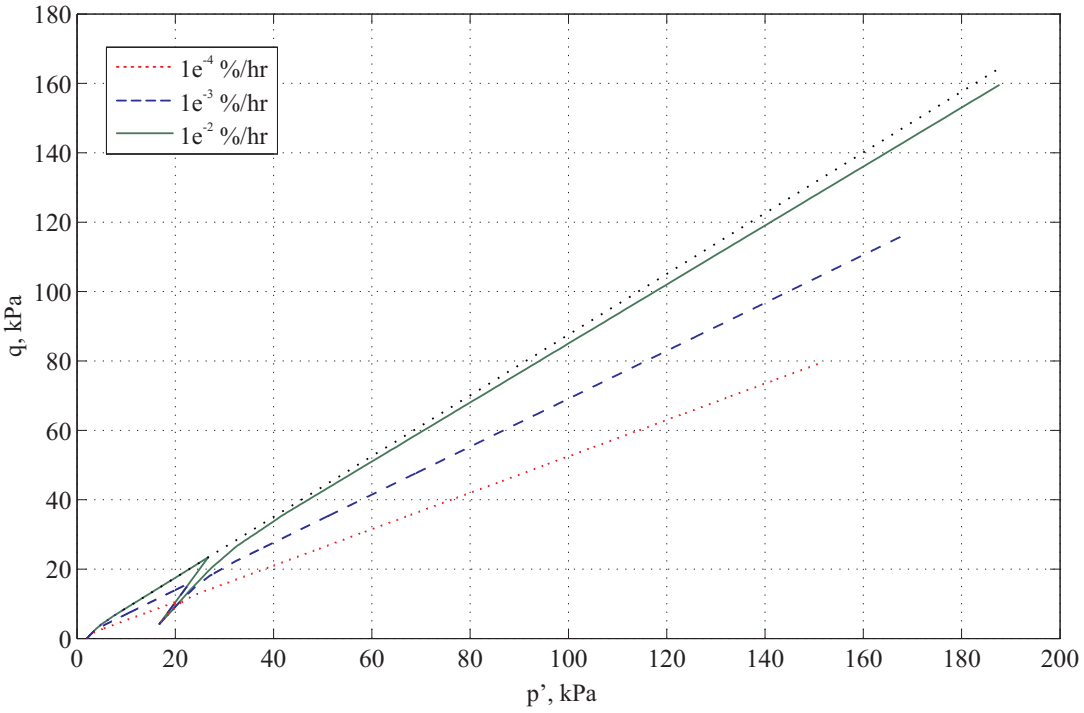

Figure 5.10: Man-led SRD model stress relaxation tests, stress path plot

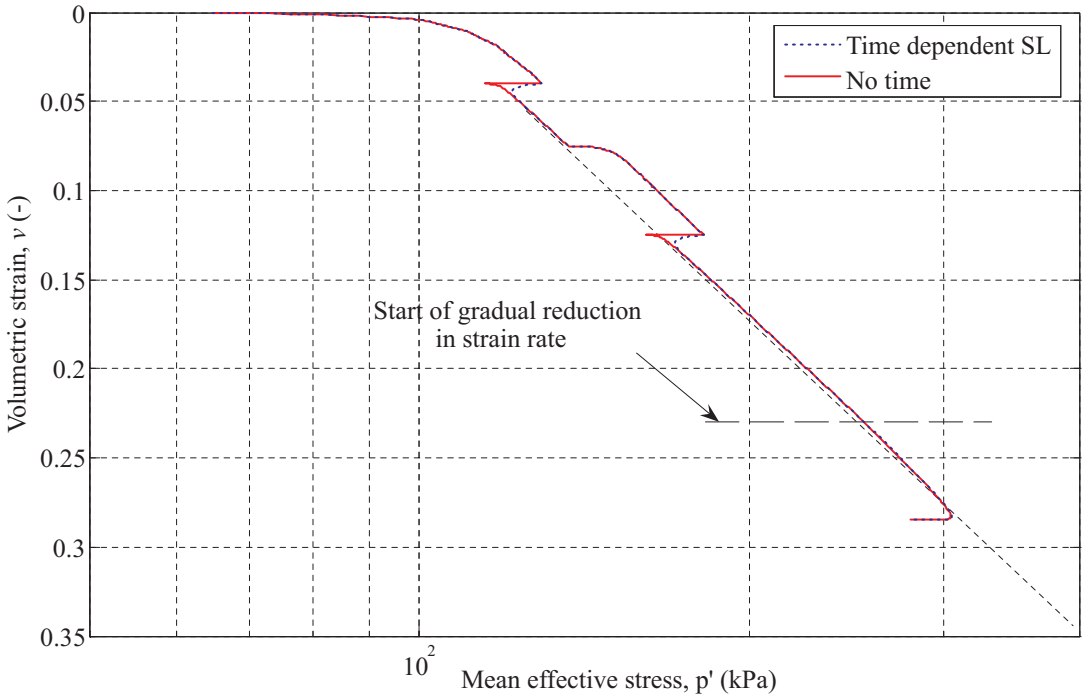

Figure 5.11: Man-led SRD model gradual change in strain rate tests, $v - \log p'$ plot

5.2.6 Gradual change in strain rate (GCS) tests

The GCS tests were devised to explore how the predicted soil state could transit between isotaches more gradually than in the SRS tests. The procedure for these tests was to initially perform a SRS test to establish the trends then to gradually reduce the strain rate to that of the reference strain rate and monitor the results. The initial portion of the test was stepped between $1e^{-3}$%/hr and $1e^{-4}$%/hr and then the rate was linearly reduced to $1e^{-6}$%/hr, over a period of 24 hours. Two versions of the same test have been included in this section: one with a decay constant α of 1 for strain decelerations, giving instantaneous relaxations between strain rates, the other with an α value of 0.05 for decelerations, allowing an exponential decay.

Figure 5.11 shows the effects of the step rate of strain initial section of the test followed by a gradual reduction in strain rate. The 'No time' test used an α of 1 and the 'Time dependant SL' test an α of 0.05 for strain decelerations. The time dependent string length plot shows the effect of varying the α value in eliminating the undershoot in the stresses generated after a strain deceleration. The effects of the exponential damping model can be seen clearly in Figure 5.12, where the string length modification factor is defined as the current string length divided by the reference string length. A mod-

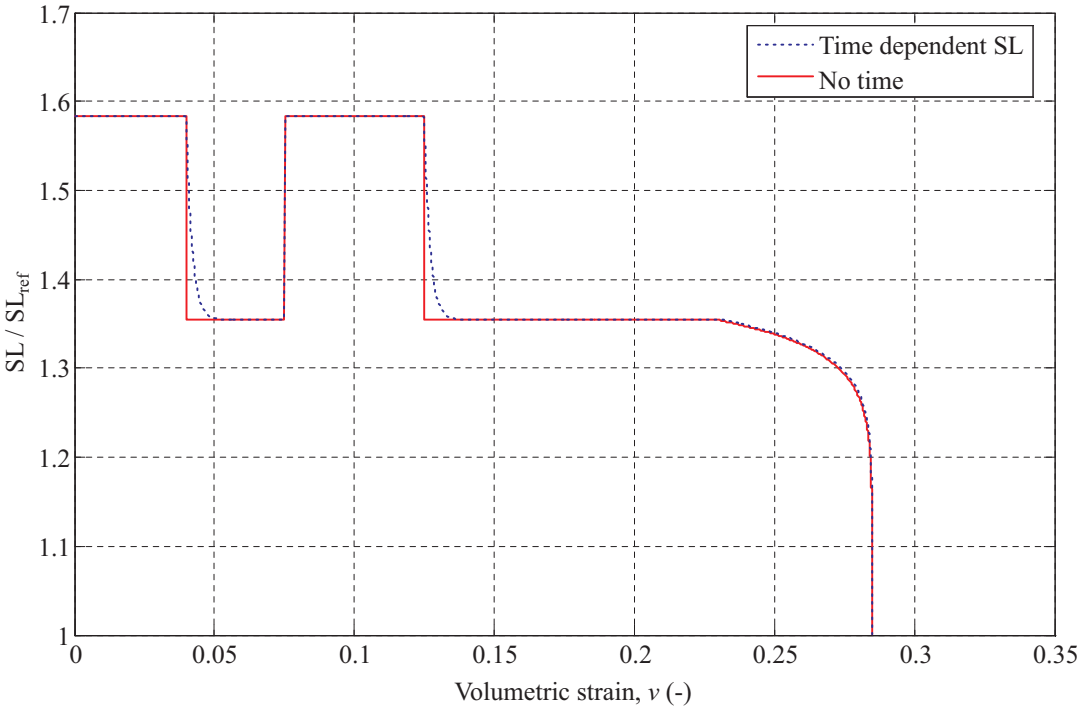

Figure 5.12: Changes in string length modification factor during the gradual change in strain rate tests

ification factor of $(1 + \ln(2)\beta)$=1.173 would equate to the soil being strained at the reference strain rate, with the modification factor converging on a value of 1 as the strain rate drops below the reference rate (Equation 5.10). It can be seen that the strain accelerations are reflected immediately in the string lengths, while for the strain decelerations under time dependent control the string lengths exponentially reduce to the target string length. The time dependency (α value) can be seen not to affect the gradual relaxation of the string lengths as the relative change in string length in any one increment is much smaller than those generated by a step change in strain rate.

The stress paths seen in Figure 5.13 show that under step changes of strain rate the paths exhibit similar behaviour to that seen in Figure 5.8, with the path returning to the same stress level after a period of straining at a lower strain rate through the mobilisation of a higher stiffness in the soil. The gradual change in strain rate phase starts at a mean stress of 250kPa, with the stiffness reducing at an increasing rate leading to the curved path in stress space.

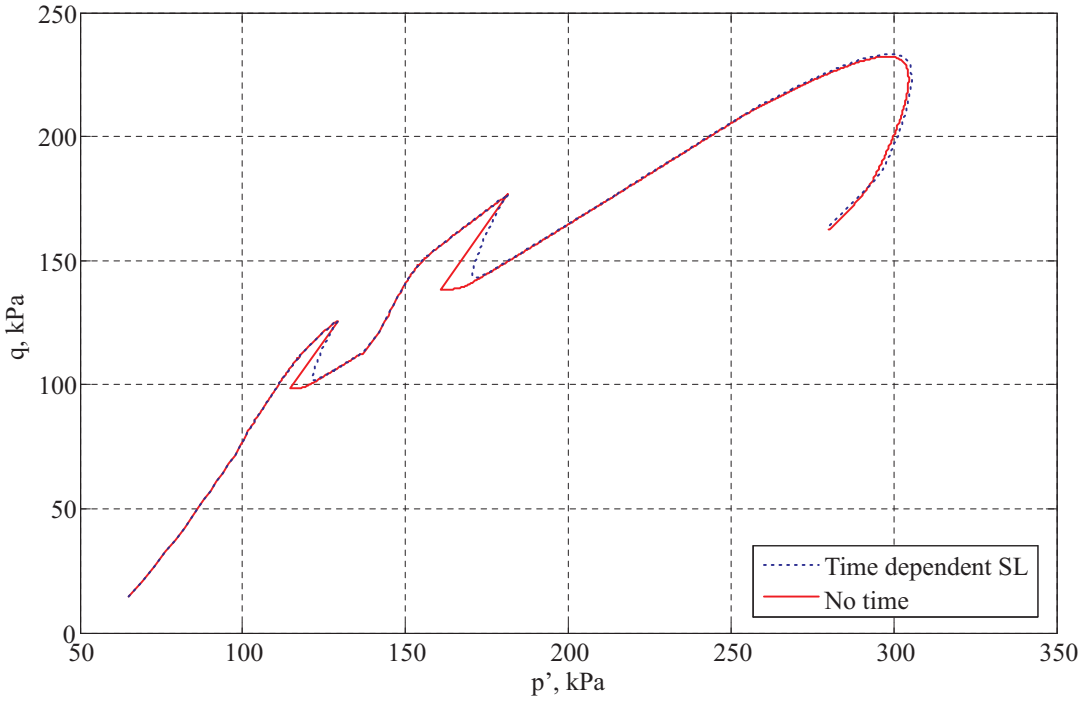

Figure 5.13: Man-led SRD model gradual change in strain rate tests, stress path plot

5.2.7 Discussion

Although the man-led SRD approach shows realistic behaviour in the production of parallel isotaches during the CRS and SRS tests, the behaviour predicted in other circumstances leaves room for improvement. This is especially true of the stress path predicted after a period of stress relaxation, with the man-led approach predicting a persistent drop in shear stress. It is likely from the testing done by Den Haan (2001) that this should not be the case and that the shear stress should return to the previous level, as shown in Figure 4.2 on page 78. On a fundamental level there is some behaviour that the man-led approach will never be able to model accurately.

The string lengths are dependent on the movement of the man, that is *all* the string lengths, including those which are currently not taut and thus where the corresponding bricks are not moving. For strain accelerations this does not prove to be too much of a problem as an increase in rate increases the string lengths, giving a larger elastic zone. The current point of strain will always lie inside the elastic zone upon an increase in strain rate. For decelerations, on the other hand, a shortening of all the string lengths will lead to the yield surface contracting and some bricks that may not have been moving prior to the deceleration could be caused to move, leading to a reduction in stresses

in future accelerations, as seen in Figure 5.10.

If the man controls all the string lengths globally, the behaviour of the soil is entirely dictated by the strain rate applied. If instead the strain rate dependency is dictated by the movement of the individual bricks then different proportions of soil (bricks) can behave differently simultaneously. For example, imagine a period where the entire soil body is experiencing creep and all the bricks are moving with an ever decreasing rate of strain. If then a small strain acceleration is applied to the soil, only the shortest strings would become taut and hence the attached bricks experience the effects of the acceleration. The longer strings would not become taut and hence the behaviour of the attached bricks would still be that of continued creep, with the strain rate decreasing. Thus at one point in time two bricks could be experiencing different strain rate effects, with any combination of direct strain rate and time dependent effects possible.

The brick-led approach leads to a more flexible model for the strain rate dependency and will be fully explored in Section 5.3.

5.3 Brick-led Strain Rate Dependency

In the brick-led strain rate dependency model the string length in any increment is a product of the strain rate of the individual bricks during that increment, rather than being globally defined by the movement of the man. Strain rate dependency was the main focus of the man-led approach and the prediction of time dependent behaviour was not focused upon. In the brick-led model this too will be investigated to show that the framework is able to account for both strain rate and time effects.

5.3.1 Iterative approach

As the string lengths are dependent upon the strain rate of the individual bricks, and the strain rate is dependent on the string lengths, in any increment there must be an iterative process. The initial movement of a brick is calculated using the reference string length as this is the shortest the strings can become. As the string lengths are at their shortest the brick is then moving at its maximum rate for that increment, so the string length increases in response to the increase in strain rate compared with the reference strain rate. As this happens, slack is introduced into the system as the brick moves to a point where the string is no longer taut and the initial estimate is shown to introduce too much movement. For the next iteration the movement of the brick is

reduced and thus the strain rate is reduced, shortening the strings, and increasing the strain rate for the next increment. This iteration repeats until the difference between the current and previous string lengths has become sufficiently small in comparison to the length of the string itself.

This iterative process of finding the string lengths can lead to unstable oscillations in the calculations, so that damping factors have to be introduced into the routine. The damping factors include only applying half the calculated change in string length in any one increment and an exponential damping factor on the calculation of strain accelerations to limit the maximum change in string length in any one iteration. These factors have a negligible effect on the generated stresses; they just allow the SRD routine to reach a point of convergence more easily.

As described in Chapter 3, the BRICK program calculates the movements of each brick after subtracting the plastic strain reduction from the current string lengths. This process allows purely plastic movements to still generate elastic strains and hence stress changes. The calculation of the plastic strain reduction is done iteratively, as it is essentially calculated from the movement of the individual bricks, but is applied globally to them in the next iteration. If the string lengths were to be iteratively calculated in the same way, there would be a problem with the effects of the plastic strain reduction interfering with the calculation of the string lengths and vice versa.

In the first BRICK iteration the plastic strain reduction is set to zero as the brick movements have not been calculated before the point at which the plastic strain reduction needs to be applied. This means that the first brick movement calculation is devoid of the effects of the plastic strain reduction. The SRD routine calculates the new rate dependent string lengths in the first iteration only, leaving subsequent iterations free to account for the effects of the plastic strain reduction.

The MATLAB code containing the formulation of the brick-led SRD model can be found in Appendix B.4.2.

5.3.2 Accounting for time

It was established in Section 5.1.1 that the decay in strain rate during creep should be linear with the logarithm of time (equations 5.8 and 5.9) in Figure 5.14. The man-led SRD model runs with an exponential rather than a logarithmic decay for all strain

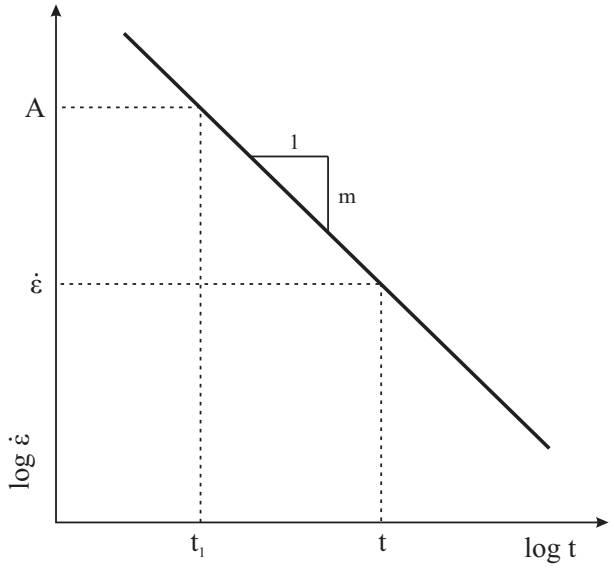

Figure 5.14: Visualisation of Equation 5.8

decelerations, as seen in Equation 5.13. To make accurate long term predictions of the effects of creep the formulation of the time dependent effects must be of a logarithmic form. The BRICK model is implemented in an incremental routine with no monitoring of the passage of time apart from the incremental time increase, i.e. cumulative time is not tracked. This leads to a difficulty when calculating the logarithmic decay as there is no value of t_1 (as defined in Figure 5.14) to use in the calculations.

Although t_1 is unknown, the string lengths during the previous time increment ($\mathrm{SL_{prev}}$) are known. Knowing the previous string lengths allows the current decay to be back-calculated, using the reference strain rate and an estimated time to reach this rate. Each strain rate can be associated with a unique time as shown in Figure 5.14. The previous strain rate ($\dot{\varepsilon}_{\mathrm{prev}}$) can be calculated by rearranging Equation 5.10 and substituting $\dot{\varepsilon}_{\mathrm{prev}}$ for $\dot{\varepsilon}$ creating Equation 5.14.

$$\dot{\varepsilon}_{\mathrm{prev}} = \dot{\varepsilon}_{\mathrm{ref}}(e^{\left(\frac{(\mathrm{SL_{prev}}/\mathrm{SL_{ref}})-1}{\beta}\right)} - 1) \tag{5.14}$$

If the period over which creep is decreasing is set to have an upper limit and a specific strain rate is associated with that limit, then the previous time can be calculated from Equation 5.15. It is assumed that the upper time limit for creep is 10^8 seconds which equates to roughly 31 years and 8 months, sufficiently long for most practical problems. Using the results from Bishop (1966), it can be shown that for London Clay this time

would relate to a strain rate of $1e^{-13}$-/s. This is adopted as the reference strain rate, $\dot{\varepsilon}_{\text{ref}}$.

$$\text{t}_{\text{prev}} = 10^{\left(\log\left(10^8\right) - \left(\log\left(\frac{\dot{\varepsilon}_{\text{prev}}}{\dot{\varepsilon}_{\text{ref}}}\right)\frac{1}{m}\right)\right)} \tag{5.15}$$

where:

t_{prev} = time in seconds at the end of the previous BRICK increment.

It should be noted that time in the ARUP finite element program SAFE is computed in seconds so the reference strain rate and associated time have both been specified in seconds. As the time increment is known so the current time is simply the previous time plus the time increment, Equation 5.16.

$$\text{t} = \text{t}_{\text{prev}} + \delta\text{t} \tag{5.16}$$

The current strain rate predicted by the logarithmic decay (Equation 5.8) can then be calculated using the current time, t, by Equation 5.17.

$$\dot{\varepsilon} = 10^{\log\left(\dot{\varepsilon}_{\text{ref}}\right) + max\left(0, \left(\frac{\log\left(10^8\right) - \log\left(\text{t}\right)}{1/m}\right)\right)} \tag{5.17}$$

The string lengths for use in the current increment are adjusted in the usual way using Equation 5.10. The back calculation of the previous time and the current strain rate is visualised in Figure 5.15.

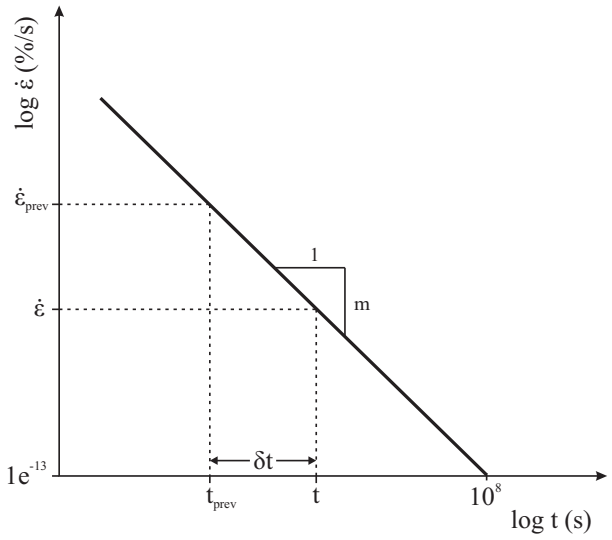

Figure 5.15: Framework for the calculation of the current strain rate

5.3.3 Initial tests

As the formulation of the strain rate dependency has not changed between the man-led and brick-led models it should be safe to assume that the basic test results (CRS etc.) will exhibit similar behaviour. The testing in this section will therefore concentrate on behaviour that was problematic with the man-led model. The tests include:

- Step change in strain rate tests
- Stress relaxation tests
- Swelling and recompression tests

The parameters used for the brick-led formulation of the model are given in Table 5.2.

BRICK parameters used in Section 5.3		
BRICK parameter	Code name	Value
Initial strains	SN(NC)	[0, 0, 0, 0, 0, 0]
Initial stresses	SS(NC)	[2, 0, 0, 0, 0, 0]
Reference string lengths	SLr(NB)	$[4.2e^{-5}, 1.1e^{-5}, 2.1e^{-4}, 4.2e^{-4}, 1.1e^{-3}, 2.1e^{-3} 4.1e^{-3}, 0.011, 0.021, 0.04]$
Stiffness reduction	GGMAX(NB)	[0.92, 0.75, 0.53, 0.29, 0.13, 0.075, 0.044 0.017, 0.0035, 0]
Initial conditions	ZERO(2)	[0, 2]
Lambda*	λ^*	0.1
Kappa*	κ^*	0.02
Iota	ι	0.0041
Beta constant	BETA(1)	4
Number of bricks	NB	10
Number of components	NC	6 - Full 3D (Triaxial testing)
Time decay constant	m	1.0386
Reference strain rate	$\dot{\varepsilon}_{\text{ref}}$	$1e^{-13}$/s
Viscous constant	β	0.23
Note: The string lengths are initially slack and the original position for all the bricks is the origin in strain space.		

Table 5.2: BRICK parameters for the brick-led SRD model testing

5.3.4 Step change of strain rate (SRS) tests

These tests were designed to check that the brick-led SRD model still exhibits the correct behaviour during 1D consolidation SRS tests. The results have been overlaid on those of CRS tests.

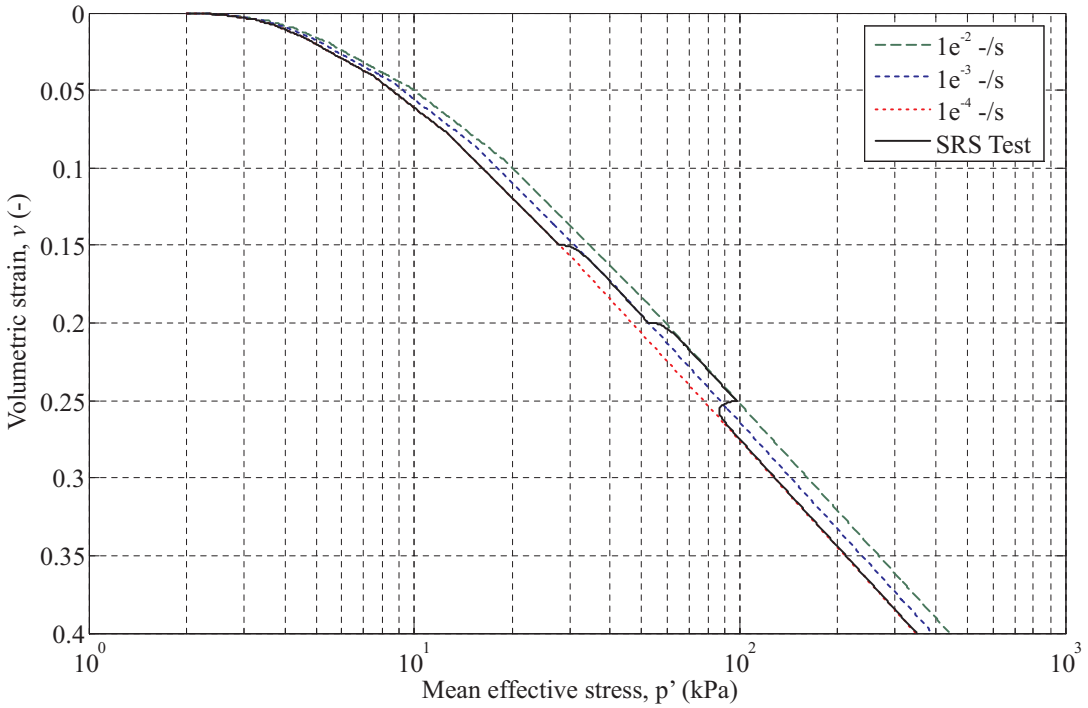

Figure 5.16: Brick-led SRD model SRS test results, $v - \log p'$ plot

Figure 5.16 shows the SRS tests plotted as volumetric strain versus the logarithm of mean effective stress. The isotach behaviour is clearly observable with the the strain accelerations causing a near immediate increase in stress, comparable to the behaviour observed in Figure 5.8 for the man-led model. During the strain decelerations the behaviour is also similar when compared to the man-led results generated with an $\alpha = 0.05$ (Figure 5.11). Both models predict a convergence upon the new CRS path with increasing strain. This agrees well with the behaviour observed in Batiscan clay by Leroueil et al. (1985), as seen in Figure 2.23 on page 25. This figure shows the step changes of strain rate leading to a rapid convergence of the test path upon the new isotache. The stress paths for the CRS tests in Figure 5.17 show a very different trend to that seen in Figure 5.6. The brick-led model predicts no change in gradient for an increase in strain rate whereas the man-led model did. Although there is no experimental data to support either case, the theoretical relationship between strain rate and the current stiffness is coaxial, being the same for both shear and volumetric

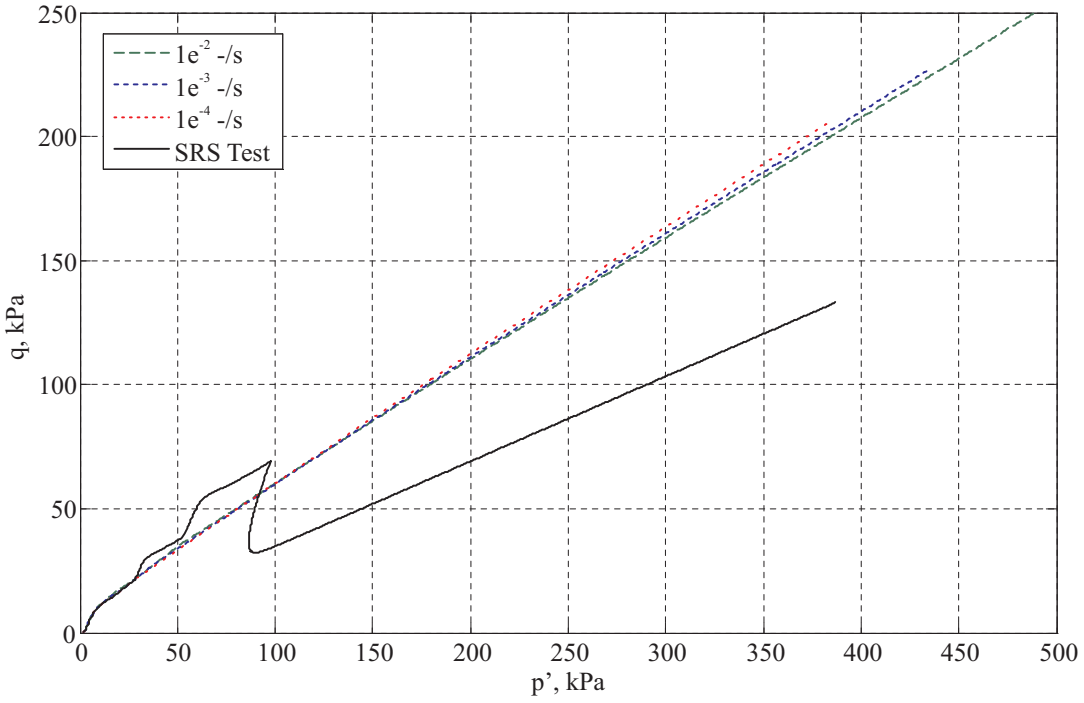

Figure 5.17: Brick-led SRD model SRS test results, stress path plot

strain. It could be argued that due to the coaxial relationship the stresses should follow the same gradient independent of the strain rate. The stress path for the SRS test, also shown in Figure 5.17, shows a divergence from the paths from the CRS tests. This is most probably an effect caused by the incremental approach incorporated in the Brick model, with the change in mean stress being related to the current stress level (Equation 3.29 on page 53). That is, if the path undershoots the previously predicted stress path, there is no way for it to return to it without an increase in stiffness.

5.3.5 Stress relaxation tests

The tests were conducted in a similar way to those done in Section 5.2.5 with the soil being one-dimensionally compressed to 20% volumetric strain then being held at constant volume for 5000 seconds, after which the compression recommenced. This was repeated with three different strain rates.

Figure 5.18 shows the the relaxation behaviour as the stresses fall at constant volume, as seen previously in Figure 5.9. Although the duration of all the tests is the same, the amount of relaxation each test undergoes varies. This can be more clearly seen in Figure 5.19 where the minimum stresses generated in the relaxation phases are different

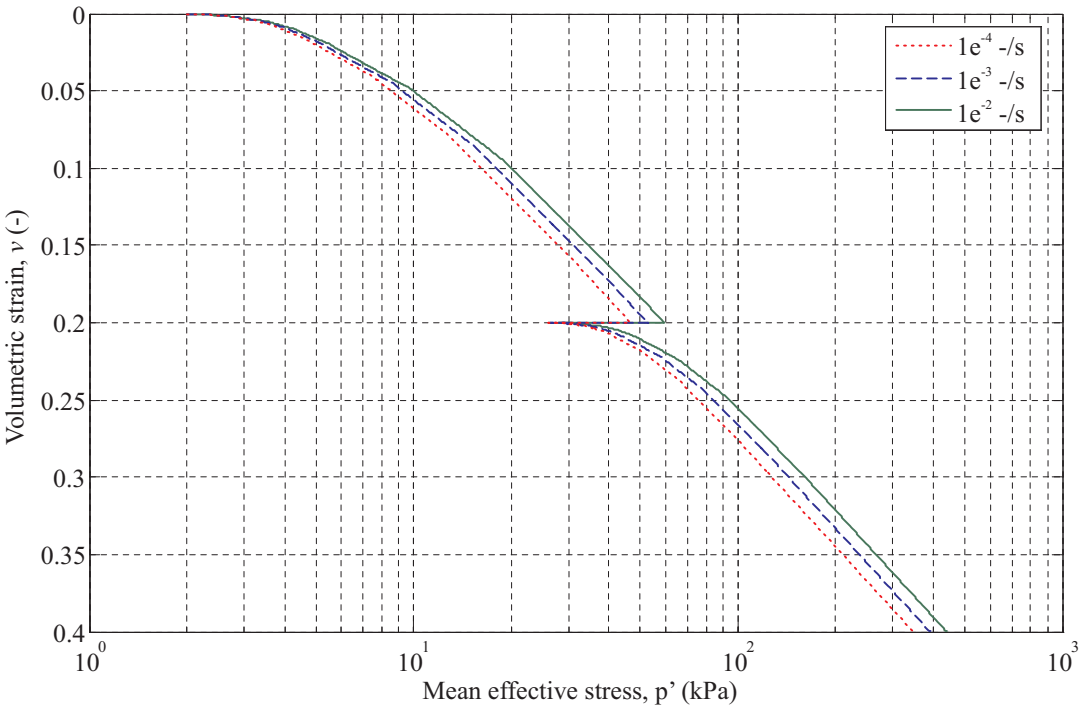

Figure 5.18: Brick-led SRD model stress relaxation tests, $v - \log p'$ plot

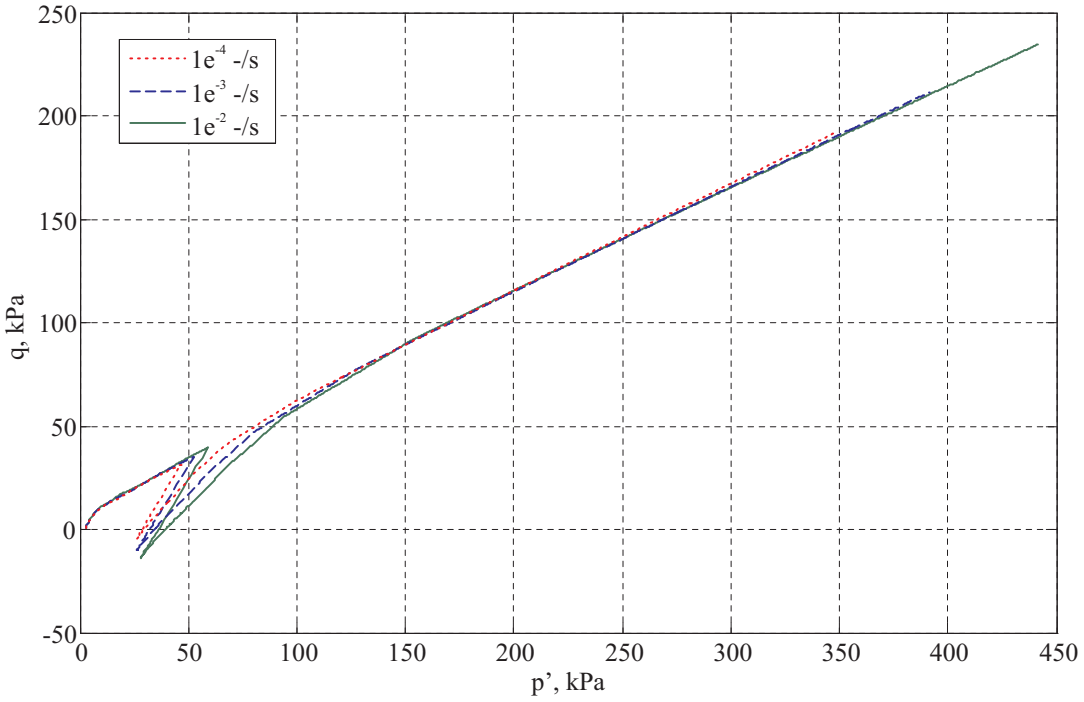

Figure 5.19: Brick-led SRD model stress relaxation tests, stress path plot

for each test. As the test conducted at $1e^{-4}$-/s is already following the lowest isotache, the relaxation period generates the lowest stresses. Conversely, the $1e^{-2}$-/s test exhibits the highest stresses both in isotach behaviour and in relaxation. It should be noted that in the current tests the stresses rejoin the same, approximately constant gradient stress path as they did in the tests by Den Haan (2001), illustrated in Figure 2.42 on page 42. This was one of the main flaws of the man-led model as the stress paths generated did not rejoin the path predicted without the relaxation (Figure 5.10).

5.3.6 Swelling and recompression tests

One final check was carried out to check that the SRD model was not adversely affecting the prediction of behaviour in simple one-dimensional compression, swelling and recompression tests, as explored with the BOI model in Section 4.5.2. In this test the soil was first one-dimensionally compressed to 20% volumetric strain at a strain rate of $1e^{-4}$-/s. The soil was then swollen back to an OCR of 20, approximating the in-situ conditions found in surface deposits of London Clay (King 1981). The soil was then recompressed to 40% volumetric strain to ensure that the NCL was correctly rejoined. The recompression phase was run at three different rates.

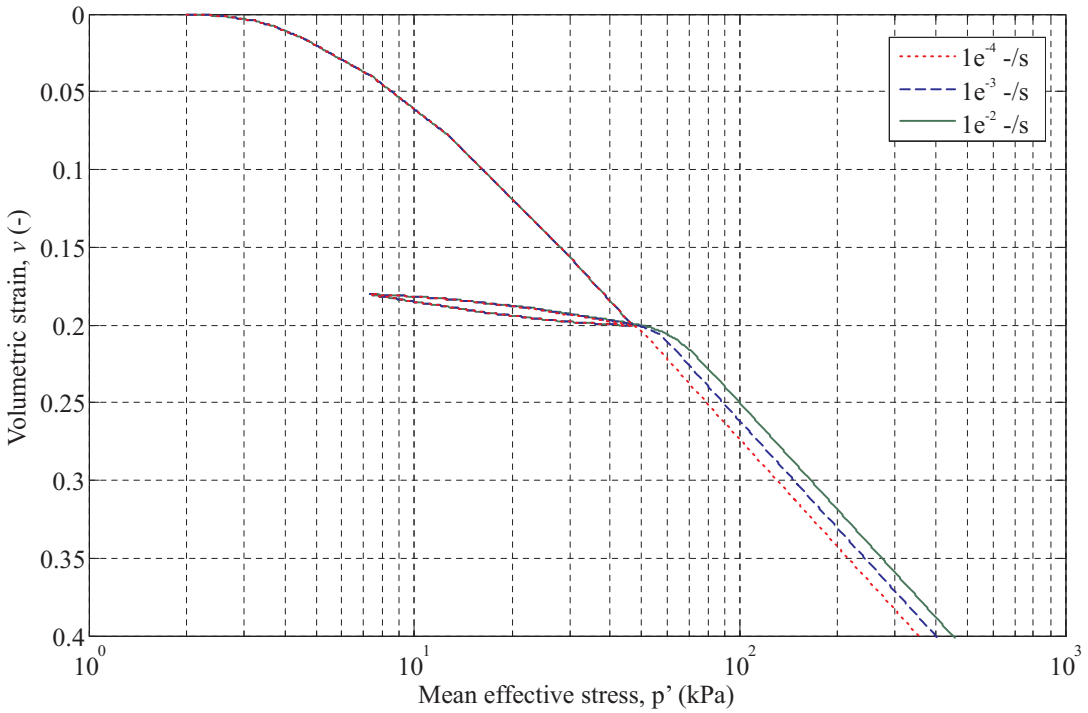

Figure 5.20: Brick-led SRD model swelling and recompression tests, $v - \log p'$ plot

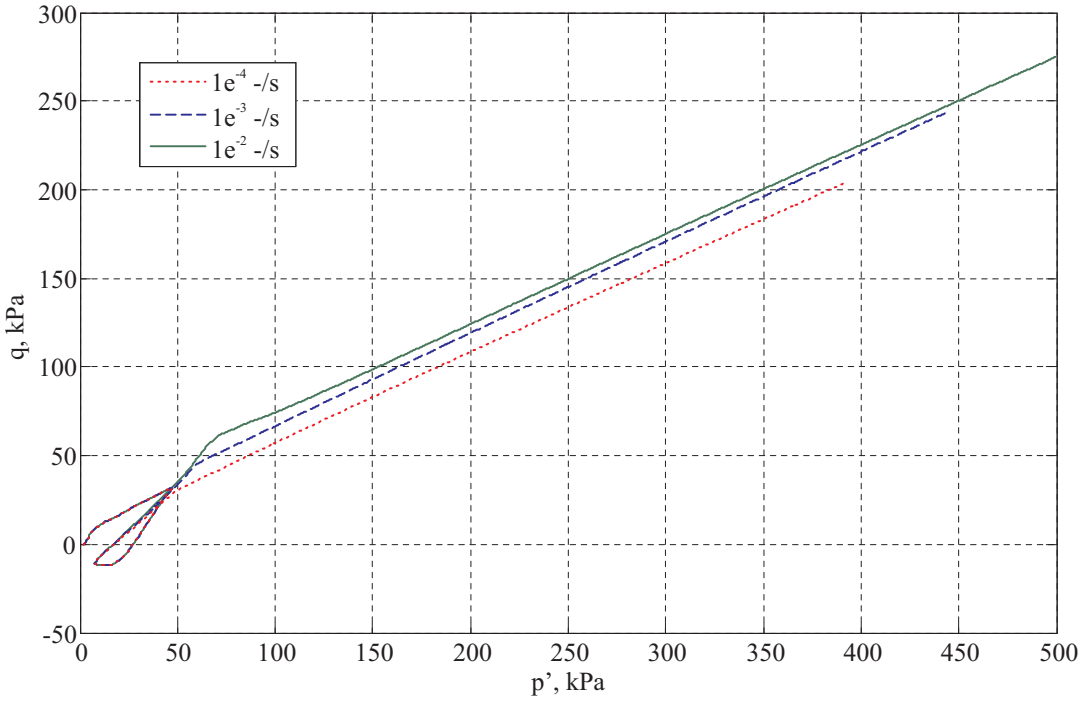

Figure 5.21: Brick-led SRD model swelling and recompression tests, stress path plot

From Figure 5.20 it can be seen that the isotache NCL lines are still created, as seen in Figure 5.16. The test conducted at a constant strain rate ($1e^{-4}$-/s) shows the correct behaviour with the recompression line rejoining the previous NCL at the correct stress. The stress path plot, Figure 5.21, also shows the rapid regaining of the preconsolidation stresses during the recompression phase of this test.

It should be noted that the above tests using the brick-led SRD model are based on Theory 2 of the Brick model. The new code could therefore be directly imported into the finite element program Safe (which uses a version of Theory 2).

5.4 Benchmarking the SRD Model

Section 5.3 has focused upon examining the trends shown by the brick-led SRD model. On the plots of volumetric strain versus mean stress the isotach behaviour was always shown correctly. The stress path plots are harder to interpret as there are no experimental plots available for comparison. In this section the model has been benchmarked against other information that is available in previous literature. This includes results of SRS shearing tests and shear stiffnesses in undrained triaxial compression and extension tests. The aim of this is to show that the work done in Section 5.3 can be applied

to the modelling of a variety of soils in undrained shearing as well as one-dimensional compression.

5.4.1 Graham et al. (1983)

Graham et al. (1983) presented an undrained shear test conducted with step changes in strain rate on a natural sample of Belfast Clay. To undertake a simulation of this test, where the data was available to calibrate the model, such as the applied rates of straining it was used directly, but where such data was not available it was sourced elsewhere. The stiffness degradation curve was taken to be the same as that of London Clay. The duration of each test stage was back calculated from Figure 5.22(a). Table 5.3 gives details of the step changes in strain rate and Table 5.4 the BRICK parameters used.

Location of step changes in strain rate	
Strain rate (%/h)	Strain limit (% Axial strain)
0.5	6
Relaxation	-
0.5	7.8
5	10
0.5	12.5
0.05	13.5
5	15.8
0.5	18
0.05	18.5
0.5	19
Relaxation	-
0.5	20

Table 5.3: SRS data from Graham et al. (1983)

Figure 5.22 shows a comparison between the stress strain curves presented in Graham et al. (1983) and those generated by the brick-led SRD model. It can be seen that generally the comparison is very good with similar behaviour during the step changes in strain rate being observed. This proves that the SRD model is able to recreate strain rate dependent behaviour in undrained shearing. The strain softening of the soil is not predicted well, although this is a product of the BRICK model rather than the SRD adaptation. The stress history of the Belfast clay was modelled by consolidating the soil to an effective vertical stress of 60kPa, then allowing it to swell back to the estimated

SRD model parameters used in Section 5.4.1		
BRICK parameter	Code name	Value
Initial strains	SN(NC)	[0, 0, 0, 0, 0, 0]
Initial stresses	SS(NC)	[2, 0, 0, 0, 0, 0]
Reference string lengths	SLr(NB)	$[4.2e^{-5}, 1.1e^{-5}, 2.1e^{-4}, 4.2e^{-4}, 1.1e^{-3}, 2.1e^{-3} 4.1e^{-3}, 0.011, 0.021, 0.04]$
Stiffness reduction	GGMAX(NB)	[0.92, 0.75, 0.53, 0.29, 0.13, 0.075, 0.044 0.017, 0.0035, 0]
Initial conditions	ZERO(2)	[0, 2]
Lambda*	λ^*	0.372
Kappa*	κ^*	0.054
Iota	ι	0.0041
Beta constants	BETA(2)	[4, 3]
Number of bricks	NB	10
Number of components	NC	6 - Full 3D (Triaxial testing)
Time decay constant	m	1.0386
Reference strain rate	$\dot{\varepsilon}_{\text{ref}}$	$1e^{-13}$/s
Viscous constant	β	0.1
Note: The string lengths are initially slack and the original position for all the bricks is the origin in strain space.		

Table 5.4: BRICK parameters for Graham et al. (1983) simulation

in-situ stress of 40kPa (the sample was taken from a depth of 4m and the water table was at the surface). This gives an overconsolidation ratio of 1.5 which lies within the range of 1.2-1.8 given by Crooks & Graham (1976). The viscous constant β (Table 5.4) was calibrated by an iterative approach, attempting to fit the observed behaviour. Currently this is the only way of assessing what the β value will be. The λ^* and κ^* values were back calculated from the data given in Crooks & Graham (1976) and are higher than those of London Clay. As already noted, the shape of the stiffness degradation curve was assumed to be the same as that of London Clay, although the magnitude of the strains for the reference string lengths were calculated with Equation 5.11 using the London Clay string lengths as the testing string lengths (SL_{test}) and an assumed strain rate of 0.5%/h for the testing rate ($\dot{\varepsilon}_{\text{test}}$).

Figure 5.23 shows the engaged tangential stiffness of the soil during the SRS tests, with a G_{max} of 12MPa being predicted for Belfast Clay. During the relaxation phases at

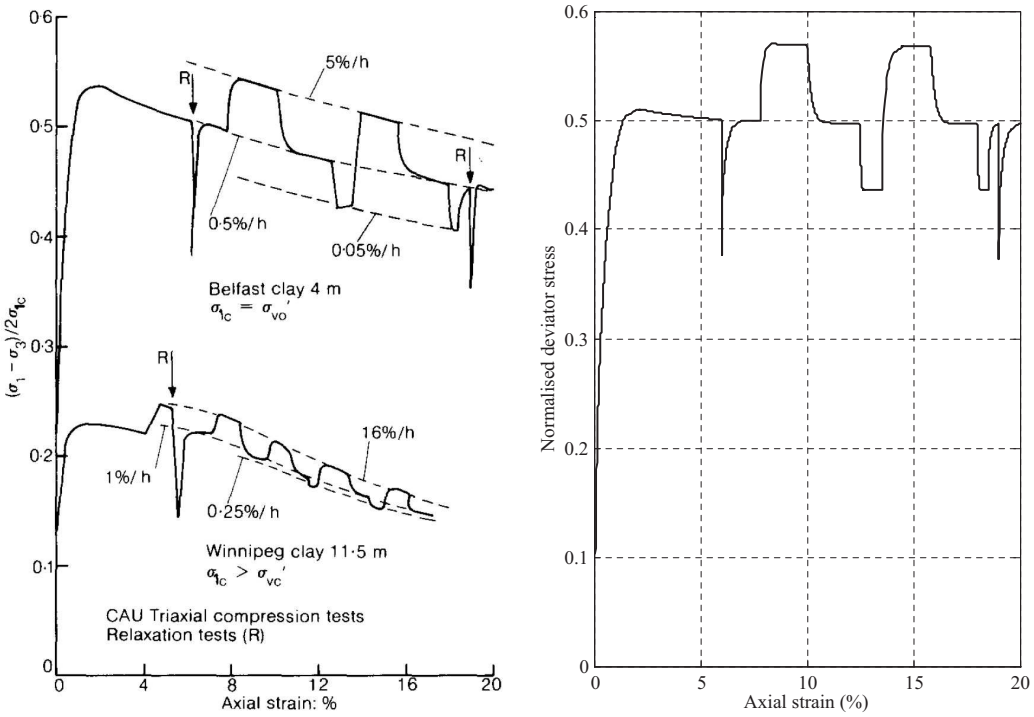

(a) Stress-strain curves for triaxial compression tests with step-changed strain rates and relaxation procedures

(b) Stress-strain curves generated by SRD model

Figure 5.22: Graham et al. (1983) comparison

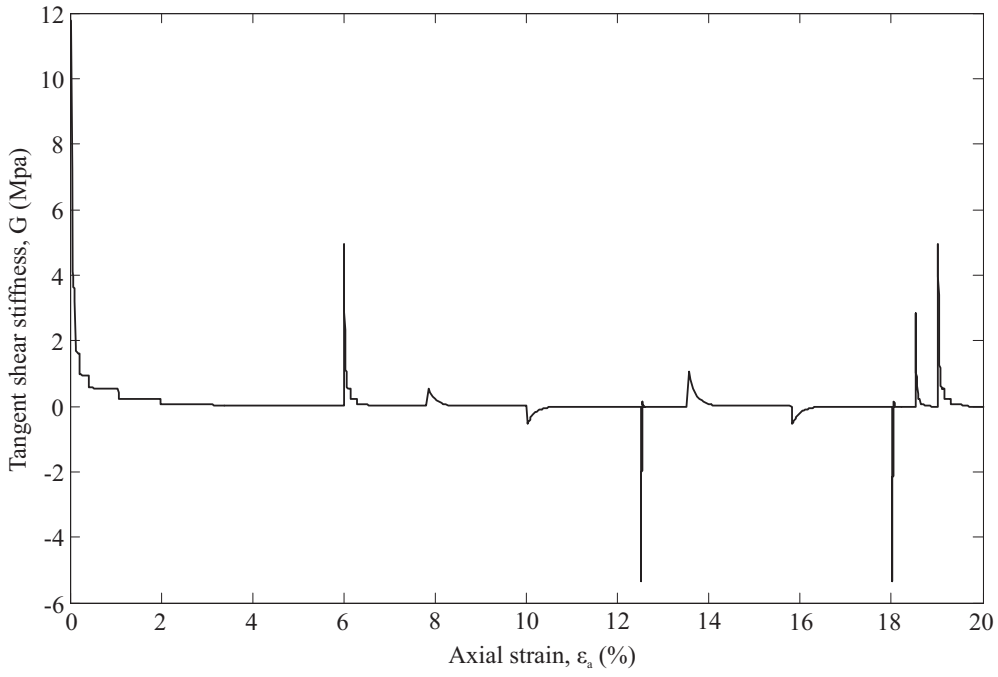

Figure 5.23: Stiffness developed during SRS tests

6% and 19% axial strain the soil regained 40% of its original stiffness over a relatively short stress relaxation period.

5.4.2 Gasparre (2005)

It was shown in Section 4.7 that the BOI time dependency implementation into the Brick model was able to recreate the trends shown in the Gasparre (2005) tests. As the brick-led SRD model combines the effects of time dependency with strain rate dependency, it too should be able to simulate the trends seen in Gasparre's work.

The SRD model needs more information about the strain rate dependency of London Clay than was presented in Gasparre (2005). The necessary information was taken from other sources, namely Sorensen (2006) and Sorensen et al. (2007a). To allow a set of parameters for the SRD model to be developed two sets of data need to be present, these being a SRS test showing the soil's susceptibility to strain rate effects and a creep or stress relaxation test over a stated time period to allow the time dependency and reference strain rate to be calibrated. The exact shape of the stiffness degradation curve in regard to the proportion of soil represented by each brick is not crucial. It has been shown by Sorensen et al. (2007a) that the magnitude of the viscous effects in both natural and reconstituted London Clay are the same even though their stiffness degradation curves have different shapes. This can be seen in Figure 5.24 where α defines the relationship between the axial strain rate, $\dot{\varepsilon}_a$, and deviator stress, q, in Equation 5.18 (Sorensen et al. 2007a), where A_s is a material constant.

$$\log(q) = \alpha \log(\dot{\varepsilon}_a) + A_s \tag{5.18}$$

Most of the SRS and CRS tests presented in Sorensen (2006) were conducted on reconstituted London Clay samples and hence the presence of TESRA behaviour (see Section 2.2.4) was unrepresentative of the behaviour of natural samples. There were however two tests conducted on natural London Clay using a SRS approach, these being tests S1LC and S2LC. The London Clay samples for test S1LC were taken from between 13.95m and 15.45m below ground level at the Heathrow Terminal 5 site. From Gasparre (2005) the unit weight of London Clay is 19.4kPa. This equates to an in-situ mean effective stress of between 283 and 303kPa for sample S1LC, assuming a K_0 value of 1.88 and the water table to lie at the surface of the London Clay layer at a depth of 6m. Sorensen estimated that the previous overburden pressure was around 2MPa. This gives the Brick model sufficient information to model the geological history of the

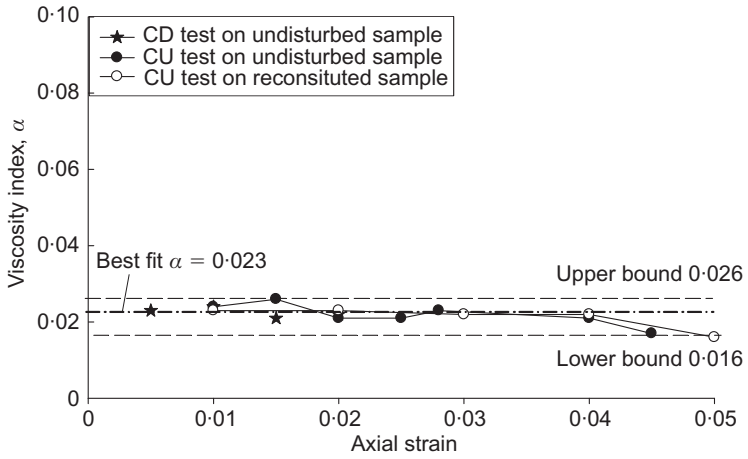

Figure 5.24: Viscosity index from tests on London Clay, Sorensen et al. (2007a)

sample in preparation for modelling the laboratory tests conducted on sample S1LC. Rather than model the test as a SRS test, CRS tests were simulated with the maximum and minimum strain rates to give the zone of possible effects. Figure 5.25(a) shows the pre-peak behaviour of sample S1LC during SRS tests and Figure 5.25(b) shows the bounding envelope generated by the SRD model. It can be seen that the two are very compatible. For the purposes of this test the viscous constant, β, was set to 0.23 which equates to a viscosity index, α, of 0.023 over the relevant stress range.

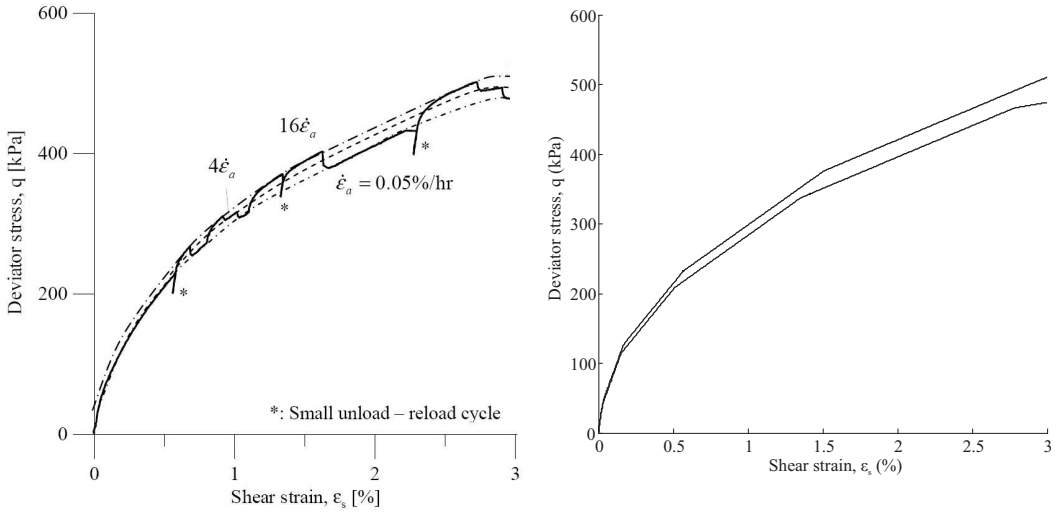

(a) Stress-strain behaviour during triaxial compression tests on London clay

(b) Stress-strain behaviour predicted by the SRD model

Figure 5.25: Sorensen (2006) test comparison

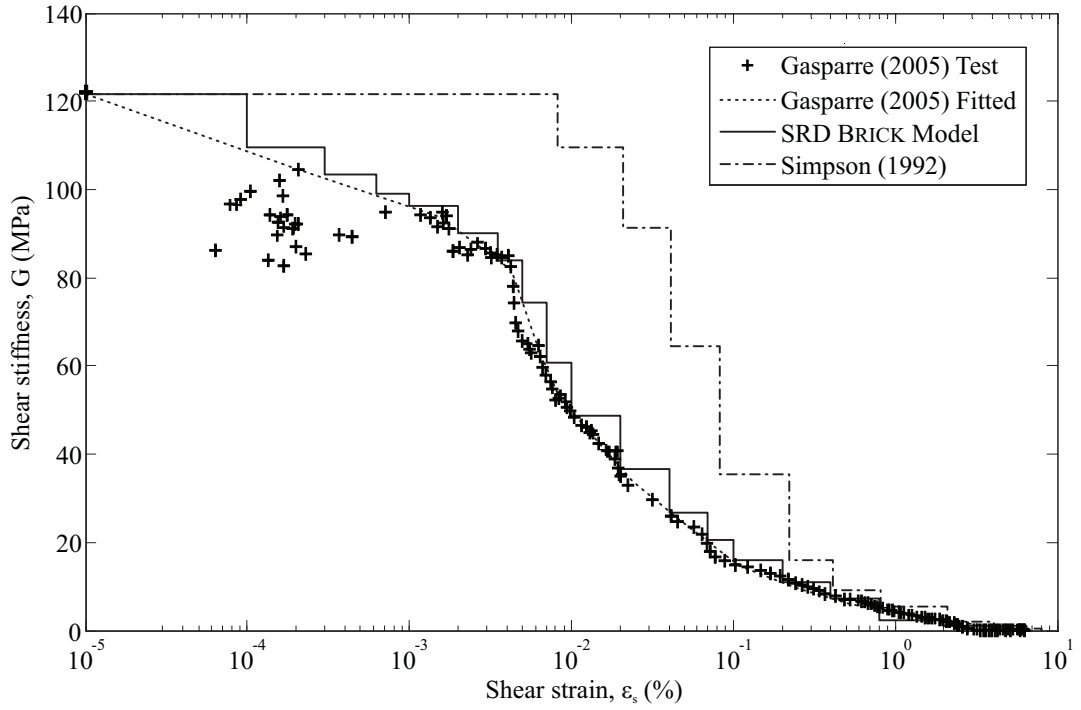

Figure 5.26: Fitting the BRICK parameters to Gasparre (2005)

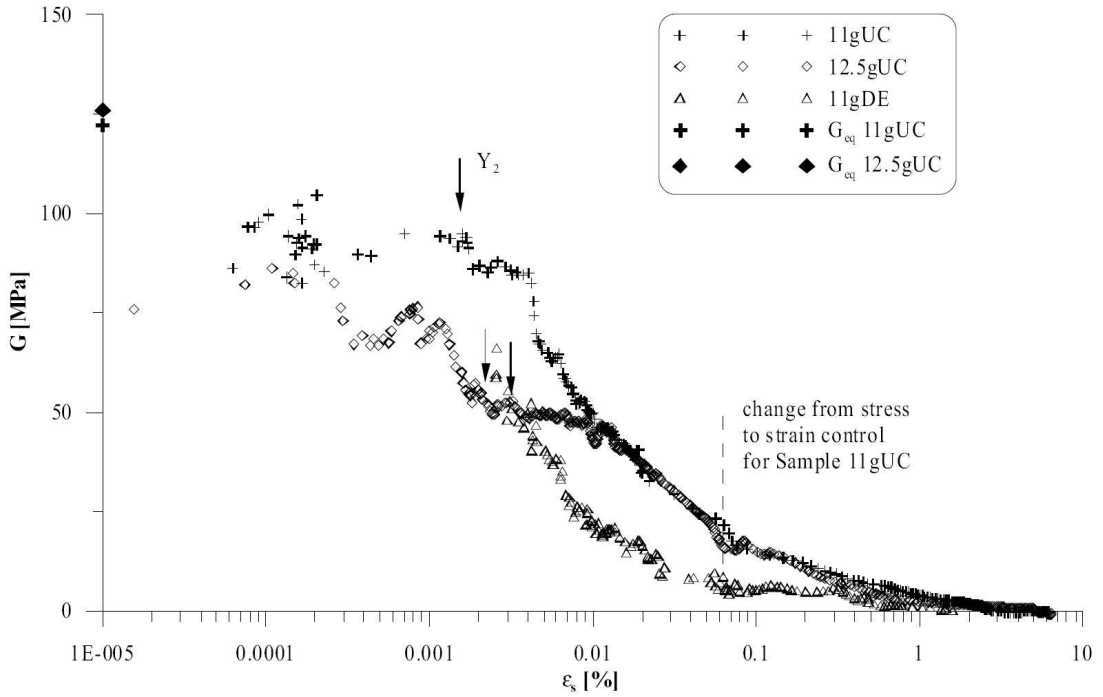

Figure 5.27: Stiffness degradation for samples from sub-unit B2(c) sheared from their in situ stress state, Gasparre (2005)

The stiffness degradation curve could be fitted directly to the stiffness degradation curve given in Gasparre (2005). Although the sample from which the curve was generated was not the same sample used for the stress path rotation test, it is from the same lithological unit (King 1981). A comparison between the string lengths for the original BRICK model (Simpson 1992b) and those used in the current modelling is presented in Figure 5.26. The stiffness degradation curve derived by Gasparre (2005) has also been included for comparison (see Figure 5.27). It should be noted that the number of bricks for the test was increased from 10 to 18 to give a smoother tangential stiffness degradation curve.

The time dependency parameter, m, was calibrated with the long term creep tests done by Bishop (1966) on natural samples of London Clay as seen in Figure 2.13 on page 17, which also shows that the gradient (m) is independent of the initial strain rate. Table 5.5 gives a list of all the parameters used when modelling the Gasparre tests. The testing sequence for each test was unchanged since it was modelled using the BOI approach, so the sequence can be found in Table 4.2 on page 105. The duration of the holding periods in Gasparre (2005) was variable, being dependent upon the measured strains in the sample. The tests involving creep were held for a number of days while those without creep were only held for three hours so as to keep the testing procedure the same as used by Atkinson et al. (1990).

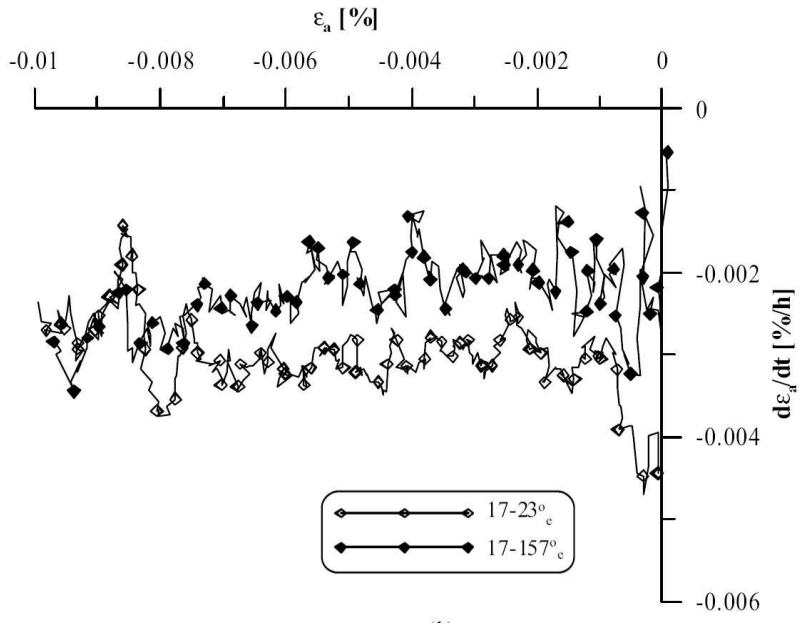

Figure 5.28: Strain rates for Sample 17SH during approach paths, Gasparre (2005)

SRD model parameters used in Section 5.4.2		
BRICK parameter	Code name	Value
Initial strains	SN(NC)	[0, 0, 0, 0, 0, 0]
Initial stresses	SS(NC)	[2, 0, 0, 0, 0, 0]
Reference string lengths	SLr(NB)	$[5e^{-7}, 1.5e^{-6}, 3.125^{-6}, 5e^{-6}, 1e^{-5}, 1.75e^{-5}, 2.5e^{-5}, 3.5e^{-5}, 5e^{-5}, 0.0001, 0.0002, 0.00035, 0.0005, 0.001, 0.002, 0.004, 0.01, 0.0323]$
Stiffness reduction	GGMAX(NB)	[0.9, 0.85, 0.815, 0.79, 0.74, 0.69, 0.61, 0.5, 0.4, 0.3, 0.22, 0.17, 0.13,0.09,0.06,0.02,0.009,0]
Initial conditions	ZERO(2)	[0, 2]
Lambda*	λ*	0.1
Kappa*	κ*	0.02
Iota	ι	0.0054
Beta constants	BETA(2)	[4, 3]
Number of bricks	NB	18
Number of components	NC	6 - Full 3D (Triaxial testing)
Time decay constant	m	1.0386
Reference strain rate	$\dot{\varepsilon}_{\text{ref}}$	$1e^{-13}$-/s
Test strain rate	$\dot{\varepsilon}_{\text{test}}$	$6.95e^{-8}$-/s
Viscous constant	β	0.23
Note: The string lengths are initially slack and the original position for all the bricks is the origin in strain space.		

Table 5.5: SRD BRICK parameters for modelling Gasparre (2005)

As brick-led SRD simulations are affected by the rate of straining, the rate at which the testing in Gasparre (2005) was conducted also needed to be known. Figure 5.28 plots the applied axial strain rate, $\dot{\varepsilon}_a$, for increasing axial strain, ε_a. As the brick-led SRD model has a logarithmic relationship to strain rate, the variation in the plots shown in Figure 5.28 would have little effect on the string lengths. If the plots were replotted on a log scale of strain rate, the variation would be negligible. The applied axial strain rate, $\dot{\varepsilon}_a$, was taken to be -0.0025%/h. Applying Equation 5.11, the string lengths from the stiffness degradation plots shown in Figure 5.26 could be converted to the reference values to account for the effects of strain rate as follows:

$$\begin{aligned}
\frac{\mathrm{SL_{test}}}{\mathrm{SL_{ref}}} &= 1 + \beta\, ln\left(\dot{\varepsilon}_{\mathrm{test}}/\dot{\varepsilon}_{\mathrm{ref}} + 1\right) \\
\frac{\mathrm{SL_{test}}}{\mathrm{SL_{ref}}} &= 1 + 0.23\, ln\left((0.0025/(100 * 60 * 60))/1e^{-13} + 1\right) \\
\frac{\mathrm{SL_{test}}}{\mathrm{SL_{ref}}} &= 3.564
\end{aligned} \tag{5.19}$$

The λ* and κ* values were taken directly from the BRICK model as presented in Simpson (1992b) but, as the Iota value affects the maximum predicted stiffness of the soil, it was changed to fit the maximum stiffness seen in the Gasparre (2005) tests shown in Figures 5.26 and 5.27.

Short approach path with the effects of creep (17SH)

These were the first stress history tests run by Gasparre (2005) and aimed to investigate the results shown by Clayton & Heymann (2001), with the stress history effectively being erased by the effects of creep, Figure 5.29. The modelling procedure was the same as stated in Section 4.7 (see Table 4.3 on page 108). The modelling of the geological stress history was done without modelling viscous effects as, due to the large times involved, the effects of creep, if modelled, would lead to the string lengths relaxing back to their shortest values. It is with these short string lengths that the geological history was modelled. The laboratory testing was done at a constant rate of strain as stated in Table 5.5.

The holding period conducted in the 17SH tests was modelled as a period of creep, with the string lengths shortening with increasing time. After a period of straining, in normal circumstances the strings attached to bricks that were previously moving are still taut in the next increment. With the effects of creep shortening the string lengths and thus moving the bricks, when the man continues to move the strings lengthen again and the response of the soil is initially elastic. The response is stiffer than the plastic response that would have occurred had it not being for the holding period.

The tangential stiffness, G, was plotted against shear strain, ε_s, Figure 5.30, for comparison with the experimental data, Figure 5.29. The approach paths were followed in both compression and extension directions before the stiffness was measured during the extension undrained shearing stage. Figure 5.30 shows that the brick-led SRD model can successfully simulate the erasing of the recent stress history by creep. This is shown

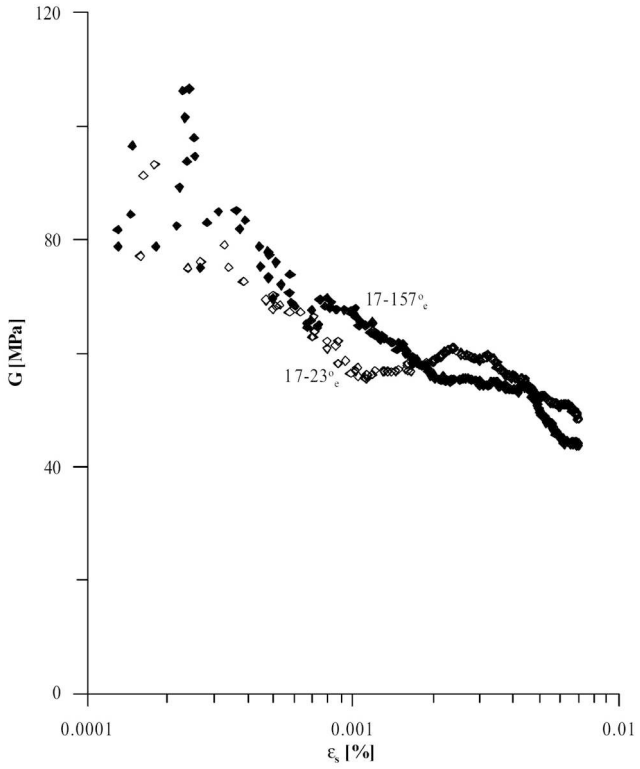

Figure 5.29: Shear stiffness during the undrained shear tests on sample 17SH, Gasparre (2005)

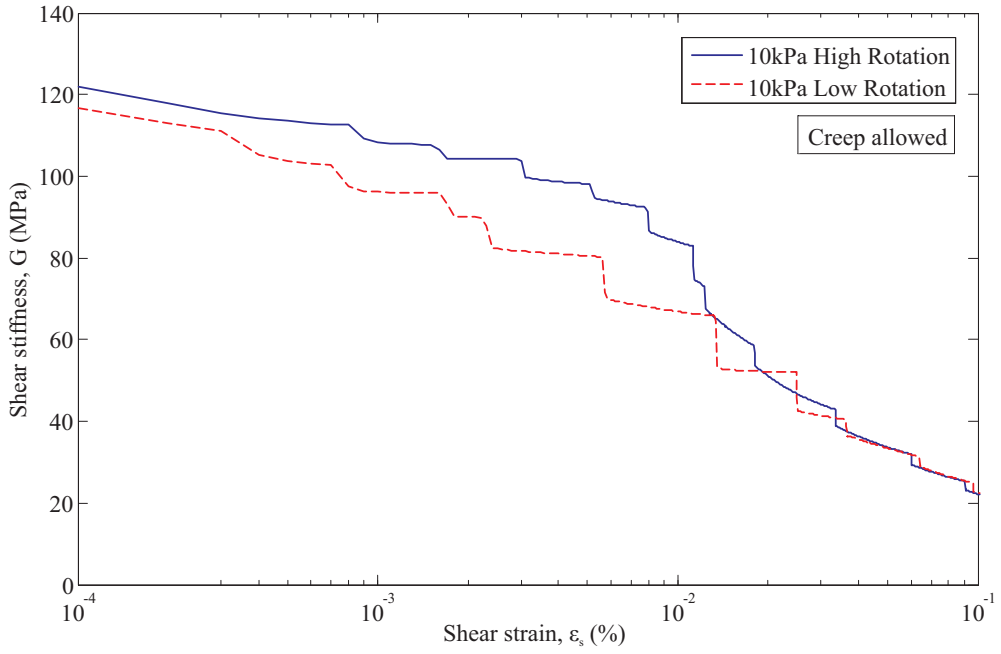

Figure 5.30: Stiffness degradation following 10kPa approach paths with creep allowed

in both the initial stiffness and in the close match of the curves in Figure 5.30. The predicted stiffness is now independent of the stress path rotation as shown by Clayton & Heymann (2001) (see Figure 2.10 on page 13).

Short approach path without the effects of creep (17.3SH)

The second test run by Gasparre (2005) was designed to confirm that the equal stiffnesses during the 17SH tests were due to the effects of creep. The detailed simulation procedure is contained in Table 4.4 on page 111. It was mentioned in Section 4.7.3 that the two sets of tests, 17SH and 17.3SH, were not conducted under exactly the same conditions. For the purposes of the current modelling a direct simulation of the 17.3SH tests has been completed using the data in Table 4.4. The 17.3SH tests involve a short approach path as in the 17SH tests, but without the holding period to allow for the occurrence of creep. The 17.3SH tests were able to recreate the results shown in Atkinson et al. (1990) where a period of rest was not allowed and the stiffness measured was dependent on the rotation of the stress path (see Figure 2.8 on page 11).

The results generated by Gasparre (2005), Figure 5.31, show the degree of rotation in the stress path acting to control the measured stiffness. The results of the simulation of the 17.3SH tests are shown in Figure 5.32. It can be seen that the initial stiffness agrees with the trends shown in the physical test results. The scatter in Figure 5.31 makes the plot harder to interpret but the separation of the plots for the high and low rotation tests is clearly visible down to $1e^{-3}\%$, at which point the scatter becomes too great to draw any clear conclusions. The amount of strain required to cause a marked drop in stiffness also agress well between the numerical and physical modelling, about 0.005% in both cases. The simulation results also agree well with the trends seen in Atkinson et al. (1990). Due to the lack of a holding period, upon the continued straining in the same direction (low rotation) the Y_1 yield surface is already engaged giving a lower stiffness.

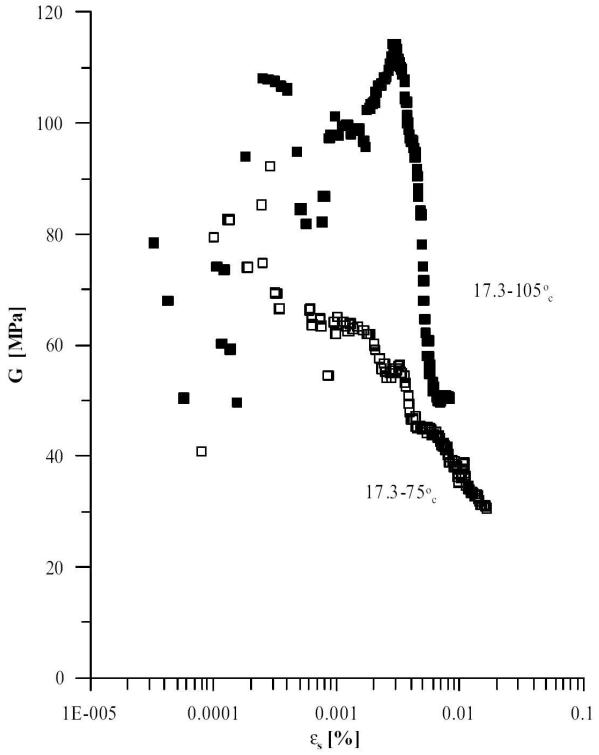

Figure 5.31: Shear stiffness for the undrained shear test on sample 17.3SH, Gasparre (2005)

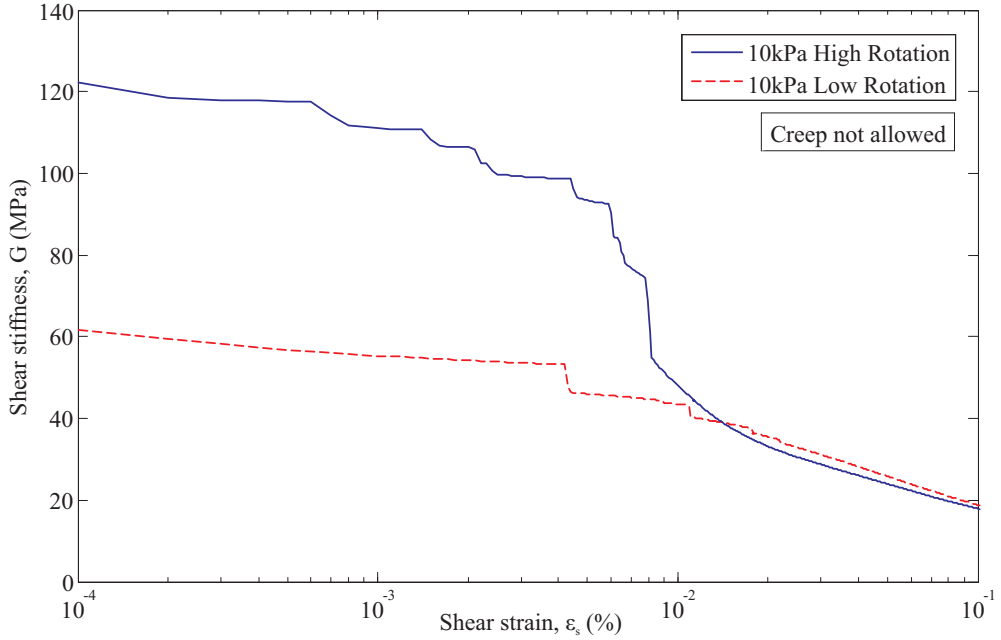

Figure 5.32: Stiffness degradation following 10kPa approach paths with no creep allowed

Long approach path with the effects of creep (17.3SH-L)

The final tests run by Gasparre (2005) were designed to investigate the effects of creep after a long approach path. In the 17SH and 17.3SH tests the approach paths were always within the Y_2 yield surface with applied stress deviations of 10kPa. For the 17.3SH-L tests the approach paths were 100kPa long, allowing the soil to engage the Y_2 yield surface. The simulation procedure is contained within Table 4.5 on page 115 and the experimental results are shown in Figure 5.33. The effects of creep can be seen in the relatively high stiffness for the low rotation test, which is much higher than the stiffness seen in the 17.3SH tests without the effects of creep. In the short approach path tests with creep (17SH) the degradation in stiffness was similar in both high and low rotation cases. This is due to the persistent effect of the geological stress history, with the recent approach paths not being of sufficient magnitude to erase these effects. When the same tests are run with long approach paths (17.3SH-L) it can be seen that the magnitude of the approach paths was sufficient to erase much of the geological stress history, leading the soil to show different stiffness degradation curves depending on the rotation of the path while at the same time showing a high initial stiffness due to the effects of creep.

The simulation results are shown in Figure 5.34. It can be seen that the initial stiffnesses match the physical results reasonably well, allowing for the scatter in the physical test results. Similar degradation trends are evident in both the physical and numerical tests.

5.4.3 Comparing the SRD model with Bricks on Ice

The tests conducted by Gasparre (2005) have now been simulated using both the SRD and Bricks on Ice (BOI) models. This section directly compares the simulation results to assess the effect of changing the model.

In the 17SH tests with the inclusion of the holding period after a short approach path, the physical tests results showed that creep can erase the effects of the recent stress history, with both high and low rotation paths showing a similar initial stiffness (Figure 5.29). This pattern of results was simulated very well by the BOI model with both rotations showing very similar initial stiffnesses (Figure 5.35), although the low rotation path (LR) shows a higher initial stiffness than the high rotation stress path (HR), which is incorrect. The SRD Brick model results showed all the features seen in the physical testing. The initial stiffnesses for the high and low rotation tests were very

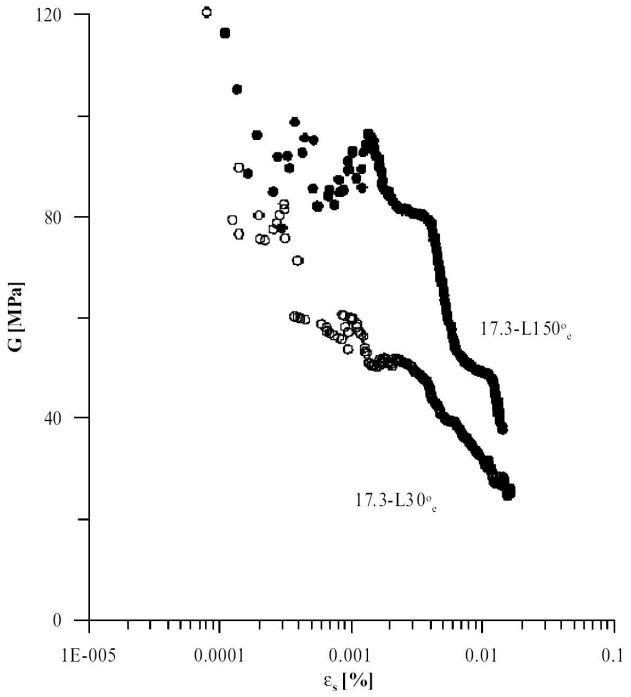

Figure 5.33: Shear stiffness during the undrained shear tests on sample 17.3SH-L, Gasparre (2005)

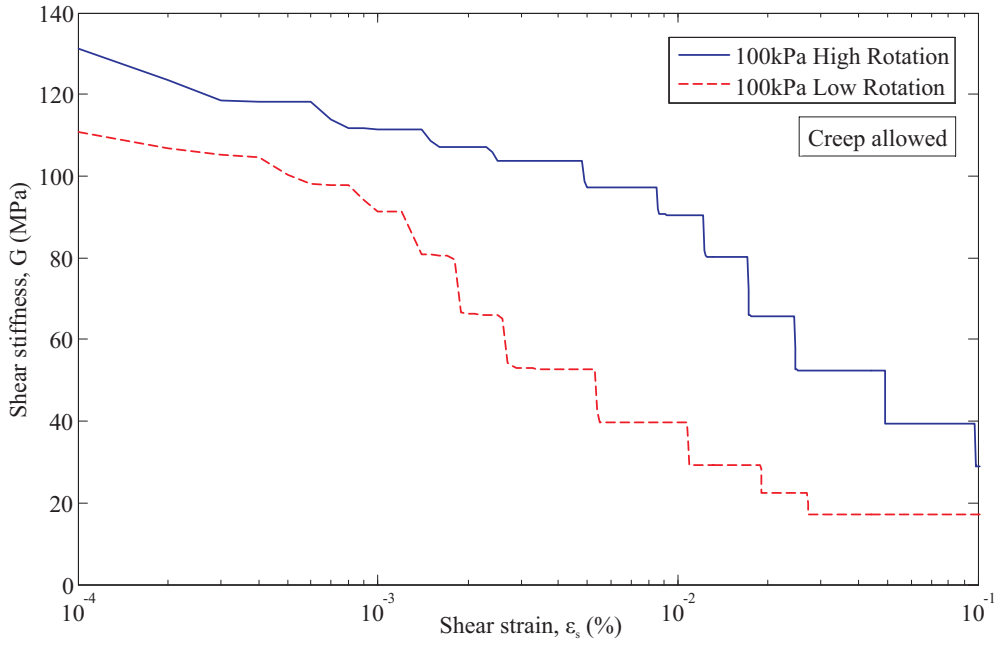

Figure 5.34: Stiffness degradation following 100kPa approach paths with creep allowed

similar to each other (Figure 5.35), but the high rotation test gave a marginally higher stiffness, which can be seen in the physical test results. The stiffnesses at intermediate strains were generally very similar but with a marginally higher stiffness in the high rotation test. Overall, the reduction in stiffness showed a very close correlation between the numerical and physical results, being roughly a fifty percent reduction in stiffness over the range of strains in the physical test (about 0.007%). The BOI model gave a slightly better prediction of this drop in stiffness, but the predictions made by the SRD Brick model were more accurate at small strains.

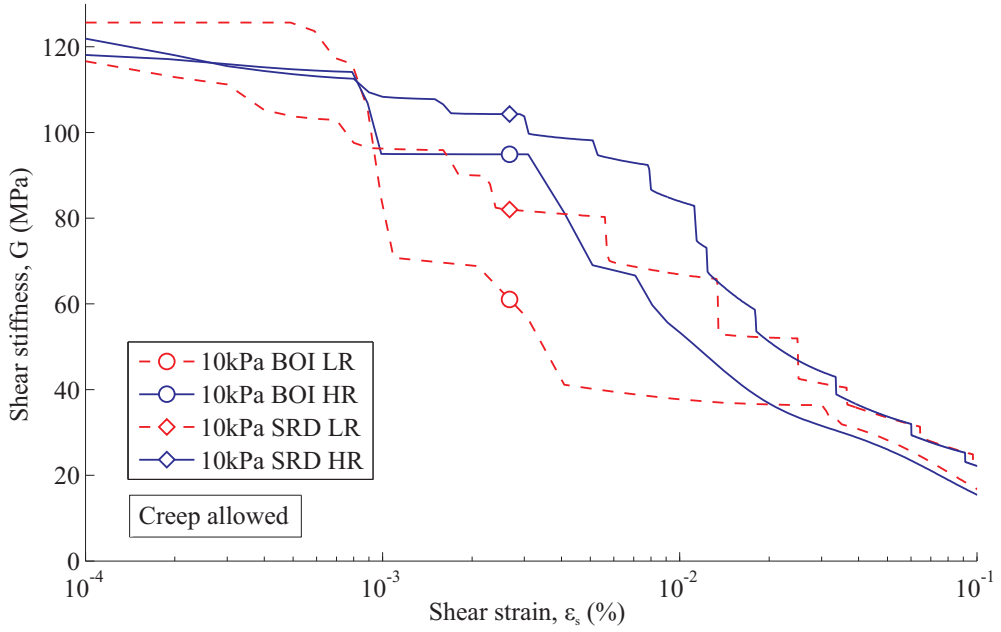

Figure 5.35: Comparison of SRD and BOI models for short approach path tests with creep

In the 17.3SH tests the degree of rotation directly affected the initial stiffness, with the high rotation path showing a higher initial stiffness and the low rotation stress path demonstrating an approximately 50% lower initial stiffness (Figure 5.31). Both the BOI and SRD models were able to simulate the 50% reduction in initial stiffness seen in the physical results, as well as the subsequent higher stiffness path seen in the high rotation test (Figure 5.36). The results would be expected to be similar for both numerical models as creep is not present.

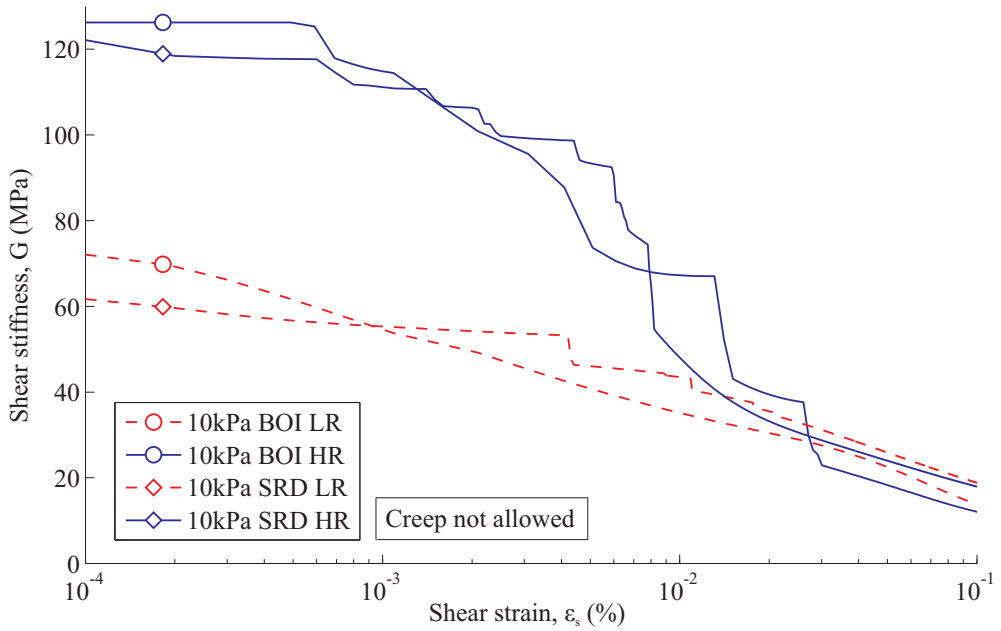

Figure 5.36: Comparison of SRD and BOI models for short approach path tests without creep

The 17.3SH-L tests, with the long approach paths and a holding period to allow for the effects of creep, showed again the high initial stiffness in the low stress path rotation test due to the presence of creep (Figure 5.33). The intermediate strain behaviour demonstrated the persistent effects of the stress history with the low rotation test exhibiting a consistently lower stiffness than the high rotation test. In the modelling done with the BOI model these trends were recreated, but with a much more severe drop in stiffness during the low rotation test (Figure 5.37). This was thought to be due to the long approach stress path developing much of the available stiffness for the low rotation test prior to the holding period. Thus after the initial high stiffness has been utilised, the stiffness drops rapidly to the large strain stiffness. The low rotation test also generated a higher initial stiffness than the high rotation test, seen previously in Figure 5.35. The SRD Brick model managed to successfully predict the correct arrangement of initial stiffness, with the stiffness degradation occurring more rapidly in the low rotation test than in the high, as seen in the physical tests.

It is clear from the SRD and BOI model simulations that creep can be a major factor in determining the small strain stiffness response of a soil. The effects of short approach stress paths can be completely erased by the effects of creep, leaving the creep to govern the small strain stiffness and the geological stress history to determine the

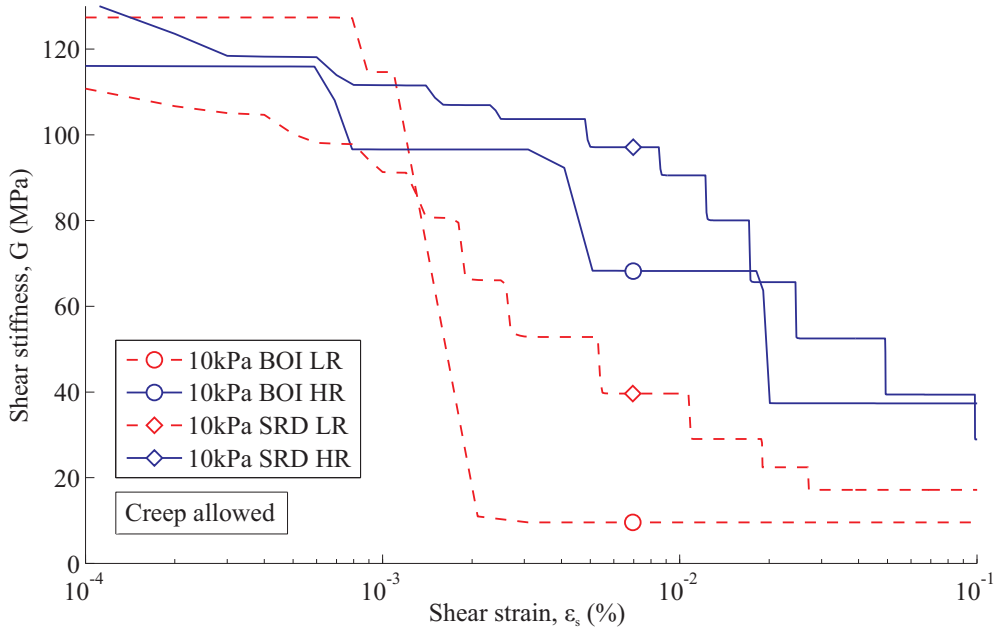

Figure 5.37: Comparison of SRD and BOI models for long approach path tests with creep

intermediate and large strain stiffnesses. Whilst both the SRD and BOI models can generate the trends seen in the physical tests, the SRD model generally gives more accurate predictions, especially in the small strain region.

5.5 Discussion

The SRD Brick model represents a clear improvement in the modelling of strain rate and time dependent effects over the BOI model. The SRD Brick model is able to deal with both isotach strain rate behaviour and time dependent effects such as creep and stress relaxation through the implementation of the newly developed rate dependency framework.

Prediction of the results presented by both Graham et al. (1983) and Gasparre (2005) shows that the model can not only predict SRS behaviour but also the effect of creep on the recent stress history. The results of the simulation of the Gasparre (2005) tests show that the SRD Brick model can successfully predict the increase in initial stiffness due to the effects of creep on low rotation stress path tests, shown by Gasparre et al. (2007) and Clayton & Heymann (2001). The model is also able to predict the usual effect of the recent stress history, with the rotation of the stress path having a direct

effect on the predicted initial stiffness of the soil, as shown by Gasparre et al. (2007) and Atkinson et al. (1990).

In previous investigations into the recent stress history, the predicted stiffness has always been stated as being dependent upon the rotation in the stress path. Although this is true, it can also be related to a rotation of the strain path in strain space. In the tests done by Gasparre (2005) the approach paths were obviously stress controlled. To generate a constant p' stress path in the Brick model, the main component of strain is shear strain, with small increments of volumetric strain being required to compensate for the plastic volumetric strains generated by the bricks. The final triaxial extension or compression stages in both the physical tests and numerical simulations are strain controlled so that the rotation in the strain path would always be approximately 0° or 180°. The stress path rotations applied, under strain control, in Gasparre (2005) would also correspond to approximately 0° and 180° rotations in the strain path, with little or no variation between tests.

6

Finite Element Modelling

6.1 Introduction

As a constitutive model for soil, BRICK describes the behaviour of soil given an applied change in strain. If a constitutive model, such as BRICK, is to be of use in the analysis of engineering problems it must be first implemented into a finite element program, such as SAFE. Unlike the classical methods of geotechnical analysis, limit analysis and limit equilibrium, the finite element method is capable of satisfying the requirements for a full theoretical solution. These requirements are: equilibrium, compatibility, the material constitutive model, and boundary conditions (both force and displacement). Finite element analysis is capable of solving complex geotechnical problems by discretising the soil domain using a mesh. The discrete areas are known as finite elements and, for a two-dimensional analysis, they can be either triangular or quadrilateral in shape (SAFE uses a quadrilateral mesh).

In this chapter the SRD BRICK model is implemented into the finite element program, SAFE. The implementation is then benchmarked against an equivalent MATLAB analysis to check the model has been implemented correctly. Two case histories are then analysed using the implemented SRD BRICK model. The first is the construction of the westbound running tunnel, part of the Jubilee Line extension, at St James's Park, London. The second is the construction and long term heave monitoring of a deep basement in Horseferry Road, London.

6.2 Implementation into SAFE

The first stage in implementing the new SRD BRICK model in SAFE was to get it running correctly within the ARUP BRICK program. This program essentially reproduces the calculations necessary at a single gauss point in a full finite element analysis.

BRICK does not have the capability to deal with pore water pressures. Rather it is designed to emulate in effective stress terms the tests done on a soil specimen in the laboratory so that the correct parameters can be chosen for the BRICK model. The details of the implementation of the SRD BRICK model into the BRICK program can be found in Appendix C.

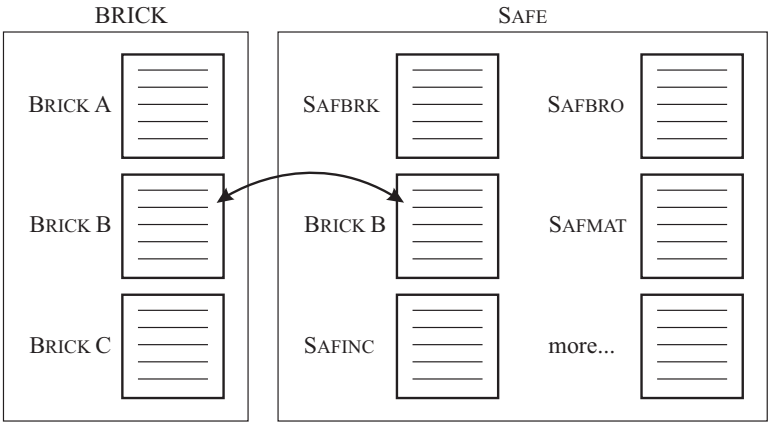

Figure 6.1: Implementation of the SRD model into SAFE

One of the advantages of using the BRICK program and SAFE applications in combination is that the BRICK code can be input directly into SAFE by copying across the BRICKB module, Figure 6.1. As was explained in Section 3.5, BRICKB is the heart of the BRICK program, with the remaining code simply passing variables to the routine. The main difference between the formulation of the strain rate dependency model in SAFE and the BRICK program concerns the storage of the variables between increments. Because the BRICK program is only doing calculations for a single point in the soil, the storage of variables between increments is relatively easy as they can be passed directly back to BRICKA for use in the future. In SAFE the variables need to be saved for every gauss point which means that a much more complicated system of storage needs to be implemented. The BRICK program also has no concept of time natively, so constant rate of strain tests have to be done by keeping the increment size constant. SAFE on the other hand is able to cope with a direct input of time for each increment. A detailed account of the features of SAFE can be found in Oasys (2006) and further information on the implementation of the BRICK model into SAFE can be found in Appendix D.1.

6.3 Model Validation

Before the results generated by a finite element analysis can be treated as reliable, testing should be completed to ensure that the constitutive model employed is functioning correctly with a simple analysis. For SAFE, the simplest test involves a single element with four gauss points. Running a model of this form tests its ability to converge on a single solution, thereby checking whether the constitutive model is stable.

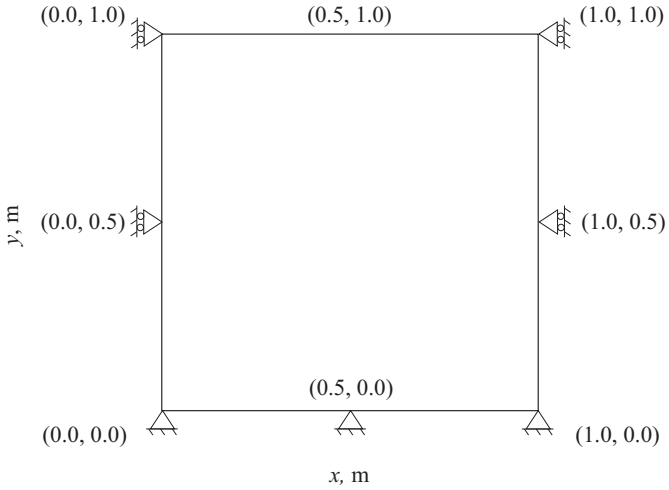

Figure 6.2: Single finite element

An element measuring 1m x 1m was used to test the effects of both strain rate and time. The element is shown in Figure 6.2; the nodes are located at the mid-point of each edge and the corners. It can be seen that boundary conditions have been specified on 3 sides, with the base being fixed in both x and y directions and the sides being fixed only in the x direction. For the material assigned to the element, the properties of London Clay have been used and are given in Table 6.1, with the string lengths being those from Kanapathipillai (1996). The Y-Coord parameter represents the intercept of

BRICK parameters used in Section 6.3

Description	Theory	λ^*	κ^*	ι	ν	β_G	β_ϕ	n	G_{vh}/G_{hh}
London Clay	2	0.1	0.02	0.0019	0.2	4	3	1	1

Description	Consolidation parameters			Mu	Iteration tolerance	Max first strain inc.
	Type	Y-Coord (m)	Gamma Gd (kN/m^3)			
London Clay	1D	1.143e^6	1.4e^{-4}	1.3	0.01	0.001

Table 6.1: Soil parameters for London Clay - single element analysis

the vertical effective stress gradient with the y-axis. In normal tests this would give an indication of whether the soil was overconsolidated. The Gamma Gd parameter is the unit weight of material for calculating the pre-consolidation pressure which was 160kPa for the current test. For this single element the Y-Coord is set to a very large value and Gamma Gd to a very small value, giving little variation of the pre-consolidation pressure vertically through the element.

A downward vertical displacement of 50mm was applied to the nodes along the top of the element, and the vertical effective stress was recorded at each gauss point. The decay constant, m, for all SRD BRICK tests was set to 1.0386, with a reference strain rate, $\dot{\varepsilon}_{\text{ref}}$, of $1e^{-13}$/s. The values of the viscous constant, β, and the time increment, t, are specified along with the results in Figure 6.3. Figure 6.3(a) shows the predicted

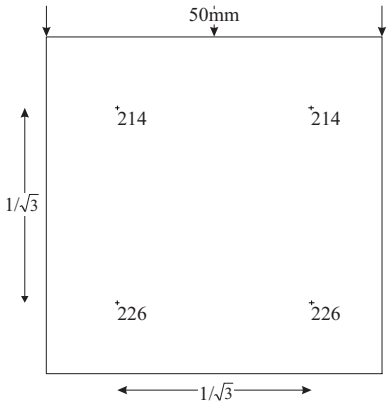

(a) Stresses using BRICK

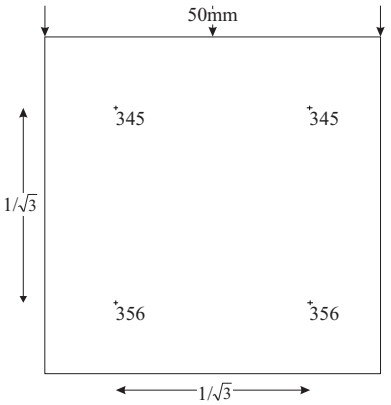

(b) Stresses using SRD BRICK t=1day, β=0.1

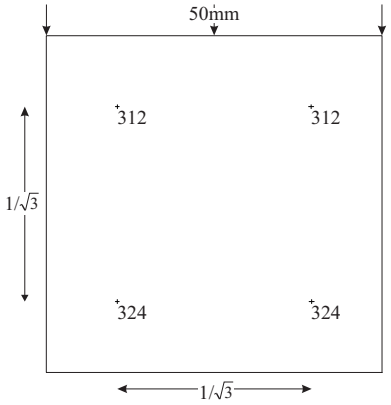

(c) Stresses using SRD BRICK t=10 days, β=0.1

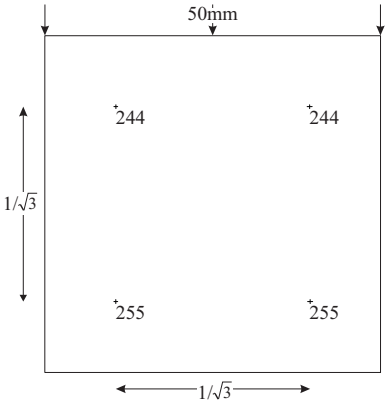

(d) Stresses using SRD BRICK t=1 day, β=0.023

Figure 6.3: Single element test result comparison

vertical effective stresses after the applied displacement for the BRICK model. The reference string lengths in the SRD BRICK model were set to the same lengths as those in the BRICK model to allow a direct comparison of the results. Figure 6.3(b) shows higher stresses due to the effects of the SRD model. Upon an increase in time, the predicted stresses are lower, Figure 6.3(c). Changing the viscous constant to a lower value also acts to lower the predicted stresses, Figure 6.3(d), these being below those in Figure 6.3(b) but above those predicted by the BRICK model. The results show that the SRD model is functioning as expected within the SAFE finite element program, but the accuracy of the results also needs to be checked. The only way to check the accuracy of the results it to compare them to an equivalent MATLAB analysis.

Both the MATLAB and SAFE analyses have been run using the 6 component BRICK model, so the easiest calculated stresses to compare are those of mean effective stress, p', which can be directly extracted from the SAFE analysis for any gauss point. To obtain equivalent results as those from SAFE, the MATLAB analysis had to run through the same stages. This included the initialisation stage which establishes the stress history. In this stage a vertical effective stress, σ'_v, of 160kPa was applied to the soil followed by swelling back to the in-situ stress ($p' = 20.9$kPa). In the MATLAB analysis the soil was subjected to a σ'_v of 160kPa using Equation 6.1 to monitor the increase in σ'_v. This equated to a p' of 112.5kPa and a shear stress, t_y, of 41.1kPa.

$$\sigma'_v = p' + \frac{2t_y}{\sqrt{3}} \tag{6.1}$$

The results of the comparison are shown in Table 6.2, where it can be seen that the SAFE results and the predictions by MATLAB lie within 1% of each other. The top left hand gauss point was considered for the purposes of the comparison.

Stage	SAFE p' (kPa)	MATLAB p' (kPa)	Difference (%)
Initialisation	20.9	20.8	-0.48
50mm displacement applied			
BRICK prediction	161	162.48	0.92
SRD BRICK, $t = 1$ day, $\beta = 0.1$	236	233.69	-0.98
SRD BRICK, $t = 10$ days, $\beta = 0.1$	217	216.93	-0.03
SRD BRICK, $t = 1$ day, $\beta = 0.023$	179	177.47	-0.85

Table 6.2: Verification of single element test

Such a close agreement, even though BrickB is sitting in a much more complex environment, gives a large amount of confidence in the results. The changes to the convergence of the Brick model that have been implemented into Safe, but not into the simplified Matlab version, could account for the small discrepancies seen between the results. From this comparison it can be concluded that the SRD Brick model is functioning correctly in Safe.

6.4 Case History 1: Jubilee Line Extension

The Jubilee Line extension was one of the largest tube expansions in central London in recent years. The new lines passed under sensitive existing buildings, justifying the inclusion of a wide range of monitoring techniques within the construction contract. This enabled the monitoring of building settlements for safety purposes, with a secondary purpose of providing high quality data for use in numerical modelling. One of the most interesting cases was the construction of the twin running tunnels beneath St James's Park, a greenfield site where the surface displacements were carefully monitored (Nyren et al. 2001). From previous tunnel constructions a conservative estimate of 2% was adopted for the design volume loss (Standing & Burland 2006). North of the lake in the park volume loss was below 2% as expected, but south of the lake the volume loss was up to 3.3% (Nyren et al. 2001). Volume loss is defined as the volume of the settlement trough measured at the surface divided by the volume of the tunnel, Equation 6.2 (Mair 2008).

$$V_l = \frac{V_s}{\pi D^2/4} \tag{6.2}$$

where:

V_l = volume loss for defining tunnelling efficiency (%),
V_s = volume of transverse settlement trough per metre length of tunnel (m^3/m),
D = diameter of tunnel (m).

The soil profile shown in Figure 6.4 consists of four distinct beds, the upper-most of which is a 4.5m thick layer of Made Ground / Alluvium, overlying a 2.7m thick bed of Terrace Gravel. Underneath lies a 34.3m thick layer of London Clay, overlying the very stiff Woolwich and Reading Clay beds. The tunnels themselves have a 4.85m external diameter with a 200mm thick expanded precast concrete segment lining (Dimmock & Mair 2007). The fact that the section of the westbound running tunnel south of the lake experienced the greatest volume loss was possibly a product of the lower than usual

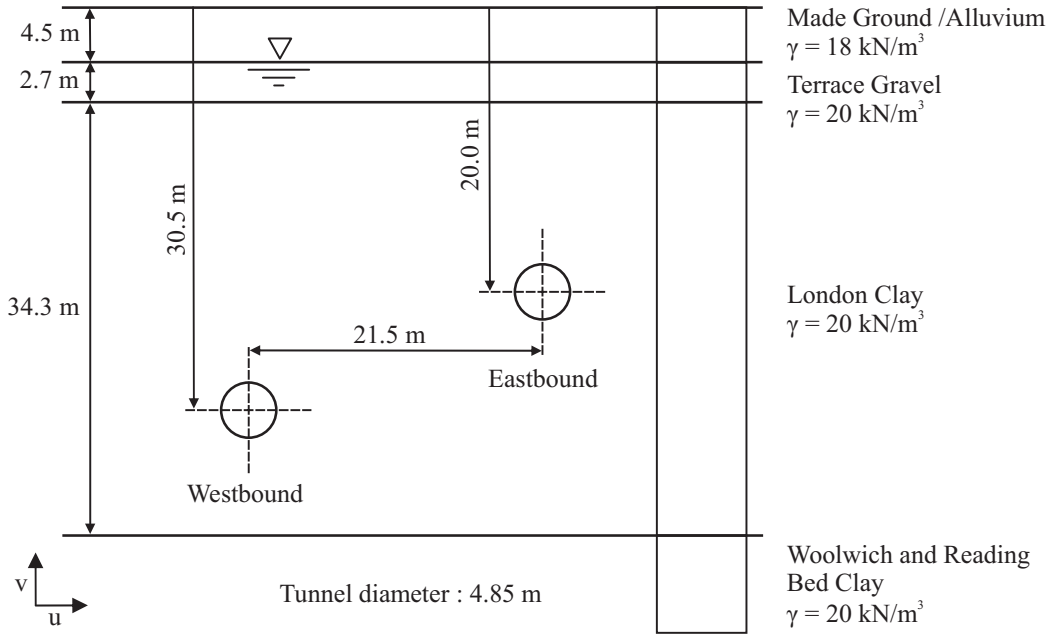

Figure 6.4: Soil profile and tunnel geometry at St James's Park, after Addenbrooke et al. (1997)

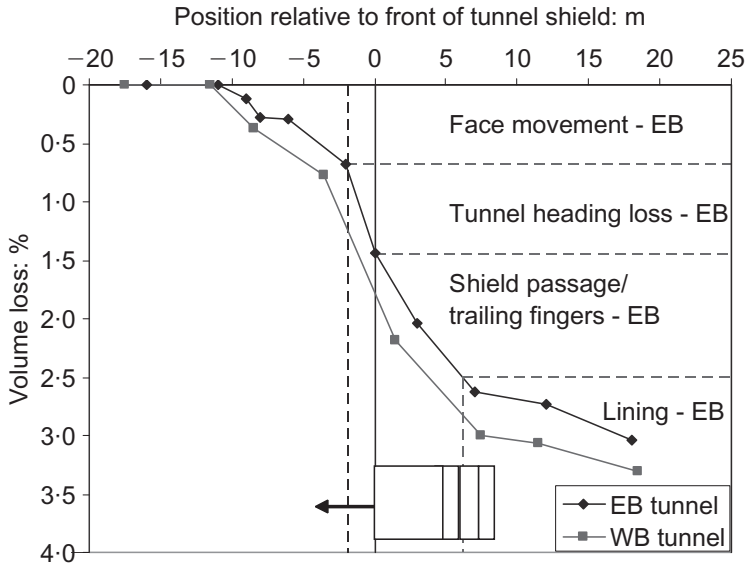

Figure 6.5: Progression of volume loss at St James's Park, Dimmock & Mair (2007)

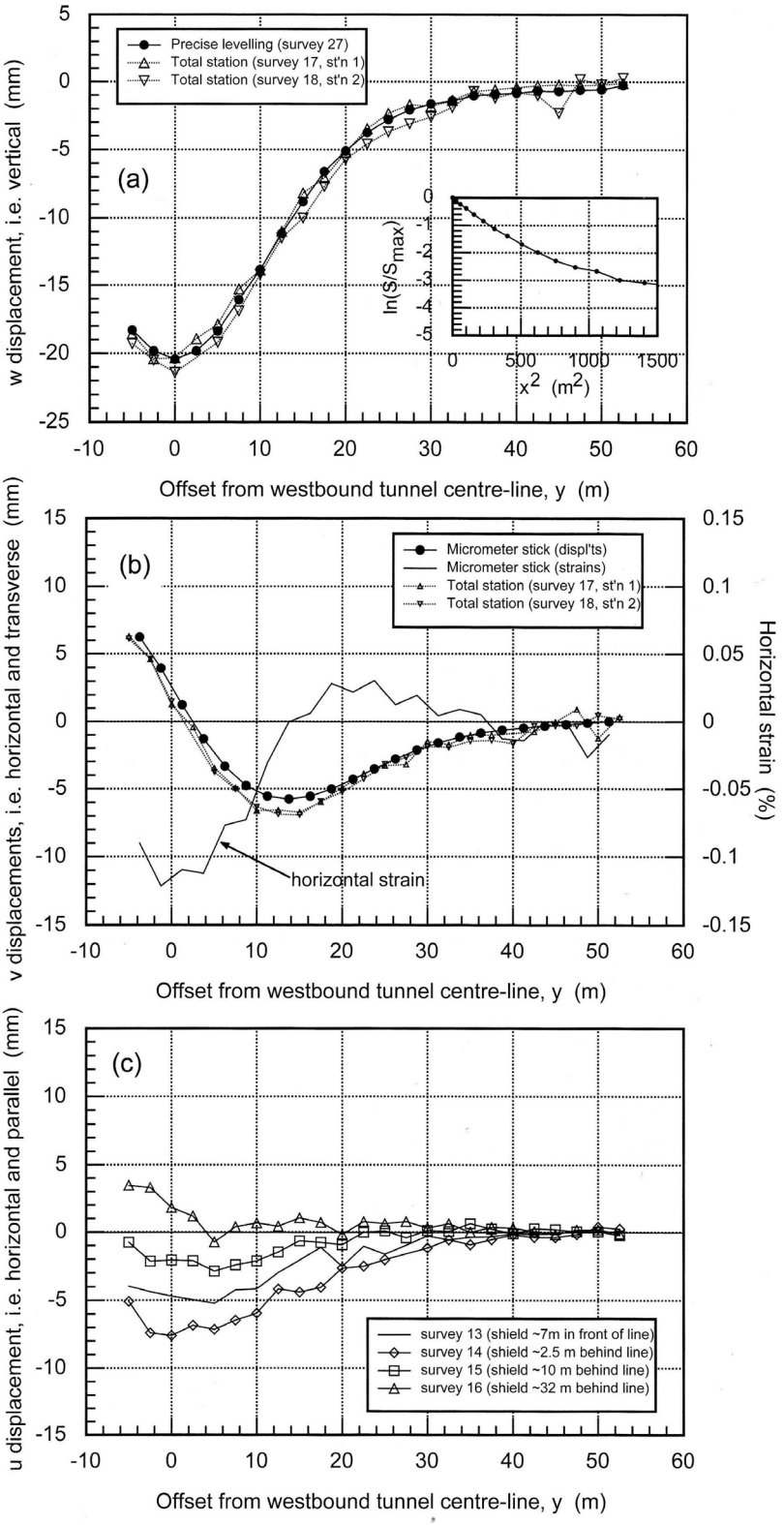

Figure 6.6: Monitoring data from the St James's Park twin tunnels, Nyren et al. (2001)

undrained strengths, varying permeabilities and the very rapid rate of advance of the tunnel face (45m/day), (Nyren et al. 2001). The entire 3.3% volume loss experienced was assumed to be due to the extraction of material at the tunnel boundary, the progression of this loss being shown in Figure 6.5. It can be seen that 55% of the total volume loss was experienced before the face of the tunnel boring machine (TBM) passed the instrumented section. A further 35% of the volume loss was attributed directly to the shield passage and the remaining 10% to the installation of the lining. The surface displacement plots from Nyren et al. (2001) have also been included for comparison with previous and current work, Figure 6.6.

6.4.1 Previous work

The unexpected volume loss experienced made the St James's Park twin tunnels an interesting case to model. Thus much work has gone into attempting to predict the shape of the settlement trough based on the known volume loss. The first authors to model the St James's Park tunnels were Addenbrooke et al. (1997) who used various isotropic and anisotropic soil models, Table 6.3, to calculate the surface displacements. The models used accounted for the small strain stiffness of London Clay exhibited in the laboratory tests done as part of the site investigation. Models J4 and L4 were isotropic, with AJ4 being anisotropic. In all except two of the models, equations were used to define the stiffness degradation curve, being trigonometric in the case of models J4 and AJ4 and logarithmic in the case of L4. In models J4 and AJ4 the straining mode was directly linked to the reduction in stiffness with the shear strain reducing shear stiffness and volumetric strain reducing bulk stiffness. In model L4 stiffnesses were reduced co-axially with increasing shear or volumetric strains. None of the models naturally accounted for the effect of recent stress history, though model L4 was modified to generate a high stiffness following a stress reversal to allow the model to approximate the effect of recent stress history. The surface displacements generated by the various models are shown in Figure 6.7 where the field data is taken from Standing, Nyren, Longworth & Burland (1996). Models AJ4i and AJ4ii differ in the stiffness ratio, m', where m' = shear modulus in vertical plane (G_{vh}) / Young's modulus in the vertical plane ($E_v{}'$) and thus controls the shear stiffness of the soil. $n' = E_v{}'$ / Young's modulus in the horizontal plane ($E_h{}'$) and controls the anisotropic stiffness. Table 6.3 gives the various n' and m' values along with the achieved volume loss (V_l), from which it can be seen that model AJ4ii is significantly less stiff in shear than model AJ4i as the value of m' is lower.

Soil model	n'	m'	V_l (%)
Isotropic linear elastic / perfectly plastic	-	-	1.89
Anisotropic linear elastic / perfectly plastic	0.625	0.444	1.89
Model J4	-	-	3.2
Model L4	-	-	3.3
Model AJ4i	0.625	0.444	3.2
Model AJ4ii	0.625	0.2	3.2

Table 6.3: Volume loss achieved, Addenbrooke et al. (1997)

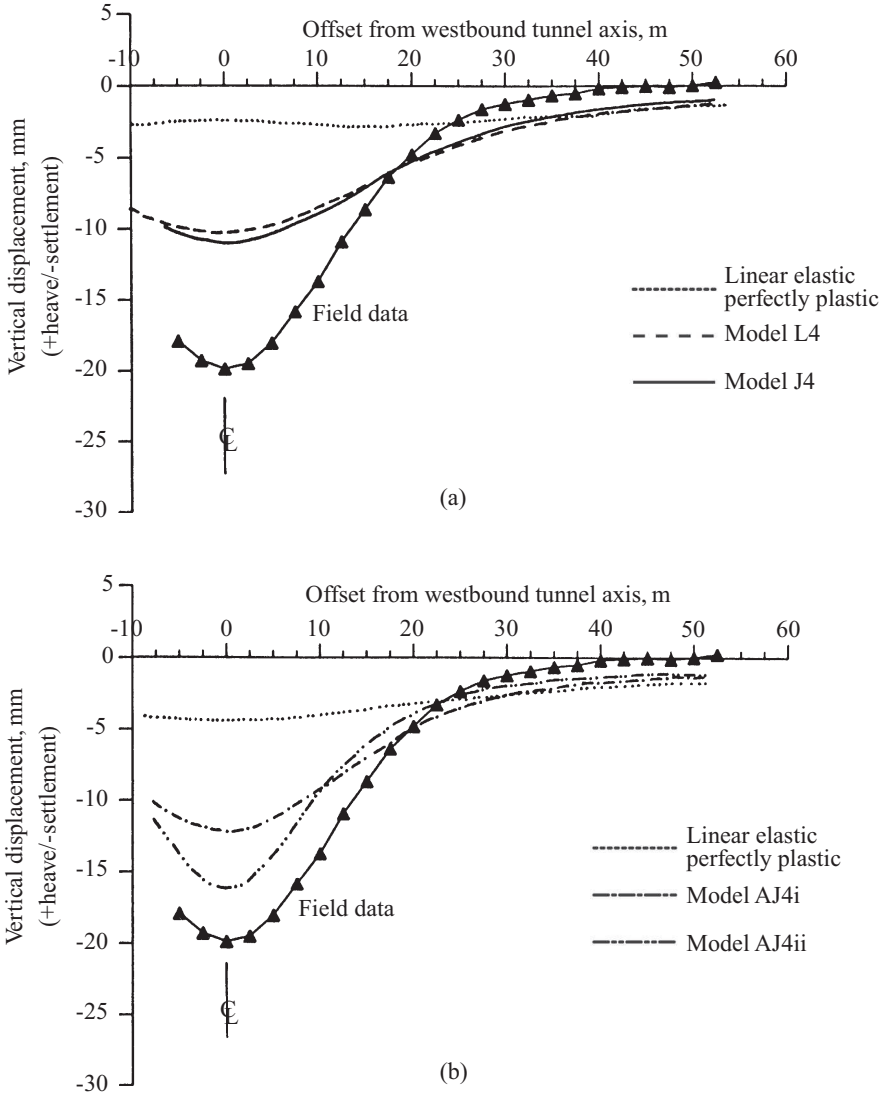

Figure 6.7: Surface settlement profiles for the westbound tunnel: (a) isotropic models; (b) anisotropic models, after Addenbrooke et al. (1997)

The plots shown in Figure 6.7 demonstrate the poor fit of both isotropic and anisotropic linear elastic models when estimating surface displacements above the westbound tunnel, being able to achieve only a -2.3mm (11.6% of actual displacement) and -4.5mm (22.7%) centreline vertical displacement respectively. Models L4 and J4 improved this estimation generating a -10.5mm (52.8%) and -11.1mm (55.8%) displacement respectively. The stiffer anisotropic model AJ4i generated a -12.5mm (62.8%) displacement but by far the largest displacement was that of the less stiff anisotropic model AJ4ii with a -16.6mm (83.4%) predicted displacement. One common trend seen in all the finite element simulations is the presence of relatively large far-field dispacements. In Figure 6.7 it can be seen that the field data show very small displacements once a distance of 40m from the tunnel centreline is reached, whereas the finite element displacement never decreases to a similar level, even at a distance of 52.5m. The finite element mesh used in the Addenbrooke et al. (1997) analysis is shown in Figure 6.8.

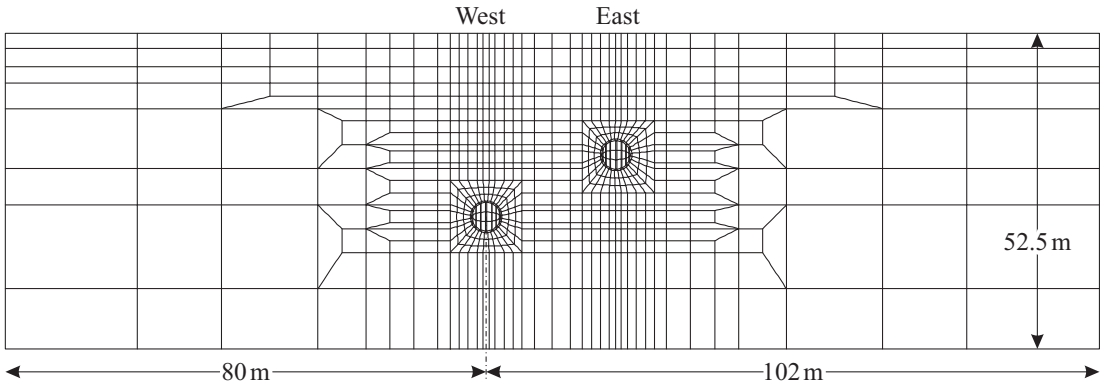

Figure 6.8: Finite element mesh for St James's Park, Addenbrooke (1996)

Grammatikopoulou et al. (2008) remodelled the St James's Park tunnels using the modified 3-SKH model, M3-SKH, described in Section 2.3.3. This kinematic hardening model incorporates the effects of recent stress history and the small strain stiffness associated with London Clay. Two scenarios were considered, one without the effects of creep, allowing the stress history to have an effect on the soil stiffness, and one assuming that the creep periods have erased any memory of the stress history. The total erasure of the stress history requires a centralising of the yield and history surfaces around the current stress state, Figure 6.9.

The predicted stiffnesses for configuration A and configuration B are shown in Figure 6.10, for both undrained triaxial compression (TXC) and extension (TXE) tests. The first set of analyses, denoted by the letters 'sh' in Figure 6.10, simulated the stress

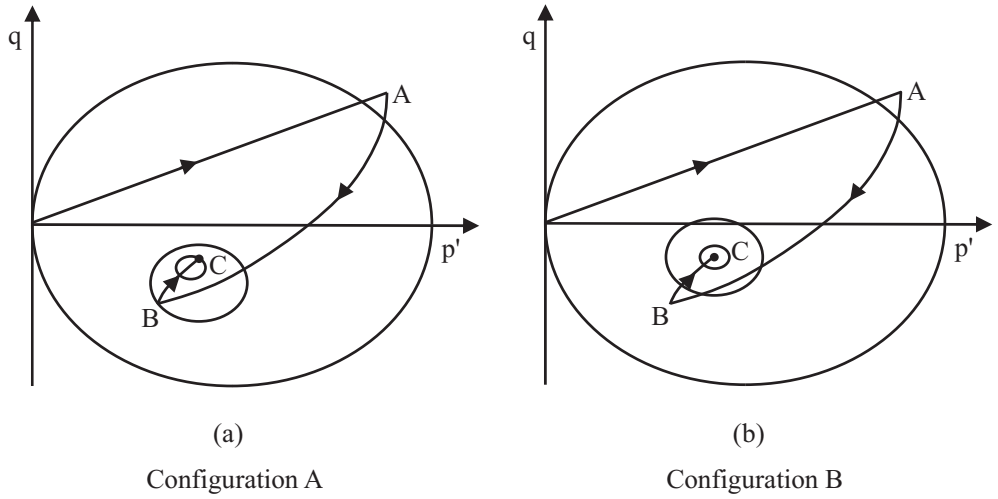

(a) Configuration A (b) Configuration B

Figure 6.9: a) Configuration of the kinematic surfaces at the end of the assumed geological history for an element of London Clay in the vicinity of the tunnels b) centring of the kinematic surfaces at the end of the geological history, Grammatikopoulou (2004)

history shown in Figure 6.9a, before the simulation of the shearing stages. The second set of analyses, denoted by the letters 'sh-c' in Figure 6.10, used the same stress history but centralised the yield surfaces upon the final stress state, as seen in Figure 6.9b before shearing. The 'sh' tests show the initial stiffness being dependent upon the rotation of the stress path. The TXC test shows a lower stiffness as the most recent stress history of the soil is also in compression (path BC in Figure 6.9) meaning a low rotation in the stress path, as demonstrated by Atkinson et al. (1990) in Figure 2.8 on page 11. In the 'sh-c' tests the initial stiffness is equal in both directions as the yield surfaces have been centralised, as demonstrated by Clayton & Heymann (2001) in Figure 2.10 on page 13.

Grammatikopoulou et al. (2008) conducted two finite element analyses, M3-SKH-1 using the parameters from the 'sh' tests and M3-SKH-2 using the 'sh-c' parameters. The parameters for model M3-SKH-1 were derived from tests on reconstituted material from Canon's Park (Jardine 1985) which were found to generate a higher stiffness than that used by Addenbrooke et al. (1997). In the analysis 'M3-SKH-1 softer' the parameters that define the hardening modulus were reduced to match the behaviour predicted by the Addenbrooke et al. (1997) model. It can be seen in Figure 6.11 that this softening of the model helps in the estimation of the vertical displacements, increasing the accuracy of analysis M3-SKH-1 from -13.0mm (65.3%) to -14.6mm (73.4%). As the

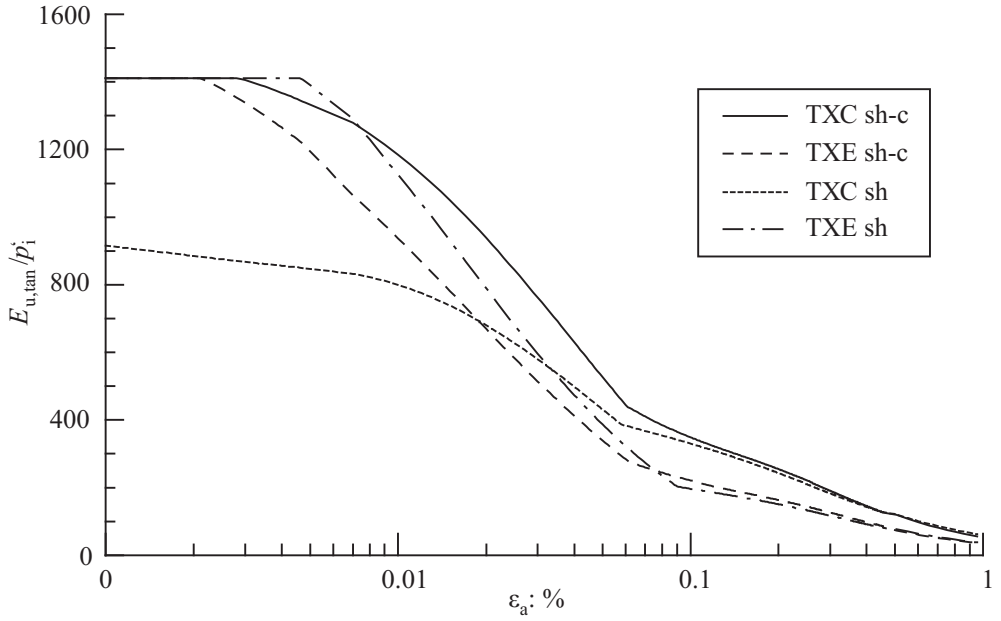

Figure 6.10: Comparison of predictions of modified three-surface model (M3-SKH) for analyses sh-c and sh. Normalised stiffness-strain curves for stress histories shown in Figure 6.9, after Grammatikopoulou et al. (2008)

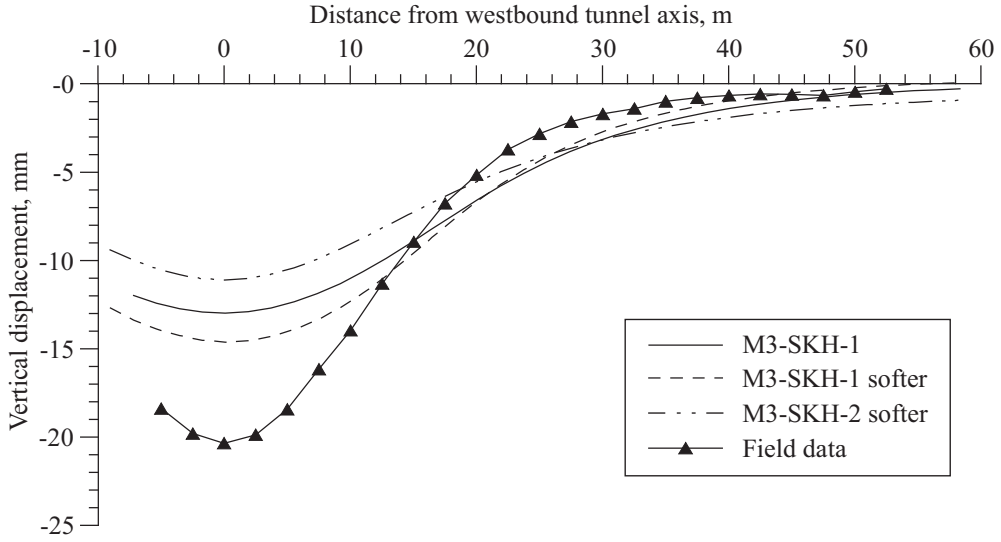

Figure 6.11: Comparison of ground surface settlement profiles predicted by M3-SKH model, adapted from Grammatikopoulou et al. (2008)

softer parameters improved the estimations, Grammatikopoulou et al. (2008) repeated analysis M3-SKH-2 using only the softer parameters giving a vertical displacement of -11.1mm (55.8%). First impressions of the plots would suggest that accounting for the effect of creep leads to a less accurate estimation of the settlements than an estimation done without accounting for creep. However it was shown in the tests done by Gasparre (2005) that the effects of creep after a long stress path caused a high initial stiffness at very small strains but that the effects of the stress history were still present at intermediate strains. Thus erasing the entire stress history may not be an adequate approximation of the effects of creep. The mesh used in the modelling was identical to that used in Addenbrooke et al. (1997).

6.4.2 Assumptions and mesh

The overall geometry of the finite element model was the same as that used by Addenbrooke et al. (1997) but instead of being hand drawn the mesh was generated using SAFE's built in mesh generation algorithm. To generate meshes within SAFE the geometry of the problem must be supplied via a series of defined regions. To help the algorithm deal with changes in mesh density across the problem and to minimise the number of geometric anomalies, the number of mesh segments on each edge of a region can be defined. For modelling the St James's Park twin tunnels the mesh needed to be finest in the regions immediately around the tunnel and vertically up to the surface, hence the large number of defined regions in this area in Figure 6.12.

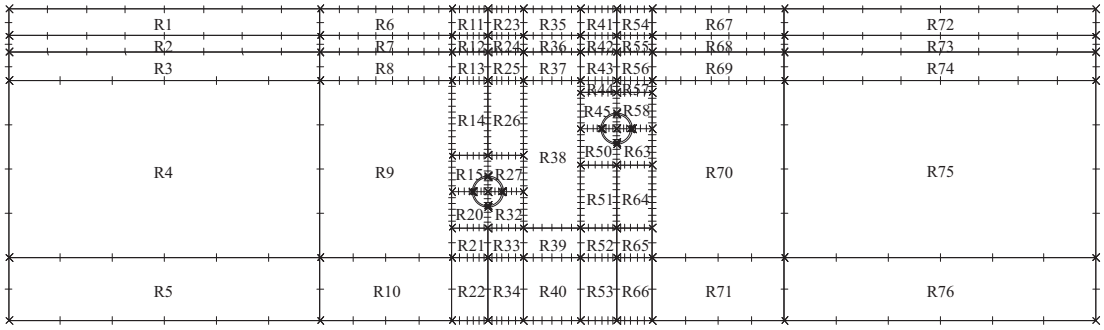

Figure 6.12: Regions for SAFE mesh generation, St James's Park twin tunnels

Generating a mesh from these regions gives an output similar to that in Figure 6.8, but with a higher density of elements around and above the tunnels, as shown in Figure 6.13. Boundary conditions were applied to the left, right and bottom boundaries, with the left and right boundaries being fixed horizontally and the bottom boundary nodes being fixed both horizontally and vertically.

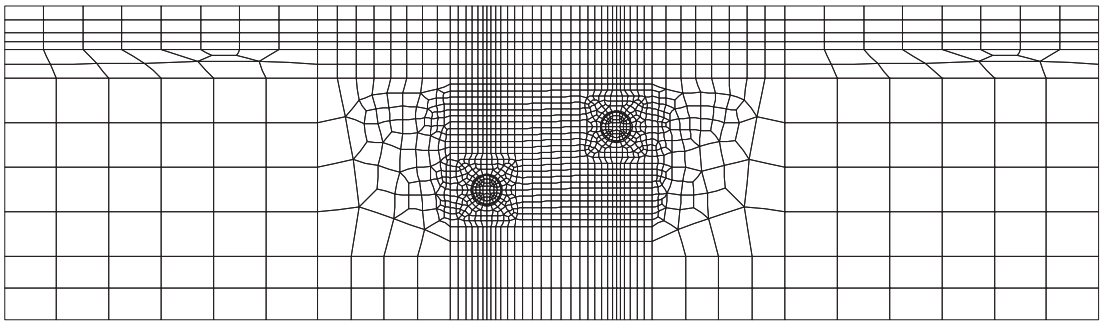

Figure 6.13: Finite element mesh, St James's Park twin tunnels

The volume loss was modelled as an undrained process due to the rapid rate of advance of the tunnel heading. The pore water pressures were taken to be hydrostatic from the top of the Terrace Gravel bed, as indicated in Figure 6.4. In the Addenbrooke et al. (1997) and Grammatikopoulou et al. (2008) analyses the method for applying the volume loss was the 'volume loss control method' (Potts & Zdravkovic 2001b), where the tunnel lining is represented by a series of point loads at the nodes on the perimeter of the lining. As these loads are reduced so the volume of the tunnel reduces and the volume loss is generated. Due to the large amount of tunnel modelling conducted by Arup Geotechnics another method for introducing volume loss has been developed specifically for use with Safe. This method involves generating a suction within the tunnel along with a reduction in the stiffness of the tunnel material to allow a volume loss to be created.

A parametric study was conducted to assess the effect of the number of nodes on the perimeter of the tunnel lining, n, on the volume difference due to the approximation, Figure 6.14. This shows that the % difference in volumes rapidly decreases and is sufficiently small for $n > 40$. In the current mesh the perimeter of the tunnel has been modelled using 48 linear elements which gives a 0.29% volume difference when compared to a perfectly circular tunnel.

Three main analyses were undertaken to facilitate a comparison between the SRD model developed in Chapter 5 and other soil models. These analyses used the following models for the London Clay stratum: Mohr-Coulomb (see Section 2.3.1) as it is still extensively used in industry for finite element analysis; Brick, to give a benchmark with which the SRD model can be compared; and SRD Brick.

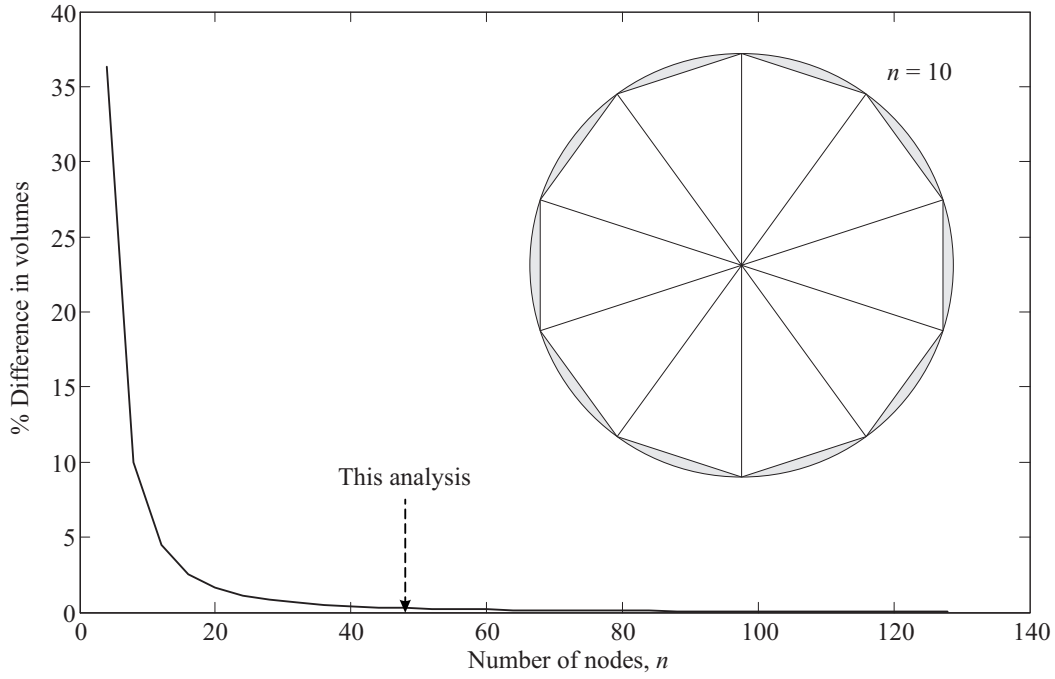

Figure 6.14: Parametric study on the effect of number of nodes used to approximate the tunnel lining

Only the soil model for the London Clay layer was changed between each analysis, with the Made Ground, Terrace Gravel and Woolwich & Reading beds being represented by Mohr-Coulomb models. As the behaviour of London Clay is well documented, the use of a complex soil model that can recreate this behaviour is justified. This is not true for the other layers in the analysis, with the parameters either being much more variable (Made Ground) or the contribution to the result simply not great enough to warrant a complex model (Woolwich & Reading Beds).

Constant model parameters

The parameters for the Made Ground / Alluvium, Terrace Gravels and Woolwich & Reading beds, as used by Addenbrooke et al. (1997), are given in Table 6.4. As the Woolwich & Reading beds were deemed to have a minimal effect on the surface displacements, a c' value of 200kPa was assumed for the layer. The Made Ground / Alluvium layer was assumed to have a dilation angle of 0° to represent the loose nature of the soil.

	Made Ground / Alluvium	Terrace Gravel	Woolwich and Reading Beds
Strength parameters	$c' = 0$ kPa $\phi' = 35.0°$	$c' = 0$ kPa $\phi' = 35.0°$	$c' = 200$ kPa $\phi' = 27.0°$
Angle of dilation (v')	0°	17.5°	13.5°
Bulk unit weight, kN/m^3	$\gamma_{dry} = 18$ $\gamma_{sat} = 20$	$\gamma_{sat} = 20$	$\gamma_{sat} = 20$
Young's modulus, E', (kPa)	5000	$6000z$	$6000z$
Poisson's ratio, ν	0.3	0.2	0.2
Earth pressure coefficient, K_0	0.5	0.5	1.5
Note: z is the distance below the ground surface in metres			

Table 6.4: Constant model parameters - St James's Park, Addenbrooke et al. (1997)

The analysis was initialised in drained conditions to allow the dissipation of excess pore water pressures throughout the soil. At the end of the initialisation run the strains were reset to zero so they had no influence on the subsequent output. SAFE modelled the overconsolidation in this initialisation using specified K_0 and g values where g defines the profile of the initial vertical effective stress with depth and is equal to:

$$g = y + (\sigma'_v/(\gamma_{sat} - \gamma_w)) \text{ beneath the water table and}$$
$$g = y + (\sigma'_v/\gamma_{dry}) \text{ above the water table} \quad (6.3)$$

where:

y = ordinate of any point in the zone,
g = intercept of the effective stress line on the y-axis.

g is a constant for each material zone, provided the ground surface is horizontal and there are no variations of overburden pressure across the zone (Oasys 2006). The principles of the g values are illustrated for the current analysis in Figure 6.15.

6.4.3 Mohr-Coulomb analysis

The Mohr-Coulomb model is a widely used soil model in commercial finite element analyses, due to the ease of obtaining parameters from a site investigation and interpreting results. It was decided to analyse the St James's Park twin tunnels using a Mohr-Coulomb model for the London Clay to allow a comparison between the results obtained with this model and those generated by more complex models.

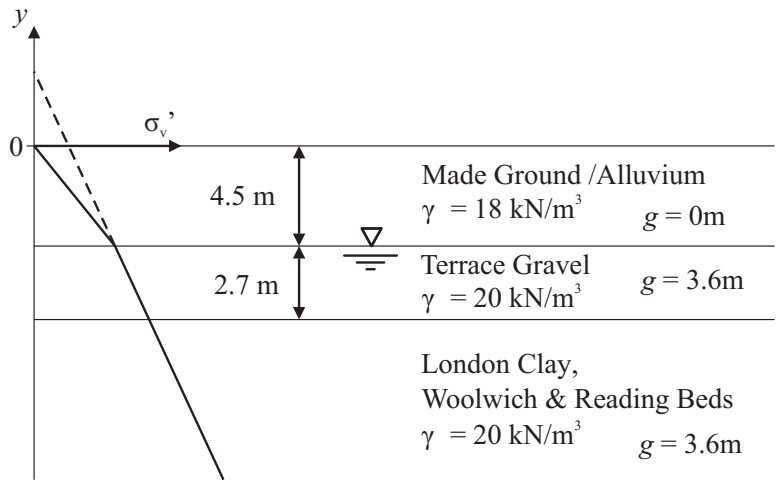

Figure 6.15: Calculation of g for St James's Park

The problem was initialised with the parameters from Table 6.4 along with the drained London Clay parameters from Table 6.5, after which the displacements were reset to zero and the London Clay layer changed to undrained. The volume loss was introduced by changing the material inside the tunnel boundary to a drained linear elastic material with a reduced stiffness and applying a negative pore water pressure to this material to force a volume change.

	London Clay	
	Drained	Undrained
Strength parameters	$c' = 0$ kPa $\phi' = 25.0°$	$c = 150$ kPa
Angle of dilation (v')	12.5°	-
Bulk unit weight, kN/m^3	$\gamma_{sat} = 20$	$\gamma_{sat} = 20$
Young's modulus, (kPa)	$E' = 6000z$	$E_u = 6000z$
Poisson's ratio, ν	0.2	0.498
Earth pressure coefficient, K_0	1.5	1.5
Note: z is the distance below the ground surface in metres		

Table 6.5: Mohr-Coulomb parameters for London Clay - St James's Park

An iterative approach is required to calculate the correct amount of volume loss at the surface based on the suction and reduction in stiffness applied to the linear elastic material of the tunnel. As this process is occurring under undrained conditions in the London Clay layer, the volume loss at the surface is assumed to equal the volume loss at the tunnel boundary. Volume losses within the drained layers above the London Clay

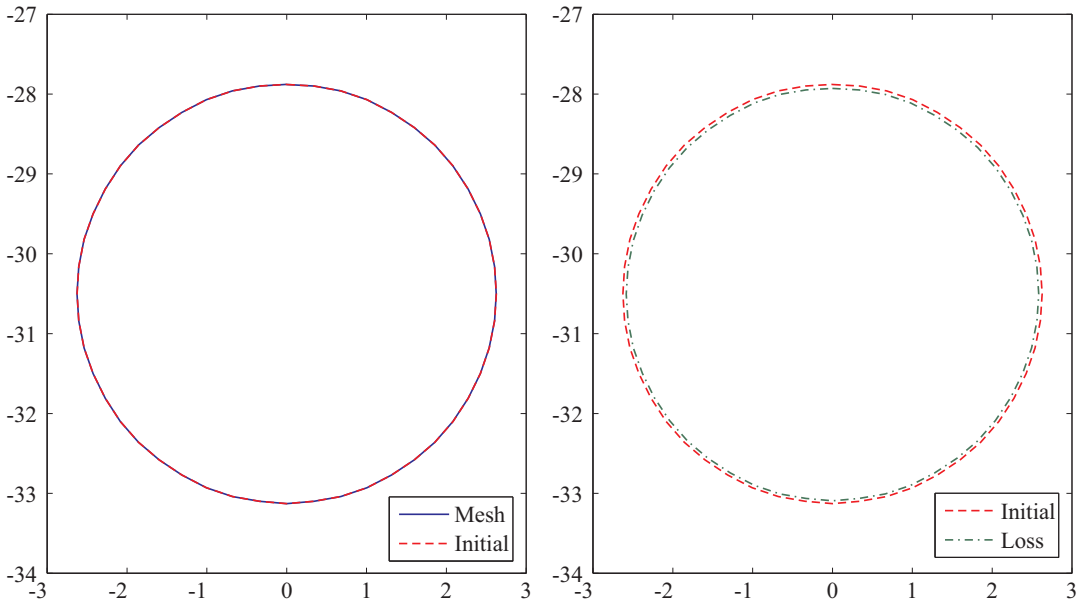

(a) Before and after initialisation

(b) Before and after volume loss

Figure 6.16: Tunnel geometry comparison

are assumed to be negligible, which can be confirmed in the analysis by checking the volumetric strains. As the tunnel shape is specified in the mesh before the initialisation stage takes place, the exact shape and volume of the tunnel could change during this stage. Figure 6.16(a) shows a comparison between the tunnel geometry as specified in the mesh and the geometry extracted after the initialisation. It can be seen that negligible deformation occurred during the initialisation. For accuracy, instead of basing the volume loss on the area of a perfect circle as is done in Equation 6.2, it was based on the exact volume of the tunnel prior to the excavation taken from the mesh geometry. For the Mohr-Coulomb modelling the volume loss at the tunnel (Figure 6.16(b)) was 3.25% while the volume loss at the surface (seen in Figures 6.17(a) and 6.18) was calculated to be 3.28%. The volumetric strains within the surface layers were found to be negligible and therefore the assumption that the volume loss at the surface was equal to that at the tunnel boundary under undrained conditions was confirmed. The surface volume loss was calculated using the trapezium rule applied to the vertical displacement at each node over the entire surface boundary. The volume loss that occurs after the excavation was seen as outside of the scope of the current analysis

The contours of predicted vertical displacement are shown in Figure 6.17(a). As the site is greenfield and the strata have been modelled as horizontal, the displacements are symmetrical about the westbound tunnel centreline. By re-plotting the data from the

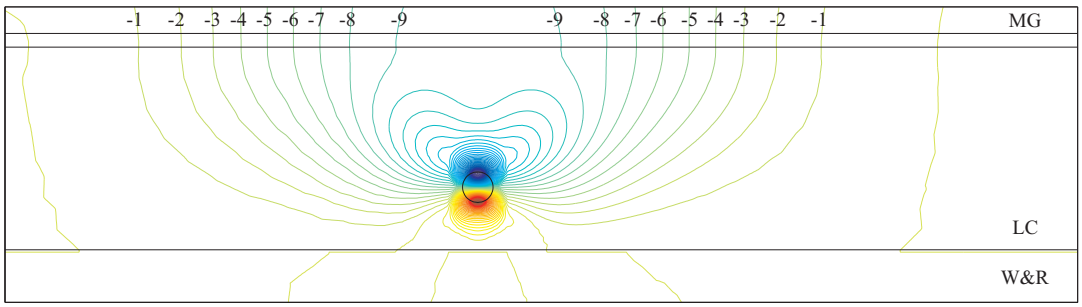

(a) Contours of vertical displacement, units in mm

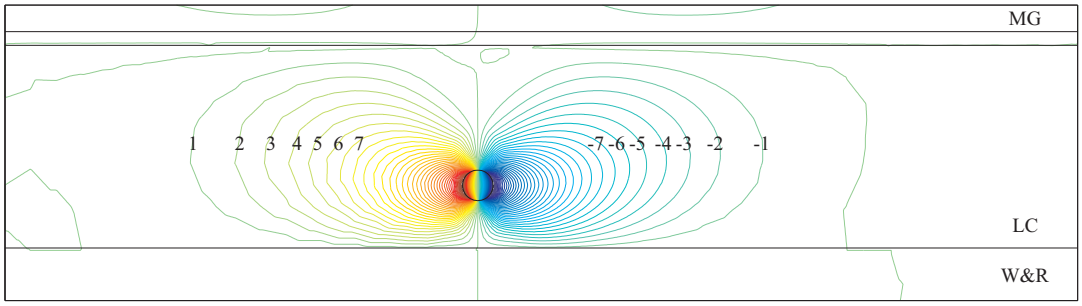

(b) Contours of horizontal displacement, units in mm

Figure 6.17: Displacement contours for the Mohr-Coulomb analysis of St James's Park

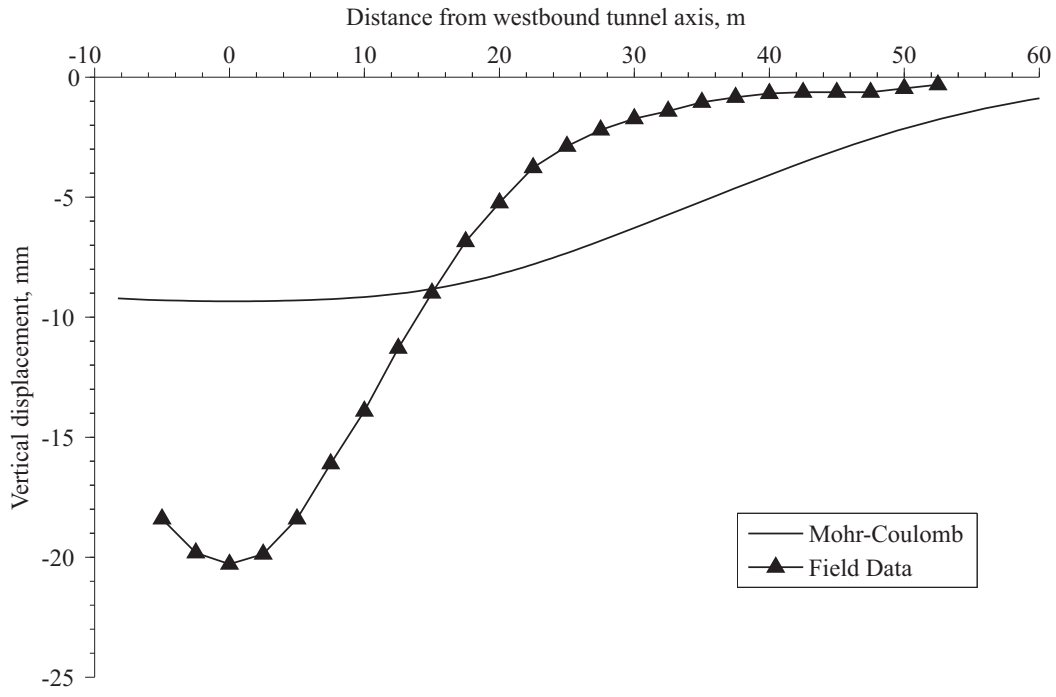

Figure 6.18: Surface displacement plot for the Mohr-Coulomb analysis

nodes along the surface boundary the settlement trough can be visualised, Figure 6.18. The maximum displacement was -9.3mm (46.7%) which shows there is much room for improvement. The Mohr-Coulomb analysis predicts a far wider settlement trough than is seen in the field, leading it to predict a lower centerline vertical displacement for the same volume loss. The horizontal displacement plot (Figure 6.17(b)) shows a similar width of displacement field. Due to their high stiffness and cohesion, very little movement is predicted within the Woolwich and Reading beds.

6.4.4 BRICK analysis

The next stage in the modelling was to use the BRICK model and re-run the analysis completed in Section 6.4.3. As BRICK accounts for the effect of the recent stress history on the soil, parameters need to be fed into SAFE to allow for this to be correctly modelled, included in Table 6.6. The same assumption for the initial thickness of the London Clay layer, namely 200m, has been made as in Section 4.7. As the remaining London Clay layer is 34.3m thick, this would imply a removal of 165.7m of overburden. For the BRICK string lengths and soil proportions, the parameters presented in Kanapathipillai (1996) have been used as they were developed for use in London Clay based on back analysis of the Heathrow Express trial tunnel, Table 6.7.

BRICK parameters used in Section 6.4.4									
Description	Theory	λ^*	κ^*	ι	ν	β_G	β_ϕ	n	G_{vh}/G_{hh}
London Clay	4	0.1	0.02	0.0019	0.2	4	3	1	1

Description	Consolidation parameters			Mu	Iteration Tolerance	Max first strain inc.
	Type	Y-Coord (m)	Gamma Gd (KN/m^3)			
London Clay	1D	165.7	20	1.3	0.01	0.001

Table 6.6: BRICK soil parameters for London Clay - St James's Park analysis

Unlike the Mohr-Coulomb model, BRICK is able to model the stress history of the soil, which forms the initialisation stage. In this stage, SAFE first applies the preconsolidation vertical stress to the BRICK modelled layer. This is then removed and the soil is swelled back to the in-situ vertical stress as defined by the mesh. The initialisation stage enables future stages to start with the correct brick positions and hence, estimations of K_0. The predicted non-linear K_0 with depth profile can be seen Figure 6.19.

London Clay		
String	String Length	G/G_{max}
1	$3.040e^{-5}$	0.92
2	$6.0863e^{-5}$	0.75
3	$1.0143e^{-4}$	0.53
4	$1.2106e^{-4}$	0.29
5	$8.200e^{-4}$	0.13
6	0.00171	0.075
7	0.00352	0.044
8	0.00969	0.017
9	0.02223	0.0035
10	0.0646	0

Table 6.7: BRICK string parameters for St James's Park

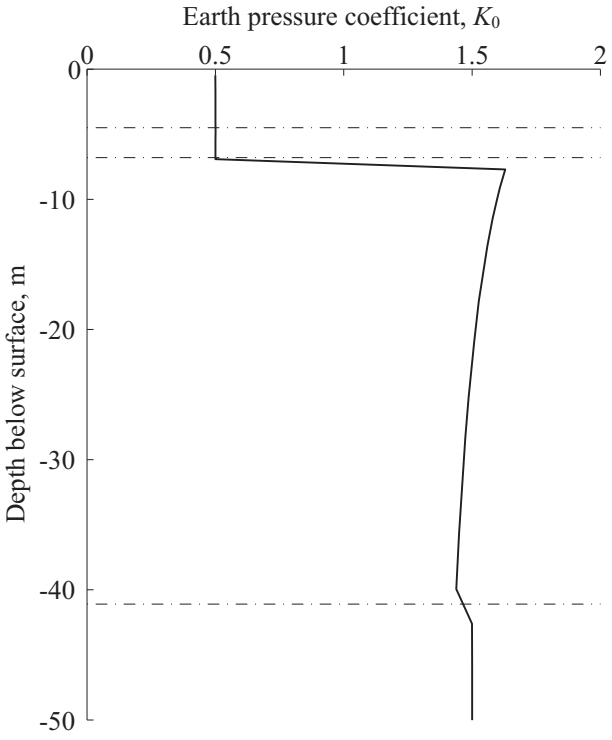

Figure 6.19: BRICK predicted K_0 profile

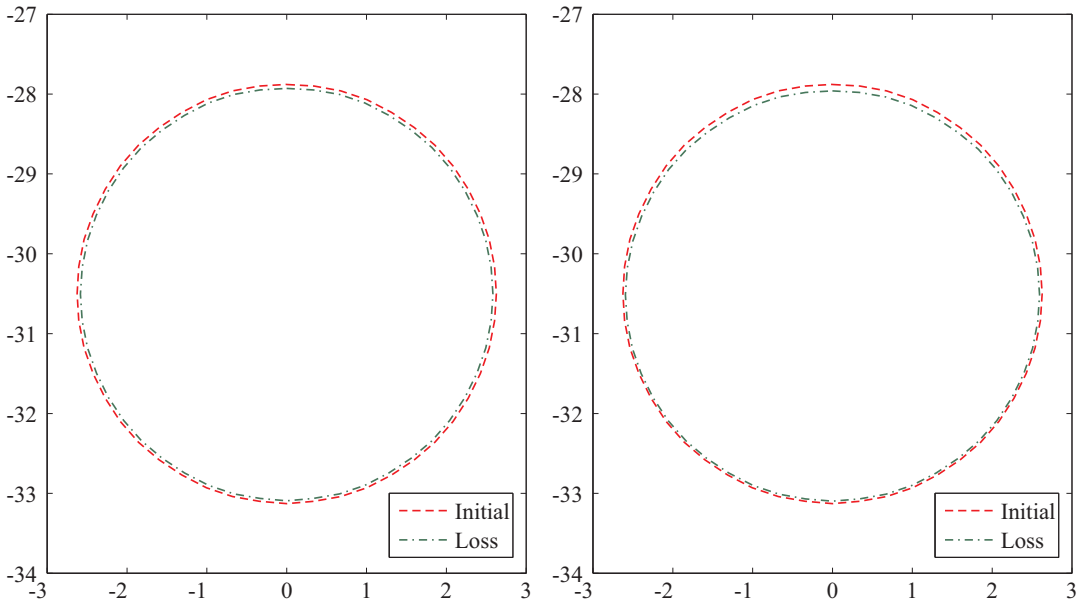

(a) Movement for Mohr-Coulomb analysis

(b) Movement for BRICK analysis

Figure 6.20: Mohr-Coulomb and BRICK tunnel geometry comparison

The volume loss generated during the Mohr-Coulomb analysis caused the tunnel boundary to contract equally in all directions, Figure 6.20(a). When the analysis was re-run using the BRICK model the movements became greater at the crown of the tunnel and smaller at the invert and the sides, Figure 6.20(b). This shows that BRICK predicted a different deformation pattern leading to higher vertical displacements for the same volume loss.

The displacement contour plots for the BRICK analysis in Figure 6.21 show a slightly narrower concentration of displacements when compared with the Mohr-Coulomb plots in Figure 6.17. This leads to a more concentrated surface settlement trough as seen in Figure 6.22. The maximum vertical displacement for the BRICK analysis was -12.9mm (64.8%). The horizontal displacements in Figure 6.21(b) show an upwards vertical shift when compared with the Mohr-Coulomb predictions in Figure 6.17(b), indicating that more horizontal movement is being generated above the tunnel than below. This fits with the predicted movement of the tunnel boundaries, Figure 6.20. These results show that the modelling of the stress history in an advanced soil model can serve to increase the accuracy of predictions completed using finite element analysis.

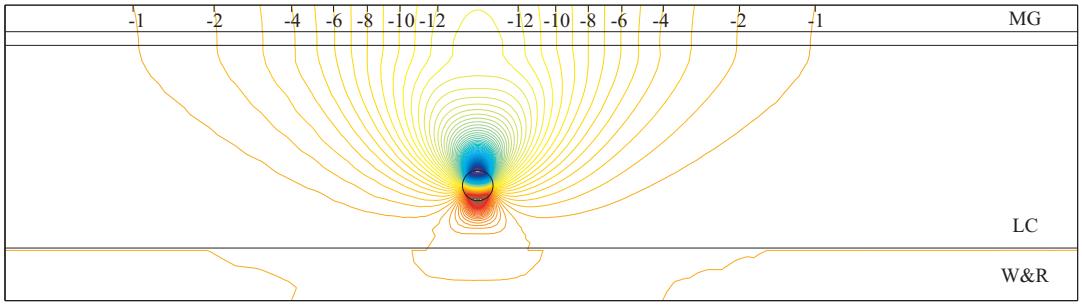

(a) Contours of vertical displacement, units in mm

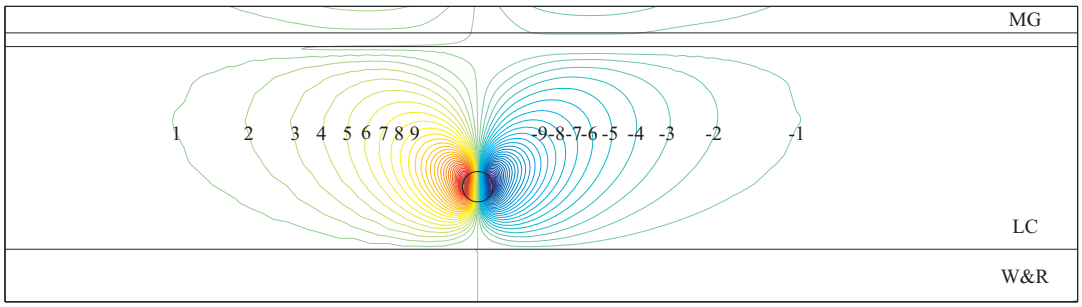

(b) Contours of horizontal displacement, units in mm

Figure 6.21: Displacement contours for the BRICK analysis of St James's Park

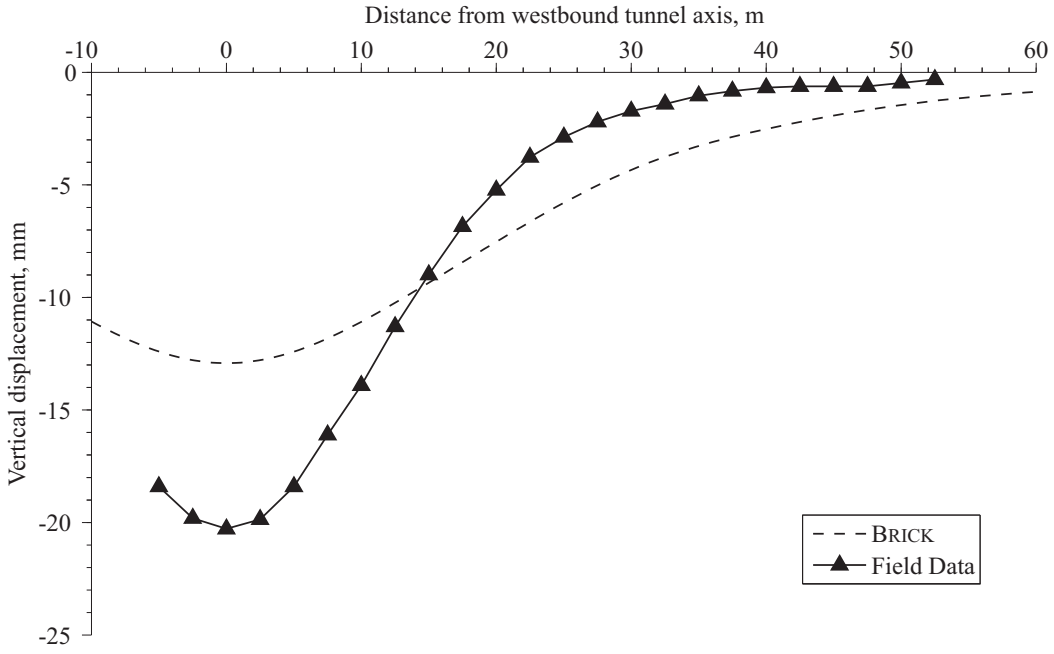

Figure 6.22: Surface displacement plot for the BRICK analysis

6.4.5 SRD BRICK analysis

The SRD Brick analysis utilised the same initial conditions as the Brick analysis but with a modified set of string lengths (Table 6.8) and a set of rate parameters (Table 6.9). Due to the disparity between the practical (Kanapathipillai 1996) and laboratory (calibrated from Gasparre (2005)) string lengths it was decided to use the practical string lengths which are known to give accurate predictions in real problems. Based on the lack of calibration data for the string length reduction, the assumption that the initial string lengths are halved due to the effects of creep was made (Kanapathipillai 1996).

London Clay		
String	String length	G/G_{max}
1	$1.52e^{-5}$	0.92
2	$3.04315e^{-5}$	0.75
3	$5.0715e^{-5}$	0.53
4	$6.053e^{-5}$	0.29
5	$4.1e^{-4}$	0.13
6	$8.55e^{-4}$	0.075
7	0.00176	0.044
8	0.004845	0.017
9	0.011115	0.0035
10	0.0323	0

Table 6.8: SRD Brick string parameters for St James's Park

The rate parameters remained unchanged from the analyses run on the Gasparre (2005) tests in Section 5.4.2. The only additional parameter required is the duration over which the volume loss occurred. From Figure 6.5 it is known that the total volume loss occurred during a tunnel face advance of approximately 32m. With the rate of advance of the TBM being around 45m/day, the duration of the volume loss worked out to be 0.711 days.

Parameter	Value
Time decay constant, m	1.0386
Reference strain rate, $\dot{\varepsilon}_{\text{ref}}$	$1e^{-13}$/s
Viscous constant, β	0.23
Time increment, days	0.711

Table 6.9: SRD Brick rate parameters for St James's Park

The model was initialised in the same way as was done in the BRICK analysis, except using the shorter string lengths. This was to account for the long creep period associated with the geological stress history, with the result that at the time the tunnel was constructed, the strings were at their shortest. As the strain rate during the geological period is unknown and sufficient time has elapsed, it is far easier to ignore the lengthening and shortening of the strings during the geological history and simply model it with the shortest string lengths. There would be no predicted difference in the subsequent soil behaviour as a result.

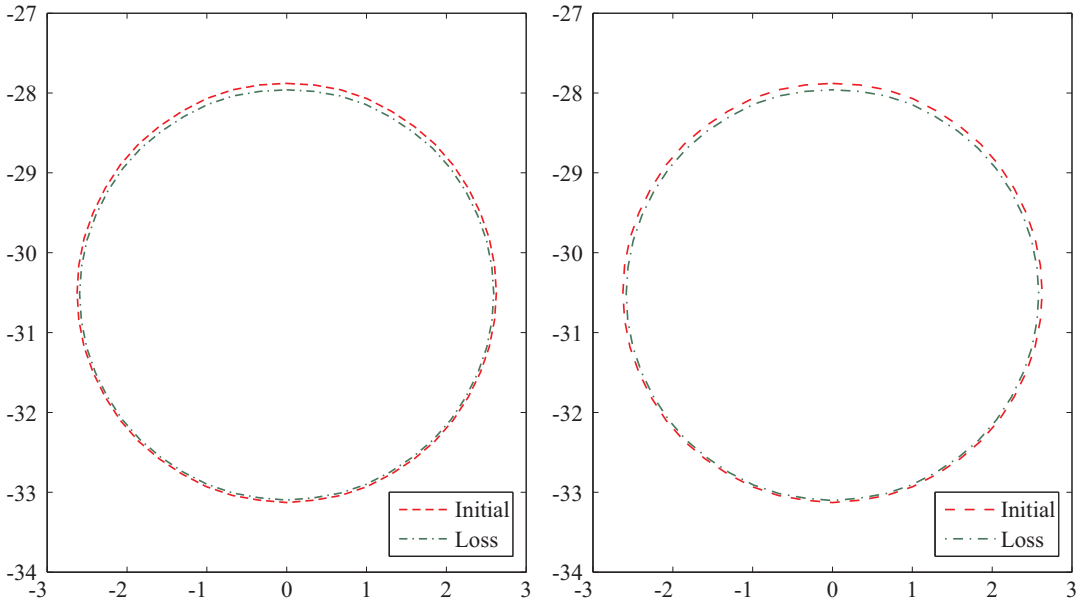

(a) Movement for BRICK analysis (b) Movement for SRD BRICK analysis

Figure 6.23: SRD BRICK and BRICK tunnel geometry comparison

After the volume loss had been introduced the deformed tunnel boundaries for the SRD BRICK and BRICK analyses were compared to assess where the movements were taking place, Figure 6.23. There is only a marginal difference, with the displacement at the crown of the tunnel for the SRD BRICK analysis being greater and the displacements at the sides and the invert being reduced. A further analysis of these trends will be conducted in Section 6.4.6.

The displacement contours are shown in Figure 6.24 and show a further reduction in the width of the displacement field for both horizontal and vertical displacements. This reduction in width allows the SRD BRICK model to predict a deeper surface trough than the BRICK model for the same degree of volume loss. The maximum displacement seen in Figure 6.25 is -17.25mm (86.7%).

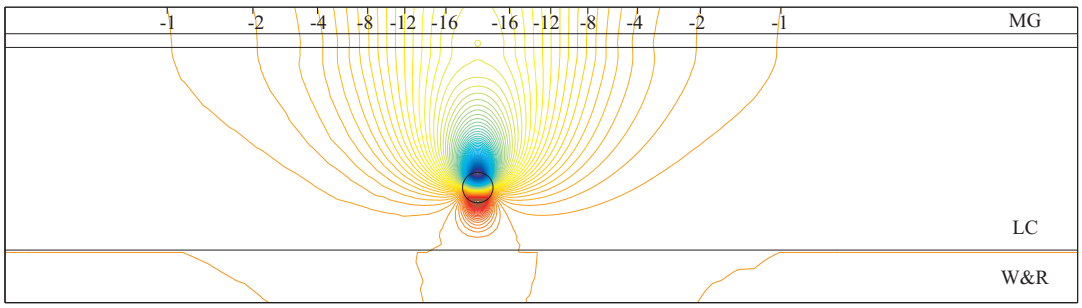

(a) Contours of vertical displacement, units in mm

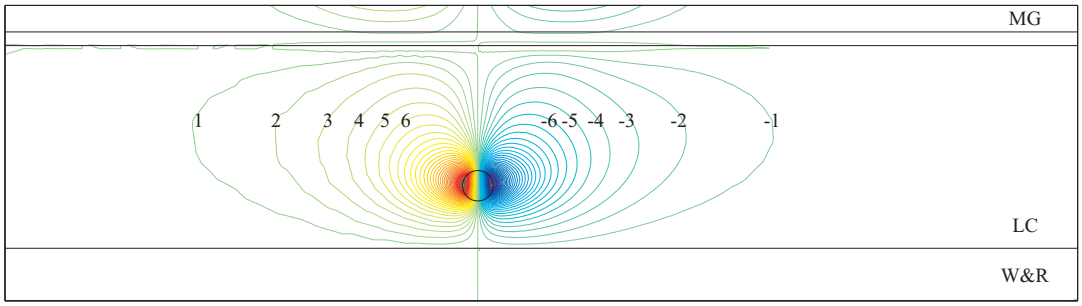

(b) Contours of horizontal displacement, units in mm

Figure 6.24: Displacement contours for the SRD Brick analysis of St James's Park

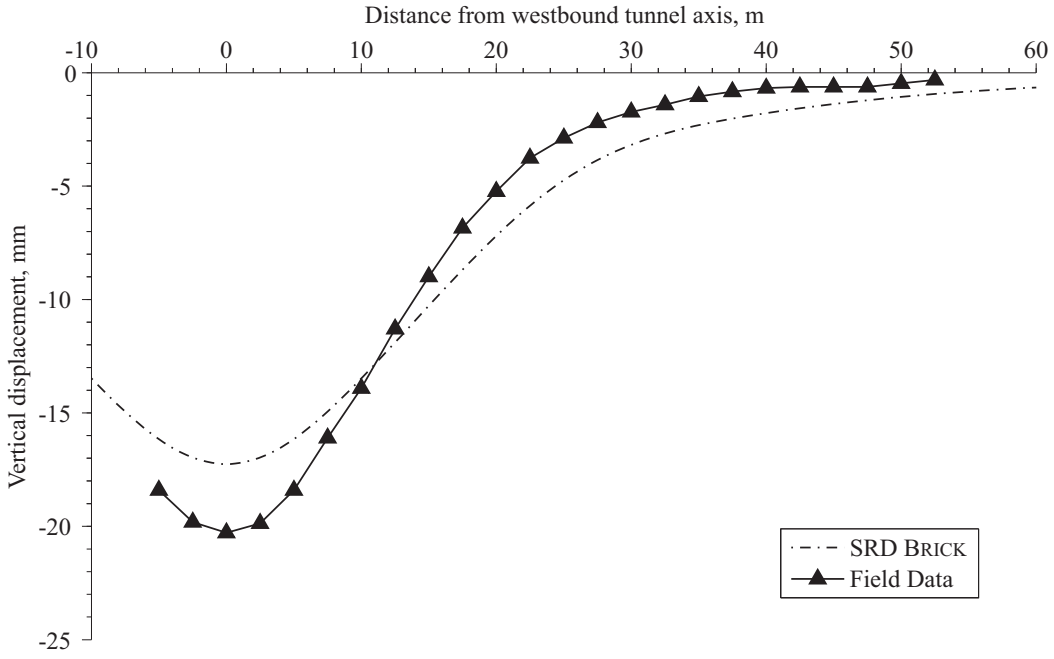

Figure 6.25: Surface displacement plot for the SRD Brick analysis

6.4.6 Discussion

A comparison between the displacement plots for the three soil models and the field data from Nyren et al. (2001) is presented in Figure 6.26. The maximum settlements for each model have been inserted into Table 6.10. Whilst the increasing complexity of the models increased the accuracy of the settlement trough, it was still not possible to create the same magnitude of settlement as seen in the field. One reason for this could be the relatively large far field displacements in the finite element analyses which reduce the depth of the trough centre. Extensive finite element meshes are, of course, recommended in order to attempt to reduce the boundary effects. The displacements are more localised in the SRD Brick predictions due to the viscous effects leading to an increased capacity for elastic strains which act to dissipate the applied volume loss over a smaller area.

Analysis model	Maximum vertical displacement, mm	Predicted/ field (%)
Field data	-19.9	-
Mohr-Coulomb	-9.3	46.7
Brick	-12.9	64.8
SRD Brick	-17.25	86.7

Table 6.10: Maximum vertical displacements for St James's Park

The horizontal displacement and strain are also plotted for comparison with the field data. Again the improvement between models can be seen, but the correct magnitudes are not predicted. The field data suggests much larger displacements and strains than are predicted by the current modelling. One interesting feature seen in the field data for the horizontal displacements, Figure 6.26(b), is the lack of symmetry about the centreline of the westbound tunnel, whereas the finite element analyses all predict a symmetrical response. The lack of symmetry in the field data could be a product of asymmetric ground conditions on the site.

To show the propagation of the displacements from the tunnel the vertical displacements were plotted along the centreline of the westbound tunnel from the surface to the outer boundary of the tunnel, Figure 6.27(a). It can be seen that the displacements increase towards the tunnel from the predicted surface displacement to a maximum at the crown of the tunnel. From the results plotted by Addenbrooke et al. (1997) values of between 43 and 57mm were predicted at the tunnel boundary. The Mohr-Coulomb

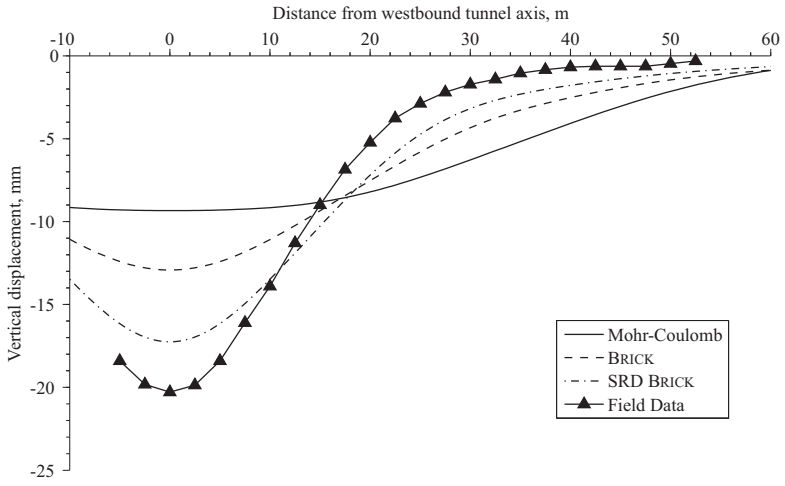

(a) Vertical displacement plot comparison

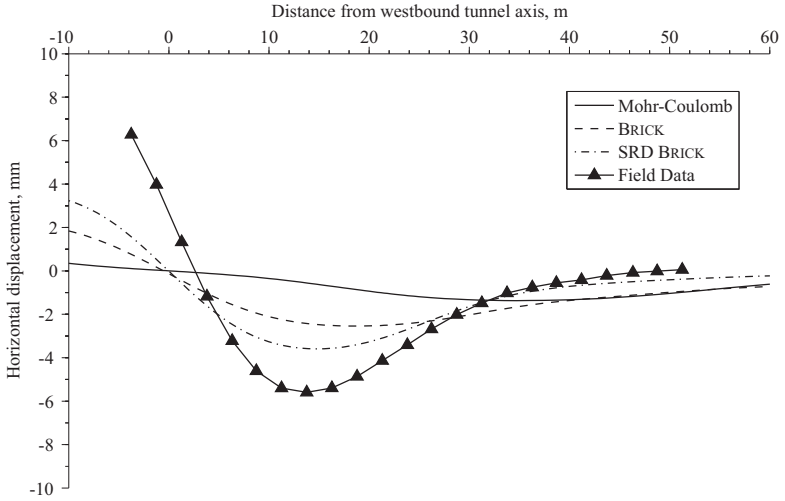

(b) Horizontal displacement plot comparison

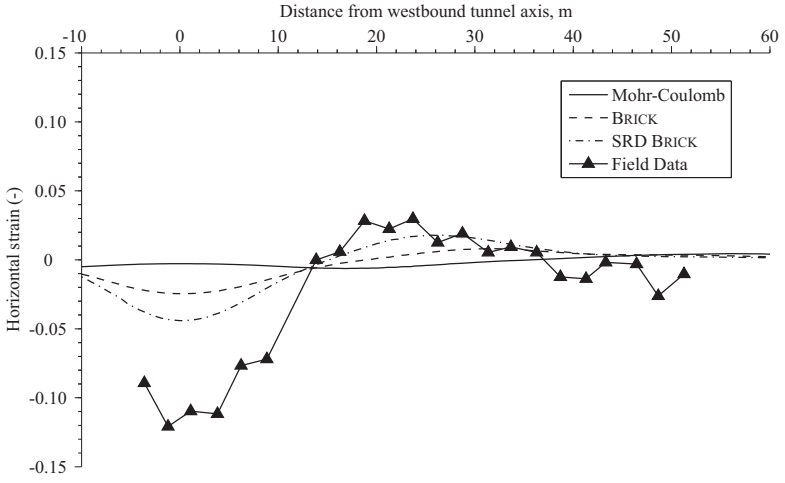

(c) Horizontal strain plot comparison

Figure 6.26: Surface comparison plots for St James's Park

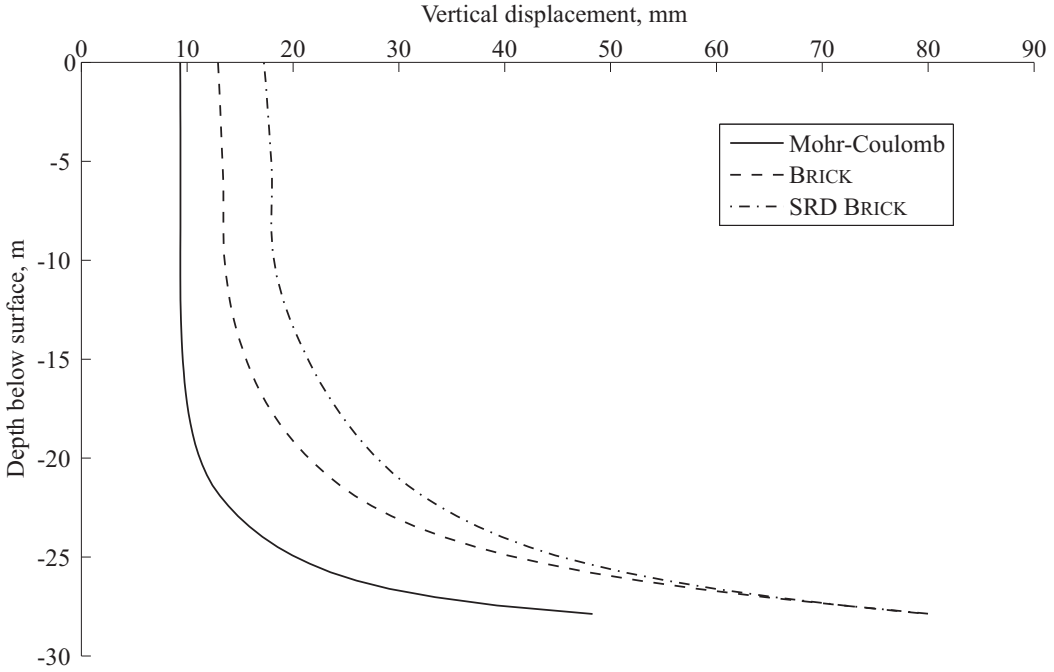

(a) Propagation of vertical displacement with depth

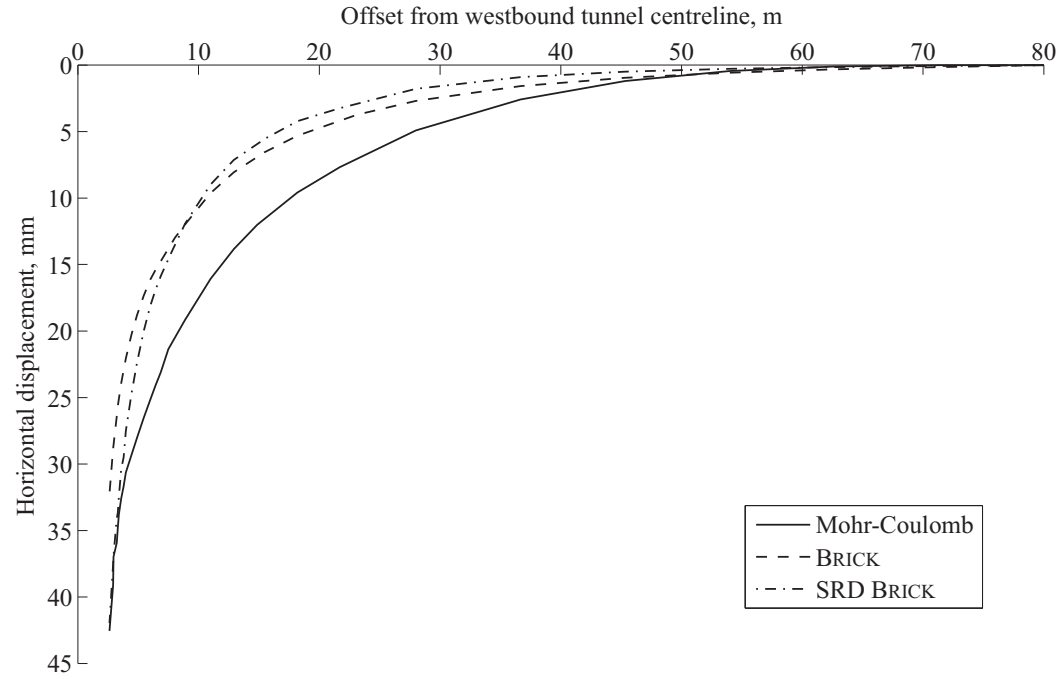

(b) Propagation of horizontal displacement with distance from centreline

Figure 6.27: Propagation of displacements analysis of St James's Park

analysis result falls within this band with a tunnel movement of 45mm, but the Brick and SRD Brick models predict much larger movements, 77 and 80mm respectively. The horizontal displacements plotted are from the horizontal centreline of the tunnel at a depth of 30.5m beneath the surface, Figure 6.27(b). The far-field displacements are very small, increasing to a maximum at the tunnel boundary. Addenbrooke et al. (1997) predicted values of between 37 and 44mm at the tunnel boundary. In this case the current modelling lies much closer to that done by Addenbrooke et al. (1997) with the Mohr-Coulomb model predicting a 43 mm displacement, and the Brick and SRD Brick models predicting a 32 and 42mm displacement respectively. One interesting thing to note about the Brick and SRD Brick predictions is the cross-over at 9m from the tunnel centre, with the SRD Brick model predicting a higher horizontal displacement before and lower after when compared with the Brick model.

A number of assumptions or approximations have had to be made to enable the current modelling, these include:

- a linear applied strain rate with time relationship, during tunnel construction;
- the use of a 2D analysis to model what in reality is a complex 3D problem;
- halving the string lengths for the SRD Brick analysis;

The volume loss was modelled as occurring in a single stage and linearly with time. When compared with the plot of volume loss with tunnel heading progress in Figure 6.5, this can be seen to be a fair approximation. Little extra benefit would be gained by attempting to model the non-linear relationship measured in the field.

Tunnelling analyses are complex 3D problems, with the volume loss being attributable to varied mechanisms. The approximations of the 2D analysis may limit the ability to model the details of tunnel excavation and construction, such as the progression of the heading and installation of the lining behind the TBM, but for the purposes of predicting the surface displacements the current analysis may be thought acceptable.

The assumption that the string lengths are halved by the effects of creep has yielded good results in St James's Park analysis. Back-analysis of a such a complex factor such as the string lengths would probably yield more accurate results in the current analysis, but the applicability of the back-calculated values to other analyses such as those in Section 6.5 would be harder to justify, without further back-analysis. With

further laboratory testing of the strain rate dependency of the stiffness degradation curve for London Clay, this assumption could be eliminated. To assess the sensitivity of the SRD Brick analysis to the reduction in the string lengths a parametric study was conducted. This involved re-running the SRD Brick analysis with different string lengths, varying from 20% of their normal length (Table 6.7) upto 100% of their usual length.

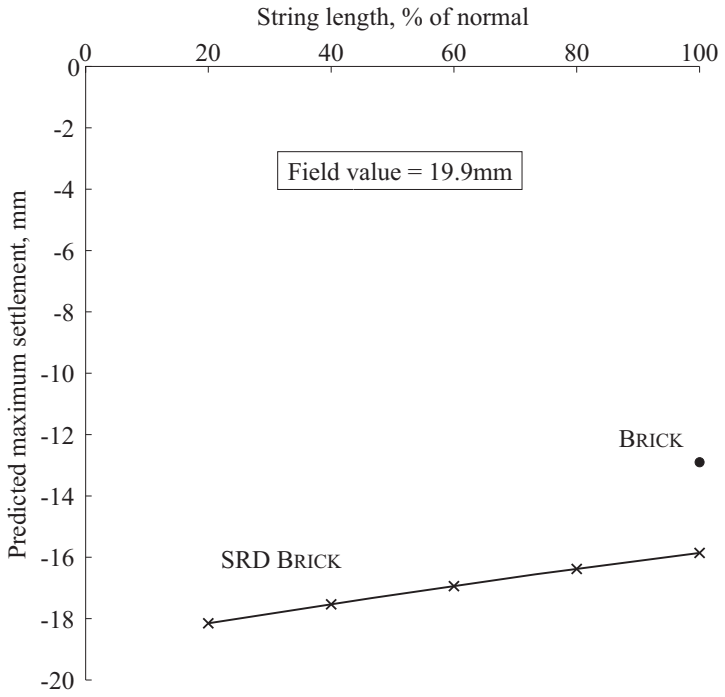

Figure 6.28: Parametric study into the effect of the string length on the predicted surface displacements for St James's Park

It can be seen in Figure 6.28 that although the string lengths used do make a difference to the settlements predicted, the effects are not as great as those generated by the inclusion of viscosity. This can be seen by comparing the Brick predictions with the SRD Brick predictions. The parametric study shows that the current analyses are relatively insensitive to changes in the string length, with the predictions lying within +4.4% and -8.1% of the settlement calculated with the string lengths halved.

The modelling of the tunnel lining, long term behaviour of the tunnel and the modelling of the eastbound tunnel were seen as outside the scope of the research and have not been taken into account in the current analysis.

6.5 Case History 2: Horseferry Road

At Horseferry Road a deep basement was constructed in London Clay and the heave of the basement was measured for a period of 21 years, which makes it one of the longest case histories of its type. Although the monitoring information is relatively limited, the analysis of the excavation is still deemed of value due to the long period of monitoring and possible interplay of primary and secondary swelling effects.

6.5.1 Background

Excavation of the basement began in June 1966 and was completed in November 1967. The basement was completed to ground level in May 1968. Due to unforeseen circumstances the superstructure was never completed and the site lay derelict (but still monitored) until June 1989, at which point the site was redeveloped. The location of the site can be seen in Figure 6.29, with the analysed section shown in Figure 6.30 and also marked on the site plan. The monitoring data from the first five years was published by May (1975) and can be seen in Figure 6.31. Before the redevelopment was started, a ground investigation was carried out in February 1989. The ground investigation showed a scour hollow to lie partially beneath the site. SPT results from the hollow showed the gravel towards the base of the hollow to be loose to medium dense (Chapman 1999). The relevant borehole information from the 1989 site investigation has been placed onto the section where appropriate. The location and extent of the scour hollow can be clearly seen beneath the west diaphragm wall. Figure 6.31 shows the heave data presented in May (1975) along with the associated initial displacement predictions based on an earlier site investigation using one-dimensional swelling theory. The locations of the monitoring points are shown on the site plan (Figure 6.29).

6.5.2 Assumptions and mesh

Details about the temporary prop arrangement for the basement construction are not available. Fortunately the locations of the temporary props are not of present concern as they are of importance for the behaviour of the wall during construction, rather than the behaviour of the soil during the long heave period.

Figure 6.32 shows a diagrammatic section through the basement. The exact locations of the columns within the basement are unknown so to allow the finite element model to account for the sub-structure, a pressure load equivalent to the weight of the floor slabs within the basement was applied to the basement slab. This pressure was taken

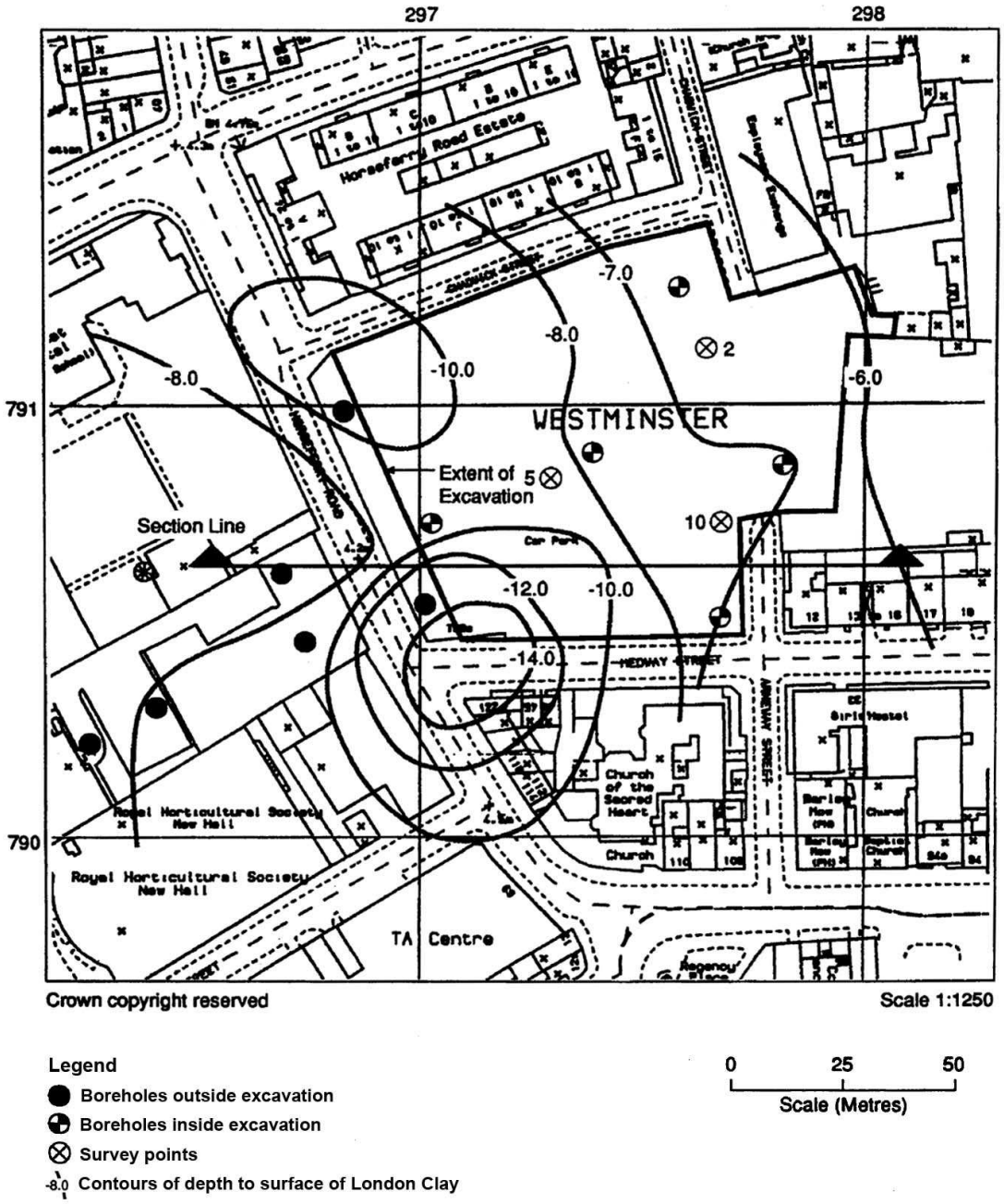

Figure 6.29: Horseferry Road site plan, after Chapman (1999)

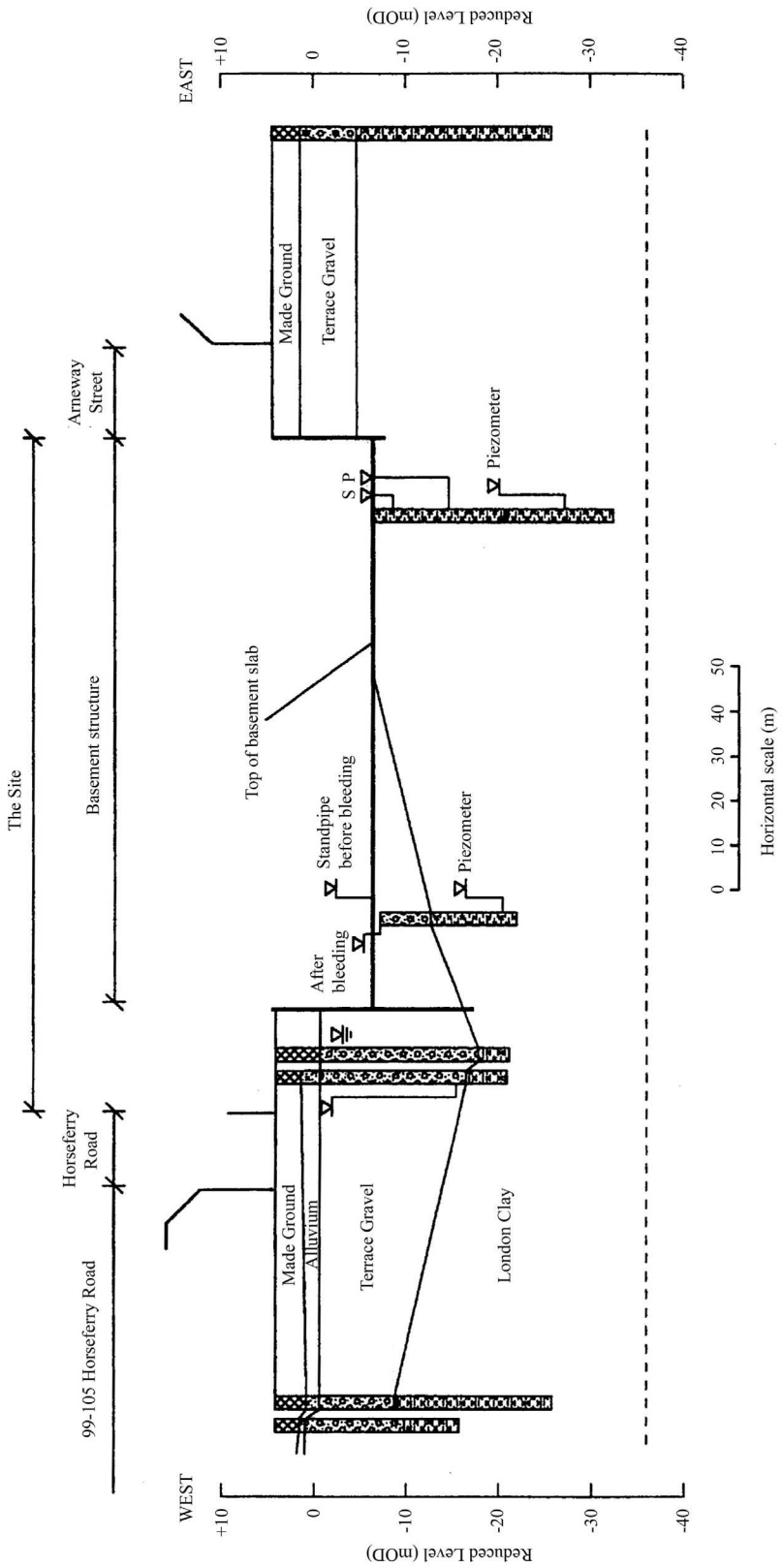

Figure 6.30: Site section showing relevant borehole information, Chapman (1999)

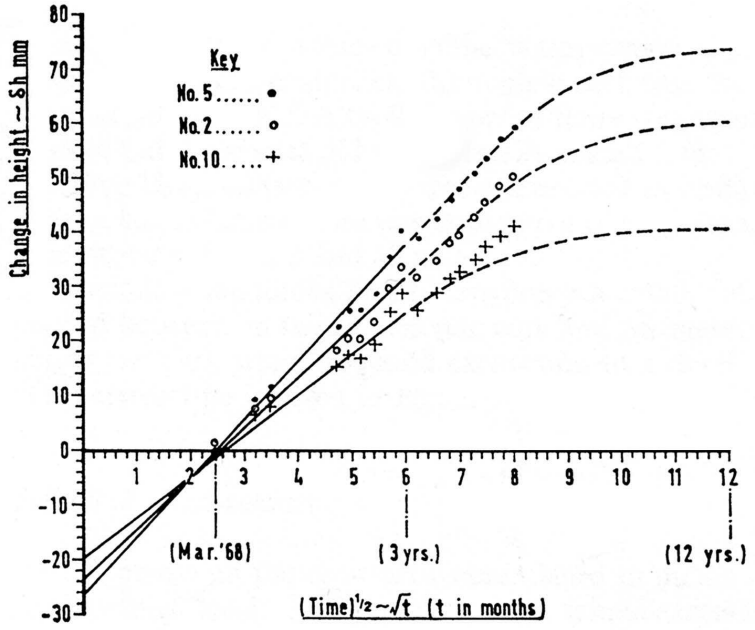

Figure 6.31: Original heave data with initial predictions, May (1975)

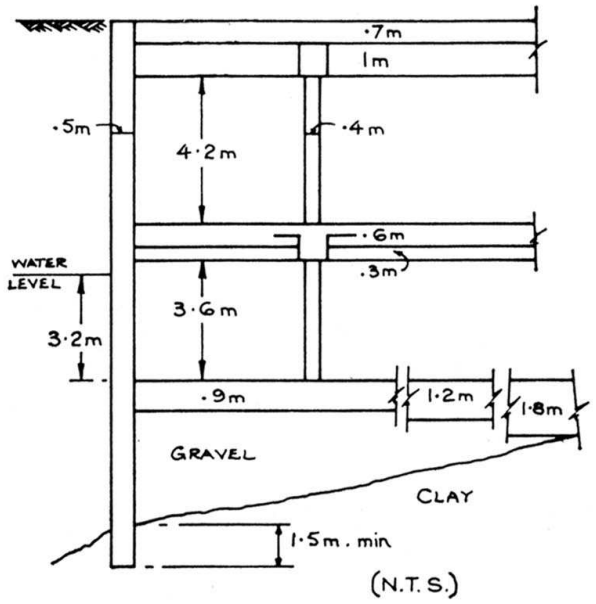

Figure 6.32: Diagrammatic section of the basement, May (1975)

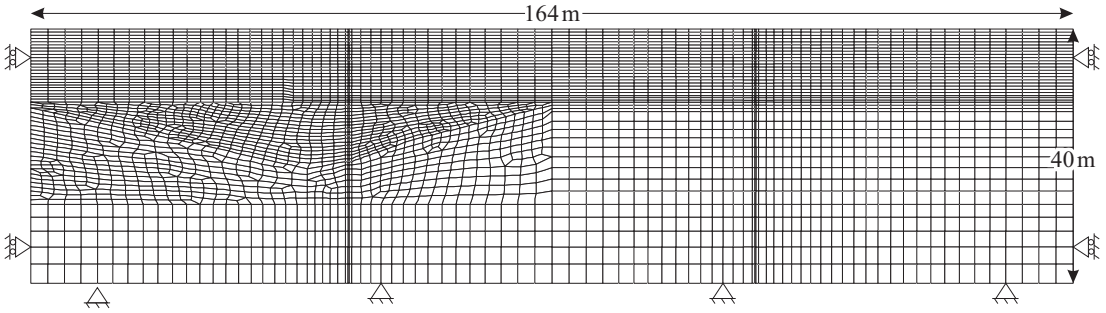

Figure 6.33: Finite element mesh for Horseferry Road

to be 48.2kN/m^2, as stated in May (1975).

Figure 6.30 shows the geometry of the soil layers as indicated by the borehole logs. These have been adopted into the mesh geometry as seen in Figure 6.33. It was shown previously (Section 6.4.3) that the Mohr-Coulomb model is not able to accurately predict the behaviour of London Clay and it has therefore not been used in the modelling of the London Clay layer in the Horseferry Road analysis. The parameters for the Terrace Gravel are different to those used in the St James's Park analysis, due to the presence of the scour hollow in the 1989 site investigation, and are given in Table 6.11. Due to the lack of previous test data, conservative values have been adopted for the Alluvium and Made Ground.

	Made Ground	Alluvium	Terrace Gravel
Strength parameters	$c' = 0$ kPa $\phi' = 25.0°$	$c' = 0$ kPa $\phi' = 25.0°$	$c' = 0$ kPa $\phi' = 38.0°$
Angle of dilation (υ')	0°	0°	0°
Bulk unit weight, kN/m^3	$\gamma_{dry} = 18$	$\gamma_{dry} = 20$	$\gamma_{dry} = 20$ $\gamma_{sat} = 20$
Young's modulus, E', (kPa)	1500	4500	4500
Poisson's ratio, ν	0.2	0.2	0.2
Earth pressure coefficient, K_0	0.561	0.561	0.384

Table 6.11: Mohr-Coulomb parameters for the Horseferry Road analysis

The London Clay layer was modelled using the Brick model with the same parameters as were developed in Section 6.4. The only parameter not used in the undrained analyses in Section 6.4 was the permeability of the London Clay layer, which has a large impact

on the development and dissipation of excess pore water pressures and, hence, heave. Different approaches to permeability were initially modelled, including permeability dependent on depth, on mean stress and constant permeability. Full details of the analyses are given in Appendix D.2.2, but only the results with permeability varying with mean stress are discussed here. The permeability of the soil was governed by Equation 6.4 (Potts & Zdravkovic 2001a).

$$k = k_0 e^{(-ap')} \tag{6.4}$$

where:

k = permeability of the soil,
k_0 = minimum soil permeability,
a = material constant.

This permeability relationship was most critical in the areas of London Clay which were directly below the level of the finished basement slab. During typical analyses with k decreasing with depth the excess pore water pressures generated are not sufficiently dissipated during the construction period. This can lead to the generation of negative effective stresses due to the high excess pore water pressures. Equation 6.4 increases the permeability in these areas as the mean stress reduces, so that the build up of excess pore water pressures higher than the total vertical stress can be avoided. By back analysis from the permeability values used in Addenbrooke et al. (1997) the a parameter was calculated to be 0.0104 for a k_0 value of $1e^{-8}$m/s.

It was explained in Section 6.4.2 that the parameter g used in the SAFE program relates to the intercept of the effective stress profile for the stratum with the y-axis . The values of g for the Horseferry Road model are given in Figure 6.34, with the profile being at the western extreme of the section shown in Figure 6.30.

The concrete diaphragm walls and basement slab were modelled as linear elastic materials with a Young's modulus of 16GPa and a Poisson's ratio of 0.2. Temporary props were added at the top of the diaphragm walls after the first excavation stage. The concrete was modelled as a no-flow drainage boundary.

The construction of the deep basement at Horseferry Road took place over a 17 month period, so the excavation of the basement could not be assumed to take place under undrained conditions. Thus a coupled consolidation analysis was utilised during the

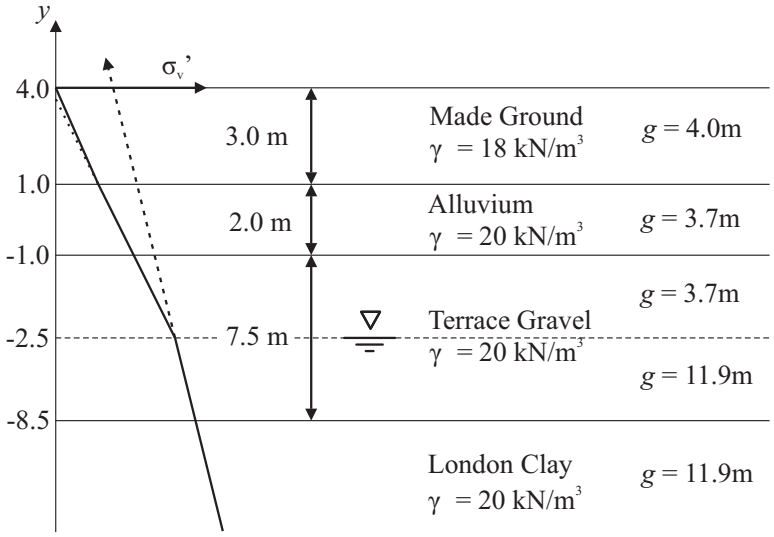

Figure 6.34: Calculation of g for Horseferry Road

Stage description		Duration (days)	Steps	Cum. time (days)
Initialisation		0	1	0
Construction	Installation of basement walls	120	4	120
	Excavation stage 1, +0.5m	120	4	240
	Installation of temporary props			
	Excavation stage 2, -3.0m	120	4	360
	Excavation stage 3, -5.0m	60	3	420
	Excavation stage 4, -6.5m	60	3	480
	Cast base slab	30	3	510
Monitoring	March 1968 heave	180	6	690
	March 1969 heave	360	6	1050
	March 1973 heave	1460	10	2510
	March 1980 heave	2555	7	5065
	March 1990 heave	3650	10	8715

Table 6.12: Horseferry Road finite element model stage analysis

construction phase, as well as during the monitoring period for the London Clay layer. The upper layers were taken to be drained throughout. The various stages used in the finite element analysis are given in Table 6.12. The boundary conditions for the mesh are shown in Figure 6.33. The edges of the mesh were modelled as no-flow boundaries.

6.5.3 BRICK & SRD BRICK analyses

The stage sequences were followed as shown in Table 6.12. The parameters for the Brick and SRD Brick models were the same as those given in Sections 6.4.4 and 6.4.5. As the monitoring data for Horseferry Road was limited, the main aim of the analysis was to predict the heave displacements correctly. Although pore pressures underneath the basement were not monitored during the construction or afterwards, the predicted pressures will be presented to compare the effects of the Brick and SRD Brick models. Figure 6.35 shows a comparison of the pore water pressures developed during the construction sequence. It can be seen that for both the Brick model (Figure 6.35(a)) and the SRD Brick model (Figure 6.35(b)) the maximum excess pore water pressures are developed directly beneath the base slab, in the London Clay layer. To show the build up and dissipation of excess pore water pressure in this region, the pore pressures at point A shown in Figure 6.35(a) have been plotted with time in Figure 6.36.

As the basement was excavated the vertical stress in the soil was lowered and the London Clay layer tended to swell. This led to negative pore pressures being developed in the soil closest to the base of the excavation, as the construction continued, as seen in Figure 6.36. The predictions for both the Brick and SRD Brick models displayed a similar trend. The Brick model predicted a faster decrease in pressure and a minimum pressure of -28.5kPa, compared with the slower decrease and minimum pressure of -10.9kPa predicted by the SRD Brick model. Once the basement slab was completed and the load of the basement substructure was applied, the pore pressures dissipated as the soil heaved. The Brick model predicted a rapid increase in pore pressure over the first 6 months of the monitoring period. The increase then decayed, reaching pre-construction levels after 81 months (Figure 6.36).

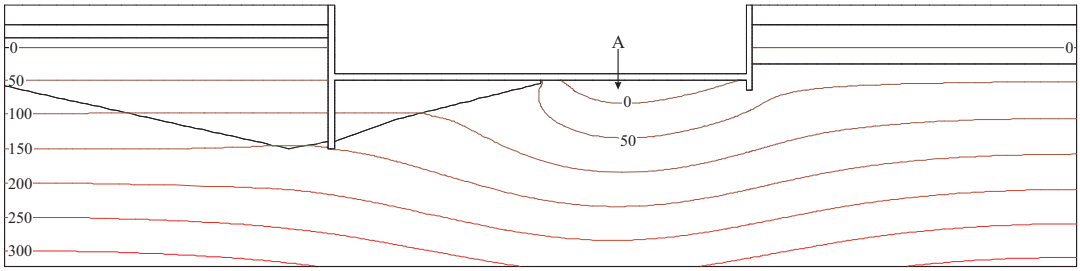

(a) BRICK model prediction

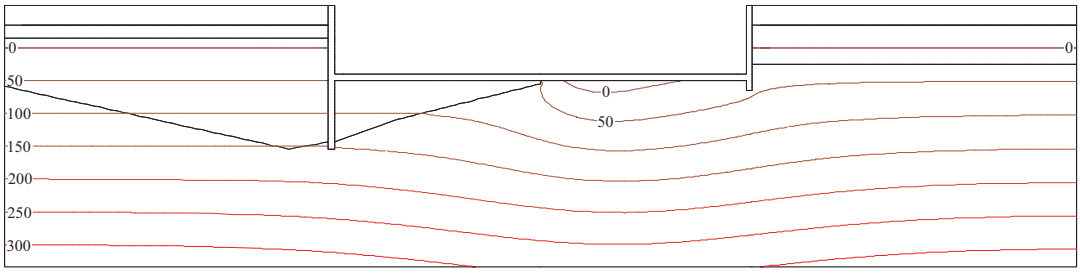

(b) SRD BRICK model prediction

Figure 6.35: Contours of pore water pressure immediately after the basement slab construction

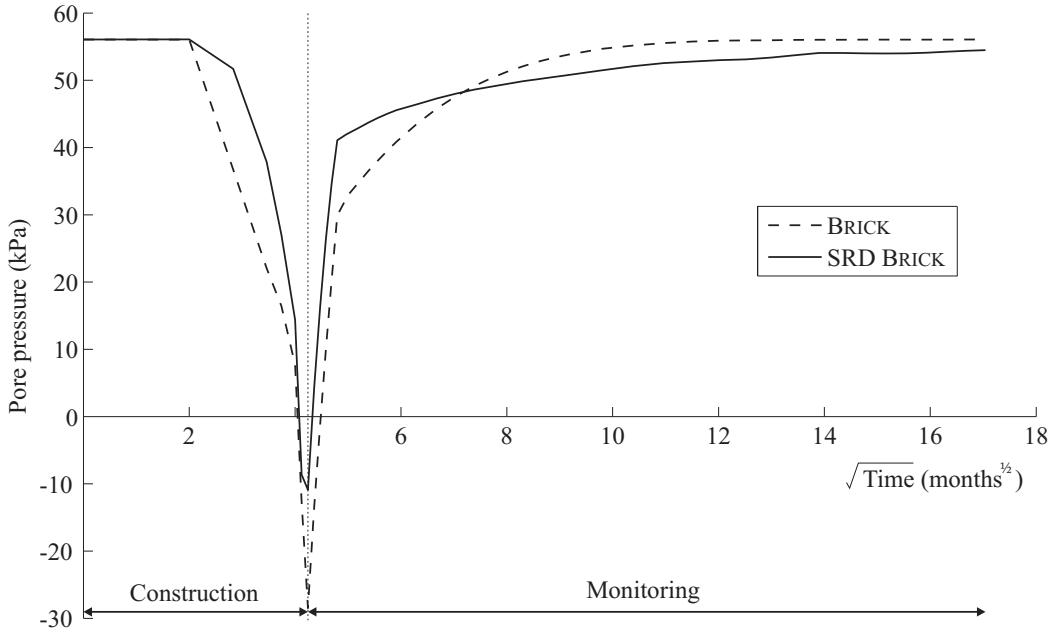

Figure 6.36: Change in pore pressure with time at Point A

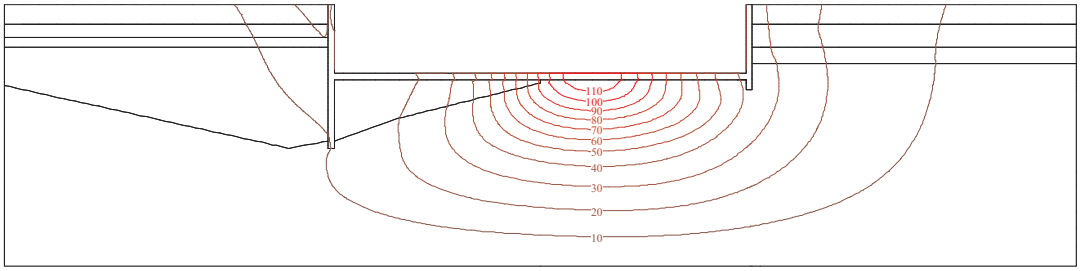

(a) BRICK model prediction

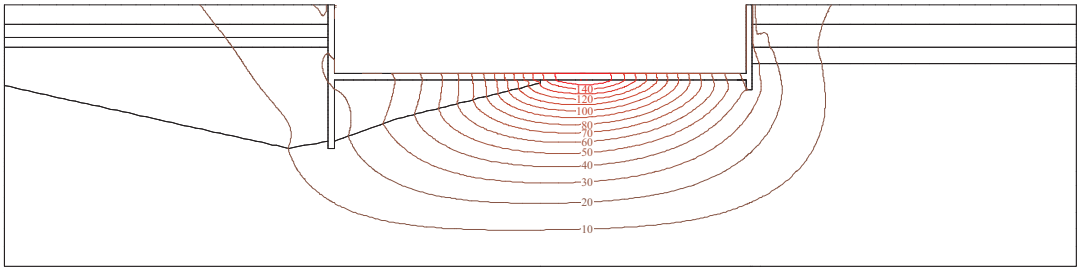

(b) SRD BRICK model prediction

Figure 6.37: Contours of resultant displacement for March 1990

The SRD BRICK model displays the same sharp increase in pressures during the first 6 months, but the following decay is much slower than that shown by the BRICK model, due to the secondary swelling effects predicted by the SRD BRICK model. This continued swelling generates small excess pore water pressures which is why the predicted excess pore water pressures in Figure 6.36 never reach zero.

Figure 6.37 shows a comparison of the resultant displacements generated during the 21 year heave period. It can be seen that both BRICK and the SRD BRICK model predict the same location of the maximum displacement, which as would be expected is the same location as the maximum excess pore water pressure shown in Figure 6.35. The displacements are concentrated across the basement slab (BRICK 110mm, SRD BRICK 160mm) with a relatively small amount of heave predicted at the diaphragm walls (BRICK & SRD BRICK 40mm). The SRD BRICK model predicts a much higher concentration of contours across the basement slab. A similar increased concentration was also seen when modelling the St James's Park tunnels in Section 6.4.

The propagation of the maximum heave displacements with time is shown in Figure 6.38. The predictions for the very early heave (1 month) are almost identical for both models, with the BRICK model then predicting a more rapid heave than the SRD BRICK model. As the heave in the BRICK model is directly tied to the excess pore pressures

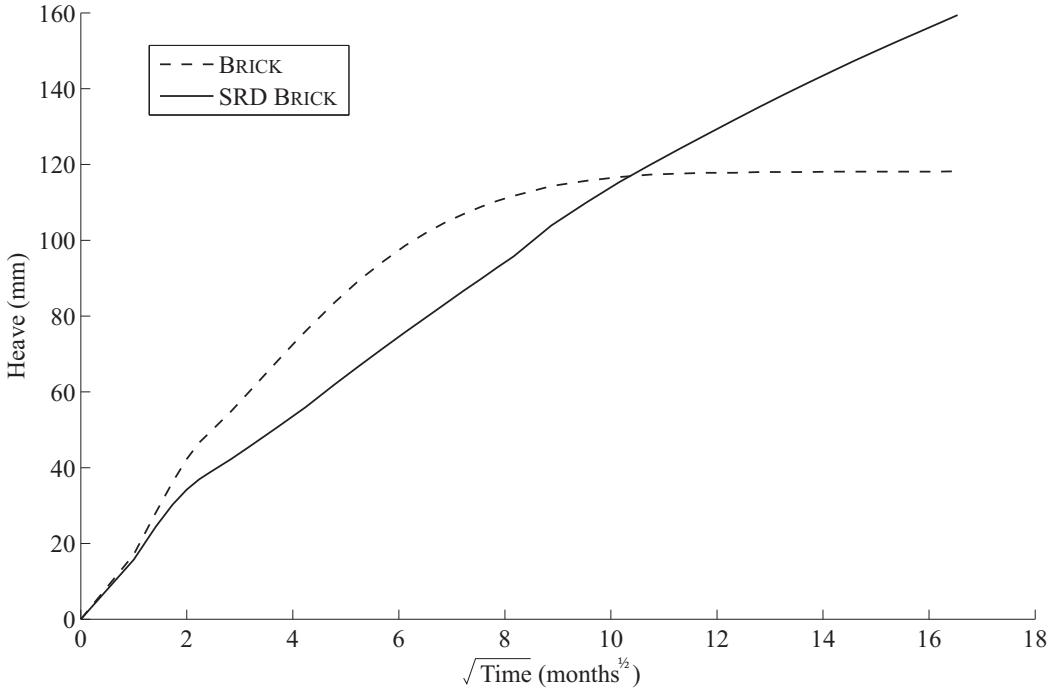

Figure 6.38: Heave predictions starting from September 1967

that exist below the basement slab, the rate of heave dramatically slows around the 81 month point, at which the excess pore pressures were almost completely dissipated (Figure 6.36). As the SRD BRICK model is able to take into account creep, the heave displacements continue even after 90% of the excess pore pressures have dissipated, leading to a much higher predicted displacement. The time origin for the data presented in Figure 6.38 is taken to be the end of the construction of the basement slab, September 1967.

For the purposes of comparison the field data for Point 5 (Figure 6.31) are taken to be comparable to the maximum heave displacements across the finite element section (Figure 6.38). The field monitoring of heave started in March 1968, 6 months after the basement slab was completed. Thus to enable a comparison between the finite element predictions and the field data, the predicted displacements were reset to zero after 6 months, Figure 6.39. The field data was taken from both May (1975) and Chapman (1999), and is indicated accordingly.

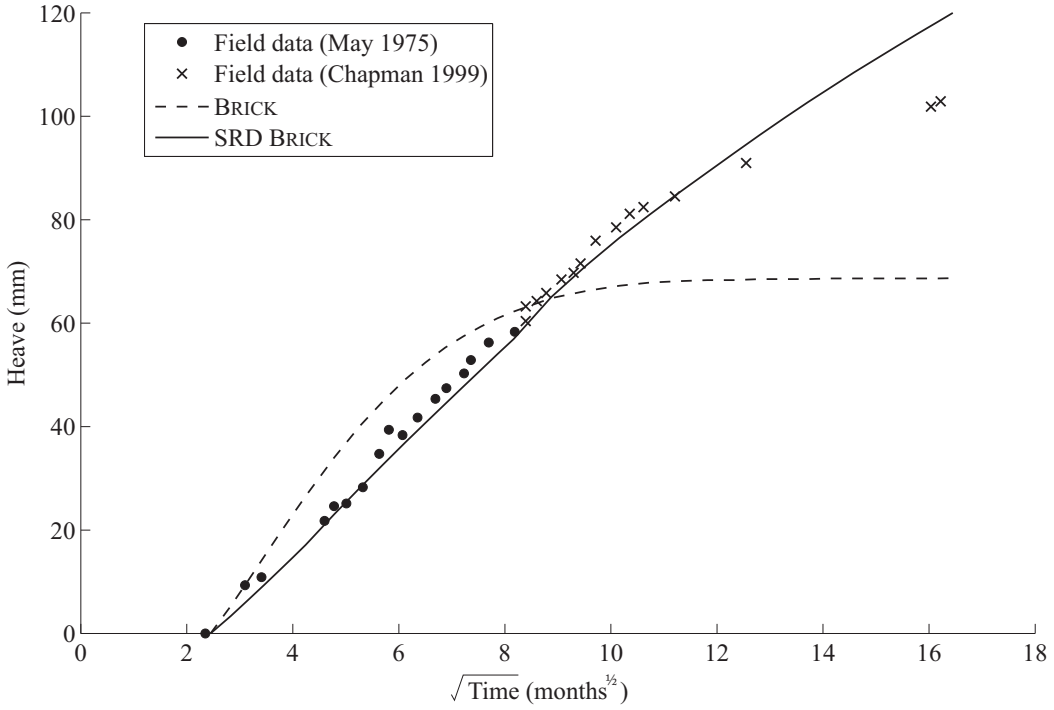

Figure 6.39: Comparison of heave predictions with field measurements

6.5.4 Discussion

Horseferry Road was seen as a valuable case history due to the long period over which heave displacements were monitored, although the monitoring was limited solely to these displacements. The use of both the BRICK and SRD BRICK models allows the net effects of secondary swelling to be seen. Approximations or assumptions have had to be made in the modelling specifically in regard to the:

- temporary prop arrangement used during construction;
- parameters used for the strata overlying the London Clay layer (these were developed in conjunction with ARUP Geotechnics);
- permeability model used for the London Clay layer;
- stiffness of the concrete used for the basement;
- reduction in the string lengths.

The temporary prop arrangement and the overlying strata parameters were seen as less important to the long term heave behaviour of the London Clay, than to behaviour during the construction process. As previously mentioned in Section 6.5.2, several different variations of the permeability model for the London Clay were tried, details of

which are given in Appendix D.2.2. The chosen model utilises a stress dependent permeability to increase the permeability below the excavation, eliminating the generation of negative effective stresses. The permeability data from Addenbrooke et al. (1997) was used to calibrate the model due to the lack of site measurements from Horseferry Road. Future work could explore the sensitivity of the predictions to the stiffness of the concrete used in the basement slab, but this was outside the scope of the current work. The string lengths for the SRD model were assumed to be half the length of those used in the BRICK model as discussed previously in Section 6.4.6.

Model	Heave displacement	Predicted/ field
Field data	102.9 mm	-
BRICK	69.7 mm	67.7%
SRD BRICK	120.6 mm	117.2%

Table 6.13: Comparison of predicted heave displacements

The comparison of the predicted displacements to the field data (Figure 6.39) shows the large effect that creep can have on the long term behaviour of London Clay. Wherever possible, accurate predictions are desired but, where the predictions do not match the observed behaviour, it is better to over-predict rather than under-predict. This will lead to a conservative design, rather than an unconservative one. Table 6.5.4 shows that the BRICK model under-predicts the heave displacements by 32.3% whereas the SRD model over-predicts the displacements by 17.2%. The SRD BRICK analysis shows a very close fit to the field data for the first 14 years (13^2 months) with the predictions gradually diverging towards the 21 year mark. Further calibration of the string lengths used in the SRD BRICK model could lead to predictions even closer to the field data, but currently the data to allow this calibration do not exist. Stress path tests measuring the stiffness degradation curve at a constant rate of strain would allow the calibration of the string lengths in the SRD BRICK model.

7

Summary and Conclusions

7.1 Introduction

The main aim of the current work was to introduce viscous effects into the Brick constitutive model. The newly developed SRD Brick model is able to demonstrate isotach strain rate behaviour, as well as time dependent effects such as creep and stress relaxation. The key points and conclusions have been drawn out of the work, and the following four sections aim to summarise these findings. Ideas for future work are presented in the final section.

7.2 The BRICK Model

The formulation and development of the Brick model was discussed in Chapter 3. The parameters for both the two and three-dimensional models were introduced, along with their formulation and the derivation of other geotechnical parameters such as those used in triaxial testing.

The analogue of the Brick model (Simpson 1992b) was used to explain the more complex aspects of soil behaviour such as the small strain stiffness and effects of recent stress history. This included demonstrative and computed brick paths plotted in strain space, with axes of volumetric and shear strain. The stress paths predicted by the Brick model were explained using the positions of the bricks relative to the man. During undrained shearing, a reduction in the mean stresses indicates that the bricks were initially at a lower volumetric strain in strain space than the man. Conversely, an increase in mean stress indicates that the bricks were at higher volumetric strain than the man, indicating an overconsolidated deposit. The stress path predicted during undrained shearing is a unique product of the positions of the bricks relative to the man.

Work done to see if a unique critical state line could be simulated, involved running a number of undrained shear tests on both lightly and heavily overconsolidated soil. This showed that the BRICK model does not predict the dilative behaviour required to satisfy the critical state framework. When the BRICK predictions during undrained shear with varying overconsolidation ratios were compared with the physical test results from Sketchley & Bransby (1973) a similar pattern was found. Often overconsolidated samples fail on the dry side of the critical state line due to the localisation of the strains.

7.3 Bricks on Ice

Chapter 4 reported initial attempts at modifying the BRICK model to incorporate viscous effects. The work of Den Haan (2001) was first recreated in a MATLAB translation of the BRICK model. Den Haan (2001) accounted for the effects of creep by allowing the bricks to continue their previous motion into the next BRICK increment, but at a logarithmically decreasing rate. This concept was named 'Bricks on Ice'. The original brick deceleration formula was changed to reflect the need for co-axial viscous effects which was explained in Section 4.4. From a comparison of the original work presented in Den Haan (2001) and the present recreation, it was clear that the theory had been interpreted correctly and that model had been correctly implemented. Modifications to the deceleration model were seen to correct the minor overshoot of the NCL seen in the swelling and recompression test.
The term stress relaxation, in an oedometer test, refers to the reduction of stresses at a constant volumetric strain, which is known to occur after a period of compression. Den Haan (2001) noted that after a period of swelling the direction of creep effects changed leading to an increase in stresses at constant volumetric strain. This behaviour was termed 'strain fixation' by Den Haan (2001) and was successfully predicted by the Bricks on Ice model.

A series of tests was conducted on the Bricks on Ice model to assess the effect the model had on the native BRICK behaviour and its suitability for use in the finite element program SAFE. These tests were: swelling and recompression, undrained shearing of normally consolidated soil, undrained shearing with varying overconsolidation ratios, undrained shearing with a holding period prior to shearing and virgin creep tests. The results showed that the Bricks on Ice model was able to recreate the increase in stiffness due to the effects of creep, but that this also led to a change in gradient of the normal consolidation line. This change in gradient is caused by the effect of the continued

motion of the bricks during one-dimensional or isotropic compression.

Modifications were made to the BRICK model to rectify the Bricks on Ice model's inability to generate parallel isotache lines. This was a manual modification which, although it successfully managed to generate isotach behaviour, involved manipulation of the initial brick positions, which is not a fundamental solution to the problem. The modified brick positions allowed the recreation of CRS parallel isotache lines, but would not be able to predict the behaviour seen in SRS tests due to the lack of strain rate dependency in the Bricks on Ice model.

The Bricks on Ice model was then used to simulate the tests conducted by Gasparre (2005) which investigated the effects of creep on the recent stress history. It was shown in the physical modelling that creep was able to erase the effects of the recent stress history, following short approach paths (within the Y_2 yield surface). However, for long approach paths (engaging the Y_2 yield surface), although the initial stiffness was controlled by the effects of creep, the stiffness during the intermediate strains was still seen to be governed by the recent stress history. The Bricks on Ice simulations were able to recreate the effects of creep on the stiffness response seen in the physical tests, at intermediate and large strains. With creep allowed, the Bricks on Ice model consistently predicted a higher stiffness in the low stress path rotation test than in the high stress path rotation test, which was unrealistic. This was caused by the direction of the continued motion of the Bricks.

The dimensionless creep constant in the Bricks on Ice approach is a very difficult parameter to calibrate, needing data for the creep rate degradation with time. The model also assumes that the soil follows a logarithmic decay in strain rate with time, which is the case for London Clay (Singh & Mitchell 1968) but may not be the case for all soils.

7.4 Strain Rate Dependent String Lengths

The concept of strain rate dependent string lengths was proposed by Sorensen (2006), who saw the concept as a method of introducing the effect of strain rate into the BRICK model. By allowing the current strain rate to dynamically effect the length of the strings, Sorensen (2006) realised that the current stress level could be varied. Increasing the length of the strings would give rise to a increase in elastic strains and a step increase in stress. Conversely decreasing the string lengths reduces the elastic

capacity a hence leads to a step decrease in stress. The concept was purely theoretical, being implemented for the first time in the current work.

In Chapter 5 a framework was developed to allow strain rate effects to be combined with effects of time dependency. Within the framework, for any given strain rate above a reference strain rate, a unique isotache line was predicted. Upon a change in strain rate a step change in isotache line was predicted as seen in the tests by Leroueil et al. (1985). The reference strain rate was defined as the rate at which both time and strain rate effects are negligible, equal to $1e^{-13}$-/s or a decay period of approximately 32 years. The different forms of mathematical law that could be used to govern the strain rate dependency of the string lengths were explored, with the employed form being that proposed by Sorensen (2006). On its own, the strain rate law predicts instantaneous jumps between strain rate isotache lines. While this may be a satisfactory approximation for high strain rates, allowing the model to jump to a $1e^{-13}$-/s isotache would preclude modelling of time dependent effects.

To allow the framework to to correctly account for increases in time, the rate at which the model could change between the strain rate isotache lines was governed by a separate time dependent function. This function took the form of the logarithmic decay function proposed by Singh & Mitchell (1968). With both models in place within the framework, both strain rate and time dependent behaviour could theoretically be predicted.

There were two possible approaches for the implementation of the framework with the Brick model. The distinguishing feature was what defined the current rate of strain in the model, the man or the individual bricks. If the rate of movement of the man (applied strain) is allowed to dictate the strain rate behaviour, the calculations are simple, as the velocity of the man is defined at the start of each Brick increment. The disadvantage with this approach is that the strain rate effects are applied globally to all bricks independent of whether they were moving or not. In the brick-led approach the length of each string is governed by the velocity of the associated brick. This requires an iterative loop to calculate the balance of brick movement and change in string length as they are co-dependent. The brick-led method was considered more rigorous and, after CRS and SRS tests were simulated using both approaches, it was adopted. The new Brick model was termed the strain rate dependent (SRD) Brick model.

Further SRS simulations with the SRD Brick model showed that it was able to predict Isotach behaviour while at the same time being able to model time dependent effects such as stress relaxation and creep. In a simulation of the SRS tests conducted by Graham et al. (1983) it was shown that strain rate dependent behaviour could also be observed in triaxial compression tests.

The SRD Brick model was finally benchmarked against the tests that formed the investigation into the effect of creep on the recent stress history conducted by Gasparre (2005). The modelling of the Gasparre tests was conducted with the same methodology as used for the Bricks on Ice recreation except that the number of bricks used in the analysis was increased. This had the effect of increasing the resolution possible in the stiffness degradation curves. The results of the simulation of the Gasparre (2005) tests showed that the SRD Brick model can successfully predict the increase in initial stiffness due to the effects of creep on low stress path rotation tests, shown also by Clayton & Heymann (2001). The model is also able to predict the normal effect of the recent stress history, with a low stress path rotation test displaying a lower initial stiffness than an equivalent test with a high stress path rotation.

The SRD Brick model represented a clear improvement in the modelling of strain rate and time dependent effects over the Bricks on Ice model. The SRD Brick model was able to deal with both Isotach strain rate behaviour and time dependent effects such as creep and stress relaxation through the implementation of the newly developed rate dependency framework.

7.5 Finite Element Modelling

In Chapter 6 the SRD Brick model was implemented into the Safe finite element program. To verify the model, a simple single element test was conducted and compared against the Matlab translation of the SRD Brick model. The test involved applying a vertical displacement to the element and monitoring the stresses at the four gauss points. The time over which the displacement was applied and the viscous constant were varied, to fully test the new model. The results were found to be acceptably close to the Matlab generated results.

Two case histories were analysed using the implemented SRD Brick model. The first was the construction of the westbound running tunnel, part of the Jubilee Line exten-

sion beneath St James's Park, London. For this tunnel, many previous numerical analyses had been run to attempt to predict the unusually large surface settlement trough that was seen in the field monitoring (Addenbrooke et al. (1997), Grammatikopoulou (2004)). The effect of creep on the predicted settlement trough was also investigated by Grammatikopoulou et al. (2008) who, using the M3-SKH model, idealised the effect of creep by centralising the yield and history surfaces on the current stress point. Grammatikopoulou et al. (2008) showed that using this method for the modelling of creep gave worse predictions of the settlement.

Three soil models for the London Clay layer were used in the present modelling of the St James's Park tunnel. These were: the Mohr-Coulomb model (to enable comparison with a widely used model), the Brick model (to show the effect of modelling the small stain stiffness and stress history) and the SRD Brick model (to demonstrate the effects of viscous soil behaviour). The maximum vertical surface displacements were compared for all three models for the same amount of volume loss. The predictions made by the Mohr-Coulomb model gave rise to a very wide, relatively shallow settlement trough with a maximum displacement of only 9.3mm. The Brick model improved the analysis by narrowing the settlement trough, allowing the prediction of of a deeper (12.9mm) settlement trough. By introducing strain rate dependency into the analysis the SRD Brick model was able to further narrow the settlement trough leading to a 17.25mm settlement, amounting to 86.7% of the measured field displacement. The results of this analysis showed that due to the relatively high strain rate associated with the tunnel's construction the predictions could be improved by the use of a model that accounts for rate of strain. A parametric study was conducted to assess the effect of the shortening of the string lengths on the SRD Brick model predictions, which showed that the analysis was relatively insensitive to changes in string length when compared with effects of the viscous constant.

The second case history was that of Horseferry Road, a deep basement in London in which the heave of the basement slab after construction was monitored over a period of 21 years. Due to the age of the project (1960s), the only monitoring data available for comparison was the measured heave of the basement slab. The construction of the slab was modelled in multiple stages, with consolidation allowed to occur during this period. As the Mohr-Coulomb gave poor results in the modelling of St James's Park tunnel, it was not used for the modelling of Horseferry Road.

The results showed that the Brick model was able to predict the primary settlements due to the dissipation of the pore water pressures, but that after a period of eight years the excess pore water pressures had completely dissipated and the heave ceased. This was expected as the Brick model has no way to account for time dependent effects, leading to a predicted 69.7mm displacement, 68% of the observed value. The SRD Brick model accurately predicted the combined primary consolidation and creep behaviour over the initial fourteen year period, but over-predicted the heave by 17% over the full 21 year period, with a predicted 120.6mm displacement.

It may be concluded that the SRD Brick model is capable of improving predictions in cases where viscous effects are deemed to have a possible influence. In the case of strain rate dependency this was identified in the modelling of a tunnel construction where the tunnel heading was moving at around 45m/day. In the case of time dependent behaviour, such as creep, the modelling of the long term heave of a basement in London Clay showed again that the predictions are improved by the use of a viscous soil model. While viscous effects have had a relatively large impact on the current analyses these effects may not always be as significant. Other factors currently discounted may also contribute, the most notable of which is the possible effect of anisotropy in the tunnelling analysis.

7.6 Future Research

There are some areas for future research that could cast light on the assumptions made in the current work. Much research has been conducted on London Clay, but even for this soil there are still gaps in the knowledge required to calibrate an advanced constitutive model reliably.

- The generation of a stiffness degradation curve *at a known constant rate of strain.* It is known that viscous behaviour effects the stiffness of the soil, but by how much the strain rate effects the stiffness degradation curve is unknown. In conducting a strain path reversal test at a constant rate of strain the effects of strain rate on the stiffness degradation curve can be assessed.
- The current strain rate dependency framework makes an assumption that the rate at which the soil is initially sheared affects the rate from which the strain rate decays. Currently the initial rate from which the strain rate decays, is taken to be equal to the previously applied strain rate, but there are no experimental data currently to back up this assumption.

- There is also scope for further tests to be conducted into the effect of creep on the recent stress history. The tests conducted by Gasparre (2005) are as yet unrepeated, and some results from the current work are backed up by a single physical test.

There are a number of aspects that were seen as outside the scope of the current work and could form interesting future studies in their own right.

- The generation of contours of incremental strain energy as seen in Burland & Georgiannou (1991). This would allow the visualisation of the effects of the SRD Brick model in comparison to the original Brick model.
- Modelling of the tunnel lining installation and long term settlement of the St James's Park case study, including the construction of the second, eastbound tunnel as attempted by Wongsaroj, Soga & Mair (2007).
- Further analysis of the Horseferry Road case history to include a parametric study into the effect of the stiffness of the basement slab on the measured heave. Advanced models for the concrete could also be incorporated to vary its stiffness with time.
- Modelling of creep rupture, in samples at sufficiently high deviator stresses. The SRD Brick model might be able to predict behaviour not only during primary consolidation and secondary compression but also tertiary creep.

The Brick model has historically been developed for analysis of London Clay. Advanced testing on other soils would allow the Brick model to be calibrated, diversifying the applications for the model.

References

Addenbrooke, T. I. (1996). *Numerical Analysis of Tunnelling in Stiff Clays*, PhD Thesis, Imperial College, London.

Addenbrooke, T. I., Potts, D. M. & Puzrin, A. M. (1997). The influence of pre-failure soil stiffness on the numerical analysis of tunnel construction, *Géotechnique* **47**, No. 3: 693–712.

Al-Tabbaa, A. & Wood, D. M. (1989). An experimentally based 'bubble' model for clay, *NUMOG 3, Niagra Falls* pp. 91–99.

Ali, F. H. (1984). *The time dependent behaviour of clay during cylindrical cavity expansion*, PhD Thesis, University of Sheffield.

Atkinson, J. & Bransby, P. (1978). *The Mechanics of Soils: An Introduction to Critical State Soil Mechanics*, McGraw-Hill.

Atkinson, J. H. (2000). Non-linear soil stiffness in routine design, *Géotechnique* **50**, No. 5: 487–508.

Atkinson, J. H. & Sallfors, G. (1991). Experimental determination of soil properties. General Report to Session 1, *Proceedings of the 10th European Conference on Soil Mechanics and Foundation Engineering, Florence* **3**: 915–956.

Atkinson, J. H., Richardson, D. & Stallebrass, S. E. (1990). Effect of recent stress history on the stiffness of overconsolidated soil, *Géotechnique* **40**, No. 4: 531–540.

Biscontin, G. & Pestana, J. M. (2001). Influence of peripheral velocity on vane shear strength of an artificial clay, *Geotechnical Testing Journal* **24**, No. 4: 423–429.

Bishop, A. W. (1966). The strength of soils as engineering materials, *Géotechnique* **16**, No. 2: 91–130.

Bjerrum, L. (1967). Engineering geology of Norwegian normally-consolidated marine clays as related to settlements of buildings, *Géotechnique* **17**, No. 2: 81–118.

Bodas, T. (2008). *Numerical modelling of the time dependent behaviour of clays*, PhD Thesis, Imperial College London.

Burland, J. B. (1989). Ninth Laurits Bjerrum Memorial Lecture: "Small is Beautiful" - the stiffness of soils at small strains, *Canadian Geotechnical Journal* **26**: 499–516.

Burland, J. B. & Georgiannou, V. N. (1991). Small strain stiffness under generalised stress changes, *Proceedings of the 10th European Conference on Soil Mechanics and Foundation Engineering, Florence* **1**: 41–44.

Chapman, T. (1999). Horseferry Road basement, long term heave data, Arup *Geoguide 1999-10 TC* .

Clayton, C. R. I. & Heymann, G. (2001). Stiffness of Geomaterials at very small strains, *Géotechnique* **51**, No. 3: 245–255.

Collins, I. F. (2005). The concept of stored plastic work or frozen elastic energy in soil mechanics, *Géotechnique* **55**, No. 5: 373–382.

Crooks, J. H. A. & Graham, J. (1976). Geotechnical properties of the Belfast estuarine deposits, *Géotechnique* **26**, No. 2: 293–315.

Den Haan, E. J. (2001). *Bricks on Ice*, GeoDelft Eureka project nr. 511200.

Di Benedetto, H. & Tatsuoka, F. (1997). Small strain behaviour of geomaterials: modelling of strain effects, *Soils and Foundations* **32**, No. 2: 127–138.

Di Benedetto, H., Tatsuoka, F. & Ishihara, M. (2002). Time-dependent shear deformation characteristics of sand and their constitutive modelling, *Soils and Foundations* **42**, No. 2: 1–22.

Dimmock, P. S. & Mair, R. J. (2007). Volume loss experienced on open-face London Clay tunnels, *Proceedings of the ICE: Geotechnical Engineering* **160**, Issue GE1: 2–11.

Duttine, A., Tatsuoka, F., Lee, J. & Kongkitkul, W. (2009). Viscous property of toyoura sand over a wide range of shear deformation rate and its model simulation, *Soils and Foundations* **49**, No. 2: 231–248.

Einav, I. & Randolph, M. (2006). Effect of strain rate on mobilised strength and thickness of curved shear bands, *Géotechnique* **56**, No. 7: 501–504.

Gasparre, A. (2005). *Advanced laboratory characterisation of London Clay*, PhD Thesis, Imperial College London.

Gasparre, A., Nishimura, S., Minh, N. A., Coop, M. R. & Jardine, R. J. (2007). The stiffness of natural London Clay, *Géotechnique* **57**, No. 1: 33–47.

Graham, J., Crooks, J. H. A. & Bell, A. L. (1983). Time effects on the stress-strain behaviour of natural clays, *Géotechnique* **33**, No. 3: 327–340.

Grammatikopoulou, A. (2004). *Development, implementation and application of kinematic hardening models for overconsolidated clays*, PhD Thesis, Imperial College, London.

Grammatikopoulou, A., Zdravkovic, L. & Potts, D. M. (2008). The influence of previous stress history and stress path direction on the surface settlement trough induced by tunnelling, *Géotechnique* **58**, No. 4: 269–281.

Hardin, B. O. (1978). *The nature of stress-strain behaviour for soils. State-of-the-art report.*, American Society of Civil Engineers, New York.

Heymann, G. (1998). *The stiffness of soils and weak rocks at very small strains*, PhD Thesis, University of Surrey, Guildford.

Hight, D. W., Jardine, R. J. & Gens, A. (1987). The behaviour of soft clays. Embankments on soft clays, *Public Works Research Centre, Athens* **Ch. 2**: 33–158.

Jardine, R. J. (1985). *Investigations of pile-soil behaviour with special reference to the foundations of offshore structures*, PhD Thesis, Imperial College, University of London, London.

Jardine, R. J. (1992). Some observations on the kinematic nature of soil stiffness, *Soils and Foundations* **29**, No. 3: 436–447.

Jardine, R. J., Potts, D. M., St John, H. D. & Hight, D. W. (1991). Some practical applications of a non-linear ground model, *Proceedings of the 10th European Conference on Soil Mechanics and Foundation Engineering, Florence* **1**: 223–228.

Jardine, R. J., Symes, M. J. & Burland, J. B. (1984). The measurement of soil stiffness in the triaxial apparatus, *Géotechnique* **34**, No. 3: 323–340.

Jovičić, V. & Coop, M. R. (1998). The measurement of stiffness anisotropy in clays with bender element tests in the triaxial apparatus, *ASTM Geotechnical Testing Journal* **21**, No. 1: 3–10.

Kanapathipillai, A. (1996). *Review of the Brick model of soil behaviour*, MSc Thesis, Imperial College, London.

King, C. (1981). The stratigraphy of the London Basin and associated deposits, *Tertiary Research Special Paper,* **6**, Backhuys, Rotterdam.

Kongsukprasert, L. & Tatsuoka, F. (2003). Viscous effects coupled with ageing effects on the stress-strain behaviour of cement-mixed gravel, *Proceedings of the 3rd International Symposium on the Deformation Characteristics of Geomaterials, IS Lyon* pp. 569–577.

Ladd, C. C. (1977). Stress deformation and strength characteristics, *Proceedings of the 9th International Conference of Soil Mechanics and Foundation Engineering, Tokyo* pp. 421–494.

Leroueil, S. (1995). Could it be that clays have no unique way of behaving during consolidation?, *Compression and Consolidation of Clays, Yoshikuni & Kusakabe eds., Balkema* pp. 1039–1048.

Leroueil, S., Kabbaj, M., Tavernas, F. & Bouchard, R. (1985). Stress-strain-strain rate relation for the compressibility of sensitive natural clays, *Géotechnique* **35**, No. 2: 159–180.

Mair, R. J. (1993). Developments in geotechnical engineering research: application to tunnels and deep excavations, *Proceedings of the ICE: Civil Engineering* **93**: 27–41.

Mair, R. J. (2008). Tunnelling and geotechnics: new horizons, *Géotechnique* **58**, No. 9: 695–736.

May, J. (1975). Heave on a deep basement in the London Clay, *Proceedings of the 2nd Conference on the Settlement of Structures (COSOS), Pentech Press, London* pp. 177–183.

Mesri, G. & Choi, Y. K. (1985). The uniqueness of the end-of-primary (EOP) void ratio-effective stress relationship, *Proceedings of the 11th International Conference of Soil Mechanics and Foundation Engineering, San Fransisco* pp. 587–590.

Mitchell, J. K. (1993). *Fundamentals of Soil Behavior*, John Wiley & Sons, London.

Mroz, Z. (1967). On the description of anisotropic work-hardening, *Journal of the Mechanics and Physics of Solids* **15**, No. 3: 163–175.

Mroz, Z. & Norris, V. A. (1982). *Elastoplastic and viscoplastic constitutive models for soils with application to cyclic loading. Soil Mechanics-Transient and Cyclic Loads, G.N. Pande and O.C. Zienkiewicz (eds.)*, John Wiley and Sons Ltd.

Mroz, Z., Norris, V. A. & Zienkiewicz, O. C. (1979). Application of an anisotropic hardening model in the analysis of elasto-plastic deformation of soils, *Géotechnique* **29**, No. 1: 1–34.

Muir-Wood, D. (1990). *Soil Behaviour and Critical State Soil Mechanics*, Cambridge University Press.

Nyren, R. J., Standing, J. R. & Burland, J. B. (2001). Surface displacements at St James's Park greenfield reference site above twin tunnels through the London Clay, *Building response to tunnelling;* **Vol 2**, case studies, J.B. Burland, J.R. Standing and F.M. Jardine (eds.), Thomas Telford, London, UK: 387–400.

Oasys (2001). Brick *17* Geo *suite for Windows*, Oasys Ltd, Newcastle.

Oasys (2006). Safe *18.1* Geo *suite for Windows*, Oasys Ltd, Newcastle.

Oka, F., Kodaka, T., Kimoto, S., Ishigaki, S. & Tsuji, C. (2003). Step-changed strain rate effect on the stress-strain relations of clay and a constitutive modeling, *Soils and Foundations* **43**, No. 4: 189–202.

Potts, D. M. & Zdravkovic, L. (2001a). *Finite element analysis in geotechnical engineering: Vol 1, theory*, Thomas Telford, London.

Potts, D. M. & Zdravkovic, L. (2001b). *Finite element analysis in geotechnical engineering: Vol 2, application*, Thomas Telford, London.

Richardson, A. M. & Whitman, R. V. (1963). Effect of strain rate upon undrained shear resistance of a saturated remoulded fat clay, *Géotechnique* **13**, No. 3: 310–324.

Richardson, D. (1988). *Investigations of threshold effects in soil deformations.*, PhD Thesis, City University, London.

Roscoe, K. & Burland, J. (1968). *On the generalised stress-strain behaviour of wet clay*, Cambridge University Press, New York.

Santucci de Magistris, F. & Tatsuoka, F. (1999). Time effects on the stress-strain behaviour of metramo silty clay, *Proceedings of the 2nd International Conference on the Pre-Failure Deformation Characteristics of Geomaterials, IS Torino* pp. 491–555.

Schofield, A. M. & Wroth, C. P. (1968). *Critical State Soil Mechanics*, McGraw-Hill, London.

Simpson, B. (1992a). Development and application of a new soil model for prediction of ground movements, *Peter Wroth Memorial Conference, Oxford.* pp. 628–643.

Simpson, B. (1992b). Retaining structures: displacement and design, *Géotechnique* **42**, No. 4: 541–576.

Simpson, B. (2006). Development of the Brick model, *Private communication* .

Simpson, B., O'Riordan, N. J. & Croft, D. D. (1979). A computer model for the analysis of ground movements in London Clay, *Géotechnique* **29**, No. 2: 149–175.

Singh, A. & Mitchell, J. K. (1968). General stress-strain-time function for soils, *Journal of the Soil Mechanics and Foundations Division, ASCE* **94**, No. SM1: 200–220.

Sketchley, C. J. & Bransby, P. L. (1973). The behaviour of an overconsolidated clay in plane strain, *Proceedings of the 8th International Conference on Soil Mechanics and Foundation Engineering, Moscow* pp. 377–384.

Sorensen, K. (2006). *Influence of viscosity and ageing on the behaviour of clays*, PhD Thesis, University College London.

Sorensen, K. K., Baudet, B. A. & Simpson, B. (2007a). Discussion: Influence of structure on the time-dependent behaviour of a stiff sedimentary clay, *Géotechnique* **57**, No. 9: 783–787.

Sorensen, K. K., Baudet, B. A. & Simpson, B. (2007b). Influence of structure on the time-dependent behaviour of a stiff sedimentary clay, *Géotechnique* **57**, No. 1: 113–124.

St. John, H. D. (1975). *Field and theoretical studies of the behaviour of ground around deep excavations in London Clay*, PhD Thesis, University of Cambridge, Cambridge.

Stallebrass, S. E. (1990). *Modelling the effect of recent stress history on the deformation of overconsolidated soils*, PhD Thesis, City University, London.

Stallebrass, S. E. & Taylor, R. N. (1997). The development and evaluation of a constitutive model for the prediction of ground movements in overconsolidated clay, *Géotechnique* **47**, No. 2: 235–253.

Standing, J. R. & Burland, J. B. (2006). Unexpected tunnelling volume loss in the Westminster area, London, *Géotechnique* **56**, No. 1: 11–26.

Standing, J. R., Nyren, R. J., Longworth, T. I. & Burland, J. B. (1996). The measurement of ground movements due to tunnelling at two control sites along the Jubilee Line Extension, *Proceedings of the international symposium on geotechnical aspects of underground construction in soft ground, London* pp. 659–664.

Tatsuoka, F. (2007). Keynote lecture: Inelastic deformation characteristics of geomaterial, *Soil stress-strain behaviour: measurement, modelling and analysis. Proceedings of the Geotechnical Symposium, Rome, 2006* pp. 1–108.

Tatsuoka, F., Ishihara, M. & Maruyama, N. (2000). On the structure of one-dimensional model for time-dependent deformation properties of geomaterials, *Proceedings of the Japanese Conference on Geotechnical Engineering, Gifu* **1**: 305–306.

Tatsuoka, F., Ishihara, M., Di Benedetto, H. & Kuwano, R. (2002). Time-dependent shear deformation characteristics of geomaterials and their simulation, *Soils and Foundations* **42**, No. 2: 531–540.

Vaid, Y. P. & Campanella, R. G. (1977). Time-dependent behaviour of undisturbed clay, *ASCE Journal of the Geotechnical Engineering Division* **103**, No. GT7: 693–709.

Vaid, Y. P., Robertson, P. K. & Campanella, R. G. (1979). Strain rate behaviour of Saint-Jean-Vianney clay, *Canadian Geotechnical Journal* **16**: 34–42.

Viggiani, G. (1992). Dynamic measurement of small strain stiffness of fine grained soils in the triaxial apparatus, *Proc. workshop on experimental characterization and modelling of soils and soft rocks, Napoli* pp. 75–97.

Viggiani, G. & Atkinson, J. H. (1995). Stiffness of fine-grained soils at very small strains, *Géotechnique* **45**, No. 2: 249–265.

Wongsaroj, J., Soga, K. & Mair, R. J. (2007). Modelling of long-term ground response to tunnelling under St Jamess Park, London, *Géotechnique* **57**, No. 1: 75–90.

A

BRICK Parameter Proofs

A.1 Stress-strain relationships

Proof of the relationship between in first shear and stress components via the shear modulus G.

$$\text{Shear Stress Component 1, } t_{zx} = \frac{(\sigma_z - \sigma_x)}{2}$$

$$\text{From the stiffness matrix, } \sigma_z = \frac{E}{(1+\nu)(1-2\nu)}\left[(1-\nu)\varepsilon_x + \nu\varepsilon_y + \nu\varepsilon_z\right]$$

$$\sigma_x = \frac{E}{(1+\nu)(1-2\nu)}\left[\nu\varepsilon_x + \nu\varepsilon_y + (1-\nu)\varepsilon_z\right]$$

$$\text{Therefore, } t_{zx} = \frac{E}{2(1+\nu)(1-2\nu)}\left[\varepsilon_z(1-2\nu) - \varepsilon_x(1-2\nu)\right]$$

$$\Leftrightarrow \frac{E\cancel{(1-2\nu)}}{2(1+\nu)\cancel{(1-2\nu)}}\left[\varepsilon_z - \varepsilon_x\right]$$

$$\text{Since, } G = \frac{E}{2(1+\nu)}$$

$$\text{and, } g_{zx} = \varepsilon_z - \varepsilon_x$$

$$t_{zx} = G\, g_{zx}$$

Proof of the relationship between in second shear and stress components via the shear modulus G.

$$\text{Shear Stress Component 2, } t_y = \frac{(2\sigma_y - \sigma_x - \sigma_z)}{2\sqrt{3}}$$

$$\text{From the stiffness matrix, } \sigma_y = \frac{E}{(1+\nu)(1-2\nu)}\left[\nu\varepsilon_x + (1-\nu)\varepsilon_y + \nu\varepsilon_z\right]$$

$$\sigma_x = \frac{E}{(1+\nu)(1-2\nu)}\left[\nu\varepsilon_x + \nu\varepsilon_y + (1-\nu)\varepsilon_z\right]$$

$$\sigma_z = \frac{E}{(1+\nu)(1-2\nu)}\left[(1-\nu)\varepsilon_x + \nu\varepsilon_y + \nu\varepsilon_z\right]$$

$$
\begin{aligned}
\text{Therefore, } t_y = \frac{1}{2\sqrt{3}}\frac{E}{(1+\nu)(1-2\nu)}(2\nu\varepsilon_x + 2(1-\nu)\varepsilon_y + 2\nu\varepsilon_z \ldots \\
- [\nu\varepsilon_x + \nu\varepsilon_y + (1-\nu)\varepsilon_z] \ldots \\
- [(1-\nu)\varepsilon_x + \nu\varepsilon_y + \nu\varepsilon_z]) \\
\Leftrightarrow \frac{1}{2\sqrt{3}}\frac{E}{(1+\nu)(1-2\nu)}(2(1-2\nu)\varepsilon_y \ldots \\
- (1-2\nu)\varepsilon_x(1-2\nu)\varepsilon_z) \\
\Leftrightarrow \frac{1}{2\sqrt{3}}\frac{\cancel{E(1-2\nu)}}{(1+\nu)\cancel{(1-2\nu)}}[2\,\varepsilon_y - \varepsilon_x - \varepsilon_z] \\
\Leftrightarrow \frac{1}{\sqrt{3}}\frac{E}{2(1+\nu)}[2\,\varepsilon_y - \varepsilon_x - \varepsilon_z] \\
\Leftrightarrow G\frac{(2\varepsilon_y - \varepsilon_x - \varepsilon_z)}{\sqrt{3}} \\
t_y = G\,g_y
\end{aligned}
$$

A.2 Octahedral shear strain

Proof of the octahedral shear strain relationship:

$$
\begin{aligned}
{g_{zx}}^2 &= (\varepsilon_z - \varepsilon_x)^2 = {\varepsilon_z}^2 - 2\varepsilon_{zx} + {\varepsilon_x}^2 \\
{g_y}^2 &= \left(\frac{(2\varepsilon_y - \varepsilon_x - \varepsilon_z)}{\sqrt{3}}\right)^2 = \frac{1}{3}(2\varepsilon_y - \varepsilon_x - \varepsilon_z)^2 \\
&= \frac{1}{3}(4{\varepsilon_y}^2 + {\varepsilon_x}^2 + {\varepsilon_z}^2 - 4\varepsilon_{xy} - 4\varepsilon_{yz} + 2\varepsilon_{zx}) \\
{g_y}^2 + {g_{zx}}^2 &= \frac{4}{3}({\varepsilon_y}^2 + {\varepsilon_x}^2 + {\varepsilon_z}^2 - \varepsilon_{xy} - \varepsilon_{yz} - \varepsilon_{zx}) \\
&= \frac{2}{3}\left[(\varepsilon_x - \varepsilon_y)^2 + (\varepsilon_y - \varepsilon_z)^2 + (\varepsilon_z - \varepsilon_x)^2\right] \\
\varepsilon_{ij} &= \frac{\gamma_{ij}}{2} \\
{\varepsilon_{ij}}^2 &= \left(\frac{\gamma_{ij}}{2}\right)^2 = \frac{{\gamma_{ij}}^2}{4} \\
{\gamma_{oct}}^2 &= \frac{4}{9}\left[(\varepsilon_x - \varepsilon_y)^2 + (\varepsilon_y - \varepsilon_z)^2 + (\varepsilon_z - \varepsilon_x)^2 + \frac{3}{2}({\varepsilon_{xy}}^2 + {\varepsilon_{yz}}^2 + {\varepsilon_{zx}}^2)\right] \\
&= \frac{4}{9}\left[\frac{3}{2}({g_y}^2 + {g_{zx}}^2) + \frac{3}{2}\left(\frac{{\gamma_{xy}}^2}{4} + \frac{{\gamma_{yz}}^2}{4} + \frac{{\gamma_{zx}}^2}{4}\right)\right] \\
&= \frac{2}{3}\left({g_y}^2 + {g_{zx}}^2 + \frac{{\gamma_{xy}}^2}{4} + \frac{{\gamma_{yz}}^2}{4} + \frac{{\gamma_{zx}}^2}{4}\right)
\end{aligned}
$$

B

MATLAB code

B.1 The BRICK model

The code listed in this section is a MATLAB version of the FORTRAN code that was given in Simpson (1992b) and forms the basis of modifications to the BRICK program. The code structure differs from that given in Simpson (1992b) in that 'goto' loops were taken out in favour of linear programming wherever possible.

```
function[DSS,DSNP,DSNB,ITERBR,SNT]=brick(IE,SS,SN,ZERO,SNB,...
VOLP,NC,DSN,DSS,NB,SL,SNBP,TOLBR,RLAM,RKAP,RIOT,BETA,FGK)

% Apply strain increment
PSRED=zeros(1,NC);
SNT=SN+DSN;
SSM=SS;
RILAM=RIOT/(RLAM-RIOT);
DSS=zeros(1,NC);

% Iterate to find plastic and hence stress inc
Finish=0;
ITERBR=0;
while Finish==0
  ITERBR=ITERBR+1;
  IFAILB=0;

  % Modify RIOT for BETA effect
  T=(SS(1)+0.5*DSS(1))/ZERO(2);
  TT=(SN(1)+0.5*DSN(1)-ZERO(1)-RLAM*log(T));
  TT=max(TT,0);
  BETMOD=1+BETA*TT;
  RIOTBB=RIOT/BETMOD;
  RIKAP=RIOTBB/(RKAP-RIOTBB);
  DSNP=zeros(1,NC);

  % Calc brick movements and plastic strains
  for JB=(1:NB)
    T=(SS(1)+0.5*DSS(1))/ZERO(2);
    if T<=1e-15
      error('!!!Negative Mean Stress!!!');
    end
```

```
  SLJB=SL(JB);
  % Reset T for each brick
  T=0;
  % For each component
  for JC=(1:NC)
    % Resetting to zero brick movements
    DSNB(JC,JB)=0;
    % Increase in strain on brick per component
    T1=SN(JC)+DSN(JC)-SNB(JC,JB)-PSRED(JC);
    % sum of compenents for brick
    T=T+(T1*T1);
  end
  T=sqrt(T);
  % 3D vector length finding - root sum of squares
  % T=distance of brick from new strain point or string length

  % Elastic Strain
  if T<=SLJB
    for JC=(1:NC)
      % Brick movement
      DSNB(JC,JB)=DSNB(JC,JB)+PSRED(JC);
    end
  % Plastic Strain
  else
  % Brick > string length from new strain point move brick by DSNB,
  % giving plastic strain DSNP
    T=(T-SLJB)/T;
    for JC=(1:NC)
      % Max increase in strain on brick per component
      % proportionally reduced by T
      DSNB(JC,JB)=(SN(JC)+DSN(JC)-SNB(JC,JB)-PSRED(JC))*T;
      % Sum of bricks component increase
      DSNP(JC)=DSNP(JC)+(DSNB(JC,JB)*SNBP(JB));
      % Brick movement
      DSNB(JC,JB)=DSNB(JC,JB)+PSRED(JC);
    end
  end
end

% Compute PSRED(1) from volumetric strain
T2=max(0,(VOLP(1)+DSNP(1)-VOLP(2)));
T1=DSNP(1)-T2;
PSRED(1)=T1*RIKAP+T2*RILAM;

% Compute DSS(1) and check against conversion criteria
TDSS=DSS(1);
% Reassign old increment of Mean Stress
DSS(1)=(exp((DSN(1)-DSNP(1))/RIOTBB)-1)*SS(1);
SSM(1)=SS(1)+0.5*DSS(1);
T=max(SSM(1),abs(DSS(1)));
TOLSS=T*TOLBR;
if abs(DSS(1)-TDSS)>TOLSS
  IFAILB=IFAILB+1;
end

% Compute PSRED(>1)from DSS(1)
for JC=(2:NC)
  PSRED(JC)=SSM(JC)*DSS(1)*RIOTBB/(FGK*SSM(1)*SSM(1)^1);
```

```
  end

  if ITERBR==1
    continue
  end

  % Find shear stresses DSS(>1) and check tolerance
  for JC=(2:NC)
    T=DSS(JC);
    DSS(JC)=(DSN(JC)-DSNP(JC))*SSM(1)^1*FGK/RIOTBB;
    if abs(DSS(JC)-T)>TOLSS/2
      IFAILB=IFAILB+1;
    end
  end

  % Check convergence min 7 max 50 iterations
  if ITERBR<50 && IFAILB>0
    for JC=(2:NC)
      SSM(JC)=SS(JC)+0.5*DSS(JC);
    end
  elseif ITERBR<7
    for JC=(2:NC)
      SSM(JC)=SS(JC)+0.5*DSS(JC);
    end
  else
        Finish=1;
  end
end
```

To make sure the MATLAB recreation of the BRICK model was functioning correctly, a check was completed by running a one-dimensional compression, swelling and recompression test with both codes. Figure B.1 shows the comparison between the FORTRAN and MATLAB results for the plot of volumetric strain versus mean stress. The two plots are indistinguishable for the entire test. The same can be said about the plot of mean stress versus shear stress seen in Figure B.2. These results show that the BRICK model is correctly functioning in the MATLAB code.

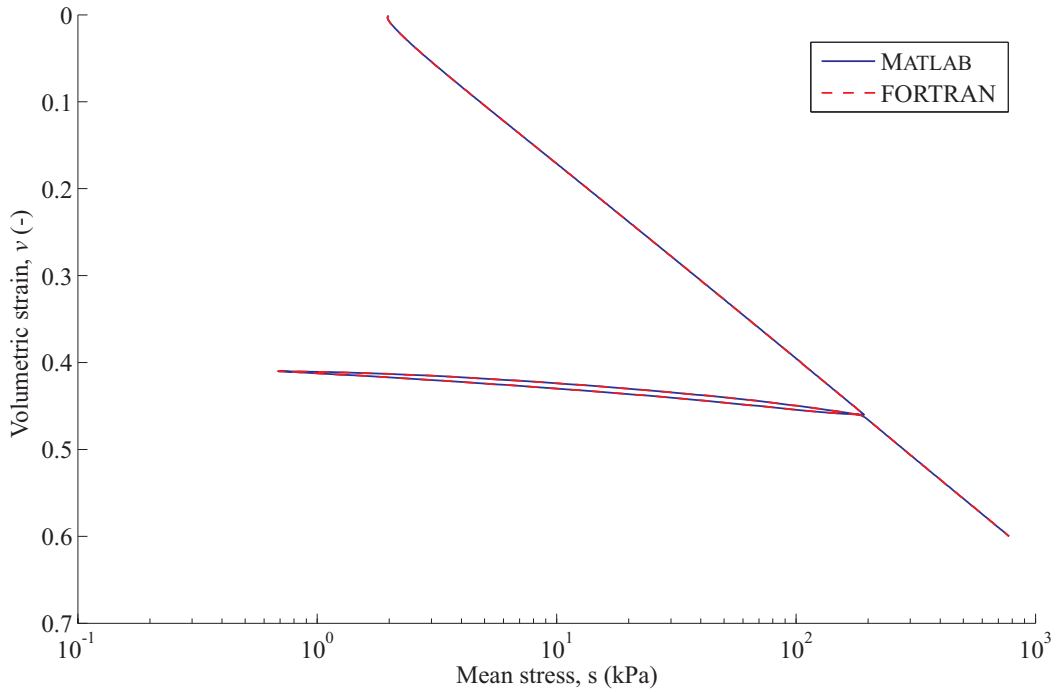

Figure B.1: Volumetric strain versus mean stress for swelling and recompression code comparison test

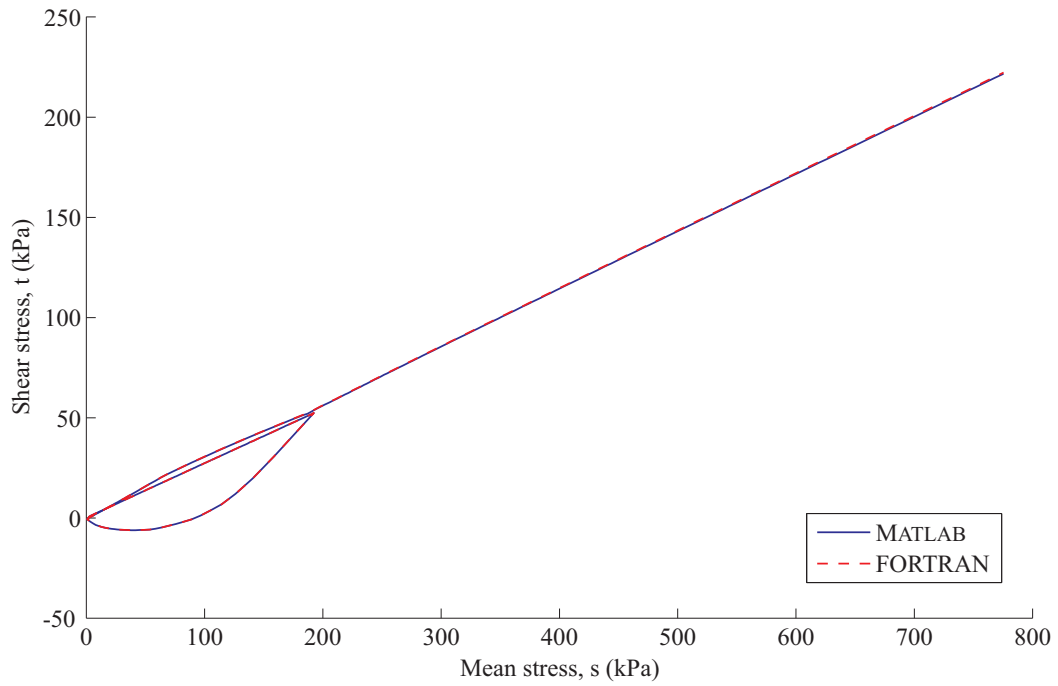

Figure B.2: Mean stress versus shear stress for swelling and recompression code comparison test

B.2 Theory code comparison

The differences in the MATLAB code between BRICK Theories 1 & 2 are given here.

Change to the calculation of RIKAP to correct kappa gradient using the beta effect.

Theory 1	Theory 2
RIKAP=RIOT/(RKAP-RIOT);	RIKAP=RIOTBB/(RKAP-RIOTBB); where: RIOTBB= ι/β_{mod}

Introduction of β_ϕ to lower increase in phi' caused by the beta effect.

Theory 1	Theory 2
-	BETMFI=1+BETA(2)*ELAMDA; BETRAT=BETMFI/BETMOD; SLJB=SL(JB)*BETRAT;

Change to PSRED(1) calculations to help convergence

Theory 1	Theory 2
PSRED(1)=T1*RIKAP+T2*RILAM;	PSRED(1)=((PSRED(1)-T2prev*RILAM)*RIKAP+T1*RIKAP)/(1+RIKAP)+T2*RILAM;

Introduction of new convergence criteria

Theory 1	Theory 2
-	if ITERBR<3 TOLSS=TOLSS*0.2; end

Change in the calculation of PSRED(>1), which controls the capacity for elastic shear strains and hence the changes in shear stress.

Theory 1	Theory 2
for JC=(2:NC) PSRED(JC)=SSM(JC) *DSS(1)*RIOTBB/ (FGK*SSM(1)*SSM(1)^1); end	for JC=(2:NC) DELF=BETA(1)*(DSN(1)-RLAM* log((SS(1)+DSS(1))/SS(1))); F=1+BETA(1)*(SN(1)+(DSN(1)*0.5)- ZERO(1)-RLAM*log(SSM(1)/ZERO(2))); DELFUF=DELF/F; if F<1 DELFUF=0; end PSRED(JC)=(SSM(JC)*RIOTBB/ (FGK*SSM(1)))*((1+DELFUF)* (DSS(1)/SSM(1)^1)+DELFUF); end

B.3 The Bricks on Ice model

The code for the implementation of the Bricks on Ice model is given in this section. Some new variables were created for the BOI model parameters and where an existing variable has been adopted for use in the BOI implementation, a 'v' has been placed after the variable name to denote 'viscous'.

```
function[DSS,DSNP,DSNB,ITERBR,SNT]=brickice3(SS,SN,ZERO,SNB...
,VOLP,NC,DSN,DSS,NB,SL,SNBP,TOLBR,RLAM,RKAP,RIOT,BETA,FGK,CREEP)

% Apply strain increment
PSRED=zeros(1,NC);
SNT=SN+DSN;
SSM=SS;
RILAM=RIOT/(RLAM-RIOT);
DSS=zeros(1,NC);
SNBV=SNB+CREEP;

% Iterate to find plastic and hence stress inc
Finish=0;
ITERBR=0;
```

```
while Finish==0
  ITERBR=ITERBR+1;
  IFAILB=0;

  % Modify RIOT for BETA effect
  T=(SS(1)+0.5*DSS(1))/ZERO(2);
  TT=(SN(1)+0.5*DSN(1)-ZERO(1)-RLAM*log(T));
  TT=max(TT,0);
  BETMOD=1+BETA*TT;
  RIOTBB=RIOT/BETMOD;
  %     RIKAP=RIOT/(RKAP-RIOT);
  RIKAP=RIOTBB/(RKAP-RIOTBB);
  DSNP=zeros(1,NC);
  DSNV=zeros(1,NC);

  % Calc brick movements and plastic strains
  for JB=(1:NB)
    T=(SS(1)+0.5*DSS(1))/ZERO(2);
    if T<=1e-15
      error('!!!Negative Mean Stress!!!');
    end
    T=0;                    % Reset T for each brick
    for JC=(1:NC)           % For each component
      DSNB(JC,JB)=0;        % Resetting to zero brick movements
      T1=SN(JC)+DSN(JC)-SNBV(JC,JB)-PSRED(JC);
      % Increase in strain on brick per component
      T=T+(T1*T1);
      % sum of components for brick
    end
    T=sqrt(T);
    % Vector length finding - root sum of squares
    SLJB=SL(JB);

    % T=distance of brick from new strain point or string length
    if T<=SLJB          % Elastic Strain
      for JC=(1:NC)
        DSNP(JC)=DSNP(JC)+(CREEP(JC,JB)*SNBP(JB));
        % Component Total movement
        DSNV(JC)=DSNV(JC)+(CREEP(JC,JB)*SNBP(JB));
        % Component Viscous movement
        % DSNB(JC,JB)=DSNB(JC,JB)+CREEP(JC,JB);
        DSNB(JC,JB)=DSNB(JC,JB)+PSRED(JC)+CREEP(JC,JB);
        % Total Brick movement
      end
    else                % Plastic Strain
      %Brick>string length from new strain point move brick by DSNB,
      %giving plastic strain DSNP
      T=(T-SLJB)/T;
      for JC=(1:NC)
        DSNB(JC,JB)=(SN(JC)+DSN(JC)-SNBV(JC,JB)-PSRED(JC))*T;
        % Max increase in strain on brick per component
        % proportionally reduced by T
        DSNP(JC)=DSNP(JC)+((DSNB(JC,JB)+CREEP(JC,JB))*SNBP(JB));
        % Component Total movement
        DSNV(JC)=DSNV(JC)+(CREEP(JC,JB)*SNBP(JB));
        % Component Viscous movement
        DSNB(JC,JB)=DSNB(JC,JB)+PSRED(JC)+CREEP(JC,JB);
        % Total Brick movement
```

```
    end
  end
end

% Compute PSRED(1) from volumetric strain
T2=max(0,(VOLP(1)+DSNP(1)-VOLP(2)-DSNV(1)));
T1=DSNP(1)-DSNV(1)-T2;
% DSNP(1)-DSNV(1)= Component String Plastic movement
PSRED(1)=T1*RIKAP+T2*RILAM;

% Compute DSS(1) and check against conversion criteria
TDSS=DSS(1);
% Reassign old increment of Mean Stress
DSS(1)=(exp((DSN(1)-DSNP(1))/RIOTBB)-1)*SS(1);
SSM(1)=SS(1)+0.5*DSS(1);
T=max(SSM(1),abs(DSS(1)));
TOLSS=T*TOLBR;
if abs(DSS(1)-TDSS)>TOLSS
  IFAILB=IFAILB+1;
end

% Compute PSRED(>1)from DSS(1)
ips=3;
BETA2=4;
if ips==1
  for JC=(2:NC)
    DELF=BETA2*(DSN(1)-RLAM*log((SS(1)+DSS(1))/SS(1)));
    F=1+BETA2*(SN(1)-ZERO(1)-RLAM*log(SS(1)/ZERO(2)));
    DELFUF=DELF/F;
    if F<1
      DELFUF=0;
    end
    PSRED(JC)=(SS(JC)*((1+DELFUF)*(DSS(1)/SSM(1))+DELFUF)*...
    RIOTBB/(FGK*SSM(1)^1));
  end
elseif ips==2
  for JC=(2:NC)
    DELF=BETA*(DSN(1)-RLAM*log((SS(1)+DSS(1))/SS(1)));
    F=1+BETA*(SN(1)+DSN(1)*0.5-ZERO(1)-RLAM*log(SSM(1)/ZERO(2)));
    DELFUF=DELF/F;
    if F<1
      DELFUF=0;
    end
  PSRED(JC)=(SSM(JC)*RIOTBB/(FGK*SSM(1)))*((1+DELFUF)*...
  (DSS(1)/SSM(1)^1)+DELFUF);
  end
else
  for JC=(2:NC)
  % This method leads to erroneous results
  % in the recompression phase
  PSRED(JC)=SSM(JC)*DSS(1)*RIOTBB/(FGK*SSM(1)*SSM(1)^1);
  % Only method to work with bricks on Ice
  end
end

if ITERBR==1
  continue
end
```

```
  % Find shear stresses DSS(>1) and check tolerance
  for JC=(2:NC)
    T=DSS(JC);
    DSS(JC)=(DSN(JC)-DSNP(JC))*SSM(1)^1*FGK/RIOTBB;
    if abs(DSS(JC)-T)>TOLSS/2
      IFAILB=IFAILB+1;
    end
  end

  % Check convergence min 7 max 50 iterations
  if ITERBR<50 && IFAILB>0
    for JC=(2:NC)
      SSM(JC)=SS(JC)+0.5*DSS(JC);
    end
  elseif ITERBR<7
    for JC=(2:NC)
      SSM(JC)=SS(JC)+0.5*DSS(JC);
    end
  else
    Finish=1;
  end
end
```

B.4 The strain rate dependency model

The code below implements the strain rate dependent approach formulated within MATLAB. In addition to the code below a configuration file must be used to control the routine, applying strain rates and monitoring stresses, as was done for both the BRICK and BOI implementations.

B.4.1 Man-led strain rate code

```
function[DSS,DSNP,DSNB,ITERBR,SNT,SLout,SLprev]=brickmsrd(Neu,...
SLprev,SS,SN,ZERO,SNB,VOLP,NC,DSN,DSS,NB,SL,SNBP,TOLBR,RLAM...
,RKAP,RIOT,BETA,FGK,CREEP,On)

SLr=SL;
if On>=1
  % Neu=1e-6; Set Neutral rate if required
  Vecstrain=0;
  for JC=1:NC
    Vecstrain=Vecstrain+(DSN(JC)^2);
  end
  Vecstrain=sqrt(Vecstrain);
  %
  SL=SLr*(1+(0.25*log((abs(Vecstrain)/Neu)+1)));
  SL(n)=SLr(n)*(1+0.1*asinh(Vecstrain/Neu));
  if On>=2; % Optional damping
    for n=1:10
      if SL(n)>SLprev(n)
        dSL=SL(n)-SLprev(n);
```

```
      else
        dSL=0.05*(SL(n)-SLprev(n));
      end
      SL(n)=SLprev(n)+dSL;
    end
  end
end
SLprev=SL;
SLout=SL/SLr;

% Apply strain increment
PSRED=zeros(1,NC);
SNT=SN+DSN;
SSM=SS;
RILAM=RIOT/(RLAM-RIOT);
DSS=zeros(1,NC);

% Iterate to find plastic and hence stress inc
Finish=0;
ITERBR=0;
while Finish==0
  ITERBR=ITERBR+1;
  IFAILB=0;
  % Modify RIOT for BETA effect
  T=(SS(1)+0.5*DSS(1))/ZERO(2);
  TT=(SN(1)+0.5*DSN(1)-ZERO(1)-RLAM*log(T));
  TT=max(TT,0);
  BETMOD=1+BETA*TT;
  RIOTBB=RIOT/BETMOD;
  RIKAP=RIOTBB/(RKAP-RIOTBB);
  DSNP=zeros(1,NC);
  DSNV=zeros(1,NC);

  % Calc brick movements and plastic strains
  for JB=(1:NB)
    T=(SS(1)+0.5*DSS(1))/ZERO(2);
    if T<=1e-15
      error('!!!Negative Mean Stress!!!');
    end
    T=0;  % Reset T for each brick
    for JC=(1:NC)  % For each component
      DSNB(JC,JB)=0;
      % Resetting to zero brick movements
      T1=SN(JC)+DSN(JC)-SNB(JC,JB)-PSRED(JC);
      % Increase in strain on brick per component
      T=T+(T1*T1);  % sum of components for brick
    end
    T=sqrt(T);
    % Vector length finding - root sum of squares
    % T=distance of brick from new strain point or string length
    SLJB=SL(JB);

    % Elastic Strain
    if T<=SLJB
      for JC=(1:NC)
        % Total Brick movement
        DSNB(JC,JB)=DSNB(JC,JB)+PSRED(JC);
      end
```

```
  % Plastic Strain
  else
  % Brick > string length from new strain point move brick by DSNB,
  % giving plastic strain DSNP
    Tout=(T-SLJB)/T;
    for JC=(1:NC)
      DSNB(JC,JB)=(SN(JC)+DSN(JC)-SNB(JC,JB)-PSRED(JC))*Tout;
      % Max increase in strain on brick per component proportionally
      % reduced by T
      DSNP(JC)=DSNP(JC)+(DSNB(JC,JB)*SNBP(JB));
      % Component Total movement
      DSNB(JC,JB)=DSNB(JC,JB)+PSRED(JC);
      % Total Brick movement
    end
  end
end

  % Compute PSRED(1) from volumetric strain
T2=max(0,(VOLP(1)+DSNP(1)-VOLP(2)-DSNV(1)));
T1=DSNP(1)-DSNV(1)-T2;

% DSNP(1)-DSNV(1)= Component String Plastic movement
PSRED(1)=T1*RIKAP+T2*RILAM;

% Compute DSS(1) and check against conversion criteria
TDSS=DSS(1);
% Reassign old increment of Mean Stress
DSS(1)=(exp((DSN(1)-DSNP(1))/RIOTBB)-1)*SS(1);
SSM(1)=SS(1)+0.5*DSS(1);
T=max(SSM(1),abs(DSS(1)));
TOLSS=T*TOLBR;
if abs(DSS(1)-TDSS)>TOLSS
  IFAILB=IFAILB+1;
end

% Compute PSRED(>1)from DSS(1)
ips=3;
% Choose calculation version
BETA2=4;
% Assign Beta-Phi
if ips==1
  for JC=(2:NC)
    DELF=BETA2*(DSN(1)-RLAM*log((SS(1)+DSS(1))/SS(1)));
    F=1+BETA2*(SN(1)-ZERO(1)-RLAM*log(SS(1)/ZERO(2)));
    DELFUF=DELF/F;
    if F<1
      DELFUF=0;
    end
    PSRED(JC)=(SS(JC)*((1+DELFUF)*(DSS(1)/SSM(1))+DELFUF)*...
    RIOTBB/(FGK*SSM(1)^1));
  end
elseif ips==2
  for JC=(2:NC)
    DELF=BETA*(DSN(1)-RLAM*log((SS(1)+DSS(1))/SS(1)));
    F=1+BETA*(SN(1)+DSN(1)*0.5-ZERO(1)-RLAM*...
    log(SSM(1)/ZERO(2)));
    DELFUF=DELF/F;
    if F<1
```

```
        DELFUF=0;
      end
      PSRED(JC)=(SSM(JC)*RIOTBB/(FGK*SSM(1)))*((1+DELFUF)*...
      (DSS(1)/SSM(1)^1)+DELFUF);
    end
  else
    for JC=(2:NC)
    % This method leads to erroneous results
    % in the recompression phase
      PSRED(JC)=SSM(JC)*DSS(1)*RIOTBB/(FGK*SSM(1)*SSM(1)^1);
    % Only method to work with bricks on Ice
    end
  end

  if ITERBR==1
    continue
  end

  % Find shear stresses DSS(>1) and check tolerance
  for JC=(2:NC)
    T=DSS(JC);
    DSS(JC)=(DSN(JC)-DSNP(JC))*SSM(1)^1*FGK/RIOTBB;
    if abs(DSS(JC)-T)>TOLSS/2
      IFAILB=IFAILB+1;
    end
  end

  % Check convergence min 7 max 50 iterations
  if ITERBR<50 && IFAILB>0
    for JC=(2:NC)
      SSM(JC)=SS(JC)+0.5*DSS(JC);
    end
  elseif ITERBR<7
    for JC=(2:NC)
      SSM(JC)=SS(JC)+0.5*DSS(JC);
    end
  else
    Finish=1;
  end
end
```

B.4.2 Brick-led strain rate code

```
function[DSS,DSNP,DSNB,ITERBR,SNT,SLout,SLprevious,Testmat]...
  =bricksrdtest2(Neu,SLprevious,SS,SN,ZERO,SNB,VOLP,NC,...
  DSN,DSS,NB,SL,SNBP,TOLBR,RLAM,RKAP,RIOT,BETA,FGK,On,Time)

SLr=SL;
SLout=zeros(1,10);

% Apply strain increment
SNT=SN+DSN;
SSM=SS;
RILAM=RIOT/(RLAM-RIOT);
DSS=zeros(1,NC);
PSRED=zeros(1,NC);
Vecstrain=zeros(1,10);
```

```
Testmat=0;

% Iterate to find plastic and hence stress inc
Finish=0;
ITERBR=0;

while Finish==0

  % Count number of Iterations
  ITERBR=ITERBR+1;
  % Reset Convergence Monitor
  IFAILB=0;

  % Modify RIOT for BETA effect
  T=(SS(1)+0.5*DSS(1))/ZERO(2);
  TT=(SN(1)+0.5*DSN(1)-ZERO(1)-RLAM*log(T));
  TT=max(TT,0);
  BETMOD=1+BETA*TT;
  RIOTBB=RIOT/BETMOD;
  RIKAP=RIOTBB/(RKAP-RIOTBB);
  DSNP=zeros(1,NC);

  % Calc brick movements and plastic strains
  for JB=(1:NB)
    T=(SS(1)+0.5*DSS(1))/ZERO(2);
    if T<=1e-15
      error('!!!Negative Mean Stress!!!');
    end
    T=0;  % Reset T for each brick
    for JC=(1:NC)  % For each component
      DSNB(JC,JB)=0;
      % Resetting to zero brick movements
      T1=SN(JC)+DSN(JC)-SNB(JC,JB)-PSRED(JC);
      % Increase in strain on brick per component
      T=T+(T1*T1);  % sum of components for brick
    end
    T=sqrt(T);
    % Vector length finding - root sum of squares
    % T=distance of brick from new strain point or string length
    SLJB=SL(JB);

    % Elastic Strain
    if T<=SLJB
      for JC=(1:NC)
        % Total Brick movement
        DSNB(JC,JB)=DSNB(JC,JB)+PSRED(JC);
      end
    % Plastic Strain
    else
    % Brick > string length from new strain point move brick by DSNB,
    % giving plastic strain DSNP
      Tout=(T-SLJB)/T;
      for JC=(1:NC)
        DSNB(JC,JB)=(SN(JC)+DSN(JC)-SNB(JC,JB)-PSRED(JC))*Tout;
        % Max increase in strain on brick per component proportionally
        % reduced by T
        DSNP(JC)=DSNP(JC)+(DSNB(JC,JB)*SNBP(JB));
        % Component Total movement
```

```
      DSNB(JC,JB)=DSNB(JC,JB)+PSRED(JC);
      % Total Brick movement
    end
  end
  % Applies only to first iteration
  % 'On' allows model to be switched on and off
  if ITERBR==1 && On==1;
    SLerr=1;
    % Convergence criteria for SRD model
    while SLerr>(SLr(JB)/10)
      Vecstrain(JB)=0;
      % Calculate vectoral strain rate
      for JC=1:NC
        Square=(DSNB(JC,JB))^2;
        Vecstrain(JB)=Vecstrain(JB)+Square;
      end
      Vecstrain(JB)=sqrt(Vecstrain(JB))/Time;

      % Monitor Calculated string length
      if Vecstrain(JB)>Vecstrain(1)
        Vecstrain(JB)=Vecstrain(1);
      end

      % Deassign string length
      SLprev(JB)=SL(JB);
      % Calculate SRD string lengths
      SL(JB)=((SLr(JB)*(1+(0.1*log((abs(Vecstrain(JB))/Neu)+1))))...
      +SLprev(JB))/2; %25 for ler

      if SL(JB)>=SLprevious(JB)
      % Allow instantaneous increase in String Lengths
      else
      % Calculate time dependent decay
        decay=-1.0683;
        Vecprevious(JB)=((exp(((SLprevious(JB)/SLr(JB))-1)/0.1))-1)*Neu;
        Tp=10^(7+(log10(Vecprevious(JB)/Neu)*decay));
        Tc=Tp+Time;

        % Apply rate dependant rule
        if Tc>2;
          CurVec(JB)=10^((max(0,(log10(Tc)-7)/(decay)))...
          +log10(Neu));
          SL(JB)=SLr(JB)*(1+(0.1*log((abs(CurVec(JB))/Neu)+1)));
          SL(JB)=SLprevious(JB)+0.05*(SL(JB)-SLprevious(JB));
        else
          SL(JB)=SLprevious(JB)+0.05*(SL(JB)-SLprevious(JB));
        end
      end
      Distance=DSNB(:,JB)*(T/(T-SLprev(JB)));
      DSNB(:,JB)=Distance*((T-SL(JB))/T);
      SLerr=SL(JB)-SLprev(JB);
    end
    SLout(JB)=SL(JB)/SLr(JB);
  end
end

% Compute PSRED(1) from volumetric strain
T2=max(0,(VOLP(1)+DSNP(1)-VOLP(2)-DSNV(1)));
```

```
T1=DSNP(1)-DSNV(1)-T2;

% DSNP(1)-DSNV(1)= Component String Plastic movement
PSRED(1)=T1*RIKAP+T2*RILAM;

% Compute DSS(1) and check against conversion criteria
TDSS=DSS(1);
% Reassign old increment of Mean Stress
DSS(1)=(exp((DSN(1)-DSNP(1))/RIOTBB)-1)*SS(1);
SSM(1)=SS(1)+0.5*DSS(1);
T=max(SSM(1),abs(DSS(1)));
TOLSS=T*TOLBR;
if abs(DSS(1)-TDSS)>TOLSS
  IFAILB=IFAILB+1;
end

% Compute PSRED(>1)from DSS(1)
ips=3;
% Choose calculation version
BETA2=4;
% Assign Beta-Phi
if ips==1
  for JC=(2:NC)
    DELF=BETA2*(DSN(1)-RLAM*log((SS(1)+DSS(1))/SS(1)));
    F=1+BETA2*(SN(1)-ZERO(1)-RLAM*log(SS(1)/ZERO(2)));
    DELFUF=DELF/F;
    if F<1
      DELFUF=0;
    end
    PSRED(JC)=(SS(JC)*((1+DELFUF)*(DSS(1)/SSM(1))+DELFUF)*...
    RIOTBB/(FGK*SSM(1)^1));
  end
elseif ips==2
  for JC=(2:NC)
    DELF=BETA*(DSN(1)-RLAM*log((SS(1)+DSS(1))/SS(1)));
    F=1+BETA*(SN(1)+DSN(1)*0.5-ZERO(1)-RLAM*...
    log(SSM(1)/ZERO(2)));
    DELFUF=DELF/F;
    if F<1
      DELFUF=0;
    end
    PSRED(JC)=(SSM(JC)*RIOTBB/(FGK*SSM(1)))*((1+DELFUF)*...
    (DSS(1)/SSM(1)^1)+DELFUF);
  end
else
  for JC=(2:NC)
  % This method leads to erroneous results
  % in the recompression phase
    PSRED(JC)=SSM(JC)*DSS(1)*RIOTBB/(FGK*SSM(1)*SSM(1)^1);
  % Only method to work with bricks on Ice
  end
end

if ITERBR==1
  continue
end

% Find shear stresses DSS(>1) and check tolerance
```

```
  for JC=(2:NC)
    T=DSS(JC);
    DSS(JC)=(DSN(JC)-DSNP(JC))*SSM(1)^1*FGK/RIOTBB;
    if abs(DSS(JC)-T)>TOLSS/2
      IFAILB=IFAILB+1;
    end
  end

  % Check convergence min 7 max 50 iterations
  if ITERBR<50 && IFAILB>0
    for JC=(2:NC)
      SSM(JC)=SS(JC)+0.5*DSS(JC);
    end
  elseif ITERBR<7
    for JC=(2:NC)
      SSM(JC)=SS(JC)+0.5*DSS(JC);
    end
  else
    Finish=1;
  end
end

VecPrev(1,:)=Vecstrain;
SLprevious=SL;
```

C

BRICK Program Modifications

C.1 Introduction

In the BRICK program, introduced in Section 3.5, the BRICK model was programmed in the FORTRAN language. To allow the easier modification of the code the original FORTRAN was translated into MATLAB and benchmarked against the BRICK program in Appendix B. In this Appendix the reverse translation of the SRD BRICK model is provided, along with the results of a SRS test and a creep test to show the model has been correctly implemented. This was an intermediate testing step, as further minor modifications to the code were needed to implement the time effects into the BRICK code within SAFE.

C.2 The Language Barrier

As the BRICK program contains much more code that the MATLAB implementation, only the key translated sections have been listed here. As there is no place to input the new variables into the code, the variables were hard coded into the routine for testing purposes:

```
C
C Set up SRDSL initial parameters
C
  SLr=SL
  RNEU=1.E-13
  RVISC=0.1
  RDEC=-1.0683
```

The core of the strain rate dependency behaviour is given in the code below:

```
C
C     Calculate Strain rate dependant String Lengths PER BRICK
C
  IF(ITERBR.EQ.1) THEN
    SLerr=1;
```

```
    DO 149 WHILE(SLerr.GT.(SLr(JB)/10))

    VECSTRAIN(JB)=0
    DO 140 JC=1,NC
140 VECSTRAIN(JB)=VECSTRAIN(JB)+(DSN(JC)*DSN(JC))
    VECSTRAIN(JB)=SQRT(VECSTRAIN(JB))
    IF(VECSTRAIN(JB).GT.VECSTRAIN(1)) VECSTRAIN(JB)=VECSTRAIN(1)
    IF(VECSTRAIN(JB).LT.1E-8) VECSTRAIN(JB)=0
    SLprev(JB)=SL(JB)
    RCORE=(ABS(VECSTRAIN(JB))/RNEU)+1
    SL(JB)=((SLr(JB)*(1+(RVISC*LOG(RCORE))))+SLprev(JB))/2
    DO 145 JC=1,NC
    DISTANCE=DSNB(JC,JB)*(T/(T-SLprev(JB)))
145 DSNB(JC,JB)=DISTANCE*((T-SL(JB))/T)

    IF (SL(JB).GT.SLprevious(JB)) THEN
      SL(JB)=SL(JB)
    ELSE
      VECPREVIOUS(JB)=((EXP(((SLprevious(JB)/SLr(JB))-1)/RVISC))-1)*RNEU
      Tp=10**(7+(LOG10(VECPREVIOUS(JB)/RNEU)*RDEC))
      Tc=Tp+1
      IF (Tc.GT.10) THEN
        MCENT=(LOG10(Tc)-7)/RDEC
        CURVEC(JB)=10**(MAX(0,MCENT)+LOG10(RNEU))
        SL(JB)=SLr(JB)*(1+(RVISC*LOG((ABS(CURVEC(JB))/RNEU)+1)))
        SL(JB)=SLprevious(JB)+0.05*(SL(JB)-SLprevious(JB))
      ELSE
        SL(JB)=SLprevious(JB)+0.05*(SL(JB)-SLprevious(JB))
    ENDIF
  ENDIF
  SLerr=SL(JB)-SLprev(JB)
149 END DO
```

C.3 Testing

Two tests were conducted to make sure the implementation into the BRICK program was functioning as expected. Test 1 involved a basic SRS test with a relaxation period, seen in Figure C.1. Test 2 involved an CRS stage followed by a period of creep and then by further applied strain, seen in Figure C.2. Both figures show isotach behaviour upon a change in strain rate. The stress relaxation test shows the lowering of stresses at constant volumetric strain and a rejoining of the initial compression line upon a recommencment of straining. The creep test shows the increase in volumetric strain at constant mean stress, with the path again rejoining the initial compression line as straining continued. The form of the behaviour is consistent with that shown in Chapter 5.

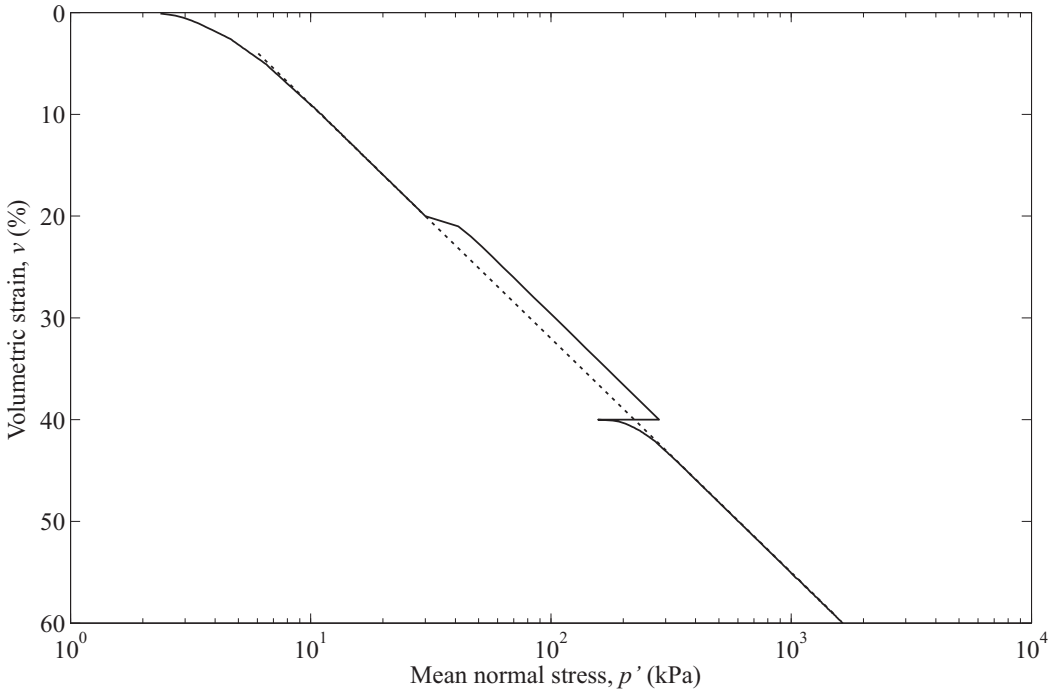

Figure C.1: Validation of the BRICK program - SRS and stress relaxation test

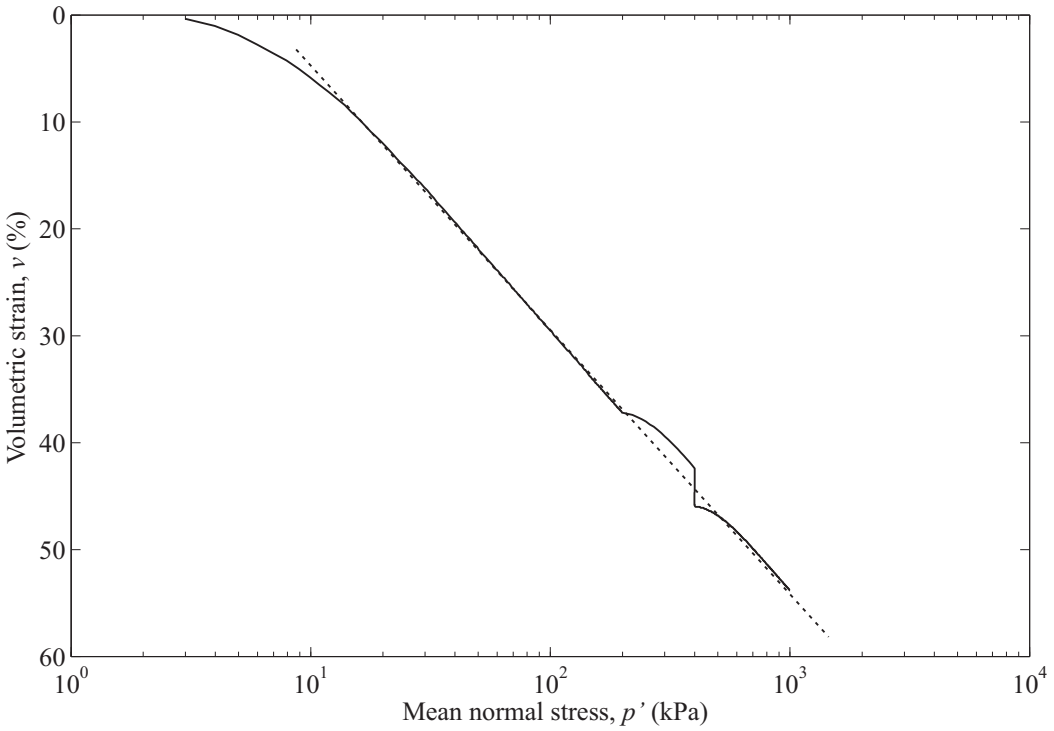

Figure C.2: Validation of the BRICK program - creep test

D

SAFE Modifications

D.1 Implementation into SAFE

Theoretically, copying the BRICKB routine from the BRICK program (Appendix C) into SAFE should be enough to implement the SRD BRICK model in the finite element program. In practice, while this ports the core programming, there are still other changes that need to be made to the SAFE program code. In the BRICK program the storage of variables is very easy as there is only a single point of calculation. In SAFE any variables such as the previous string lengths need to be stored for *every* gauss point. This can be done by utilising the spare space within the 6x6 'D' matrix:

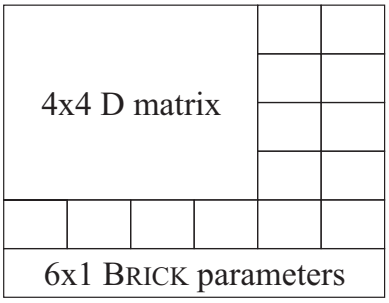

This leaves space within the matrix to store the previous string length variables which are required by the SRD BRICK routine as implemented by the following FORTRAN code:

```
    DO 115 JB=1,5
    SLprevious(JB)=D(JB,5)
115 SLprevious(JB+5)=D(JB,6)
```

SAFE has a built in concept of time in the form of the parameters CSECS and DSECS. CSECS is the cumulative time in seconds up to the end of the previous increment, while DSECS in the increment of time for the current increment. By introducing a

new variable DSECSb, the times for the current sub-increments can be split into the same proportion as the current sub-increments of strain. This allows a constant rate of strain across sub-increments.

The final variation of the SAFE BRICKB implementation of the SRD BRICK model was the inclusion of 'switches' to allow the new routine to be enabled and disabled and to assign parameters from the graphical user interface. The three SRD BRICK variables are also assigned FORTRAN variable names (the 'R' at the start denotes that it is a *real* variable and as such can take any value). The viscous constant, β, became RVISC, the decay constant, m, became RDEC and the reference strain rate, $\dot{\varepsilon}_{\text{ref}}$, became RNEU (the reference strain rate was originally called the neutral strain rate). These were implemented as switches in SAFE by the following FORTRAN code:

```
IF(RTEST(95).GT.0) THEN
  RVISC=RTEST(95)
  RDEC=RTEST(96)
  RNEU=RTEST(97)
  SRDSL=1
ELSE
    SRDSL=0
ENDIF
```

The variables RTEST(95-97) are created by the user interface of SAFE when the the SRD BRICK model is enabled in the analysis.

D.2 Finite Element Models and Runs

This section lists all the names of the attempted finite element runs completed with, where appropriate, a brief description of the assumption made. A copy of all the data files for the runs has been included on the DVD at the back of the thesis. Each run has other minor variants that are contained on the disc.

D.2.1 St James's Park

Completed finite element runs for the modelling of the volume loss experienced in the Westbound tunnel at St James's Park.

Addenbrooke Mesh	File for generation of mesh- no results.
Addenbrooke Mohr	Mohr-Coulomb model analysis.
Addenbrooke	Initial attempts at volume loss creation with reduction of stresses.
Addenbrooke Final	SRD run with full length strings to assess difference.
Addenbrooke Final Short	Final SRD run, with the string lengths halved.
Addenbrooke SRD	Initial attempt at varying the string length parameters using the SRD model. Original, Kanapathipillai (1996) and string lengths developed for the Gasparre (2005) work were tested.
Addenbrooke 09	Check on the effect of anisotropy.

D.2.2 Horseferry Road

Completed finite element runs for the modelling of the experienced heave in the deep basement at Horseferry Road.

Horseferry18.1	Initial run- no longer used.
Horseferry18.1 Consol	Consolidation analysis using a mean stress dependent permeability.
Horseferry18.1 Undrained	Undrained analysis during construction of the basement, switched to a consolidated material for the London Clay upon the completion of the base slab.
Horseferry18.1 Consol 2	Consolidation analysis of the construction and time dependent behaviour, using a constant value of permeability for the London Clay layer.
Horseferry18.1 Consol SRD	The same as analysis Consol but using the SRD Brick model with strings half the length of those in the previous runs.

E

Computing Requirements

E.1 Hardware

Both SAFE and MATLAB currently only allow a single thread to be processed at any one time. This means that the advantages of parallel processing are not utilised by either program, thus, multi-core processors will not speed up the computation times. This said if multiple instances of each program were run then multi-core processors would mean that each instance would compute in the same amount of time. The author recommends a fast dual-core processor, which at the time of writing would equate to a Intel Core2 Duo E8***. Higher processor clock speeds have a larger influence on the calculation time than increasing the number of cores for single thread applications.

The author built a PC specifically to decrease the computation times in SAFE. The specification is:

Processor:	Intel Core 2 Duo E8400 (3Ghz) overclocked to 4Ghz
Hard Drives:	2 x 640GB Western Digital in RAID 0
Memory:	4GB DDR2 PC8500 running at 1068Mhz
Graphics:	ATI Radeon 4870 512MB Edition
Power Supply:	CoolerMaster Silent 700M
Cooling:	Custom assembled water cooling system.

This represents one of the fastest systems currently available for running SAFE. Almost any computer is capable of running SAFE, but the time taken increases as the system specification lowers. Below is the lowest specification that would lead to a acceptable computation time.

Minimum requirements:

Processor:	Intel Core 2 Duo 1.86Ghz+ (the more L2 cache the better)
Hard Drive:	320GB single platter
Memory:	2GB DDR2 PC6400
Graphics:	Onboard is acceptable
Power Supply:	400W+

E.2 Software

All the work was completed by PCs running the Microsoft Windows XP Professional operating system with the latest service pack updates. The programs used to generate the work done in this thesis are listed below:

- **MATLAB version 7.0.0.19920** - used for the recreation of the BRICK model and the development of the SRD modifications to the program.
- **Oasys SAFE 18.1** - For running the finite element analyses. Currently this is the only version of SAFE that has the SRD modifications.
- **Oasys BRICK 17.9** - Used to test the SRD BRICK routine at a basic level before implementation into SAFE and to check that the MATLAB recreation of the code was working correctly.
- **Compaq Studio 6.6C** - Used to develop the BRICK and SAFE programs.
- **Corel Draw 12** - Used to create and edit vector based figures.
- **Adobe Photoshop CS3** - Used to created and edit raster based figures.
- **Plot Digitizer** - Used to create data sets from existing figures, available from http://plotdigitizer.sourceforge.net.
- **TeXnicCenter 1.0RC** - Used to write the thesis in Latex, available from http://www.texniccenter.org.